# Analytical modelling of the aeroacoustic performances of self-ventilated motors used in railway applications

Mohcene Oulmi

## To cite this version:

Mohcene Oulmi. Analytical modelling of the aeroacoustic performances of self-ventilated motors used in railway applications. Other. Ecole Centrale de Lyon, 2022. English. NNT : 2022ECDL0004 . tel-04287898

**HAL Id: tel-04287898**
**https://theses.hal.science/tel-04287898v1**

Submitted on 15 Nov 2023

N° d'ordre NNT: 2022ECDL0004

**THÈSE de DOCTORAT DE L'UNIVERSITÉ DE LYON**
**opérée au sein de l'École Centrale de Lyon**

**École Doctorale N° 162**

**Mécanique Énergétique Génie Civil Acoustique**

**Spécialité de doctorat : Acoustique**

Soutenue publiquement le 19/09/2022, par

**Mohcene OULMI**

---

# Modélisation analytique des performances aéroacoustiques des moteurs auto-ventilés de traction ferroviaire

---

Devant le jury composé de :

| | | | |
|---|---|---|---|
| Pr. | Roger, Michel | École Centrale de Lyon | Directeur de thèse |
| Pr. | Aurégan, Yves | Le Mans Université | Rapporteur |
| Pr. | Moreau, Stéphane | Université de Sherbrooke | Rapporteur |
| Pr. | Galland, Marie-Annick | École Centrale de Lyon | Présidente du jury |
| Dr. | Boualem, Benali | Alstom Transport | Examinateur |
| Dr. | Guédel, Alain | Retraité du CETIAT | Examinateur |
| Dr. | De Laborderie, Hélène | Safran Aircraft Engines | Examinatrice |

# Abstract

The reduction of the noise generated by traction motors used in railway applications has become a very important criterion during their design phase. The overall noise comes from three main sources, of vibrational, aerodynamic and magnetic natures. Among these contributions, aerodynamic noise is dominant at high rotation speeds. It is generated by the ventilation system of the motor. The use of numerical simulations to predict this noise can be very expensive and time-consuming when several geometrical parameters need to be tested. Analytical methods are suitable at the early design stage, due to their low computational time. This work is dealing with the analytical modelling of sound generation and propagation inside the ventilation systems integrated in electric motors. In the first step of this work, the geometry of each motor is divided into several subdomains, in which the sound field can be expressed as a sum of orthogonal modes. The analytical solution in each subdomain requires the determination of the modal amplitudes of the different acoustic fields. The use of the mode-matching technique allows one to calculate these coefficients by imposing the continuity of the physical quantities at each interface between two subdomains with different geometrical properties. A two-dimensional mode-matching technique is first applied to the sound generation and propagation in the fixed part of a totally-enclosed motor. The latter mainly consists of guide vanes and cooling channels. The equivalent dipoles are used in this work to model the sound generation by the impingement of the impeller wakes on the guide vanes. Then, the sound propagation in this coupled system is reproduced by the use of two transmission models which take into account the influence of the wall-thickness. An iterative method is used in order to take into account the multiple reflections of the acoustic waves between the guide vanes and the cooling channels. The mode-matching technique is then extended to significantly more complicated architectures in order to investigate how the sound can propagate inside the ventilation system of an open motor. The results obtained by the analytical models have been validated by comparison with the finite element method. A good agreement between the two methods was found. The diffraction of acoustic waves by periodic rows of rotating channels is addressed in the last part of this work in order to investigate how sound can be transmitted through the rotating parts of traction motors. These analytical models are used for parametric studies to predict the acoustic resonances that can take place in the ventilation systems integrated in traction motors.

**Keywords:** Aeroacoustics, acoustic resonance, electric motors, sound propagation, waveguides, Mode-matching method.

# Résumé

La réduction du bruit des moteurs électriques de traction ferroviaire est devenue un critère très important lors de leur phase de conception. Le bruit global rayonné par ces moteurs est de natures vibratoire, magnétique et aérodynamique. Parmi ces contributions, le bruit aérodynamique est dominant aux vitesses élevées. Il est généré par le système de ventilation du moteur. L'utilisation des simulations numériques pour prédire ce bruit est très couteuse dans la phase de conception du moteur, où plusieurs paramètres géométriques doivent être testés. Les méthodes analytiques sont avantageuses lors de cette phase de conception en raison de leur faible coût de calcul. Ce travail a pour but de modéliser la génération et la propagation du bruit à l'intérieur des systèmes de refroidissement des moteurs électriques, en utilisant une approche analytique, basée sur la technique de raccordement modal. Dans la première étape de cette étude, la géométrie de chaque moteur est décomposée en plusieurs sous-domaines de géométrie simplifiée dans lesquels l'équation de Helmholtz est séparable. Cette étape de modélisation permet de trouver une solution analytique exprimée sous forme d'une somme de modes orthogonaux. La solution analytique dans chaque élément géométrique nécessite la détermination des coefficients modaux des différents champs acoustiques. L'utilisation de la méthode de raccordement modal permet de calculer ces derniers en écrivant la continuité des grandeurs physiques à chaque interface entre deux milieux de propriétés géométriques différentes. Cette méthode est d'abord appliquée dans un cadre bidimensionnel à la génération et à la propagation du bruit à l'intérieur de la partie fixe des moteurs fermés. Cette dernière est composée principalement d'une grille d'aubes et de canaux de refroidissement. L'utilisation de dipôles équivalents a permis de modéliser la génération de bruit par l'impact des sillages du ventilateur sur la grille d'aubes. La propagation du bruit dans ce système couplé est reproduite par l'utilisation de deux modèles de transmission qui prennent en compte l'influence de l'épaisseur des parois. Une méthode itérative est utilisée par la suite afin de prendre en compte les réflexions multiples des ondes acoustiques entre la grille d'aubes et les canaux de refroidissement. La technique de raccordement modal est ensuite étendue à des architectures beaucoup plus complexes pour étudier la propagation du son à l'intérieur du système de ventilation d'un moteur ouvert. Les résultats obtenus par les différents modèles analytiques sont comparés par la suite à des calculs par la méthode des éléments finis pour validation. La diffraction des ondes acoustiques par des réseaux de canaux tournants a été abordée dans la dernière partie de ce travail, afin de simuler la transmission du bruit à travers les parties tournantes des moteurs. Ces modèles analytiques sont utilisés pour des études paramétriques afin de prédire les résonances acoustiques qui peuvent se produire dans les systèmes de ventilation des moteurs.

**Mots-clés:** Résonance acoustique, moteurs électriques, propagation acoustique, aéro-acoustique, Méthode de raccordement modal.

# Remerciements

Cette thèse de doctorat a été réalisée dans le cadre d'une collaboration entre Alstom et le Laboratoire de Mécanique des Fluides et d'Acoustique (LMFA, UMR CNRS 5509) de l'Ecole Central de Lyon (ECL). Elle a été financée par le groupe Alstom et l'ANRT (Association Nationale de la Recherche et de la Technologie). De plus, ce travail a été mené dans le cadre du Labex CeLyA (ANR-10-LABEX-0060) de l'Université de Lyon, dans le programme «Investissements d'Avenir»(ANR-16-IDEX-0005) opéré par l'ANR (Agence Nationale de la Recherche).

Je souhaite tout d'abord remercier mon directeur de thèse exceptionnel, Michel Roger, pour la qualité remarquable de son encadrement, sa disponibilité sans faille, ses conseils avisés et sa grande bienveillance tout au long de ces trois années de thèse. Grâce à lui que j'ai eu l'opportunité d'acquérir une multitude de connaissances enrichissantes. Je tiens également à adresser mes remerciements à Benali Boualem, qui m'a encadré avec dévouement au sein d'Alstom à Ornans. Sa confiance en moi et le partage de ses précieuses connaissances dans le domaine de la fabrication des moteurs de traction ferroviaire ont été d'une grande valeur pour mon travail. Un grand merci s'adresse également à Quentin Trahard pour nos échanges réguliers et sa collaboration à distance, qui ont joué un rôle important dans l'avancement de ma thèse.

Je souhaite exprimer ma profonde gratitude envers Stéphane Moreau et Yves Aurégan qui m'ont fait l'honneur d'être les rapporteurs de mes travaux de thèse. Leur contribution précieuse et leurs éclairages ont grandement enrichi mon travail. Mes remerciements s'étendent également à Marie-Annick Galland, présidente du jury de la thèse, ainsi qu'à Alain Guedel et Hélène de Laborderie, membres du jury, pour leur engagement et leur disponibilité.

Je tiens à remercier chaleureusement tous les membres du site Alstom à Ornans pour leur accueil chaleureux lors de mes courtes visites, en particulier: Coralie, Eric, Ronan, Christophe, Didier, Jean-Pierre, Andry et Gille.

Une part importante de ma gratitude est réservée à l'ensemble des membres du Laboratoire de Mécanique des Fluides et d'Acoustique (LMFA). Je tiens à exprimer ma reconnaissance envers Marie-Gabrielle Perriaux, la secrétaire du laboratoire, pour sa disponibilité et sa réactivité exceptionnelles. Je remercie Christophe Bailly, un directeur de laboratoire exemplaire, pour sa bienveillance envers les membres du laboratoire. Merci à Laurent Pouilloux pour sa résolution efficace des problèmes informatiques et sa bonne humeur. Je

suis reconnaissant envers Alexis Giauque, Lionel Le Penven et Mikhael Gorokhovski, qui m'ont apporté une aide précieuse avant le début de ma thèse. Je remercie Stéphane Auber pour ses conseils lors de mes comités de suivi de thèse. Je n'oublie pas les permanents du centre acoustique (KCA): Marc Jacob, Gilles Robert, Vincent Clair, Didier Dragna, Édouard Salze, Antonio Pereira, Pascal Souchotte et Pierre Roland.

Je tiens à souligner que le bon déroulement de cette thèse n'aurait pas été possible sans la formidable ambiance qui règne au sein du laboratoire. Mes collègues doctorants, stagiaires et post-doctorants ont été des compagnons de route exceptionnels. Je commence par remercier mes collègues du bureau A18: Mathieu, Pierre, Codor, Laura, Hugo, Alexis, Daher et Loïc. Un merci spécial à Étienne pour sa gentillesse exceptionnelle, ses encouragements, et nos mémorables séances de boxe anglaise. Merci à Léo pour nos discussions précieuses sur la méthode de raccordement modal et pour avoir été un excellent prof de ski. Merci à Gabriele pour sa contribution en tant que membre de l'équipe *mode-matching* du laboratoire. Raphaël, malgré notre compétition amicale sur les pistes de ski, je t'adresse mes remerciements. Miguel, Yann et Danny, merci pour votre humour contagieux. Mes remerciements s'étendent également à Jean, Elina, Igor, Giorgos, Nacho, Ariane, Daniel, Arthur, Courtney, Simon, Yuanyuan, Antoni, Jules, Amal, Yuling, David, Thomas, Paul, Vianny, Marion et Bertrand, qui ont tous joué un rôle essentiel dans cette aventure scientifique enrichissante.

Pour conclure, je tiens à exprimer ma reconnaissance la plus profonde envers mes parents, mon frère, mes sœurs et ma femme ♡ pour leur soutien inconditionnel, leur amour, leur patience et leur compréhension tout au long de mes études. Je ne serais pas là où je suis aujourd'hui sans leur présence et leur aide précieuse. Je ne peux pas terminer ces remerciements sans mentionner Madame Si-Youcef, Monsieur Benzaid, ainsi que tous les autres membres de ma famille et mes amis qui ont été présents tout au long de cette incroyable aventure.

# Contents

# List of Figures

# List of Tables

# Nomenclature

## Latin characters

| | |
|---|---|
| $(r, \theta, x)$ | Cylindrical coordinates |
| $(x, y, z)$ | Cartesian coordinates |
| $\underline{\mathbf{X}}$ | Matrix |
| $\mathbf{X}$ | Vector |
| $a$ | Channel width [m] |
| $a_1$ | Inter-vane channel width [m] |
| $a_2$ | Cooling channel width [m] |
| $A_n$ | Modal amplitude of the incident wave |
| $B$ | Number of blades |
| $b$ | Channel wall-thickness [m] |
| $b_1$ | Vane thickness [m] |
| $b_2$ | Wall-thickness of the cooling channels [m] |
| $c_0$ | Speed of sound [m/s] |
| $d$ | Distance between the guide vanes and the cooling channels [m] |
| $D_q$ | Modal coefficients of the downstream field |
| $f$ | Frequency [Hz] |
| $f_{nj}(r)$ | Radial shape function |
| $h$ | Annulus thickness [m] |
| $H_b$ | Block width [m] |
| $H_n^{(1)}$ | Hankel function of the first kind of order $n$ |
| $H_n^{(2)}$ | Hankel function of the second kind of order $n$ |
| $I$ | Identity matrix |
| $i_{\max}$ | Number of iterations |
| $j$ | Radial modal order of the incident wave |
| $J_n$ | Bessel function of the first kind of order $n$ |
| $k_0$ | Acoustic wave number [rad.m$^{-1}$] |
| $K_{nj}$ | Radial wave number of the mode $(n, j)$ [rad.m$^{-1}$] |
| $k_{nj}^{\pm}$ | Axial wave number of the mode $(n, j)$ [rad.m$^{-1}$] |
| $L$ | Channel length [m] |
| $L_1$ | Vane chord [m] |

| | |
|---|---|
| $L_2$ | Cooling channel length [m] |
| $L_{S_d}$ | Stator channel length [m] |
| $m_1$ | Vane index |
| $m_2$ | Channel index |
| $M_z$ | Azimuthal Mach number |
| $n$ | Azimuthal modal order of the incident wave |
| $N_Q$ | Number of azimuthal modes propagating inside the channels |
| $N_S$ | Number of positive azimuthal modes propagating in the unbounded mediums |
| $p$ | Acoustic pressure [Pa] |
| $r_0$ | Cylindrical cut radius [m] |
| $r_1$ | Inner radius [m] |
| $r_2$ | Outer radius [m] |
| $r_d$ | Channel radius [m] |
| $R_s$ | Modal coefficients of the reflected field |
| $S_1$, $S_2$ | Cross-sectional areas used for the calculation of the acoustic powers [m$^2$] |
| $t$ | Time [s] |
| $T_s$ | Modal coefficients of the transmitted field |
| $U_q$ | Modal coefficients of the upstream field |
| $V$ | Number of channels |
| $v$ | Acoustic velocity [m/s] |
| $v \cdot \mathbf{e}_{\boldsymbol{r}}$ | Radial velocity [m/s] |
| $v \cdot \mathbf{e}_{\boldsymbol{x}}$ | Axial velocity [m/s] |
| $V_1$ | Number of stator vanes |
| $V_2$ | Number of cooling channels |
| $x_0$ | Axial position of the channel inlet interface [m] |
| $x_i$ | Emission position of the incident wave [m] |
| $x_L$ | Axial position of the channel outlet interface [m] |
| $Y_n$ | Bessel function of the second kind of order $n$ |

# Greek characters

| | |
|---|---|
| $\alpha$ | Azimuthal wave number [rad.m$^{-1}$] |
| $\Delta\mathcal{P}$ | Acoustic power error |
| $\Gamma$ | Pressure-radial velocity vector |
| $\gamma$ | Iteration index |
| $\lambda$ | Acoustic wavelength [m] |
| $\mathcal{E}$, $\mathcal{Q}$, $\mathcal{X}$, $\mathcal{Y}$ | Projection integrals of radial eigenfunctions |
| $\mathcal{K}$, $\mathcal{F}$, $\mathcal{W}$, $\mathcal{G}$ | Projection integrals of radial eigenfunctions |

| | |
|---|---|
| $\mathcal{O}$, $\mathcal{B}$, $\Upsilon$, $\mathcal{A}$ | Projection integrals of radial eigenfunctions |
| $\mathcal{P}$ | Acoustic power [W] |
| $\Omega$ | Impeller rotational Speed [rad/s] |
| $\omega$ | Angular frequency [rad/s] |
| $\phi$ | Acoustic potential |
| $\Pi_n$ | Interference function |
| $\Psi$ | Eigenfunction |
| $\Psi^*$ | Complex conjugate of the eigenfunction |
| $\rho$ | Density [kg/m$^3$] |
| $\tau_s$ | Decay rate |
| $\theta_i$ | Propagation angle of the incident wave [rad] |
| $\varphi$, $\Lambda$ | Projection integrals of azimuthal eigenfunctions |
| $\Xi$ | Pressure-axial velocity vector |
| $\xi$ | Relative angles between impeller blades [rad] |

# Superscripts and subscripts

| | |
|---|---|
| (1), (2) | Superscripts used for the guide vanes and the cooling channels |
| $+, -$ | Superscripts used to indicate the propagation in the positive and negative x directions respectively |
| $2D$, $3D$ | Superscripts used for the two-dimensional and three-dimensional simulations |
| $i, r, d, u, t$ | incident, reflected, downstream channel, upstream channel, transmitted components |
| $s, q, \mu, \nu$ | Modal orders |
| $()^*$ | Complex conjugate |
| $()^{[T]}$ | Transpose matrix |

# Abbreviations

| | |
|---|---|
| LBM | Lattice Boltzmann method |
| RANS | Reynolds-averaged Navier–Stokes |

# Introduction

## General context

During the last years the noise generated by traction motors used in railway applications has become a very big environmental issue that needs to be reduced at the early design stage. The overall noise comes from three main sources, of mechanical, aerodynamic and magnetic natures (see Figure 1). During the acceleration phase, the overall noise is dominated by the magnetic contribution, which is related to the vibrations induced by the electromagnetic forces. On the other hand, at high rotational speeds the aerodynamic noise becomes the dominant contribution.This noise is generated by the ventilation system of the motor. The use of the latter is essential to maintain the motor components at allowable operating temperatures. It evacuates some of the unwanted heat produced by the electrical components of the motor, such as the windings. Various kinds of cooling systems are commonly used in practical applications. However, the most used are self-ventilated motors due to their small size. The typical configuration of a self-ventilated motor is illustrated in Figure 2. It is composed of various components such as a radial impeller, rotor, stator, housing, shaft, and windings. As can be seen, the cooling fan is mounted on the motor shaft. It rotates in the same direction and at the same rotational

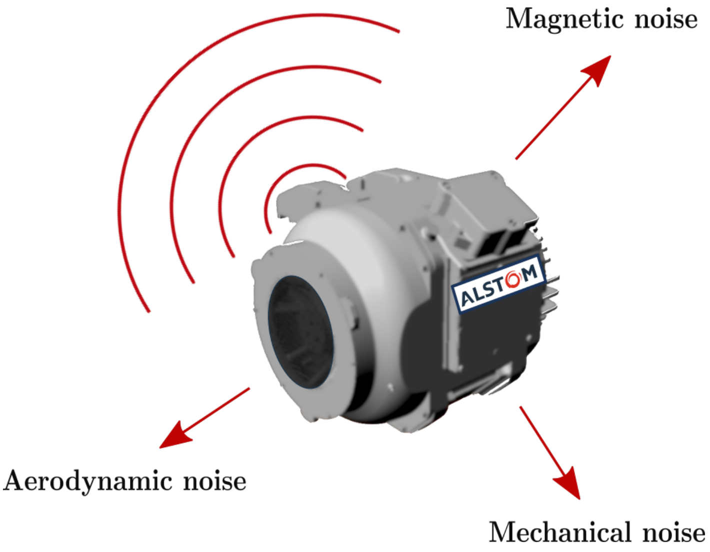

**Figure 1:** Noise sources of a traction motor.

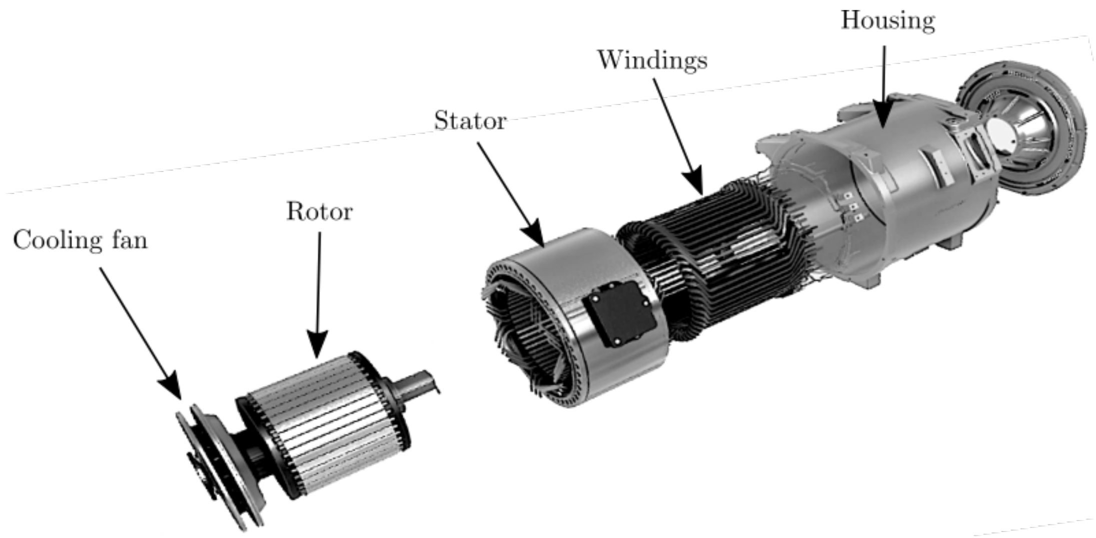

**Figure 2:** Typical elements of a self-ventilated motor used in railway applications.

speed as the motor. This cooling architecture allows the motor size to be reduced, by integrating directly the cooling fan inside the motor, and avoids using ventilation systems of large dimensions. On the other hand, the cooling process is not well optimized, since the flow provided by the fan depends mainly on the rotational speed of the motor. Consequently, the latter is poorly cooled at low rotational speeds, and sufficiently cooled at high rotational speeds. Therefore, in order to ensure the necessary airflow required for the cooling process, the motor speed must be sufficiently high. Two kinds of architectures of self-ventilated motors can be found in most practical applications:

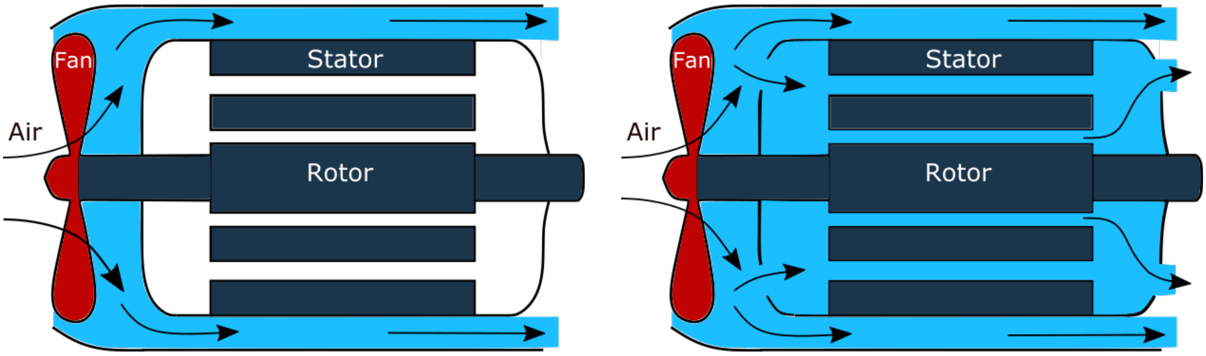

**(a)** **(b)**

**Figure 3:** (a) Totally-enclosed motor. (b) Open motor.

- **Totally-enclosed motors** (Figure 3a): in these architectures the motor components are not in direct contact with the cooling air provided by the fan, in order to protect them from ferrous metals and dust. They consist mainly of internal and external circuits separated by a rigid wall. In the external circuit, the air passes only around the motor frame. This circuit is mainly composed of a radial impeller, guide vanes and the cooling channels. In contrast, the hottest parts of the motor are cooled by the air circulating in the inner circuit. The heat absorbed by the air is then evacuated by conduction through the walls separating the two circuits, and then by convection between the walls and the air of the external circuit.

- **Open motors** (see Figure 3b): when the motor power increases, the temperature of the hottest parts of the motor becomes very high, and the cooling technique used in totally-enclosed motors becomes inefficient. Another way to improve the cooling process is to use the open architectures to allow the air to be in direct contact with the hottest parts of the motor. However, the air inside these ventilations systems passes through three different circuits: the ventilating holes integrated in the stator core, the ventilating channels integrated in the rotor core, and the air gap.

However, reducing the cooling system noise without affecting the aerodynamic and thermal performance of the motor is one of the main goals of motor designers. The thermal performance can be improved by increasing the airflow in the ventilation system. Unfortunately, the aerodynamic noise also increases rapidly with the latter. It should be kept in mind that the latter can be controlled by either reducing the acoustic sources generated in the motor, by improving its aerodynamic performance, or by limiting the transmission of acoustic waves outside the motor. In such complex configurations, the aerodynamic noise is generated by the cooling fan [61, 47] and by the interaction of turbulent flows with obstacles [68, 69, 73]. Among these contributions, the noise generated by the cooling fan is dominant. Many techniques of noise reduction in similar centrifugal fans (see Figure 4) have been already reported in the literature [49, 48, 78, 101, 102, 77]. These practical recommendations are very useful when the fan noise is radiated in conditions assimilated to free field. In the case of a traction motor, a part of the noise generated by the cooling fan is directly radiated outside the motor, and another part is transmitted through all components of the ventilation system, giving rise to a complicated confined acoustic field (see Figure 5). The fan noise can therefore be amplified when the

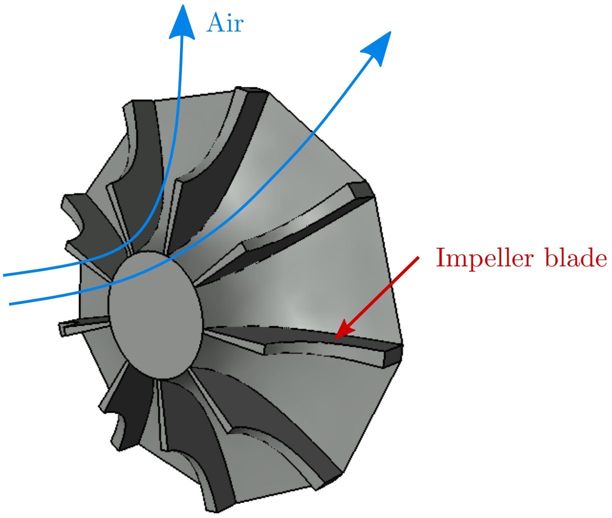

**Figure 4:** Typical configuration of a radial impeller integrated in traction motors

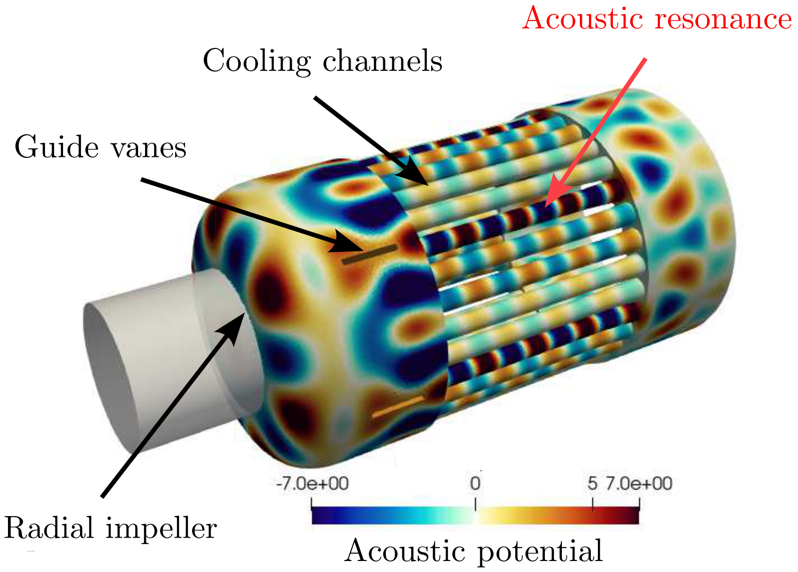

**Figure 5:** An example of propagation of acoustic waves inside the ventilation system integrated in a totally-enclosed motor (this configuration will be addressed in Chapter 1). Instantaneous acoustic potential field.

resonant frequencies of the ventilation system are excited by the blade passing frequency harmonics. To avoid that, the resonant frequencies must be identified during the design stage, in order to give the correct dimensions of the ventilation system.

The use of numerical simulations to predict the aerodynamic noise becomes more and more affordable in industrial context, especially with the growing use of the LBM (Lattice Boltzmann Method) [64, 21, 82]. Yet they can be expensive or not applicable when repeated computations must be performed, typically to investigate variable configurations involving numerous parameters. The key issue is that all geometrical details, needed for the simulations, are often not available at the early design stage. In contrast, analytical approaches are well suited and attractive at that stage, because they rely on a simplified geometry and perform with very low computational times. In a complicate architecture various analytical models of noise propagation must be set up as a successive combination of sub-models. The analytical solution of the problem is not known in the whole domain, but it can be defined in sub-domains with simplified geometry. More than a possible drawback, this has the advantage of highlighting the acoustic properties of each sub-domain separately. Many works on sound transmission in ducts with discontinuities have been reported in the literature [97, 98, 23, 93, 3, 7, 8, 16, 56]. The simplest model is the one-dimensional model which is valid at relatively low frequencies, when only plane waves can propagate inside a duct. This model can be used, for instance, to characterise the performance of mufflers used in automotive engines [76, 66, 75, 32, 74]. It was extended to arbitrary frequency by the use of the mode-matching technique [3, 7]. This technique is used to determine the modal amplitudes of the different acoustic fields generated by the diffraction of an incident wave at an interface separating two sub-domains with different properties. It is applied to electromagnetic [72] and acoustic waves [90, 59, 91, 19, 81, 45] in the frequency domain.

A key feature of all the configurations investigated in this work is that they contain a radial impeller. The transmission of acoustic waves through the impeller blades in a similar case, with sources located outside the impeller and sound transmission upstream towards the inlet, has been already investigated by Roger and Ingenito [90, 59, 60], based on three successive sub-models. The first one, was developed by Roger [90] for the scattering of a converging spiral wave by the trailing edges of the impeller blades by the use of the mode-matching technique. Then, the propagation in the inter-blades channels was addressed by Ingenito *et al* [59] using a slowly varying bent-duct approach [20]. Finally, the diffraction of the acoustic waves propagating in the inter-blade channels by the leading-edges of impeller blades was investigated again by the mode-matching method. These different sub-models can be used as guidelines in this study for the cooling fans integrated in traction motors.

# Objectives

The purpose of the present work is to provide a pre-design calculation tool with very low computational time, to be able to perform several parametric studies. This tool will be used in the early design stage to optimize the aeroacoustic performance of the ventilation systems integrated in traction motors used in railway applications. The methodology used in this work consists in decomposing the different architectures presented previously into generic components addressed separately.

The first part of this study (Chapter 1) is devoted to the sound generation and propagation inside the stationary part of the ventilation system integrated in totally-enclosed motors, using a two dimensional approach based on the mode-matching method. Two kinds of configurations are investigated in this chapter. The first one is assumed to be perfectly periodic in the azimuthal direction, and the second one is truncated.

The mode-matching technique is then applied in Chapter 2 to the sound propagation in the stationary part of an open motor.

The effects of the relative motion between a stator and a rotor on the sound propagation mechanism are investigated in Chapter 3, in order to understand how sound can be transmitted through the rotating parts of traction motors.

The last part of this work (Appendix C) deals with the aeraulic performance of self-ventilated motors, keeping in mind that the study is aimed at proposing a method for globally reducing noise and losses.

Curved walls and continuously varying cross-sections of some sub-systems could be addressed, using the multimodal analysis [70, 42, 40, 81, 4, 44]. This has not been considered in the present work.

# Chapter 1

# Analytical modelling of sound propagation in a totally-enclosed motor

## 1.1 Introduction

This chapter is devoted to sound propagation inside the ventilation system integrated in a totally enclosed motor. A typical configuration of the latter is shown in Figure 1.1. It consists of a radial impeller, guide vanes and cooling channels. A part of the noise generated by the cooling fan is radiated from the motor inlet, and another part is transmitted through the guide vanes and the cooling channels. A poorly designed ventilation system can amplify the sound generated by the fan, when the blade passing frequency harmonics coincide with its resonance frequencies. To avoid this problem, the resonance frequencies of the ventilation system must be identified during the design stage. Analytical methods are suitable at this stage, due to their low computational time. In

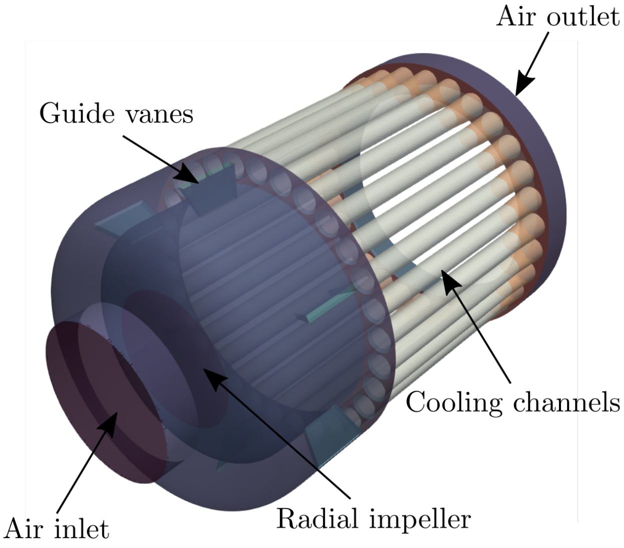

**Figure 1.1:** Typical configuration of a totally-enclosed motor used in train

contrast, the geometry must be simplified to be able to solve the problem mathematically. The methodology used in this work consists in decomposing the geometry into generic components addressed separately. In the present context, only the system consisting of guide vanes and cooling channels is considered (see Figure 1.2). Two mechanisms are investigated in this chapter. The first one, is the transmission of oblique plane waves generated by the radial impeller through a system consisting of guide vanes and cooling channels, and the second one is the sound generation by the impingement of the impeller wakes on the guide vanes.

## 1.2 Problem description

As a first step, the dimensional analysis is used in this section to identify the most important parameters, which may have a significant influence on the acoustic response of the ventilation system. The analytical modelling of sound propagation in such a complex geometry requires some simplifications. The typical configuration of the ventilation system integrated in a totally enclosed motor is shown in Figure 1.2. It consists of $V_1$ guide vanes and $V_2$ cooling channels with circular cross-section $r_c$, separated by a certain distance $d$. The two annular ducts located upstream the guide vanes and downstream the cooling channels are assumed to be semi-infinite. Therefore, the acoustic waves reflected by the ends of the geometry will not be considered in the present work. In railway applications, traction motors must rotate in both directions to allow trains to go back and forth. To maintain aerodynamic performance for any direction of rotation, designers need to use an impeller with purely radial blades and guide vanes with zero stagger angle and camber. This simplify drastically the geometry of the guide-vanes. Furthermore, the vanes must have a certain thickness in order to be able to support the mechanical forces of the motor. This, should be included in the present analysis. At most frequencies of interest,

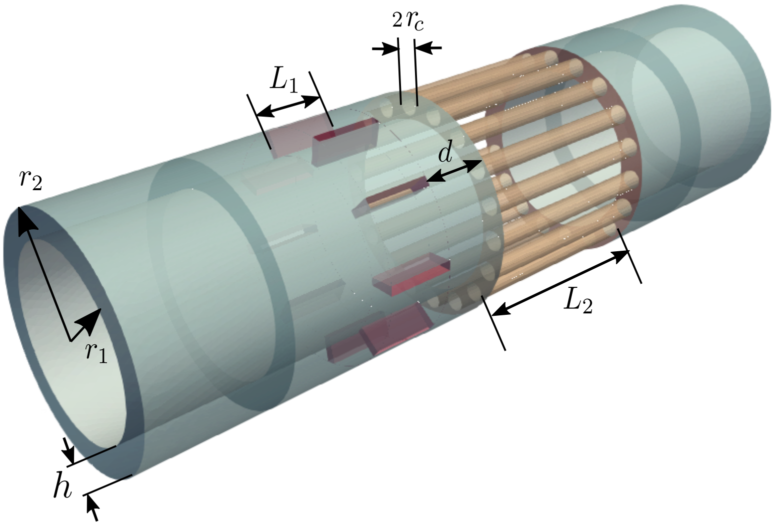

**Figure 1.2:** Typical configuration of the ventilation system used in a totally enclosed motor

the annulus-thickness, the height of vanes and the channel cross-section are smaller than acoustic wavelengths $r_c/\lambda < h/\lambda << 1$. Up to a certain frequency, no radial higher-order mode can propagate in the ventilation system. The scattering of acoustic waves occurs only in the azimuthal direction of the geometry $(\theta)$, which may justify the use of a two dimensional approach to investigate primary technological effects. For this an unwrapped cylindrical cut of the ventilation system is described in Cartesian coordinates (see Figure 1.3b).

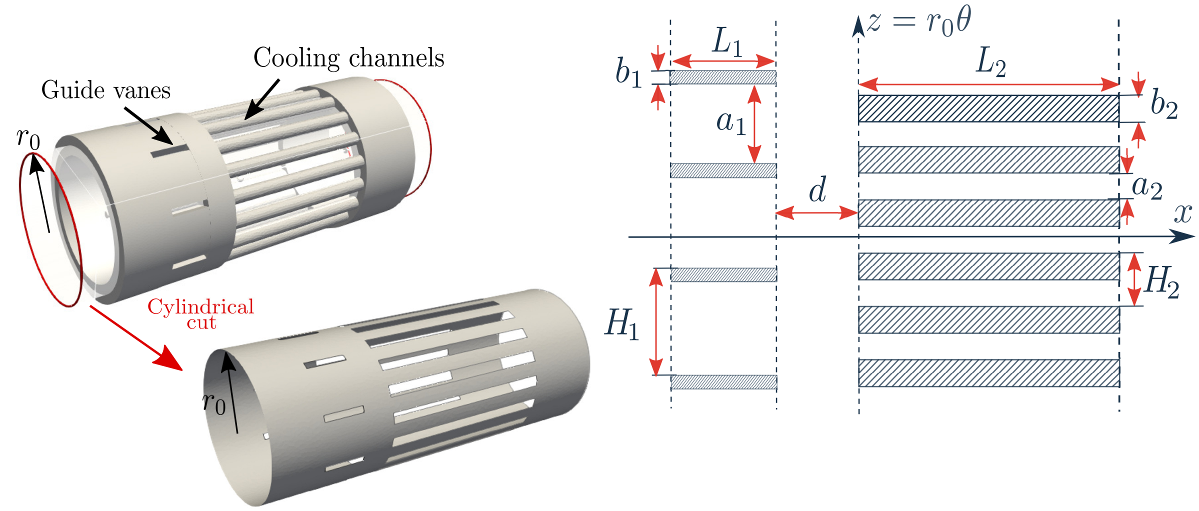

**(a)** **(b)**

**Figure 1.3:** (a) Typical configuration of the ventilation system used in traction motors , (b) Unwrapped representation of a cylindrical cut at $r_0$

The geometry can now be considered as two periodic rows of thick-walled channels separated by a distance $d$. The vanes and channels walls have respectively thicknesses $b_1$ and $b_2$ and are assumed to be perfectly rigid. The inter-vane channels and the cooling channels widths are respectively given by $a_1 = 2\pi r_0/V_1 - b_1$ and $a_2 = 2\pi r_0/V_2 - b_2$. In practice, these parameters must be evaluated from the dimensions of the realistic configuration. For that, it is more convenient to use the ratios $a_1/H_1$ and $a_2/H_2$ to describe the vanes and channels widths, where $H_1$ and $H_2$ are given by $H_1 = 2\pi r_0/V_1$ and $H_2 = 2\pi r_0/V_2$. These ratios vary from 0 when the channels are fully closed to 1 when fully open. The relationship between transverse dimensions of the two-dimensional geometry (Figure 1.3b) and those of the three-dimensional configuration (Figure 1.2) is given by $a_2/H_2 = r_c^2 V_2/(r_2^2 - r_1^2)$.

In most practical applications, the flow inside the ventilation system has a low Mach number $(M_0 < 0.1)$, and its effects on sound propagation are neglected in this investigation. Moreover, the effect of the latter is generally ignored in the case of a multimodal propagation of acoustic waves in the presence of a step discontinuity, because there is no simple way to take it into account.

The acoustic waves generated by the radial impeller propagate in the plenum towards the guide vanes. Each wave is considered as an oblique plane wave propagating with an angle $\theta_i$ defined by its modal order $n$ and its angular frequency $\omega$. These waves are scattered by the guide vanes, generating upstream and downstream acoustic fields. A part of the acoustic waves is transmitted through a row of cooling channels. These waves are partially reflected by the latter, generating an upstream field. Back-and-forth acoustic waves develop between the guide vanes and the cooling channels as shown in Figure 1.4.

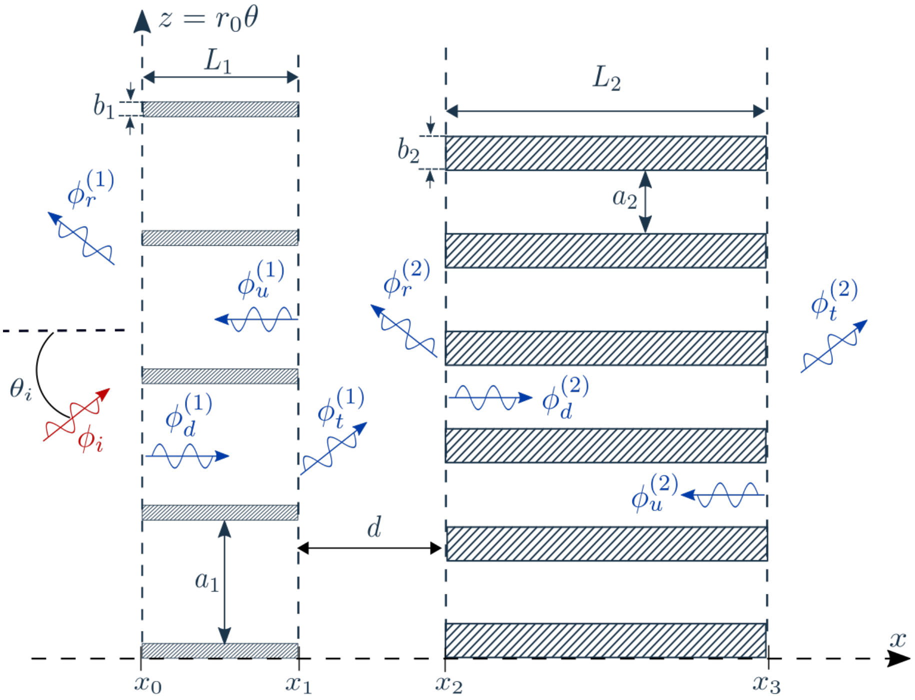

**Figure 1.4:** Two-dimensional unwrapped representation of the scattering of an acoustic wave by a system composed of two periodic rows of thick-walled channels

The response of this coupled system to any acoustic excitation may depend only on non-dimensional parameters :

$$\frac{\mathcal{P}_{(r,t)}}{\mathcal{P}_i} = \mathcal{F}\left(\frac{a_1}{H_1}, \frac{a_2}{H_2}, \frac{d}{L_1}, \frac{L_1}{a_1}, \frac{L_2}{a_2}, \frac{L_2}{a_2}, V_1, V_2, \frac{\alpha_i}{k_i}, k_0 h\right) \tag{1.1}$$

where $\mathcal{P}_{(r,t)}$ represents the acoustic power of the reflected ($\mathcal{P}_r$) or the transmitted field ($\mathcal{P}_t$), and $\mathcal{P}_i$ is the incident acoustic power.

The most straightforward way to study the propagation of sound in such a complex geometry is to split the system into two main subsystems addressed separately. They correspond respectively to the guide vanes and the cooling channels. The transmission problem can therefore be studied using two independent transmission sub-models. The outputs of each model are used as inputs of the other one. The consideration of the multiple reflections of the acoustic waves generated in the space between the two subsystems can be achieved iteratively.

Before investigating the sound propagation in this coupled system, it is appropriate to examine the response of a single isolated subsystem to an oblique plane wave. This subsystem can be either the guide vanes or the cooling channels. Since the shapes of guide vanes and cooling channels are not considered in the two-dimensional configuration (Figure 1.3b), only one transmission model needs to be developed to investigate the scattering of any incident wave. This will be presented in details in the next section.

## 1.3 Scattering of an oblique plane wave

This section is restricted to the diffraction of an oblique plane wave by a single periodic row of thick-walled channels. The acoustic response of this problem can be obtained by using the mode-matching method. The latter is usually applied to deal with problems of transmission of waves at an interface separating two mediums with different physical or geometrical properties, which includes electromagnetic [72, 6, 55, 100] and acoustic waves [90, 59, 91, 92, 18, 17, 58, 62]. It is applied in the frequency domain on the Helmholtz equation. It allows calculating the modal amplitudes of the different acoustic fields generated by the diffraction. This technique is usable when the geometry can be considered as the junction of several subdomains. The geometry investigated in this section is depicted in Figure 1.5. The channel walls have a thickness $b$ and are assumed to be perfectly rigid. The channel width is $a = 2\pi r_0/V - b$, $V$ being the number of channels.

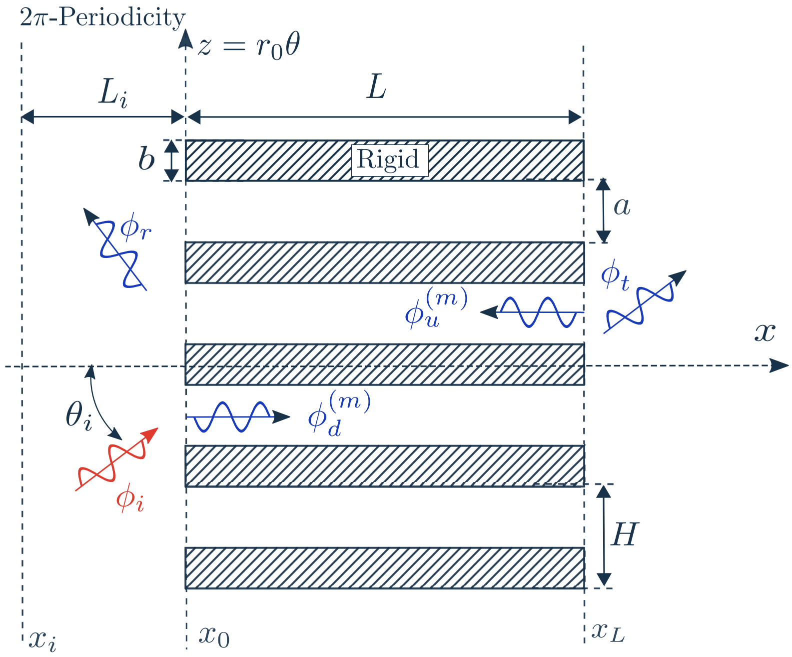

**Figure 1.5:** Two-dimensional unwrapped representation of the scattering of an acoustic wave through a row of thick-walled channels. Incident wave (red), waves generated by the diffraction of the incident wave (blue).

The incident wave of potential $\phi_i$ is scattered at the interface $x = x_0$ and generates reflected waves $\phi_r$ propagating upstream of the interface and transmitted waves $\phi_d$ into the channels. The latter propagate downstream to the open ends of channels $x = x_L$, generating a reflected field $\phi_u$ in the channels and a transmitted downstream field $\phi_t$. The mode matching technique can be used in four successive steps:

- Dividing the geometry into subdomains in which the Helmholtz equation is separable.
- Describing the sound field as a sum of orthogonal modes in each subdomain.
- Matching the acoustic fields at each interface using the continuity of pressure and axial velocity.
- Solving the matching equations by matrix inversion to get the modal modal amplitudes of the different acoustic fields.

### 1.3.1 Acoustic Potentials

The mathematical expressions of the different acoustic fields in each subdomain are obtained by solving the Helmholtz equation in a two-dimensional Cartesian coordinate system. All the acoustic fields are described by their acoustic potentials. A time harmonic factor $\mathrm{e}^{-\mathrm{i}\omega t}$ is implicitly assumed throughout this work. The Helmholtz equation is given by:

$$\frac{\partial^2\phi(x,z)}{\partial x^2}+\frac{\partial^2\phi(x,z)}{\partial z^2}+k_0^2\phi(x,z)=0 \tag{1.2}$$

where $k_0=\omega/c_0$ is the wavenumber, $\omega$ the angular frequency and $c_0$ denotes the sound speed. The analytical solution of the above equation can be found using the separation of variables. The acoustic pressure and the axial velocity are related to the acoustic potential by the following equations:

$$\begin{cases} p(x,z)=\mathrm{i}\omega\rho_0\phi(x,z) & \text{(1.3a)} \\ v(x,z)\cdot\mathbf{e}_{\boldsymbol{x}}=\dfrac{\partial\phi(x,z)}{\partial x} & \text{(1.3b)} \end{cases}$$

The incident wave $\phi_i$ is considered as an oblique plane wave emitted at the position $x_i$, and propagates upstream the interface $x_0$ with a propagation angle $\theta_i$. Because of the $2\pi$-periodicity in $\theta$, the perimeter of the cylindrical cut must be a multiple of the acoustic wavelength projected on the $z$ direction $2\pi r_0=n\lambda_z$, where $\lambda_z=2\pi/\alpha_i$, and $n$ being the number of azimuthal lobes ($n\in\mathbf{Z}$) (see Figure 1.6). The azimuthal wave number is calculated by $\alpha_i=n/r_0$. The acoustic potential of the incident waves is given by

$$\phi_i(x,z)=A_i\mathrm{e}^{\mathrm{i}\alpha_i z}\mathrm{e}^{\mathrm{i}k_i^+(x-x_i)} \tag{1.4}$$

with

$$\alpha_i=k\sin(\theta_i)=\frac{n}{r_0},\quad k_i^+=\sqrt{k_0^2-\alpha_i^2}$$

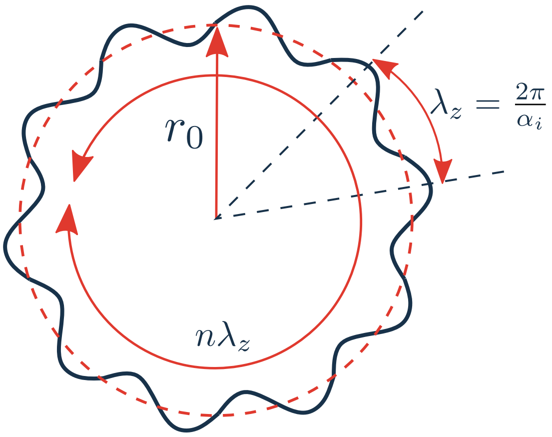

**Figure 1.6:** Number of azimuthal lobes

For a given frequency, the axial wave number $k_i^+$ can be real or pure imaginary. This corresponds respectively to cut-on and cut-off waves. The acoustic fields generated upstream and downstream the channels can be expressed as

$$\phi_r(x,z) = \sum_{s=-\infty}^{+\infty} R_s \mathrm{e}^{\mathrm{i}\alpha_s z} \mathrm{e}^{\mathrm{i}k_s^-(x-x_0)} \tag{1.5}$$

$$\phi_t(x,z) = \sum_{s=-\infty}^{+\infty} T_s \mathrm{e}^{\mathrm{i}\alpha_s z} \mathrm{e}^{\mathrm{i}k_s^+(x-x_L)} \tag{1.6}$$

with

$$\alpha_s = \frac{n+sV}{r_0}, \quad k_s^\pm = \pm\sqrt{k_0^2 - \alpha_s^2}$$

In each channel, the acoustic field must satisfy the Helmholtz equation with the rigid-wall boundary condition on $z = 0$ and $z = a$. Since the incident wave $\phi_i$ propagates with an angle $\theta_i$, the channels will not be excited in the same way. A phase-shift between the adjacent channels must be taken into account. The acoustic potentials of the downstream $\phi_d^{(m)}$ and the upstream $\phi_u^{(m)}$ propagating waves in the $m^{\mathrm{th}}$ channel are given by:

$$\phi_d^{(m)}(x,z) = \sum_{q=0}^{+\infty} D_q^0 \mathrm{e}^{imn2\pi/V} \cos\left(\alpha_q\left[z - m\frac{2\pi r_0}{V}\right]\right) \mathrm{e}^{\mathrm{i}k_q^+(x-x_0)} \tag{1.7}$$

$$\phi_u^{(m)}(x,z) = \sum_{q=0}^{+\infty} U_q^0 \mathrm{e}^{imn2\pi/V} \cos\left(\alpha_q\left[z - m\frac{2\pi r_0}{V}\right]\right) \mathrm{e}^{\mathrm{i}k_q^-(x-x_L)} \tag{1.8}$$

with

$$\alpha_q = q\frac{\pi}{a}, \quad k_q^\pm = \pm\sqrt{k_0^2 - \alpha_q^2}$$

The factor $\mathrm{e}^{imn2\pi/V}$ accounts for the phase-shift between adjacent channels.

### 1.3.2 Matching equations

The modal coefficients involved in Equations 1.5, 1.7, 1.8 and 1.6 represent the only unknowns of the problem. They need to be determined by using the mode-matching method. The number of equations needed to solve this problem is equal to $2V+2$. Since the channels are phase-shifted by a factor $\mathrm{e}^{\mathrm{i}mn2\pi/V}$, the matching equations need to be written for only the reference channel $m=0$ to reduce the number of unknowns. Then, the modal amplitudes in the adjacent channels are computed by $D_q^m = D_q^0\mathrm{e}^{\mathrm{i}mn2\pi/V}$ and $U_q^m = U_q^0\mathrm{e}^{\mathrm{i}mn2\pi/V}$. In the reference channel, the model can be reduced to a transmission problem with a step discontinuity as shown in Figure 1.7.

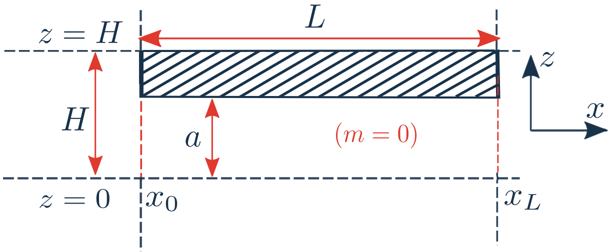

**Figure 1.7:** Reference channel

The matching equations are obtained by imposing the continuity of the acoustic pressure and the axial velocity on both interfaces of the channels $x=x_0$ and $x=x_L$. To account for the wall-thickness, an additional equation is introduced in order satisfy the rigid-wall boundary condition on the front face and the back face of the wall. This condition corresponds to a vanishing normal velocity $v.\mathbf{n} = v.\mathbf{e_x} = 0$.

#### 1.3.2.1 Channel inlet $(x=x_0)$

At the inlet interface (see Figure 1.8), the matching equations are written as

$$\begin{cases} p_i(x_0,z)+p_r(x_0,z) = p_d^{(0)}(x_0,z)+p_u^{(0)}(x_0,z) & ,0\leq z\leq a \quad (1.9a)\\ v_i(x_0,z)\cdot\mathbf{e_x}+v_r(x_0,z)\cdot\mathbf{e_x} = v_d^{(0)}(x_0,z)\cdot\mathbf{e_x}+v_u^{(0)}(x_0,z)\cdot\mathbf{e_x} & ,0\leq z\leq a \quad (1.9b)\\ v_i(x_0,z)\cdot\mathbf{e_x}+v_r(x_0,z)\cdot\mathbf{e_x} = 0 & ,a<z\leq H \quad (1.9c)\end{cases}$$

After replacing the expressions of acoustic pressure and axial velocity in Eq 1.9a and Eq 1.9b, we obtain:

$$\begin{cases} A_i\mathrm{e}^{\mathrm{i}\alpha_i z}\mathrm{e}^{\mathrm{i}k_i^+L_i} + \sum_{s=-\infty}^{+\infty} R_s\mathrm{e}^{\mathrm{i}\alpha_s z} = \sum_{q=0}^{+\infty}\left(D_q^0 + U_q^0\mathrm{e}^{-\mathrm{i}k_q^- L}\right)\cos(\alpha_q z) & (1.10a)\\ A_ik_i^+\mathrm{e}^{\mathrm{i}\alpha_i z}\mathrm{e}^{\mathrm{i}k_i^+L_i} + \sum_{s=-\infty}^{+\infty} R_sk_s^-\mathrm{e}^{\mathrm{i}\alpha_s z} = \sum_{q=0}^{+\infty}\left(k_q^+D_q^0 + k_q^-U_q^0\mathrm{e}^{-\mathrm{i}k_q^- L}\right)\cos(\alpha_q z) & (1.10b)\end{cases}$$

The next step is to perform a modal projection of Equations 1.10a and 1.10b to eliminate the $z$ variation. These equations are reduced by using the orthogonality of the

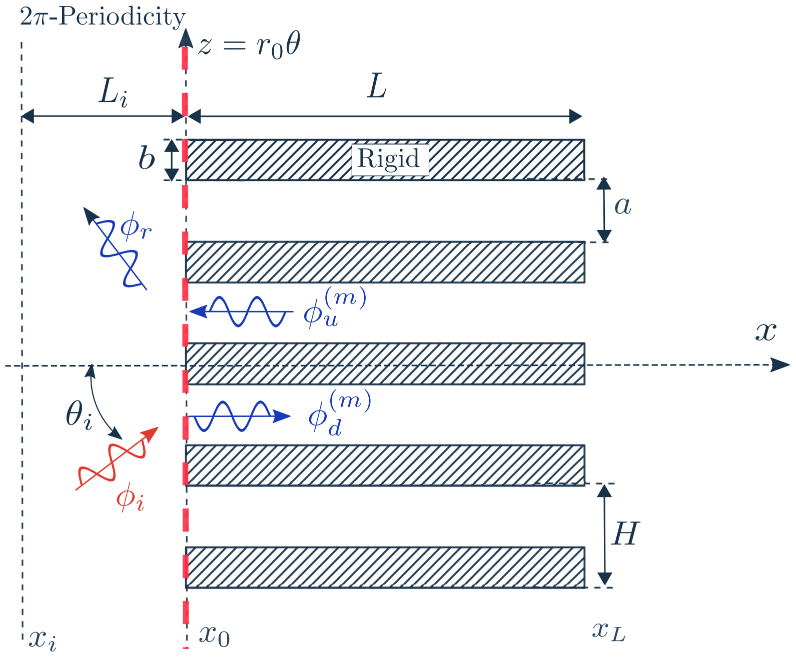

**Figure 1.8:** Acoustic potentials generated by the scattering of the incident wave at the inlet interface $x = x_0$.

eigenfunctions. The orthogonality relation is given by

$$\int_0^a \Psi_\beta(z)\Psi^*_{\beta'}(z)\mathrm{d}z = 0, \quad \text{if} \quad \beta \neq \beta' \tag{1.11}$$

where $\Psi^*_{\beta'}(z)$ is the complex conjugate of the eigenfunction $\Psi_\beta(z)$.

The use of the two sets of eigenfunctions for the modal projections is necessary in the case of a step discontinuity [53, 88, 3]. The acoustic pressure equation 1.10a must be projected on the basis related to the reference channel $\cos(\alpha_\mu z)$.

$$\int_0^a \{p_i(x_0,z) + p_r(x_0,z)\}\cos(\alpha_\mu z)\,\mathrm{d}z = \int_0^a \left\{p_d^{(0)}(x_0,z) + p_u^{(0)}(x_0,z)\right\}\cos(\alpha_\mu z)\,\mathrm{d}z \tag{1.12}$$

where $\alpha_\mu = \dfrac{\mu\pi}{a}$

In contrast, the velocity equation 1.10b needs to be projected on the eigenfunction related to the unbounded medium $\mathrm{e}^{-\mathrm{i}\alpha_\nu z}$

$$\int_0^a \{v_i(x_0,z)\cdot\mathbf{e}_{\boldsymbol{x}} + v_r(x_0,z)\cdot\mathbf{e}_{\boldsymbol{x}}\}\,\mathrm{e}^{-\mathrm{i}\alpha_\nu z}\mathrm{d}z = \int_0^a \left\{v_d^{(0)}(x_0,z)\cdot\mathbf{e}_{\boldsymbol{x}} + v_u^{(0)}(x_0,z)\cdot\mathbf{e}_{\boldsymbol{x}}\right\}\mathrm{e}^{-\mathrm{i}\alpha_\nu z}\mathrm{d}z \tag{1.13}$$

where $\alpha_\nu = \nu\frac{2\pi}{H}$

To obtain the relationship between the continuity of the axial velocity and the rigid-wall boundary condition, Equation 1.9c should be written in a different form

$$\int_0^H \{v_i(x_0,z)\cdot\mathbf{e}_{\boldsymbol{x}} + v_r(x_0,z)\cdot\mathbf{e}_{\boldsymbol{x}}\}\,\mathrm{e}^{-\mathrm{i}\alpha_\nu z}\mathrm{d}z = \int_0^a \{v_i(x_0,z)\cdot\mathbf{e}_{\boldsymbol{x}} + v_r(x_0,z)\cdot\mathbf{e}_{\boldsymbol{x}}\}\,\mathrm{e}^{-\mathrm{i}\alpha_\nu z}\mathrm{d}z \tag{1.14}$$

Combining Equations 1.13 and 1.14, we get

$$\int_0^H \left\{ v_i(x_0,z)\cdot\mathbf{e}_{\boldsymbol{x}} + v_r(x_0,z)\cdot\mathbf{e}_{\boldsymbol{x}} \right\} \mathrm{e}^{-\mathrm{i}\alpha_\nu z}\mathrm{d}z = \int_0^a \left\{ v_d^{(0)}(x_0,z)\cdot\mathbf{e}_{\boldsymbol{x}} + v_u^{(0)}(x_0,z)\cdot\mathbf{e}_{\boldsymbol{x}} \right\} \mathrm{e}^{-\mathrm{i}\alpha_\nu z}\mathrm{d}z \tag{1.15}$$

Using this new velocity equation, the rigid-wall boundary condition is implicitly taken into account in the mathematical formulation of the problem.

After accounting for the orthogonality of the eigenfunctions, the matching equations become:

$$\begin{cases} A_i \mathrm{e}^{\mathrm{i}k_i^+ L_i}\Lambda_{\mu i} + \displaystyle\sum_{s=-\infty}^{+\infty} R_s \Lambda_{\mu s} = \left( D_\mu^0 + U_\mu^0 \mathrm{e}^{-\mathrm{i}k_\mu^- L} \right) \dfrac{a}{2}(1+\delta_{\mu 0}) & (1.16\text{a}) \\ A_i k_i^+ \mathrm{e}^{\mathrm{i}k_i^+ L_i} H\delta_{\nu 0} + R_\nu k_\nu^- H = \displaystyle\sum_{q=0}^{+\infty} \left( D_q^0 - U_q^0 \mathrm{e}^{-\mathrm{i}k_q^- L} \right) k_q^+ \varphi_{\nu q} & (1.16\text{b}) \end{cases}$$

The projection integrals $\Lambda_{\mu i}$, $\Lambda_{\mu s}$ and $\varphi_{\nu q}$ are calculated analytically:

$$\Lambda_{\mu i} = \int_0^a \mathrm{e}^{\mathrm{i}\alpha_i z}\cos(\alpha_\mu z)\mathrm{d}z = \begin{cases} \dfrac{\mathrm{i}\alpha_i\left[1-(-1)^\mu \mathrm{e}^{-\mathrm{i}\alpha_i a}\right]}{\alpha_i^2-\alpha_\mu^2} & \text{, if } \alpha_\mu \neq \alpha_i \\ \dfrac{a}{2}(1+\delta_{\mu 0}) & \text{, if } \alpha_\mu = \alpha_i \end{cases} \tag{1.17}$$

$$\Lambda_{\mu s} = \int_0^a \mathrm{e}^{\mathrm{i}\alpha_s z}\cos(\alpha_\mu z)\mathrm{d}z = \begin{cases} \dfrac{\mathrm{i}\alpha_s\left[1-(-1)^\mu \mathrm{e}^{-\mathrm{i}\alpha_s a}\right]}{\alpha_s^2-\alpha_\mu^2} & \text{, if } \alpha_\mu \neq \alpha_s \\ \dfrac{a}{2}(1+\delta_{\mu 0}) & \text{, if } \alpha_\mu = \alpha_s \end{cases} \tag{1.18}$$

$$\varphi_{\nu q} = \int_0^a \cos(\alpha_q z)\mathrm{e}^{-\mathrm{i}\alpha_\nu z}\mathrm{d}z = \begin{cases} \dfrac{\mathrm{i}\alpha_\nu\left[(-1)^q \mathrm{e}^{-\mathrm{i}\alpha_\nu a}-1\right]}{\alpha_\nu^2-\alpha_q^2} & \text{, if } \alpha_q \neq \alpha_\nu \\ \dfrac{a}{2}(1+\delta_{q 0}) & \text{, if } \alpha_q = \alpha_\nu \end{cases} \tag{1.19}$$

#### 1.3.2.2 Outlet interface ($x = x_L$)

The matching equations at the channel outlet $x = x_L$ (see Figure 1.9) are derived in the same manner as for the interface $x_0$:

$$\begin{cases} p_d^{(0)}(x_L,z) + p_u^{(0)}(x_L,z) = p_t(x_L,z) & ,0 \leq z \leq a \quad (1.20\text{a}) \\ v_d^{(0)}(x_L,z)\cdot\mathbf{e}_{\boldsymbol{x}} + v_u^{(0)}(x_L,z)\cdot\mathbf{e}_{\boldsymbol{x}} = v_t(x_L,z)\cdot\mathbf{e}_{\boldsymbol{x}} & ,0 \leq z \leq a \quad (1.20\text{b}) \\ v_t(x_L,z)\cdot\mathbf{e}_{\boldsymbol{x}} = 0 & ,a \leq z \leq H \quad (1.20\text{c}) \end{cases}$$

After replacing the expressions of acoustic pressure and axial velocity in Equations 1.20a

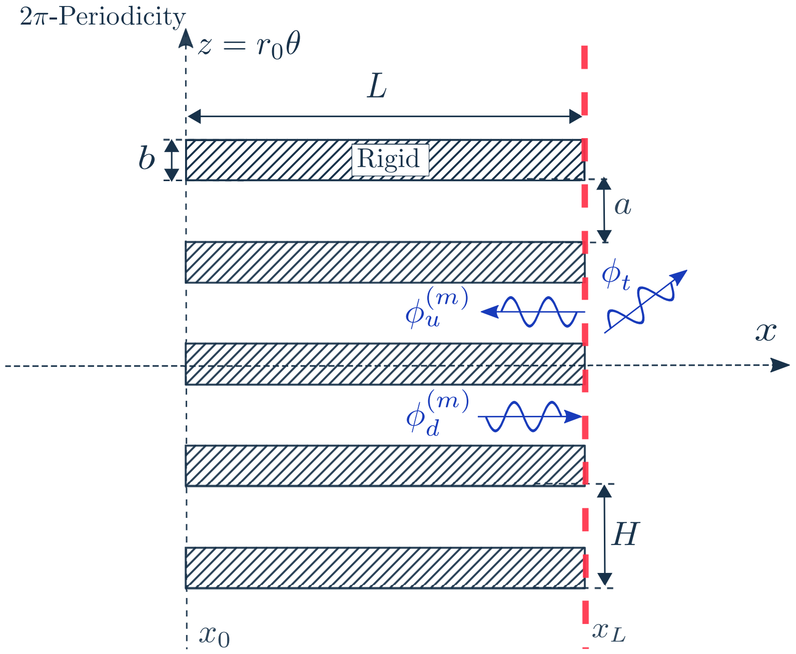

**Figure 1.9:** Acoustic potentials generated by the scattering of the incident wave at the inlet interface $x = x_L$.

and 1.20b, one obtains:

$$\begin{cases} \displaystyle\sum_{q=0}^{+\infty}\left(D_q^0 \mathrm{e}^{\mathrm{i}k_q^+ L} + U_q^0\right)\cos(\alpha_q z) = \sum_{s=-\infty}^{+\infty} T_s \mathrm{e}^{\mathrm{i}k_s^+ z} & (1.21\text{a}) \\ \displaystyle\sum_{q=0}^{+\infty}\left(k_q^+ D_q^0 \mathrm{e}^{\mathrm{i}k_q^+ L} + k_q^- U_q^0\right)\cos(\alpha_q z) = \sum_{s=-\infty}^{+\infty} T_s k_s^+ \mathrm{e}^{\mathrm{i}\alpha_s z} & (1.21\text{b}) \end{cases}$$

As before, the matching equations must be projected on the two sets of eigenfunctions. For that, Equations 1.21a and 1.21b are respectively projected on $\cos(\alpha_\mu z)$ and $\mathrm{e}^{-\mathrm{i}\alpha_\nu z}$.

$$\begin{cases} \displaystyle\int_0^a \left\{p_d^{(0)}(x_L, z) + p_u^{(0)}(x_L, z)\right\}\cos(\alpha_\mu z)\mathrm{d}z = \int_0^a p_t(x_L, z)\cos(\alpha_\mu z)\mathrm{d}z & (1.22\text{a}) \\ \displaystyle\int_0^a \left\{v_d^{(0)}(x_L, z)\cdot\mathbf{e}_{\boldsymbol{x}} + v_u^{(0)}(x_L, z)\cdot\mathbf{e}_{\boldsymbol{x}}\right\}\mathrm{e}^{-\mathrm{i}\alpha_\nu z}\mathrm{d}z = \int_0^H \left\{v_t^{(0)}(x_L, z)\cdot\mathbf{e}_{\boldsymbol{x}}\right\}\mathrm{e}^{-\mathrm{i}\alpha_\nu z}\mathrm{d}z & (1.22\text{b}) \end{cases}$$

After taking into account the rigid wall boundary condition in the velocity equation, and accounting for the orthogonality of the modal basis, the matching equations become:

$$\begin{cases} \displaystyle\left(D_\mu^0 \mathrm{e}^{\mathrm{i}k_\mu^+ L} + U_\mu^0\right)\frac{a}{2}(1+\delta_{\mu 0}) = \sum_{s=-\infty}^{+\infty} T_s \Lambda_{\mu s} & (1.23\text{a}) \\ \displaystyle\sum_{q=0}^{+\infty}\left(D_q^0 k_q^+ \mathrm{e}^{\mathrm{i}k_q^+ L} + U_q^0 k_q^-\right)\varphi_{\nu q} = T_\nu k_\nu^+ H & (1.23\text{b}) \end{cases}$$

### 1.3.3 Solving procedure

The system of linear equations defined by Equations 1.16a, 1.16b, 1.23a and 1.23b can be solved by using either a direct method or an iterative procedure. The main steps of these methods are discussed in the following sub-sections.

#### 1.3.3.1 Direct method

The most straightforward way to solve this system of linear equations, is to use a direct matrix inversion. For that, Equations 1.16a, 1.16b, 1.23a and 1.23b are written in a matrix form:

$$\underbrace{\begin{pmatrix} \underline{\boldsymbol{\mathcal{A}}_{11}} & \underline{\boldsymbol{\mathcal{A}}_{12}} & \underline{\boldsymbol{\mathcal{A}}_{13}} & \mathbf{0} \\ \underline{\boldsymbol{\mathcal{A}}_{21}} & \underline{\boldsymbol{\mathcal{A}}_{22}} & \underline{\boldsymbol{\mathcal{A}}_{23}} & \mathbf{0} \\ \mathbf{0} & \underline{\boldsymbol{\mathcal{A}}_{32}} & \underline{\boldsymbol{\mathcal{A}}_{33}} & \underline{\boldsymbol{\mathcal{A}}_{34}} \\ \mathbf{0} & \underline{\boldsymbol{\mathcal{A}}_{42}} & \underline{\boldsymbol{\mathcal{A}}_{43}} & \underline{\boldsymbol{\mathcal{A}}_{44}} \end{pmatrix}}_{\underline{\boldsymbol{\mathcal{A}}}} \underbrace{\begin{pmatrix} \mathbf{R} \\ \mathbf{D} \\ \mathbf{U} \\ \mathbf{T} \end{pmatrix}}_{\boldsymbol{\mathcal{X}}} = \underbrace{\begin{pmatrix} \boldsymbol{\mathcal{H}}_1 \\ \boldsymbol{\mathcal{H}}_2 \\ \mathbf{0} \\ \mathbf{0} \end{pmatrix}}_{\boldsymbol{\mathcal{H}}} \tag{1.24}$$

where $\boldsymbol{\mathcal{X}}$ represents the modal amplitude vector. The matrix $\underline{\boldsymbol{\mathcal{A}}}$ terms are given by

$$\begin{aligned}
\underline{\boldsymbol{\mathcal{A}}_{11}} &= \operatorname{diag}\left(Hk_\nu^-\right) &, \quad \underline{\boldsymbol{\mathcal{A}}_{32}} &= \mathrm{e}^{\mathrm{i}k_q^+L}k_q^+\varphi_{\nu q} \\
\underline{\boldsymbol{\mathcal{A}}_{12}} &= -k_q^+\varphi_{\nu q} &, \quad \underline{\boldsymbol{\mathcal{A}}_{33}} &= k_q^-\varphi_{\nu q} \\
\underline{\boldsymbol{\mathcal{A}}_{13}} &= -k_q^-\mathrm{e}^{-\mathrm{i}k_q^-L}\varphi_{\nu q} &, \quad \underline{\boldsymbol{\mathcal{A}}_{34}} &= -\operatorname{diag}\left(Hk_\nu^+\right) \\
\underline{\boldsymbol{\mathcal{A}}_{21}} &= \Lambda_{\mu s} &, \quad \underline{\boldsymbol{\mathcal{A}}_{42}} &= \operatorname{diag}\left(\mathrm{e}^{\mathrm{i}k_q^+L}\frac{a}{2}\left[1+\delta_{\mu 0}\right]\right) \\
\underline{\boldsymbol{\mathcal{A}}_{22}} &= -\operatorname{diag}\left(\frac{a}{2}\left[1+\delta_{\mu 0}\right]\right) &, \quad \underline{\boldsymbol{\mathcal{A}}_{43}} &= \operatorname{diag}\left(\frac{a}{2}\left[1+\delta_{\mu 0}\right]\right) \\
\underline{\boldsymbol{\mathcal{A}}_{23}} &= -\operatorname{diag}\left(\mathrm{e}^{-\mathrm{i}k_q^-L}\frac{a}{2}\left[1+\delta_{\mu 0}\right]\right) &, \quad \underline{\boldsymbol{\mathcal{A}}_{44}} &= -\Lambda_{\mu s}
\end{aligned}$$

and the vector $\boldsymbol{\mathcal{H}}$ terms are given by

$$\begin{aligned}
\boldsymbol{\mathcal{H}}_1 &= -A_ik_i^+\mathrm{e}^{\mathrm{i}k_i^+L_i}H, \\
\boldsymbol{\mathcal{H}}_2 &= -A_i\mathrm{e}^{\mathrm{i}k_i^+L_i}\Lambda_{\mu i}
\end{aligned}$$

As can be seen form Equation 3.18, the modal coefficient vector $\boldsymbol{\mathcal{X}}$ can be easily obtained by a direct matrix inversion $\boldsymbol{\mathcal{X}} = \underline{\boldsymbol{\mathcal{A}}}^{-1}\boldsymbol{\mathcal{H}}$.

Before solving the system of linear equations, a modal truncation of the infinite series must performed to obtain a finite number of modes. The latter varies from $-N_S$ to $N_S$ in the unbounded mediums, and form 0 to $N_Q - 1$ inside the channels. The literature on propagation problems in duct discontinuities suggests to take more modes in the wider duct to ensure the convergence of calculations [88]. It is recommended to keep the ratio $N_Q/(2N_S + 1) \approx a/H$ to satisfy the edge condition.

It should be kept in mind that the truncated matrix is always square even if the number of modes selected in each subdomain is different, because of the use of the two eigenfunctions in the modal projections.

#### 1.3.3.2 Iterative method

Another way of solving the system of linear equations is to use an iterative procedure. The multiple reflections inside the channels make the use of this method more physical than the direct method. Combining Equations 1.16a, 1.16b, 1.23a and 1.23b yield:

$$
\begin{cases}
\mathbf{R} = (I - \varphi\Lambda_s)^{-1}\Big[A(\varphi\Lambda_i - I) - 2\varphi\mathcal{U}\Big] & (1.25a) \\[2ex]
\mathbf{D} = \dfrac{1}{a/2(1+\delta_{\mu 0})}\left(A_i \mathrm{e}^{\mathrm{i}k_\mu^+ L_i}\Lambda_i + \displaystyle\sum_{s=-\infty}^{+\infty} R_s\Lambda_s - U_\mu^0 \mathrm{e}^{-\mathrm{i}k_\mu^- L}\right) & (1.25b) \\[2ex]
\mathbf{U} = (\varphi\Lambda_s - I)^{-1}(\varphi\Lambda_i + I)\mathcal{D} & (1.25c) \\[2ex]
\mathbf{T} = \dfrac{1}{H}\displaystyle\sum_{q=0}^{+\infty}\left(U_q^0 - D_q^0 \mathrm{e}^{\mathrm{i}k_q^+ L}\right)\dfrac{k_q^-}{k_\nu^+}\varphi_{\nu q} & (1.25d)
\end{cases}
$$

where

$$
\begin{aligned}
A &= A_i \mathrm{e}^{\mathrm{i}k_i^+ L_i}, \\
\mathcal{U} &= U^0 \mathrm{e}^{-\mathrm{i}k_q^- L}, \\
\mathcal{D} &= D^0 \mathrm{e}^{-\mathrm{i}k_q^+ L}, \\
\Lambda_s &= \frac{1}{a/2(1+\delta_{\mu 0})}\Lambda_{\mu s}, \\
\Lambda_i &= \frac{1}{a/2(1+\delta_{\mu 0})}\Lambda_{\mu i}, \\
\varphi &= \frac{1}{H}\frac{k_q^+}{k_\nu^-}\varphi_{\nu q} = \frac{1}{H}\frac{k_q^-}{k_\nu^+}\varphi_{\nu q}
\end{aligned}
$$

As can be seen from Equations 1.25a and 1.25b, the determination of **R** and **D** requires prior knowledge of the vector $\mathcal{U}$. The index of iterations used in this solving procedure is noted $\gamma$. In the first iteration, the reflected field inside the channels is assumed to be zero $U_q^{0(\gamma=0)} = 0$. Equations 1.25a and 1.25b are used to determine the reflection coefficient $R_s^{(\gamma=1)}$ and the transmission coefficient $D_q^{0(\gamma=1)}$ . The latter is used in Equations 1.25c and 1.25d to compute the new values of $U_q^{0(\gamma=1)}$ and $T_s^{(\gamma=1)}$. Equations 1.25a and 1.25c are solved again using the new value of $U_q^{0(\gamma=1)}$ as input. The procedure is repeated till convergence. The results are supposed to be converged when the relative variation of the modal amplitudes between two successive iterations is less than $\epsilon$, where $\epsilon \approx 0$. The different steps of the iterative method are shown in Figure 1.10.

It should be noted that the use of the this technique can involve some problems of convergence when the incident wave is cut-off. In order to avoid that, the direct method is selected in this work.

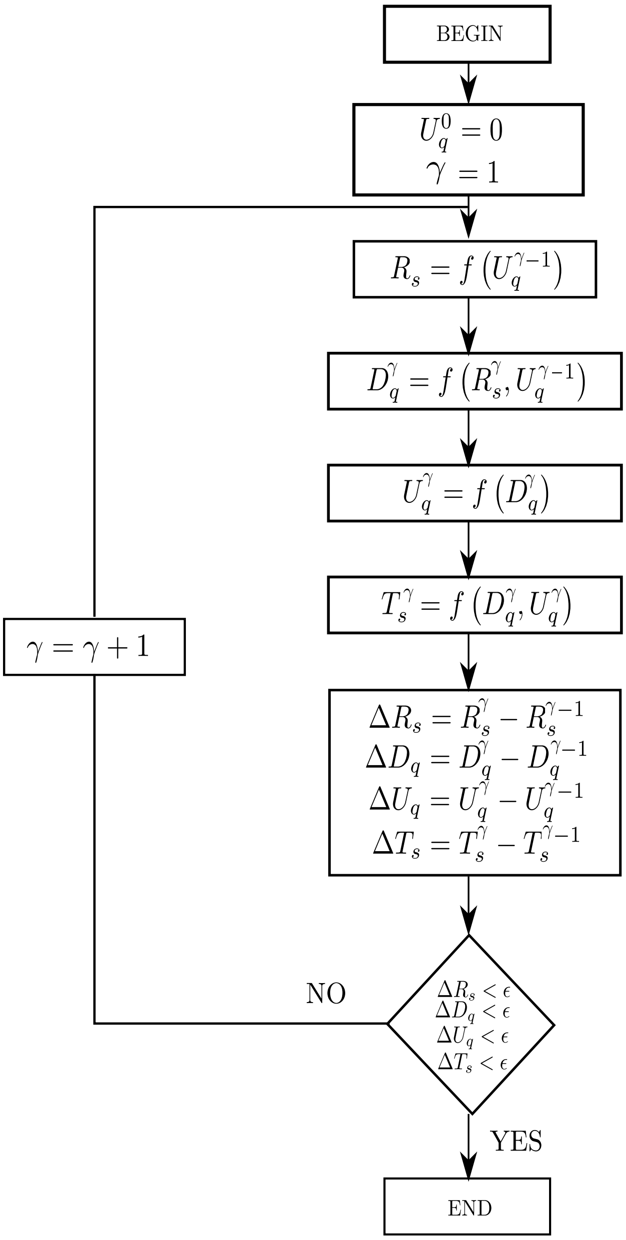

**Figure 1.10:** Iterative procedure algorithm

## 1.3.4 Numerical validation

### 1.3.4.1 Two-dimensional finite element method

In order to test the validity and the accuracy of the analytical model, a comparison with the finite element method has been performed. This method is based on discretising the geometry into small elements in which the solution of the Helmholtz equation is approximated. Consider a test case with $V = 10$ channels of length $L/H = 3.98$ ($L = 0.5$m) and width $a/H = 0.6$, placed at a radius $r_0 = 0.2$ m, as shown in Figure 1.11.

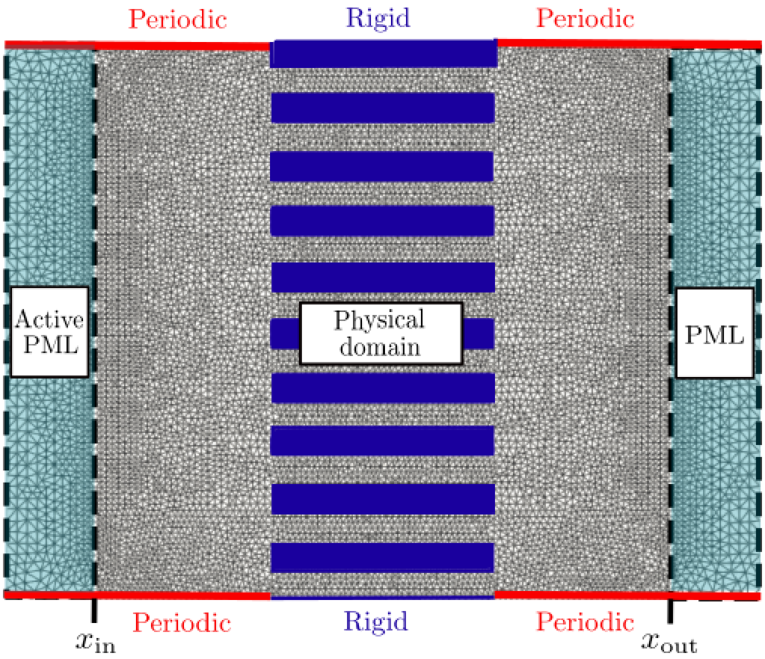

**Figure 1.11:** Two-dimensional finite element mesh showing the different regions used in the simulation. Dashed lines indicate the interfaces between the physical domain and the PML regions. The rigid-wall boundary condition is applied on the blue rectangles. Periodic boundary condition is applied on the red lines.

As can be seen the simulation domain is divided into three different subdomains :

1. The physical domain: represents the simulation domain in which the solution of the problem is found. The acoustic field must satisfy the classical Helmholtz equation.

2. A perfectly matched layer: placed downstream the cooling channels to attenuate the acoustic waves coming from the physical domain and avoid their reflection (see Figure 1.12a). The attenuation effects are introduced by applying a complex coordinate transformation on the $x$ direction [13, 26, 11, 22, 14]:

$$\tilde{x}(x) = x - \frac{\mathrm{i}}{\omega}\int_{x_{\mathrm{in}}}^{x} \sigma(s)\mathrm{d}s \tag{1.26}$$

3. An active perfectly matched layer: in which the incident wave is imposed. This layer has the particularity to attenuate the acoustic waves in only one direction of

propagation as shown in Figure 1.12b. The acoustic field in this region is expressed as a sum of an incident field $p_i$ and an attenuated reflected field $p - p_i$, where $p_i$ is imposed using the analytical expression given in section 1.3.

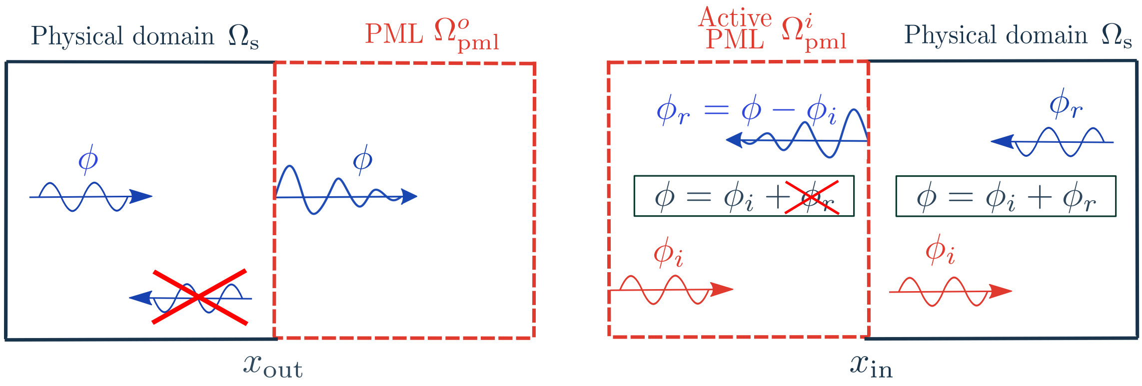

**(a)** **(b)**

**Figure 1.12:** (a) Attenuation of an acoustic wave in the perfectly matched layer. (b) Active perfectly matched layer. Incident wave (red), Attenuated field (blue)

In this work, the finite element simulation was performed by using the open source solver `FreeFem++` [51]. The use of the latter requires the implementation of the variational formulation of the Helmholtz equation, given by:

$$\underbrace{\iint_{\Omega_\mathrm{s}} \left(\frac{\partial\phi}{\partial x}\frac{\partial q}{\partial x}+\frac{\partial\phi}{\partial y}\frac{\partial q}{\partial y}-\phi q k_0^2\right)\mathrm{d}x\mathrm{d}y}_{\text{Acoustic field in the physical domain}} + \underbrace{\iint_{\Omega^i_\mathrm{pml}}\left(\frac{\partial\phi_i}{\partial x}\frac{\partial q}{\partial x}+\frac{\partial\phi_i}{\partial y}\frac{\partial q}{\partial y}-\phi_i q k_0^2\right)\mathrm{d}x\mathrm{d}y}_{\text{Incident field in the Active PML domain}}$$

$$+\underbrace{\iint_{\Omega^i_\mathrm{pml}}\left(\frac{1}{\gamma_x^i}\frac{\partial\left(\phi-\phi_i\right)}{\partial x}\frac{\partial q}{\partial x}+\gamma_x^i\frac{\partial\left(\phi-\phi_i\right)}{\partial y}\frac{\partial q}{\partial y}-\left(\phi-\phi_i\right)qk_0^2\gamma_x^i\right)\mathrm{d}x\mathrm{d}y}_{\text{The reflected field in the active PML domain}}$$

$$+\underbrace{\iint_{\Omega^o_\mathrm{pml}}\left(\frac{1}{\gamma_x^o}\frac{\partial\phi}{\partial x}\frac{\partial q}{\partial x}+\gamma_x^o\frac{\partial\phi}{\partial y}\frac{\partial q}{\partial y}-\phi qk_0^2\gamma_x^o\right)\mathrm{d}x\mathrm{d}y}_{\text{Acoustic field in the PML domain}}=0 \tag{1.27}$$

where $q$ represents the test function, and $\gamma_x^i$ and $\gamma_x^o$ are given by

$$\gamma_x^i = 1 - \frac{\mathrm{i}}{\omega}\sigma^i(x) \tag{1.28}$$

$$\gamma_x^o = 1 - \frac{\mathrm{i}}{\omega}\sigma^o(x) \tag{1.29}$$

where $\sigma^i$ and $\sigma^o$ are the absorption functions. They are given by

$$\sigma^i(x) = \sigma'(x - x_\mathrm{in})^2 \tag{1.30}$$

$$\sigma^o(x) = \sigma'(x - x_{\text{out}})^2 \tag{1.31}$$

It should be kept in mind that the absorption function depends on the frequency and the size of the PML domains ($x - x_{\text{in}}$ and $x - x_{\text{out}}$). An optimal value valid in a large range of frequencies is given by [14]: $\sigma'/c_0 = 100$.

It may be recalled that the number of elements needed depends on the maximum frequency of interest and the polynomial approximation. Using higher order approximations (P2 elements in this work) requires only 10 points per wavelength.

The instantaneous acoustic potential fields obtained by the finite element method and the mode-matching method are shown in Figures 1.13a and 1.13b respectively, for the incident mode $n = 2$ at the frequency $f = 2700 Hz$. Upstream of the interface $x = x_0$, the acoustic field is dominated by the incident wave and modulated by the reflected wave. Figure 1.14 shows the comparison between the acoustic potential profiles along different lines defined upstream, through and downstream the channels (See Figure 1.13). The potential profiles obtained by the two methods are in a good agreement. The effect of the perfectly matched layers can be seen in Figure 1.14a. The potential profile calculated by the finite element method is attenuated exponentially from the PML interface located downstream the channels ($x/L > 3$). However, for the active PML region ($x/L < 0.4$), the amplitude does not decay to zero because of the presence of the incident wave. Figure 1.15 presents the modulus of the complex-valued modal coefficients of the different acoustic fields, obtained by the mode-matching method. The blue and red bars denote cut-on and cut-off modes respectively. They indicate that only the modes of order $n + sV = [2, -8]$ and $q = [0, 1]$ are cut-on. The other modes are cut-off, attenuated exponentially on both sides of the interfaces, they do not participate in the acoustic radiation. However taking the evanescent modes into account is very important to ensure the continuity of the acoustic field at the interfaces and to accurately calculate the amplitudes of the cut-on modes.

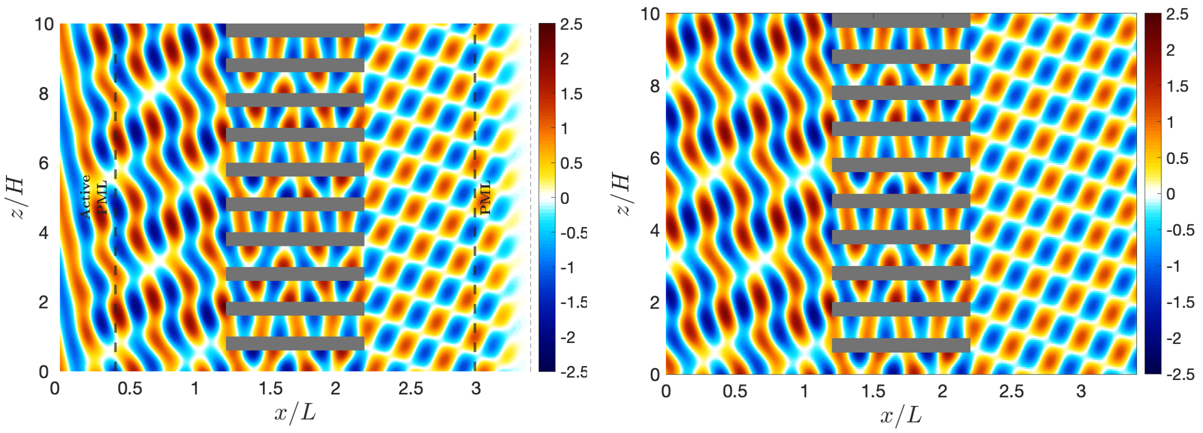

(a)

(b)

**Figure 1.13:** Real part of acoustic potential. (a) Finite element method , (b) Mode-matching method. Interfaces between the physical domain and the PML regions (- - - -).

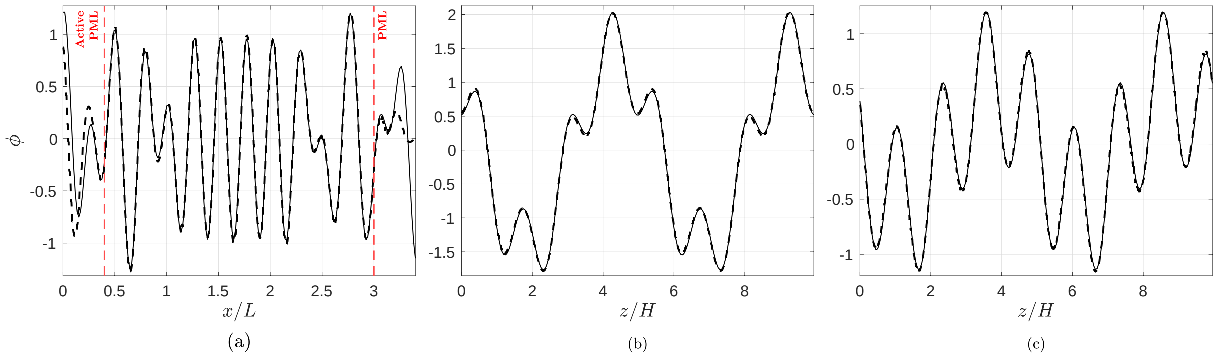

**Figure 1.14:** Instantaneous acoustic potential profiles extracted at $(a)$ $z/H = 5$ , $(b)$ $x/L = 0.8$ , $(c)$ $x/L = 2.6$, calculated by the mode-matching method (——), and the finite element method (- - - -). Interfaces between the physical domain and the PML regions (- - - -).

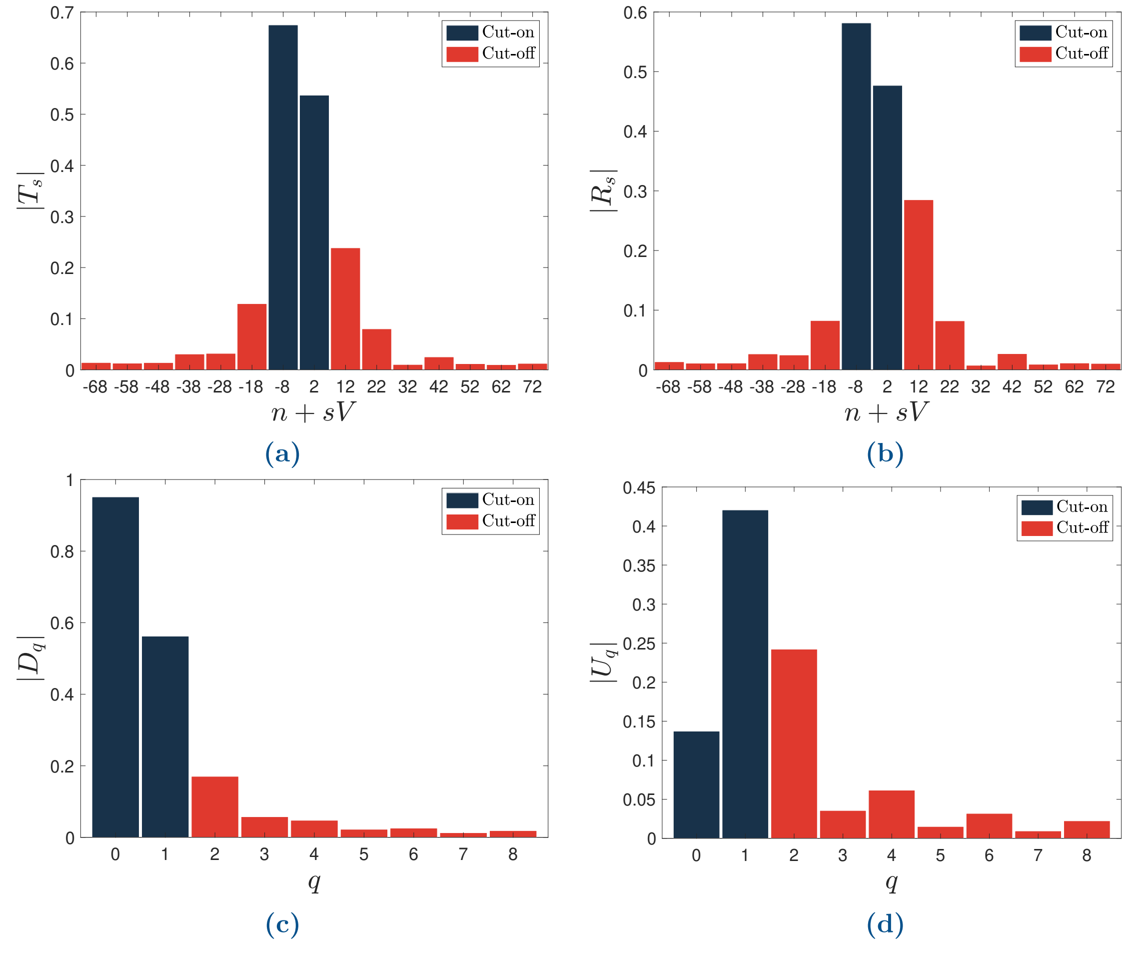

**Figure 1.15:** Modulus of the modal coefficients from the test case in Figure 1.13b. Cut-on modes (bars ■ ), cut-off modes (bars 🟥 ).

#### 1.3.4.2 Three-dimensional finite element method

In order to evaluate the limitations of the two-dimensional approach, a comparison with a three-dimensional simulation has been performed by applying the finite element method to the realistic configuration of the cooling channels (see Figure 1.16). The configuration investigated in this section consists of $V = 19$ channels with a circular cross-section

$2r_c = 0.03$m and a length $L = 0.35$m. The inner and outer radii of the annular duct are given by $r_1 = 0.13$m and $r_2 = 0.17$m.

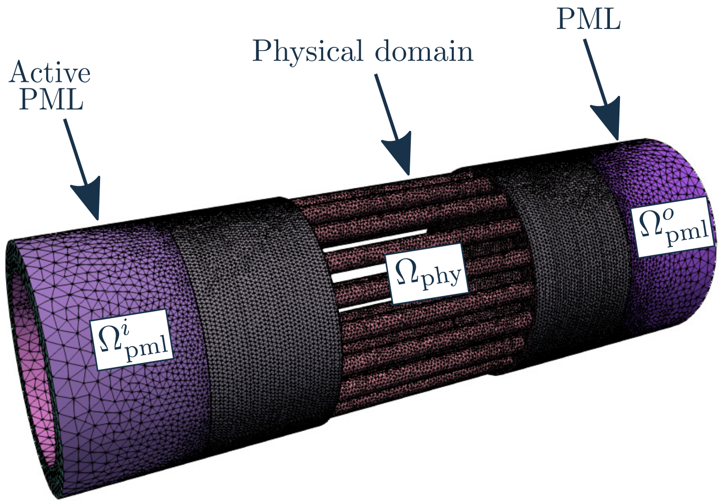

**Figure 1.16:** Three-dimensional finite element mesh showing the different regions defined in the simulation domain.

As before, the geometry is divided into three different regions corresponding to the physical domain and the perfectly matched layers. The variational formulation (3D) of the Helmholtz equation implemented in `FreeFem++` is given by:

$$\begin{aligned}
&\underbrace{\iiint\limits_{\Omega^i_{\text{pml}}}\left(\frac{\partial\phi_i^{3D}}{\partial x}\frac{\partial q}{\partial x}+\frac{\partial\phi_i^{3D}}{\partial y}\frac{\partial q}{\partial y}+\frac{\partial\phi_i^{3D}}{\partial z}\frac{\partial q}{\partial z}-\phi_i^{3D}qk_0^2\right)\mathrm{d}x\mathrm{d}y\mathrm{d}z}_{\substack{\text{Incident field in}\\ \text{the Active PML domain}}}\\
&\underbrace{+\iiint\limits_{\Omega^i_{\text{pml}}}\left(\frac{1}{\gamma^i_x}\frac{\partial\left(\phi-\phi_i^{3D}\right)}{\partial x}\frac{\partial q}{\partial x}+\gamma^i_x\frac{\partial\left(\phi-\phi_i^{3D}\right)}{\partial y}\frac{\partial q}{\partial y}+\gamma^i_x\frac{\partial\left(\phi-\phi_i^{3D}\right)}{\partial z}\frac{\partial q}{\partial z}-\left(\phi-\phi_i^{3D}\right)qk_0^2\gamma^i_x\right)\mathrm{d}x\mathrm{d}y\mathrm{d}z}_{\substack{\text{The reflected field in}\\ \text{the active PML domain}}}\\
&\underbrace{+\iiint\limits_{\Omega_{\text{phy}}}\left(\frac{\partial\phi}{\partial x}\frac{\partial q}{\partial x}+\frac{\partial\phi}{\partial y}\frac{\partial q}{\partial y}+\frac{\partial\phi}{\partial z}\frac{\partial q}{\partial z}-\phi qk_0^2\right)\mathrm{d}x\mathrm{d}y\mathrm{d}z}_{\substack{\text{Acoustic field in}\\ \text{the physical domain}}}\\
&\underbrace{+\iiint\limits_{\Omega^o_{\text{pml}}}\left(\frac{1}{\gamma^o_x}\frac{\partial\phi}{\partial x}\frac{\partial q}{\partial x}+\gamma^o_x\frac{\partial\phi}{\partial y}\frac{\partial q}{\partial y}+\gamma^o_x\frac{\partial\phi}{\partial z}\frac{\partial q}{\partial z}-\phi qk_0^2\gamma^o_x\right)\mathrm{d}x\mathrm{d}y\mathrm{d}z}_{\substack{\text{Acoustic field}\\ \text{in the PML domain}}}=0 \qquad (1.32)
\end{aligned}$$

The incident wave is imposed in the active PML region. The analytical expression of the latter in cylindrical coordinates, is given by

$$\phi_i^{3D}(r,\theta,x)=A_{n0}f_n(r)\mathrm{e}^{\mathrm{i}n\theta}\mathrm{e}^{\mathrm{i}k^+_{n0}x}\quad ,k^+_{n0}=\sqrt{k_0^2-K_{n0}^2} \qquad (1.33)$$

where $r = \sqrt{z^2 + y^2}$, $\theta = \arctan(z/y)$, and $f_{nj}(r)$ represents the function describing the propagation in the radial direction. $A_{n0}$ is the modal amplitude of the incident wave, and $K_{n0}$ is the eigenvalue of the first radial mode.

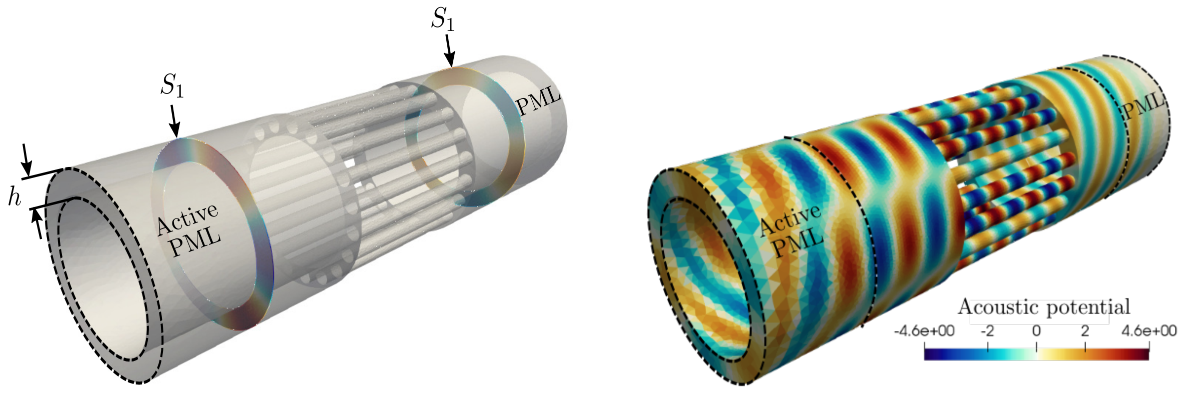

**(a)** **(b)**

**Figure 1.17:** ($a$) Typical configuration of the cooling channels used in traction motors, ($b$) Instantaneous acoustic potential field calculated by the finite element method

A mesh of about $5 \times 10^5$ tetrahedral elements was used in this simulation (see Figure 1.16). Figure 1.17b shows an instantaneous acoustic potential field calculated by the finite element method for the incident mode $n = 3$. The physical domain is limited by the plane surfaces $S_1$ and $S_2$ as shown in Figure 1.17a. The comparison between the two dimensional mode-matching technique and the finite element method ($3D$) has been performed on the modal acoustic power. The associated acoustic powers $\mathcal{P}_r^{3D}$ and $\mathcal{P}_t^{3D}$ are evaluated by integrating the acoustic intensity over the areas of cross-sections $S_1$ and $S_2$ in Figure 1.17a respectively :

$$\mathcal{P}_r^{3D} = \iint\limits_{S_1} \frac{1}{2} \mathcal{R}e \Big\langle p(x_{S_1}, y, z) \cdot v^*(x_{S_1}, y, z) \cdot \mathbf{e_x} \Big\rangle \mathrm{d}\mathbf{y}\mathrm{d}\mathbf{z} - \boldsymbol{\mathcal{P}_i^{3D}} \tag{1.34}$$

$$\mathcal{P}_t^{3D} = \iint\limits_{S_2} \frac{1}{2} \mathcal{R}e \Big\langle p(x_{S_2}, y, z) \cdot v^*(x_{S_2}, y, z) \cdot \mathbf{e_x} \Big\rangle \mathrm{d}\mathbf{y}\mathrm{d}\mathbf{z} \tag{1.35}$$

where $v^*.\mathbf{e_x}$ is the complex conjugate of the axial velocity.

The acoustic power of the incident wave can be calculated analytically as

$$\mathcal{P}_i^{3D} = k_0 \rho c_0 \pi r_2^2 k_{n0}^+ |A_{n0}|^2 \tag{1.36}$$

In the analytical model, the acoustic powers of the transmitted and reflected fields ($\mathcal{P}_t^{2D}$ and $\mathcal{P}_r^{2D}$) are evaluated from their modal coefficients:

$$\mathcal{P}_r^{2D} = k_0 \rho c_0 \pi r_0 \sum_{s=-\infty}^{+\infty} k_s^- |R_s|^2, \quad \text{if} \quad (k_s^-)^2 > 0 \tag{1.37}$$

$$\mathcal{P}_t^{2D} = k_0 \rho c_0 \pi r_0 \sum_{s=-\infty}^{+\infty} k_s^+ |T_s|^2, \quad \text{if} \quad (k_s^+)^2 > 0 \tag{1.38}$$

The acoustic power of the incident wave is given by

$$\mathcal{P}_i^{2D} = k_0 \rho c_0 \pi r_0 k_i^+ |A_n|^2, \quad \text{if} \quad (k_i^+)^2 > 0 \tag{1.39}$$

The frequency is scaled by introducing the Helmholtz number $k_0 h$, where $h = r_2 - r_1$ is the thickness of the annular duct (see Figure 1.17a). The transmitted and reflected powers calculated by the mode-matching method and the finite element method are normalized by dividing them by the incident power. Figures 1.18a and 1.18b show respectively the variations of the transmitted and reflected powers obtained by the mode-matching method and the finite element method as functions of the Helmholtz number. Comparing the transmitted powers shows a good agreement of the results obtained by the two methods, up to relatively high frequencies $k_0 h \approx 4.2$. This confirms that the two-dimensional analytical model can be used with confidence for parametric studies. When the Helmholtz number exceeds $k_0 h > 4.2$, the analytical model breaks down and overestimates the reflected power. This could be attributed to the three-dimensional effects. In this specific test-case, the first radial higher-order mode becomes cut-on at $k_0 h = 3.25$. Up to this frequency, no radial mode can propagate upstream and downstream the channels. The effect of the latter becomes more significant when the frequency exceeds $k_0 h > 4.2$, and the use of the two-dimensional approach could not be justified.

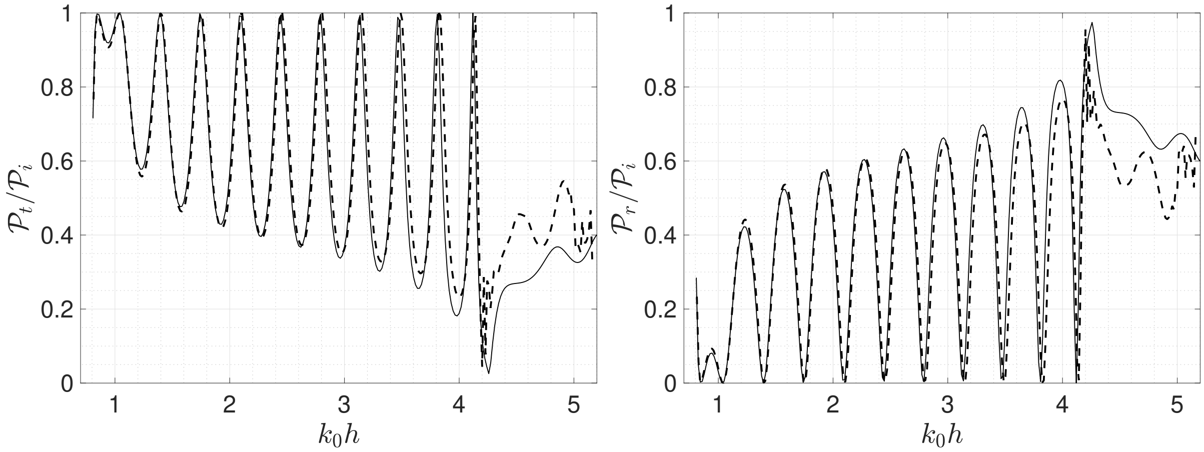

(a) (b)

**Figure 1.18:** Variation of transmitted (a) and reflected (b) powers as functions of the Helmholtz number; Mode-matching technique (——), Finite element method 3D (- - - -).

It should be noted here that the computational time of the finite element simulation for 300 frequency steps is about 39 hours on a personal computer with single core, whereas the analytical model computational time is less than 5 seconds.

### 1.3.5 Resonant frequencies

One of the most important aspects in this work, is the prediction of the resonance frequencies of the cooling channels. These frequencies are characterized by a strong amplification of the sound amplitude inside the channels. It may be observed from Figure 1.18 that the transmission peaks are harmonically dependent and they appear at the resonance frequencies of the channels. Figures 1.19a and 1.19b show respectively the instantaneous acoustic potential fields at $k_0h = 1.56$ and $k_0h = 1.74$. As can be seen from Figure 1.19b, the acoustic potential inside the channels was amplified comparing to the first frequency (Figure 1.19a). The incident wave is almost totally transmitted downstream the channels. It may be recalled that acoustic resonances are expected *a priori* when the length of the channels $L$ is a multiple of the half wavelength $\lambda/2$. But for open pipes of transverse dimension much smaller than the wavelength, an effective length larger than the true length must be considered. The resonant frequencies are obtained by

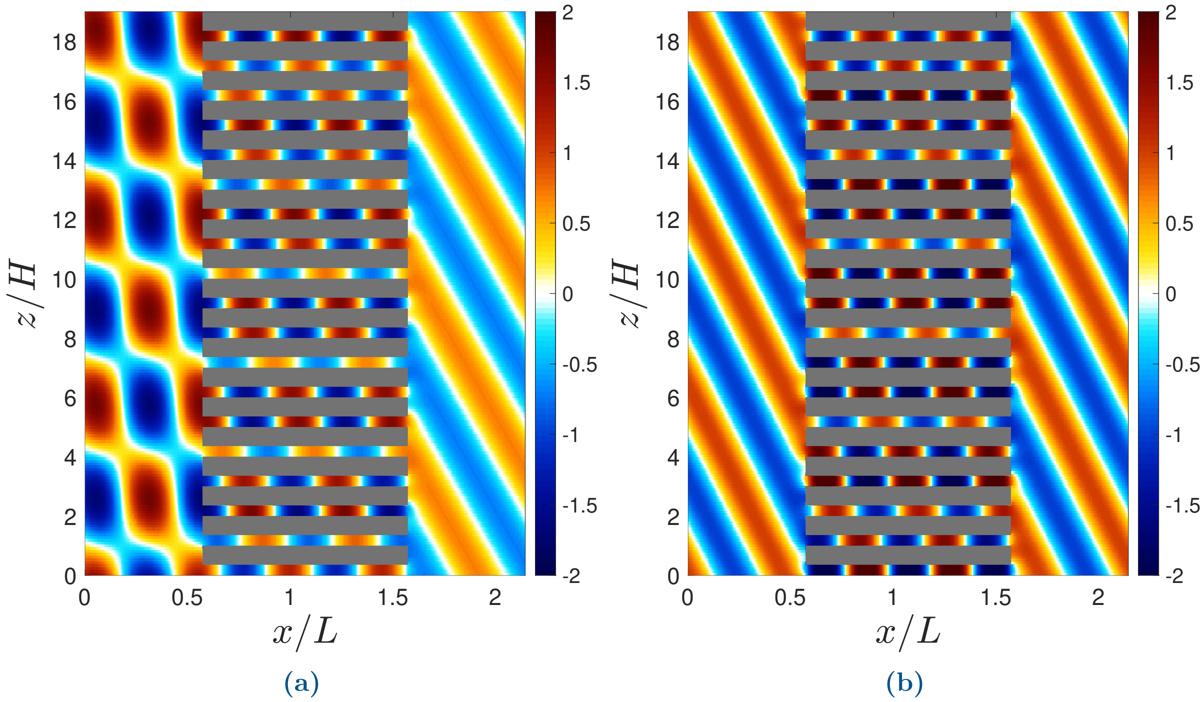

(a)

(b)

**Figure 1.19:** Instantaneous acoustic potential fields for two different frequencies from Figure 1.18. (a) $k_0h = 1.56$ , (b) $k_0h = 1.74$. $a/H = 0.3562$, $V = 19$, $r_0 = 0.15\ m$

$$f_r = \frac{n_r c_0}{2(L + \delta_L)} \tag{1.40}$$

where $n_r \in \mathbb{Z}$ represents the harmonics of the fundamental frequency, and $\delta_L$ accounts for the end corrections, which correspond to equivalent reflecting points just outside the channels [5, 66, 15, 10] (see Figure 1.20). The latter depends on the transverse dimensions of channels. It is given, for instance, by [66]:

$$\delta_L = b/2 + 0.85a \tag{1.41}$$

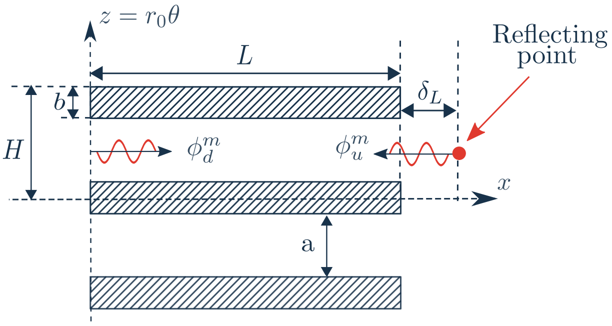

**Figure 1.20:** Illustration of the end corrections.

### 1.3.6 Influence of the number of modes

The number of modes is a very important parameter, which has a significant influence on the accuracy of the results. As mentioned earlier, several evanescent modes must be taken into account in addition to the cut-on modes in order to ensure the continuity of the acoustic field at both interfaces of the channels. The desired precision can be obtained by increasing the number of modes. The value of the latter should not be excessive, because of the computational time and the condition number $\kappa$ of the matrix $\underline{\boldsymbol{\mathcal{A}}}$. These increase with the number of modes $N_S$ as shown in Figures 1.21a and 1.21b. For large values of $\kappa$ the system of linear equations is said to be ill-conditioned. The matrix inversion will not be computed with good accuracy. There is an optimal value for the number of modes, which depends on the frequency and the transverse dimensions of the geometry.

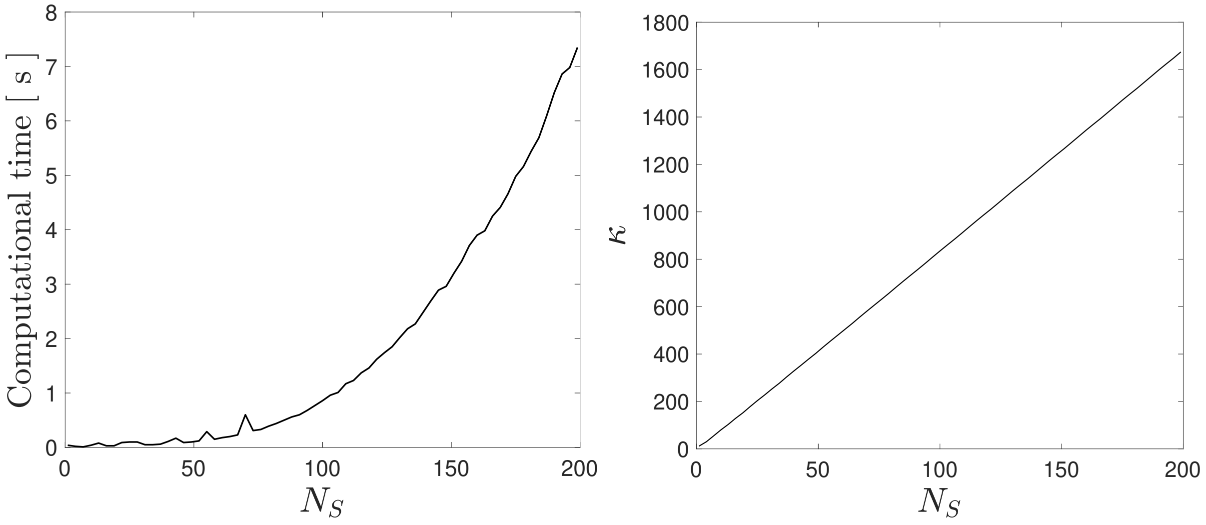

(a)

(b)

**Figure 1.21:** (a) Variation of the computational time against the number of modes. (b) Condition number as a function of the number of modes. $k_0a = 3.76$ , $V = 10$, $a/H = 0.4$, $L/a = 6.6315$, $r_0 = 0.2$.

The simplest way to determine the optimal value of the number of modes needed in a simulation, is to perform several calculations, by increasing incrementally the number of modes. The minimum value of $N_S$ is obtained when no variation between two successive calculations is observed. Figures 1.22a and 1.22b show respectively the variations of the transmitted and reflected powers as functions of the number of modes. As can be seen, the acoustic powers reach fixed values after $N_S = 20$.

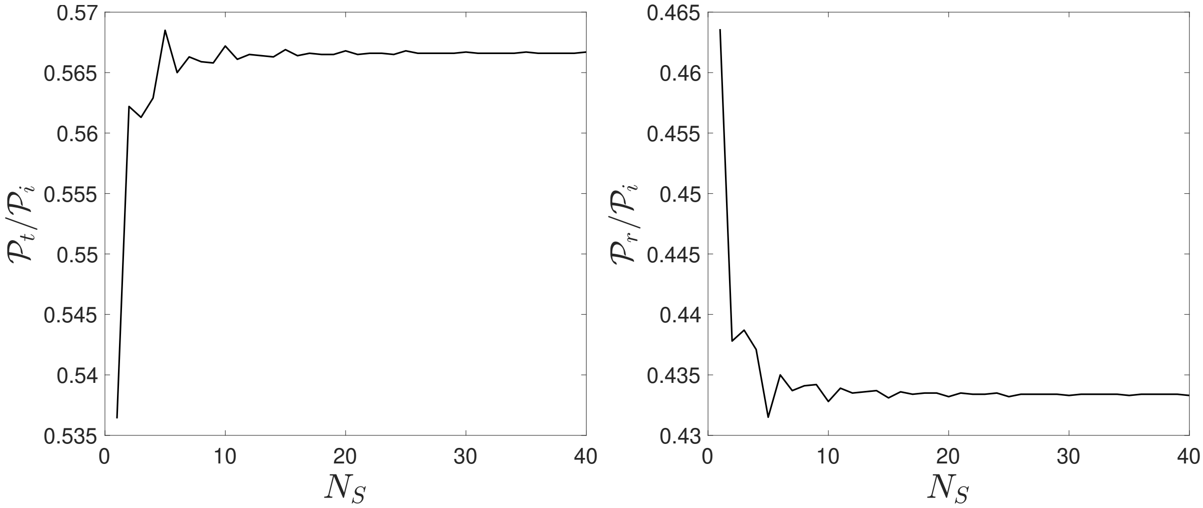

**(a)** **(b)**

**Figure 1.22:** Variation of acoustic powers against the number of modes. (a) Transmitted power. (b) Reflected power. $k_0a = 3.76$ , $V = 10$, $a/H = 0.4$, $L/a = 6.6315$, $r_0 = 0.2$.

## 1.4 Coupled system

### 1.4.1 Coupling strategy

This section presents the methodology used to deal with the problem of sound transmission through a system consisting of two periodic rows of thick-walled channels, separated by a distance $d$. The principle of superposition is used in this section in order to describe the sound field as a linear combination of modes in each region of the system. The scattering of each of these acoustic modes can be investigated by the use of the mode-matching technique. For that, the analytical model presented in the previous section will be applied to both subsystems, by taking the outputs of one subsystem as the input of the other one. The coupling strategy can therefore be divided into three successive steps. An illustration of the different steps is shown in Figures 3.12, 1.24 and 1.25.

#### 1.4.1.1 Step 1 - Scattering of the incident wave $\phi_i$ by the guide vanes

In the first step, an incident wave denoted by $\phi_i$ is scattered by the guide vanes, generating four acoustic fields, as shown in Figure 3.12. The acoustic potential of the different fields are given by:

$$\phi_i(x,z,t) = A_n \mathrm{e}^{\mathrm{i}\alpha_i z}\mathrm{e}^{\mathrm{i}k_i^+(x-x_0)}, \quad \alpha_i = k\sin(\theta_i) = \frac{n}{r_0}, \quad k_i^+ = \sqrt{k_0^2-\alpha_i^2} \tag{1.42}$$

$$\begin{pmatrix}\phi_{r,1}^{(1)}(x,z)\\ \phi_{t,1}^{(1)}(x,z)\end{pmatrix} = \sum_{s=-\infty}^{+\infty}\begin{pmatrix}R_s^{(1)}\\ T_s^{(1)}\end{pmatrix}\mathrm{e}^{\mathrm{i}\alpha_s z}\begin{pmatrix}\mathrm{e}^{\mathrm{i}k_s^{(1)-}(x-x_1)}\\ \mathrm{e}^{\mathrm{i}k_s^{(1)+}(x-x_2)}\end{pmatrix} \tag{1.43}$$

with

$$\alpha_s = \frac{n+sV_1}{r_0}, \quad k_s^{(1)\pm} = \pm\sqrt{k_0^2-\alpha_s^2}$$

$$\begin{pmatrix}\phi_{d,1}^{(1)}(x,z)\\ \phi_{u,1}^{(1)}(x,z)\end{pmatrix} = \sum_{q=0}^{+\infty}\begin{pmatrix}D_q^{(1)}\\ U_q^{(1)}\end{pmatrix}\mathrm{e}^{\mathrm{i}m_1H_1\alpha_i}\cos\Big(\alpha_q\left[z-m_1H_1\right]\Big)\begin{pmatrix}\mathrm{e}^{\mathrm{i}k_q^{(1)+}(x-x_1)}\\ \mathrm{e}^{\mathrm{i}k_q^{(1)-}(x-x_2)}\end{pmatrix} \tag{1.44}$$

where

$$\alpha_q = q\frac{\pi}{a_1}, \quad k_q^{(1)\pm} = \pm\sqrt{k_0^2-\alpha_q^2}$$

In this analysis the superscript (1) refers to the acoustic field produced by the guide vanes and the subscript 1 represents the index of iteration. The use of the analytical model developed in the previous section 1.3 allows to determine the modal amplitudes of the different fields.

#### 1.4.1.2 Step 2 - Scattering of $\phi_t^{(1)}$ by the cooling channels

The downstream acoustic waves generated by the guide vanes in the first step $\phi_t^{(1)}$ are transmitted through the cooling channels, generating four new acoustic fields, denoted by

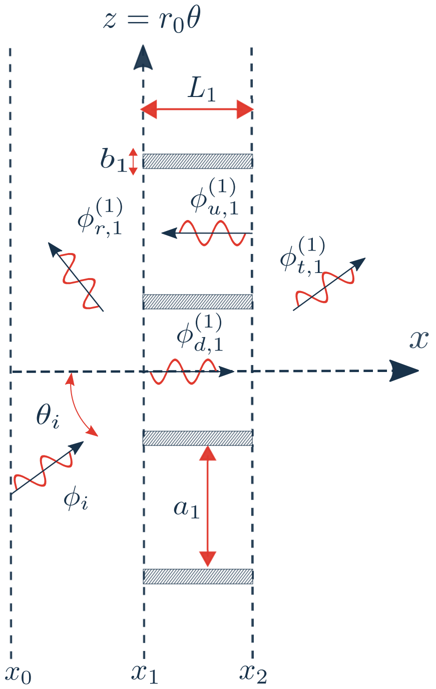

**Figure 1.23:** Scattering of the incident wave $\phi_i$ by the guide vanes in the first step.

$\phi_r^{(2)}$, $\phi_d^{(2)}$, $\phi_u^{(2)}$ and $\phi_t^{(2)}$ as depicted in Figure 1.24. To solve this problem, the acoustic excitation $\phi_t^{(1)}$ must be expanded into a sum of incident waves having different propagation angles. Each of these waves is characterized by its modal amplitude $T_s^{(1)}$ and its modal order $n_{s_1} = n + s_1 V_1$. The expression of a single excitation at the inlet interface of the cooling channels $x = x_2$, can be written as

$$\phi_s^{(1)}(x_3, z) = T_s^{(1)} \mathrm{e}^{\mathrm{i}\alpha_s z} \mathrm{e}^{\mathrm{i}k_s^{(1)+} d} \mathrm{e}^{-\mathrm{i}\omega t} \tag{1.45}$$

The scattering of each incident excitation $\phi_t^{(1)}$ can be investigated by the use of the analytical model developed in section 1.3. After applying this model to all the incident excitations, the sound field can be constructed by the superposition of all the acoustic modes generated at this step.

$$\begin{pmatrix} \phi_{r,2}^{(2)}(x,z) \\ \phi_{t,2}^{(2)}(x,z) \end{pmatrix} = \sum_{s=-\infty}^{+\infty} \sum_{\nu=-\infty}^{+\infty} \begin{pmatrix} R_{s\nu}^{(2)} \\ T_{s\nu}^{(2)} \end{pmatrix} \mathrm{e}^{\mathrm{i}\alpha_{s\nu} z} \begin{pmatrix} \mathrm{e}^{\mathrm{i}k_{s\nu}^{(2)+}(x-x_3)} \\ \mathrm{e}^{\mathrm{i}k_{s\nu}^{(2)-}(x-x_4)} \end{pmatrix} \tag{1.46}$$

with

$$\alpha_{s\nu} = \alpha_s + \frac{\nu V_2}{r_0}, \quad k_{s\nu}^{(2)\pm} = \pm\sqrt{k_0^2 - \alpha_{s\nu}^2}$$

The downstream and upstream acoustic waves in the $m_2^{th}$ channel are given by

$$\begin{pmatrix} \phi_{d,2}^{(2)}(x,z) \\ \phi_{u,2}^{(2)}(x,z) \end{pmatrix} = \sum_{s=-\infty}^{+\infty} \sum_{\mu=0}^{+\infty} \begin{pmatrix} D_{s\mu}^{(2)} \\ U_{s\mu}^{(2)} \end{pmatrix} \mathrm{e}^{\mathrm{i}m_2\alpha_s H_2} \cos\left(\alpha_\mu \left[z - m_2 H_2\right]\right) \begin{pmatrix} \mathrm{e}^{\mathrm{i}k_\mu^{(2)+}(x-x_3)} \\ \mathrm{e}^{\mathrm{i}k_\mu^{(2)-}(x-x_4)} \end{pmatrix} \tag{1.47}$$

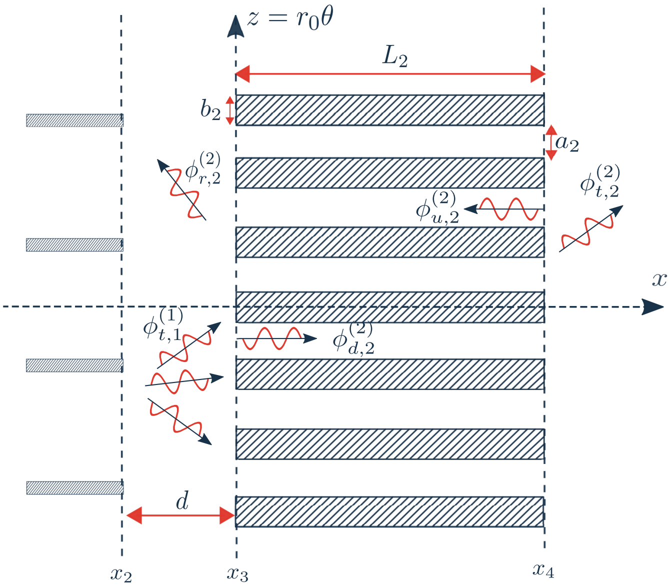

**Figure 1.24:** Scattering of the transmitted modes $\phi_t^{(1)}$ by the cooling channels in the second step.

with

$$\alpha_\mu = \mu\frac{\pi}{a_2}, \quad k_\mu^{(2)\pm} = \pm\sqrt{k_0^2 - \alpha_\mu^2}$$

#### 1.4.1.3 Step 3 - Scattering of $\phi_r^{(2)}$ by the guide vanes

The last step of the methodology deals with the diffraction of the waves reflected back towards the guide vanes (see Figure 1.25). In the same way, the acoustic field reflected by the cooling channels is expanded in a series of oblique plane waves having various propagation angles. The expression of a single excitation at the outlet interface of the

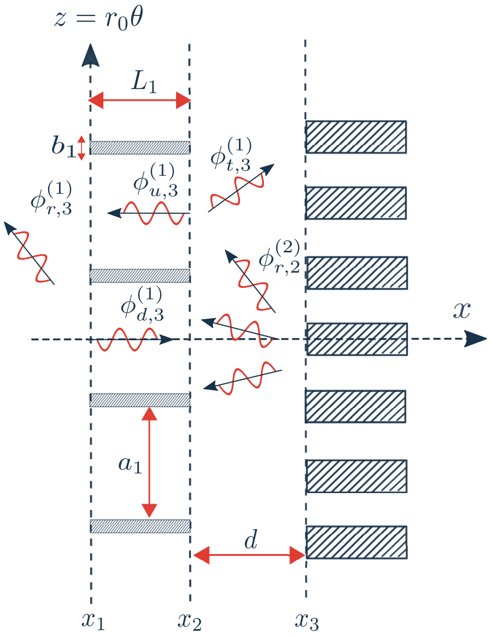

**Figure 1.25:** Scattering of the reflected field $\phi_r^{(2)}$ by the guide vanes in the third step.

guide vanes $x = x_2$, is given by

$$\phi_{s\nu}^{(2)}(x_2, z) = R_{s\nu}^{(2)} \mathrm{e}^{\mathrm{i}\alpha_{s\nu} z} \mathrm{e}^{-\mathrm{i}k_{s\nu}^{(2)-} d} \tag{1.48}$$

After superposing all possible solutions, we obtain

$$\begin{pmatrix} \phi_{r,3}^{(1)}(x,z) \\ \phi_{t,3}^{(1)}(x,z) \end{pmatrix} = \sum_{s=-\infty}^{+\infty} \sum_{\nu=-\infty}^{+\infty} \sum_{l=-\infty}^{+\infty} \begin{pmatrix} R_{s\nu l}^{(1)} \\ T_{s\nu l}^{(1)} \end{pmatrix} \mathrm{e}^{\mathrm{i}\alpha_{s\nu l} z} \begin{pmatrix} \mathrm{e}^{\mathrm{i}k_{s\nu l}^{(1)+}(x-x_1)} \\ \mathrm{e}^{\mathrm{i}k_{s\nu l}^{(1)-}(x-x_2)} \end{pmatrix} \tag{1.49}$$

with

$$\alpha_{s\nu l} = \alpha_{s\nu} + \frac{lV_1}{r_0}, \quad k_{s\nu l}^{(1)\pm} = \pm\sqrt{k_0^2 - \alpha_{s\nu l}^2} \quad ,$$

$$\begin{pmatrix} \phi_{d,3}^{(1)}(x,z) \\ \phi_{u,3}^{(1)}(x,z) \end{pmatrix} = \sum_{s=-\infty}^{+\infty} \sum_{\nu=-\infty}^{+\infty} \sum_{q=0}^{+\infty} \begin{pmatrix} D_{s\nu q}^{(1)} \\ U_{s\nu q}^{(1)} \end{pmatrix} \mathrm{e}^{\mathrm{i}m_1 H_1 \alpha_{s\nu}} \cos\Big(\alpha_q \left[z - m_1 H_1\right]\Big) \begin{pmatrix} \mathrm{e}^{\mathrm{i}k_q^{(1)+}(x-x_1)} \\ \mathrm{e}^{\mathrm{i}k_q^{(1)-}(x-x_2)} \end{pmatrix} \tag{1.50}$$

In the following, the second and the third steps must be repeated alternately until convergence, by taking the output of one subsystem as the input of the other one.

All the solutions must be superposed to get the total acoustic field in each subdomain:

$$\phi_{\xi}^{(1,2)}(x,z) = \sum_{\gamma=1}^{i_{\max}} \phi_{\xi,\gamma}^{(1,2)}(x,z), \quad \xi = \{r, t, d, u\}, \quad \gamma = \begin{cases} 1, 3, 5, ....i_{\max} - 1, & \text{if } \phi^{(1,2)} = \phi^{(1)} \\ 2, 4, 6, ....i_{\max}, & \text{if } \phi^{(1,2)} = \phi^{(2)} \end{cases}$$

$i_{\max}$ being the maximum number of iterations.

It is clear to see that the use of this procedure requires the storage of a large number of modes at each frequency, in order to be able to describe the acoustic field in each subdomain of the geometry.

### 1.4.2 Solving procedure

It should be kept in mind that the use of iterative procedure can be prohibitive when the number of iterations increases, due to the important number of modes produced at each iteration. In practice, only few modes have a significant contribution in the sound transmission mechanism. Each acoustic mode generated in the space located between the two subsystems is characterized by its decay rate $\tau_s$:

$$\tau_s^{\pm} = |\mathrm{e}^{\mathrm{i}k_s^{\pm} d}| \tag{1.51}$$

where the superscripts + and − denote respectively the propagation in positive and negative $x$ directions. The acoustic modes can therefore be classified by their decay rates (see Figure 1.26):

- $\tau_s = 1$: They represent the cut-on modes. Their amplitudes oscillate without being attenuated according to the distance between the two subsystems.
- $\tau_s \approx 0$: They represent the cut-off modes having amplitudes completely attenuated before reaching the interface of the second subsystem. This can be expected when the distance between the two subsystems is large enough.
- $0 < \tau_s < 1$: The amplitudes of the cut-off modes are not completely attenuated before reaching the interface of the second subsystem. This occurs when the distance between the guide vanes and the cooling channels is small.

It is plain to see that the cut-off modes strongly attenuated in the region between the two subsystems ($\tau_s \approx 0$) have no contribution in the transmission mechanism, and they can be neglected in the coupling procedure. This property allows to reduce drastically the number of modes used at each iteration.

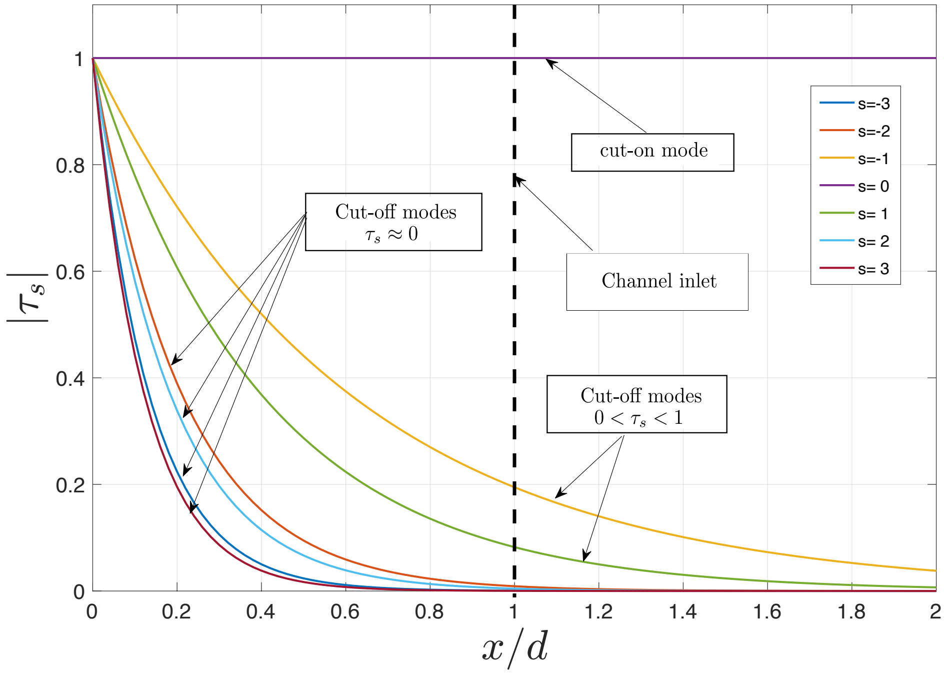

**Figure 1.26:** Variation of the decay rates as a function of $x$

## 1.4.3 Numerical validation

### 1.4.3.1 Two-dimensional finite element method

In this section the analytical model is applied to a configuration consisting of $V_1 = 9$ guide vanes and $V_2 = 19$ cooling channels, separated by a distance $d/L_1 = 1.5$. Table 1.1 lists the test-case parameters.

| $k_0a_1$ | $a_1/H_1$ | $a_2/H_2$ | $r_1$ $(m)$ | $r_2$ $(m)$ | $L_1/a_1$ | $L_2/a_2$ | $d/L_1$ | $n$ |
|---|---|---|---|---|---|---|---|---|
| 5.22 | 0.9 | 0.3563 | 0.13 | 0.17 | 1.0616 | 19.774 | 1.5 | 3 |

**Table 1.1:** Test-case parameters

To check the convergence of the calculation, the acoustic powers are plotted as functions of the number of iterations in Figure 1.27. The error associated with the iterative procedure and the filtering of acoustic modes can be written as

$$\Delta\mathcal{P} = 1 - \frac{|\mathcal{P}_t| + |\mathcal{P}_r|}{|\mathcal{P}_i|} \tag{1.52}$$

Care needs to be taken when calculating the acoustic powers after using the iterative procedure. The acoustic powers of the different fields should not be evaluated by the superposition of the modal acoustic powers of all the modes generated after $\gamma$ iterations. They may be calculated by integrating the acoustic intensity over segments defined upstream the guide vanes and downstream the cooling channels. As can be seen from Figure 1.27, the convergence is reached after only 8 iterations.

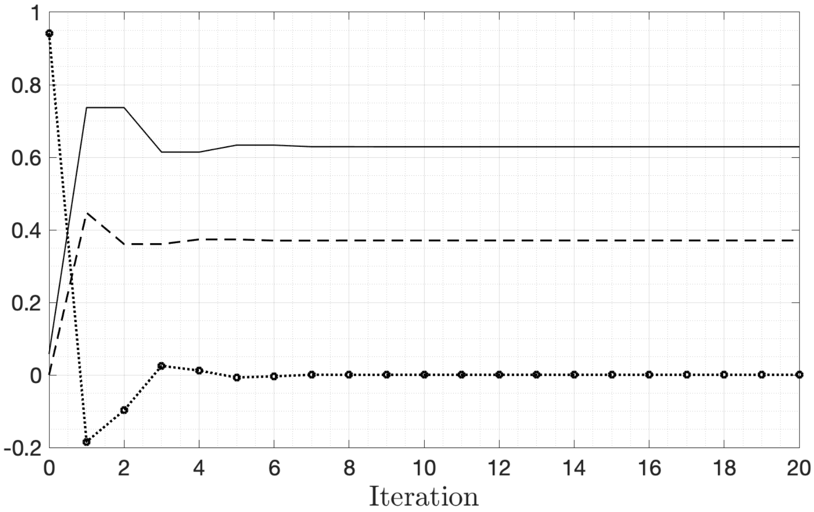

**Figure 1.27:** Convergence study. Error $\Delta\mathcal{P}$ (⋯⋯○), Normalized transmitted power $|\mathcal{P}_t/\mathcal{P}_i|$ (- - - -), normalized reflected power $|\mathcal{P}_r/\mathcal{P}_i|$ (——).

Figures 1.28a and 1.28b show respectively the real parts of the acoustic potential fields obtained by the mode-matching technique and the finite element method for an incident mode $n = 3$ at a frequency $k_0a_1 = 5.22$.

Figure 1.29 compares the acoustic potential profiles extracted along different lines defined upstream, through and downstream the coupled system. Quantitatively and qualitatively, a good agreement is obtained between the two results.

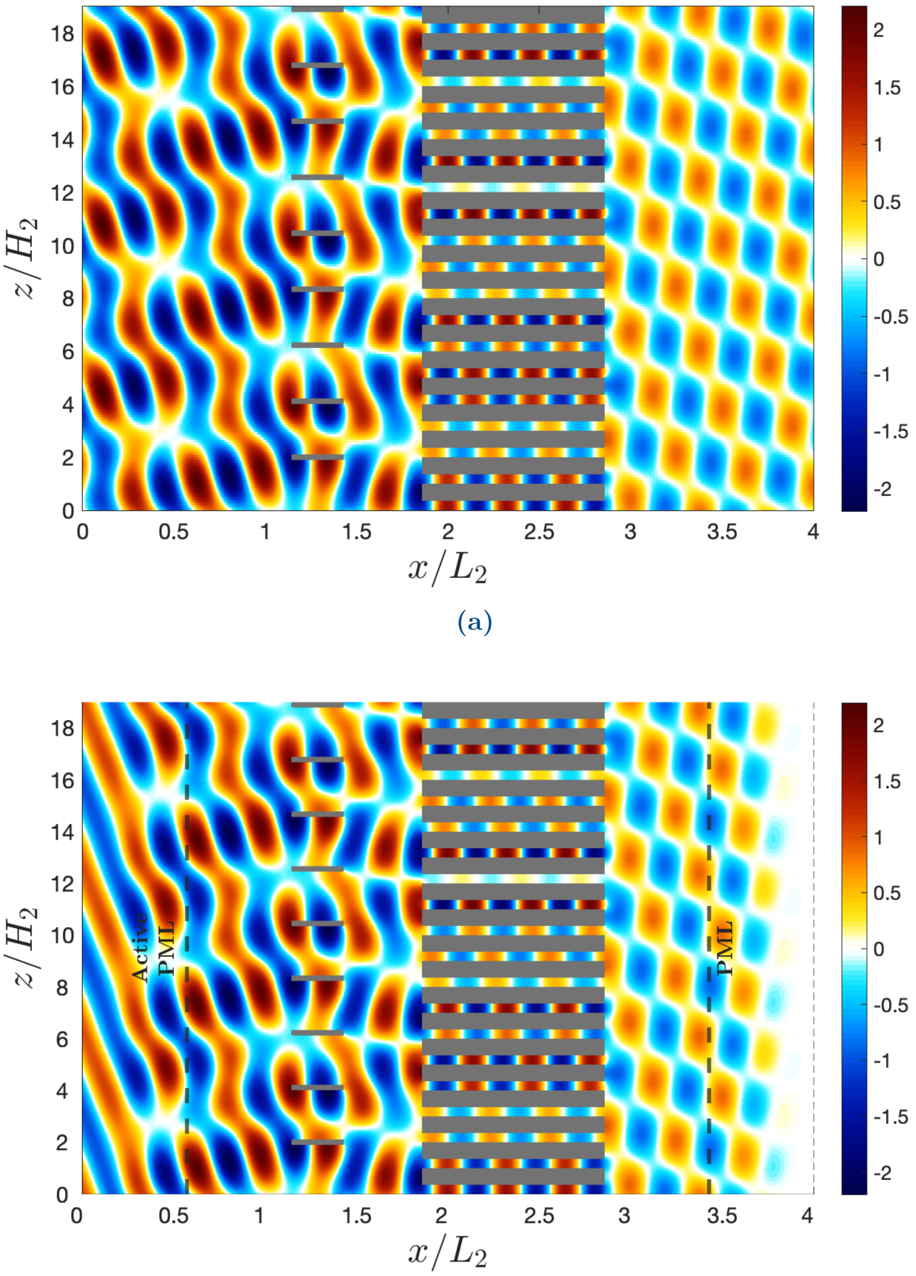

(a)

(b)

**Figure 1.28:** Instantaneous acoustic potential fields obtained by the mode-matching technique (a) and the finite element method (b).

#### 1.4.3.2 Three-dimensional finite element method

As what has been discussed in section 1.3, the comparison between the results obtained by the analytical model and the finite element method applied to the realistic geometry, allows to evaluate the limitations of the two dimensional approach. For that, the finite element method is applied to a configuration with the same parameters listed in Table 1.1. It should be mentioned that in this specific test-case the ratio $a_2/H_2 = 0.3563$ corresponds to cooling channels with a diameter $2r_d = 3\ cm$. The simulation domain is

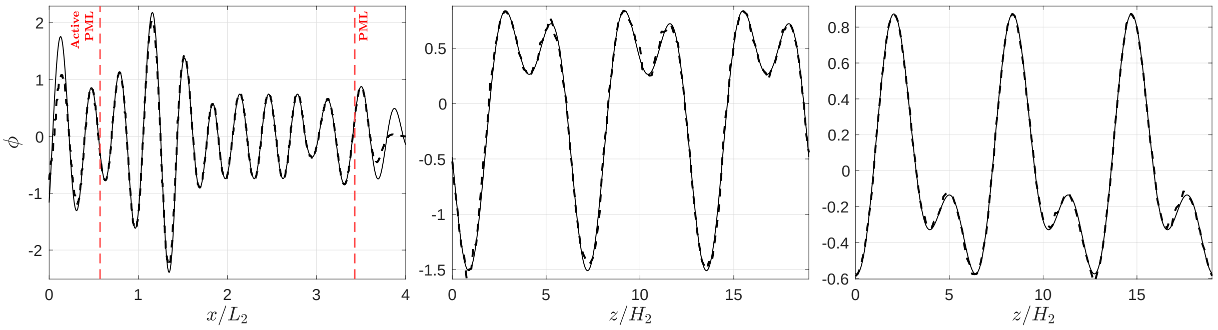

(a) (b) (c)

**Figure 1.29:** Instantaneous acoustic potential profiles extracted at three different lines (*a*) $z/H_2 = 10$ , (*b*) $x/L_2 = 0.8571$ , (*c*) $x/L_2 = 2.9523$, calculated by the mode-matching method (——), and the finite element method (----). Interfaces between the physical domain and the PML regions (----).

truncated by adding two perfectly matched layers upstream the guide vanes and downstream the cooling channels (see Figure 1.30a). The acoustic potential field obtained by the finite element method is shown in Figure 1.30b. As before, in order to evaluate the acoustic powers, two cross-sections must be defined upstream and downstream the system, as shown in Figure 1.30a. After integrating the acoustic intensity over $S_1$ and $S_2$, the reflected and transmitted powers obtained by the two methods are compared in Figures 1.31a and 1.31b respectively. Up to relatively high frequencies ($k_0 h < 4.2$), the results obtained by the two methods are in good agreement. When the frequency increases, the difference between the two results becomes significant. As previously explained, this can be attributed to the propagation of higher-order radial modes beyond a certain frequency. It should be noted that the transmission and reflection peaks at $k_0 h \approx 1.57$ are not physical. Some convergence problems involved in the iterative procedure can be observed when the frequency of an evanescent mode is close to its cut-off frequency.

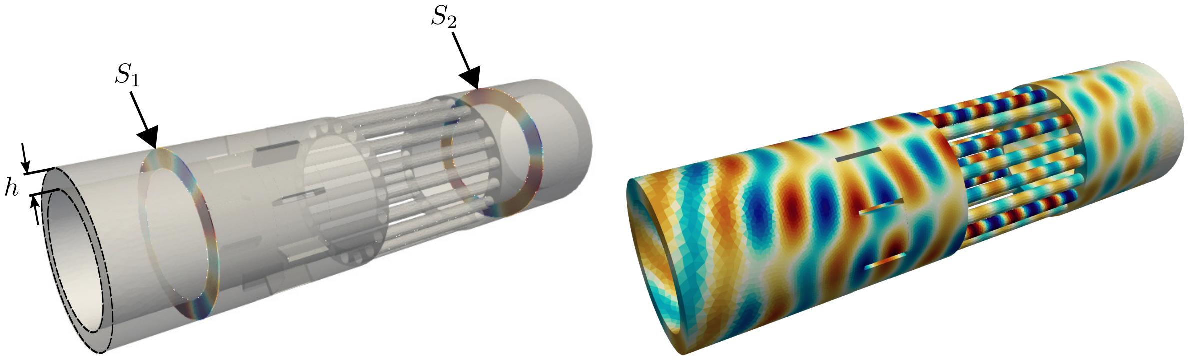

**(a)** **(b)**

**Figure 1.30:** (a) Typical configuration of the ventilation system used in traction motors, (b) Instantaneous acoustic potential field obtained by the finite element method. $f = 3000$ Hz, $n = 3$

In this specific test case, the numerical results were obtained by `FreeFem++` after about 40 hours of calculation on a personal computer, while the analytical model takes only a

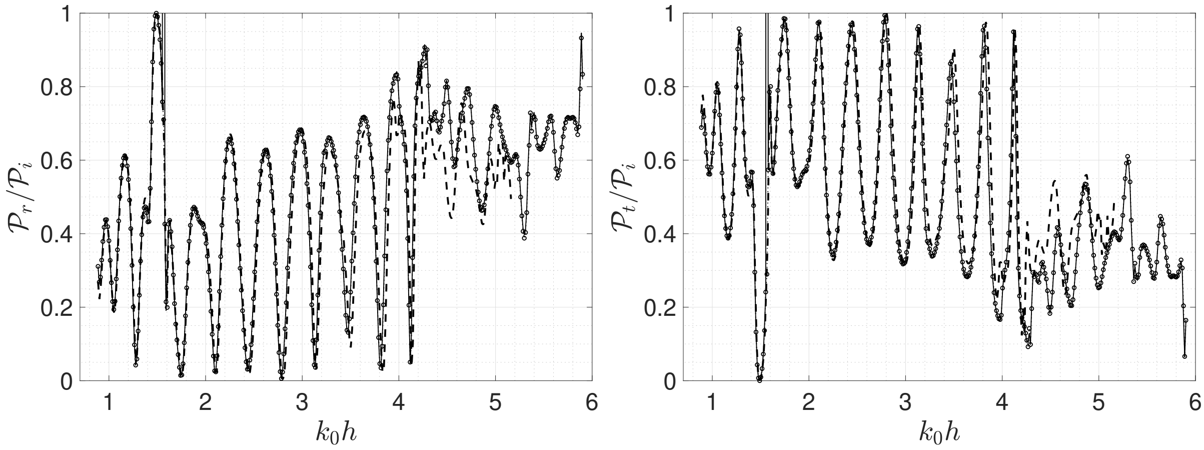

(a) (b)

**Figure 1.31:** Transmitted (a) and reflected (b) acoustic powers obtained by the mode matching technique (——), finite element method 2D (······○) and finite element method 3D (- - - -).

few minutes to get the results. In the following, the sensitivity of the coupled system to geometrical parameters will be investigated in details.

## 1.4.4 Parametric studies

### 1.4.4.1 Effect of guide vanes

In the section 1.3, the resonance frequencies of the cooling channels have been well predicted by the analytical model without taking into account the presence of the guide vanes. It is of interest to examine the influence of the latter on sound transmission, by comparing the configuration of the ventilation system given in the test-case (Table 1.1) with a configuration without guide vanes and a configuration without the cooling channels. For that, the reflected and transmitted powers calculated for each geometry are plotted as functions of the Helmholtz number $k_0a_1$ in Figure 1.32.

It is clear to see that the guide vanes have a significant influence when $k_0a_1 < 4$. Basically, the effect of guide vanes is less marked at relatively high frequencies $k_0a_1 > 4$. All transmission peaks are associated with the resonant frequencies of the cooling channels. When the frequency is less than $k_0a_1 < 4$, the height of transmission peaks is less important comparing with the configuration without the guide vanes. Two important frequencies need to be investigated in this section.

The first one corresponds to a strong attenuation of the transmitted power at $k_0a_1 = 3.5$. The instantaneous acoustic potential fields for a configuration with and without the guide vanes are respectively shown in Figures 1.33b and 1.33b at the same frequency ($k_0a_1 = 3.5$). As can be seen from Figure 1.33b, this attenuation is related to a strong reflection of the incident wave by the guide vanes, involving low transmission to the cooling channels.

The second one corresponds to a transmission peak at $k_0a_1 = 3$, which is not harmon-

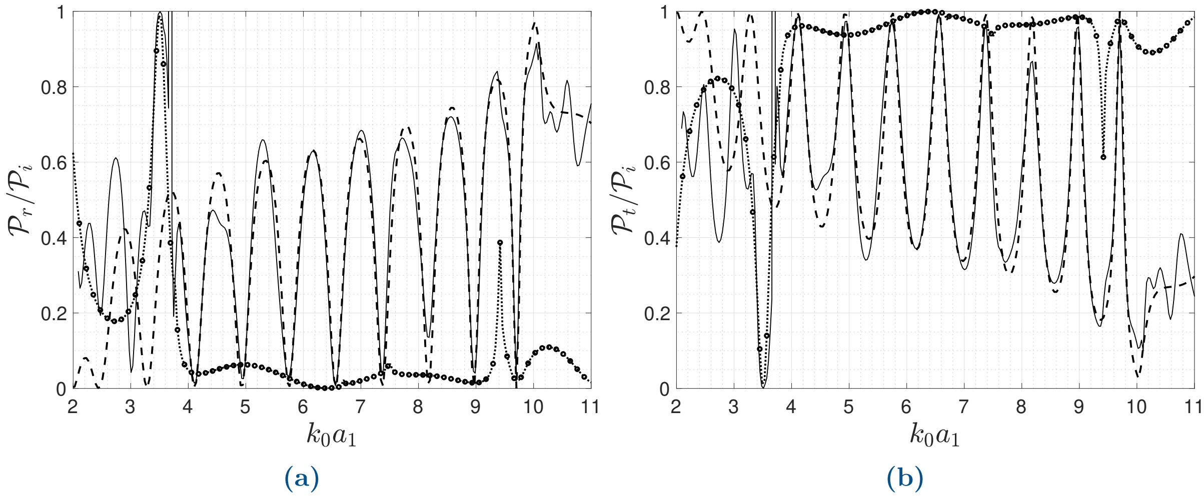

**(a)** **(b)**

**Figure 1.32:** Reflected $(a)$ and transmitted $(b)$ acoustic powers as functions of frequency. Configuration composed of $V_1 = 9$ guide vanes and $V_2 = 19$ cooling channels (——), configuration without cooling channels (⋯⋯○), configuration without guide vanes (- - - -). $n = 3$, $d = 0.15\ m$, $L_1 = 0.1\ m$, $L_2 = 0.35\ m$

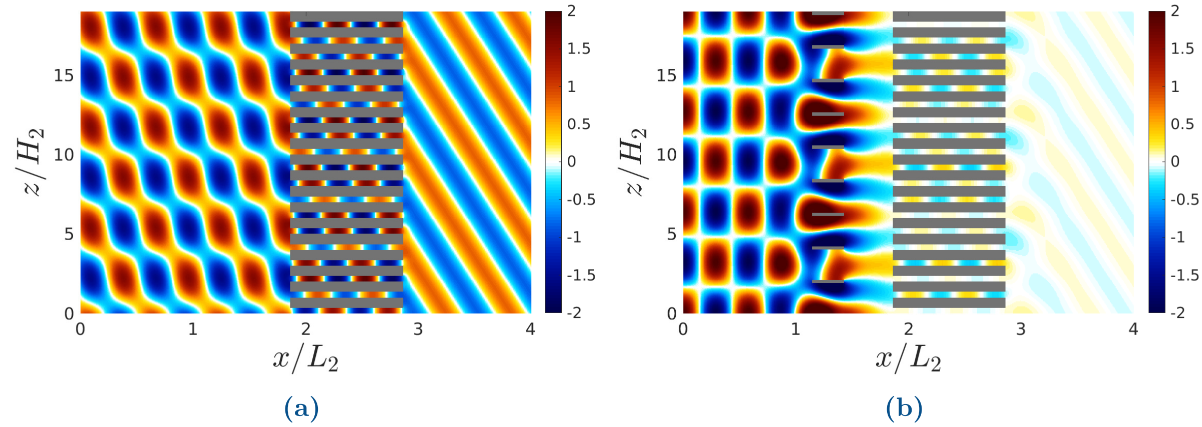

**(a)** **(b)**

**Figure 1.33:** Instantaneous acoustic potential fields calculated by the mode-matching technique. (a) Configuration without the guide vanes. (b) Configuration consisting of guide vanes and cooling channels. $k_0a_1 = 3.5$, $n = 3$.

ically dependant to the resonance frequencies of the cooling channels. To understand the origin of this peak, it is necessary to visualise the acoustic potential field at this frequency. A comparison between the acoustic potential fields of a configuration with and without the guide vanes is shown in Figure 1.34. Figure 1.34b shows an amplification of the acoustic potential in the space between the two subsystems, due to an acoustic resonance caused by the back-and-forth waves. This resonance is responsible for the transmission peak at this frequency. The influence of the distance between the two subsystems and of the wall-thickness of the cooling channels will be highlighted in the following subsections.

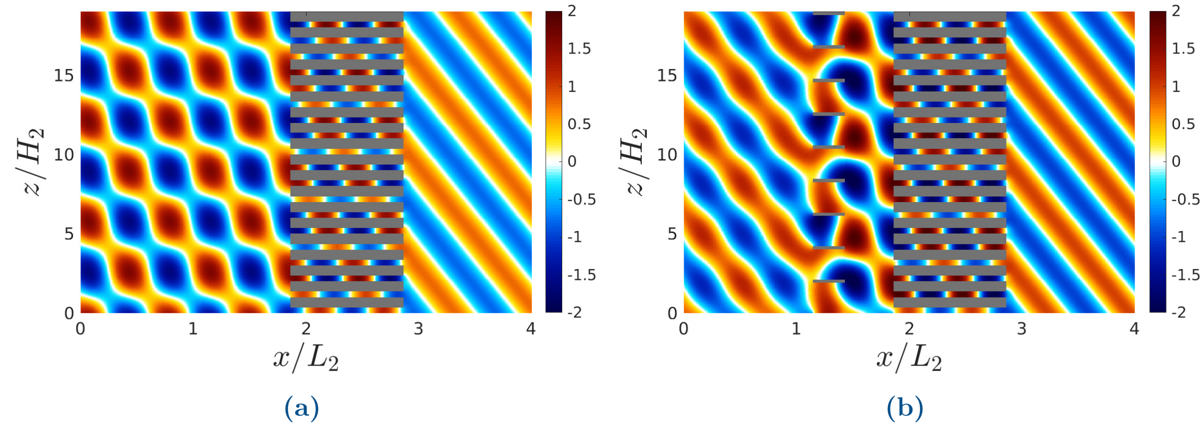

**Figure 1.34:** Instantaneous acoustic potential fields calculated by the mode-matching technique. Configuration without guide vanes. (b) configuration consisting of guide vanes and cooling channels. $k_0 a_1 = 3$, $n = 3$.

#### 1.4.4.2 Effect of distance $d$

In the previous analysis, it has been observed that the acoustic response of the cooling channels is strongly affected by the presence of the guide vanes. In order to investigate the effect of the distance between the two subsystems, three configurations with different distances $d$ have been tested $d/L_1 = 1$, $d/L_1 = 1.5$ and $d/L_1 = 2.5$. The comparison of transmitted powers obtained for the three configurations is shown in Figure 1.35. As can be seen, there is not much difference between the three configurations at relatively high frequencies $k_0 a_1 > 4$. All transmission peaks correspond to the resonance frequencies of the channels. The difference can be observed in a low frequency range, when $k_0 a_1 < 4$. It is clear to see that the frequency of the peak associated with the acoustic resonance in the space between the two subsystems is shifted in the three configurations. The instantaneous acoustic potential maps of the different configurations at the same frequency $k_0 a_1 = 3$

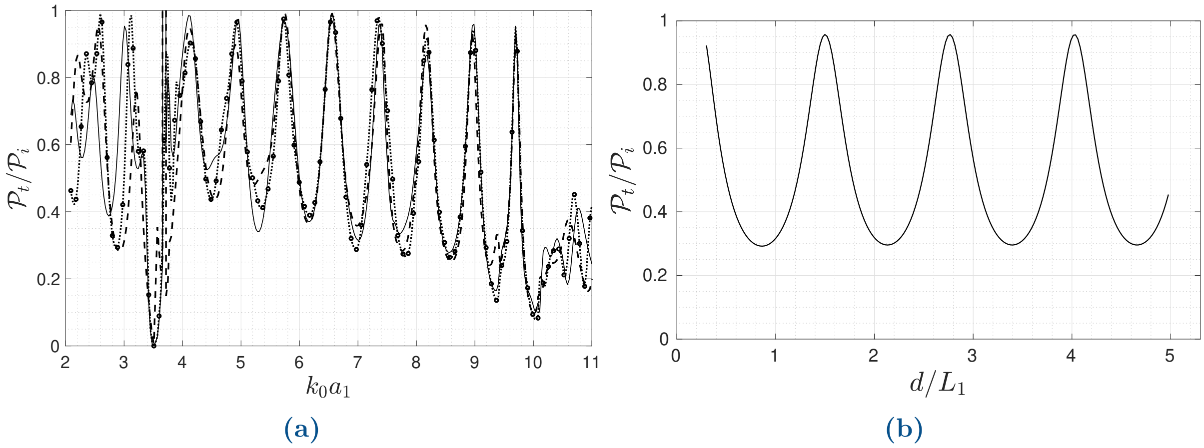

**Figure 1.35:** ($a$) Variation of transmitted powers as a function of frequency for three different distances, $d/L_1 = 1$ (⋯⋯○), $d/L_1 = 1.5$ (——), $d/L_1 = 2.5$ (- - - -). ($b$) variation of transmitted power with distance $d$. $V_1 = 9$ guide vanes and $V_2 = 19$ cooling channels. $n = 3$, $L_1 = 0.1\ m$, $L_2 = 0.35\ m$

are shown in Figure 1.36. Among these configurations, the resonance occurs only in the second one (see Figure 1.36c). To better understand how the amplitude of this peak varies with distance, several calculations have been performed by varying the distance $d$ from $d/L_1 = 0.3$ to $d/L_1 = 5$. Figure 1.35b shows the variation of the transmitted power as a function of the distance $d$. It is observed from Figure 1.35b that the power varies markedly with $d$. It varies sinusoidally between $\mathcal{P}_t/\mathcal{P}_i = 0.3$ and $\mathcal{P}_t/\mathcal{P}_i = 0.95$. This confirms that the resonance caused by the back-and-forth waves in the space between the two subsystems depends directly on the distance $d$.

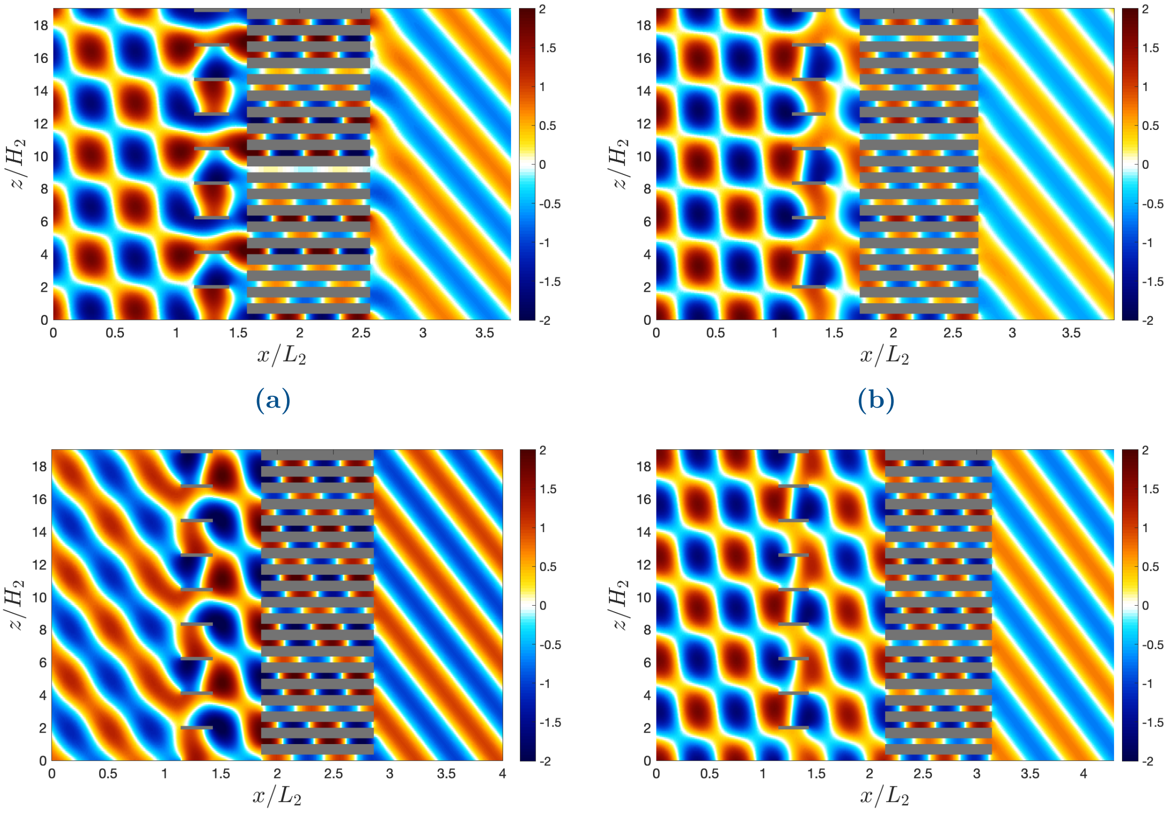

**(a)** **(b)**

**(c)** **(d)**

**Figure 1.36:** Instantaneous acoustic potential fields obtained by the mode matching technique for four different distances. (a) $d/L_1 = 0.5$, (b) $d/L_1 = 1$, (c) $d/L_1 = 1.5$, (d) $d/L_1 = 2.5$. $k_0 a_1 = 3$, $n = 3$.

#### 1.4.4.3 Effect of thickness

To get further understanding of the interactions between the two subsystems, a comparative study was performed for different wall-thicknesses of the cooling channels. The variation of transmitted power as a function of frequency is shown in Figure 1.37a for three different values of $a_2/H_2$.

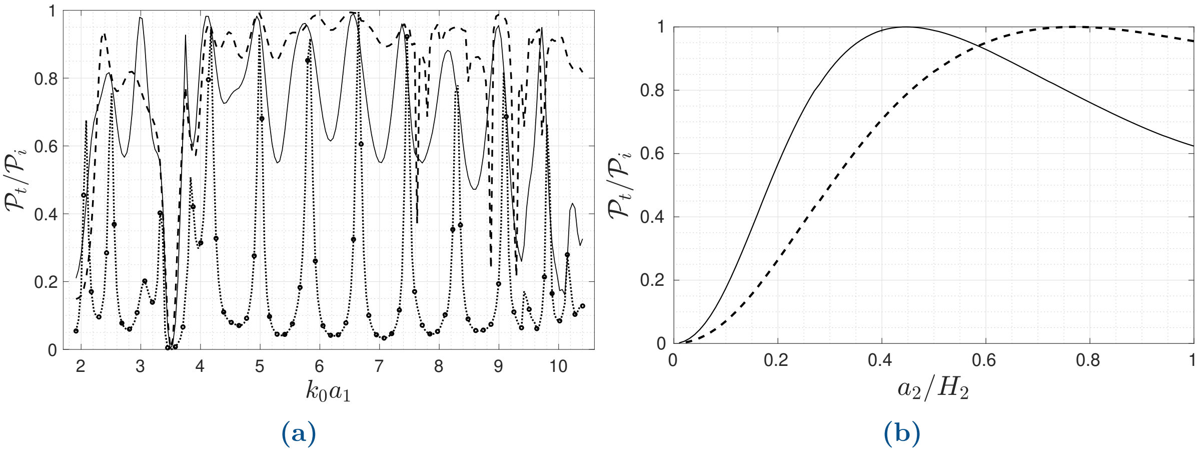

**Figure 1.37:** $(a)$ Variation of transmitted powers as a function of frequency for three different thicknesses, $a_2/H_2 = 0.9$ (dashed line), $a_2/H_2 = 0.5$ (plain line) and $a_2/H_2 = 0.1$ (symbols). $(b)$ variation of transmitted powers with the channel width, configuration composed of guide vanes and cooling channels (plain line), configuration without guide vanes (dashed line). $k_0a_1 = 3$, $n = 3$

Comparing the results, it is clear to see that the resonant frequencies are shifted comparing to the case $a_2/H_2 = 0.5$. This can be explained by the variation of the end corrections of the cooling ducts which depend on $a_2$. Moreover, the transmission peak at $k_0a_1 = 3$ is maximum in the configuration with the ratio $a_2/H_2 = 0.5$. In Figure 1.37b, the channel width $a_2/H_2$ is increased incrementally from 0 to 1, to show the variation of the transmitted power for a configuration with and without the guide-vanes. As expected, in the absence of guide vanes, the transmitted power increases with the channel width $a_2/H_2$. The maximum of transmitted power is obtained for small wall-thicknesses $a_2/H_2 \to 1$. In contrast, the acoustic response of the system is not the same in the presence of guide vanes. The maximum value of the transmitted power is reached at $a_2/H_2 = 0.45$ because of the resonance between the two subsystems (see Figure 1.38c), then it decreases when $a_2/H_2 \to 1$. This decrease in transmitted power is due to the fact that the interactions between the two subsystems are less significant. The sound field is slightly reflected by the channels, involving low interactions between the two subsystems (see Figures 1.38a and 1.38b). For large values of thickness $a_2/H_2 \to 0$, the reflection of the acoustic waves by the walls of the channels becomes dominant (see Figure 1.38d). There is a small range of thickness values in which an acoustic resonance between the two subsystems can be observed. This region is characterized by the maximum values of the transmitted power in Figure 1.37b.

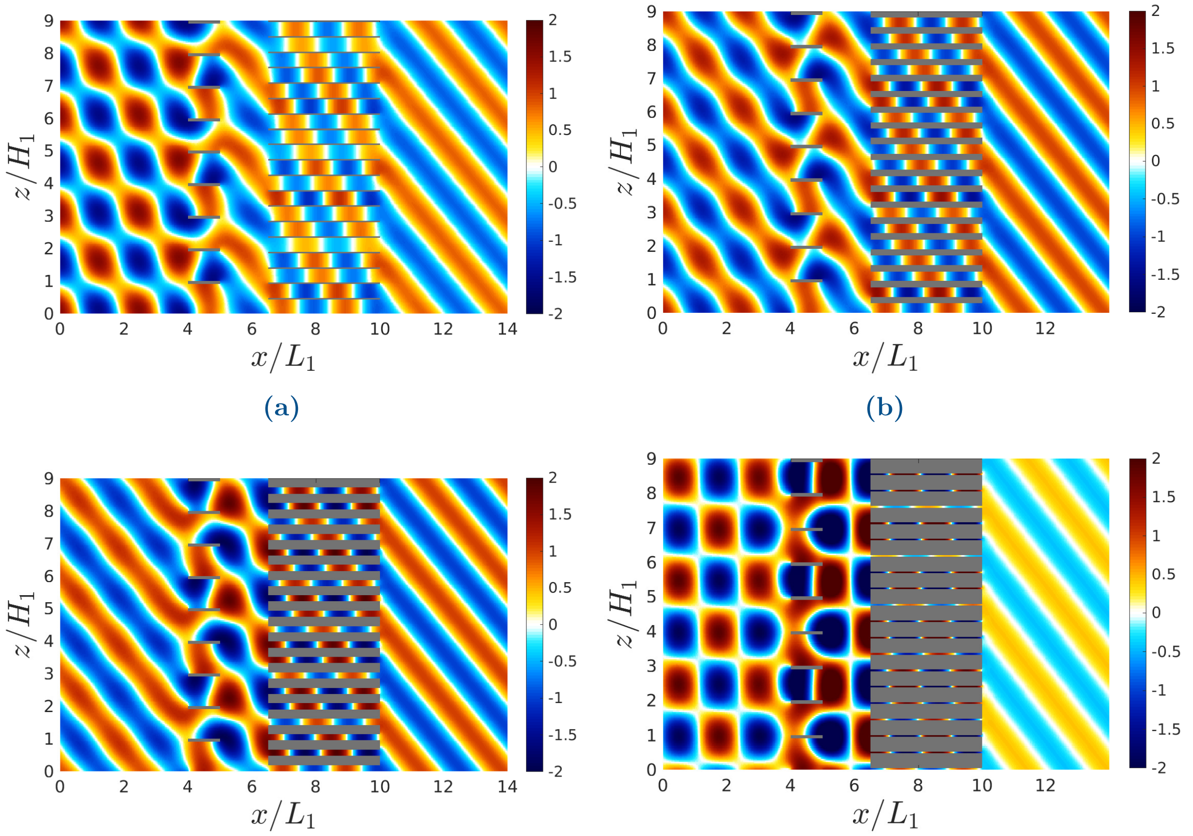

**(a)** **(b)**

**(c)** **(d)**

**Figure 1.38:** Instantaneous acoustic potential fields obtained by the mode-matching technique for four different wall-thicknesses. (a) $a_2/H_2 = 0.9$, (b) $a_2/H_2 = 0.6$, (c) $a_2/H_2 = 0.4$, (d) $a_2/H_2 = 0.1$. $k_0a_1 = 3$, $n = 3$.

## 1.5 Sound propagation inside a truncated motor

The configuration of the ventilation system investigated in the previous sections was assumed to be perfectly periodic in the azimuthal direction $\theta$, which is not always true in some practical applications. The shape and size of the motor must be adapted to the space allocated for the motor in the train. In certain applications, the motors need to be truncated in order to facilitate their integration into the bogie. This may have a significant influence on the acoustic response of the ventilation system. A typical configuration of a truncated motor is illustrated in Figure 1.39. It can be divided into two separated blocks consisting of guide vanes and cooling channels as depicted in Figure 1.40a. As can be seen, two rigid walls are located at the ends of each block of the ventilation system, which prevents the propagation of sound between the two blocks.

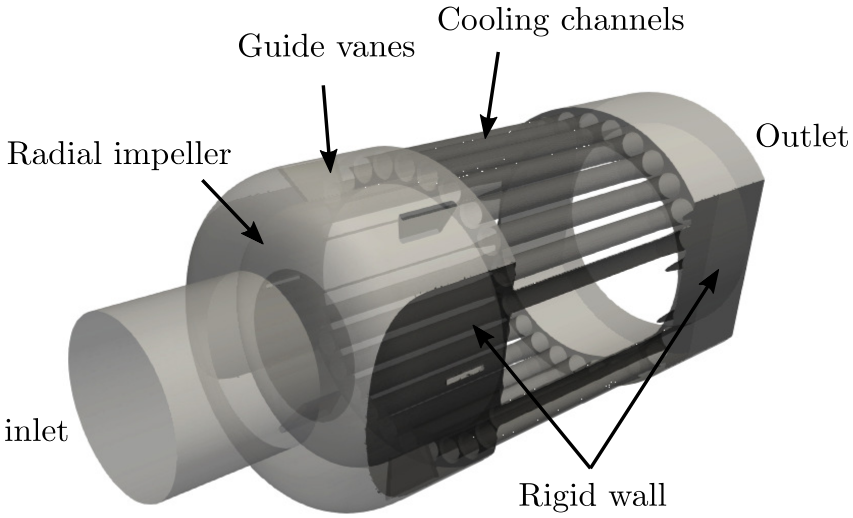

**Figure 1.39:** Typical configuration of the ventilation system of a truncated motor.

Since they are similar, the transmission problem needs to be investigated for a single block of the ventilation system. For this, a cylindrical cut at a radius $r_0$ for a single block is depicted in Figure 1.40b. As in the previous sections, the block is divided into two rows of thick-walled channels separated by a distance $d$. In contrast, a rigid-wall boundary condition must be imposed on $z = 0$ and $z = H_b$ instead of a $2\pi$-periodicity condition.

### 1.5.1 Mathematical formulation

As what has discussed earlier, the acoustic potentials have to be defined in each region of the geometry. The incident excitation is considered as a wave propagating upstream the guide vanes in the positive direction of $x$. The analytical expression of the latter is obtained by solving the Helmholtz equation with the rigid wall boundary condition applied to the walls located at the ends of the block $z = 0$ and $z = H_b$ (see Figure 1.41).

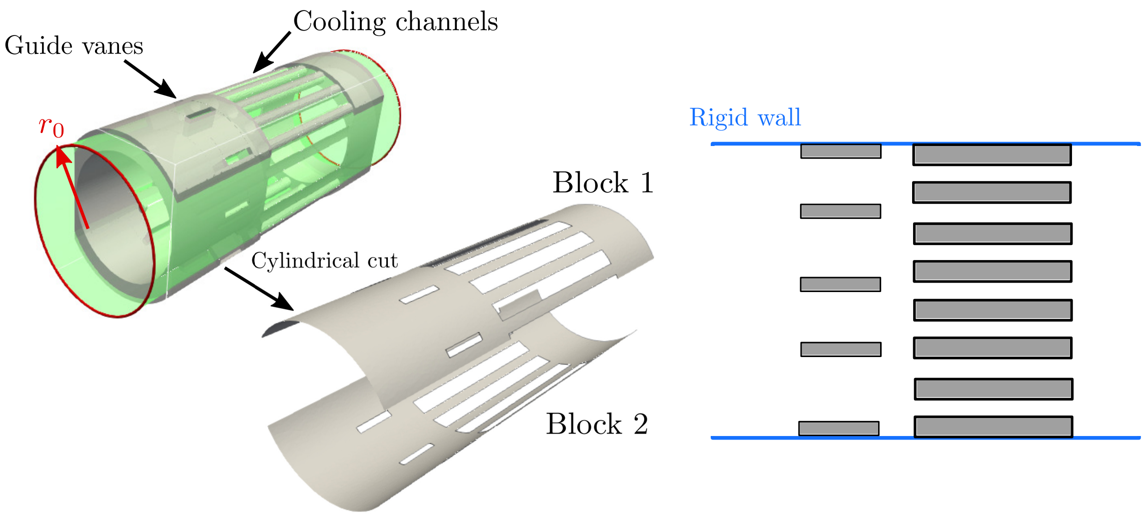

**(a)** **(b)**

**Figure 1.40:** (a) Typical configuration of the ventilation system of a truncated motor, (b) Unwrapped representation of a cylindrical cut of a single block of the ventilation system at $r_0$.

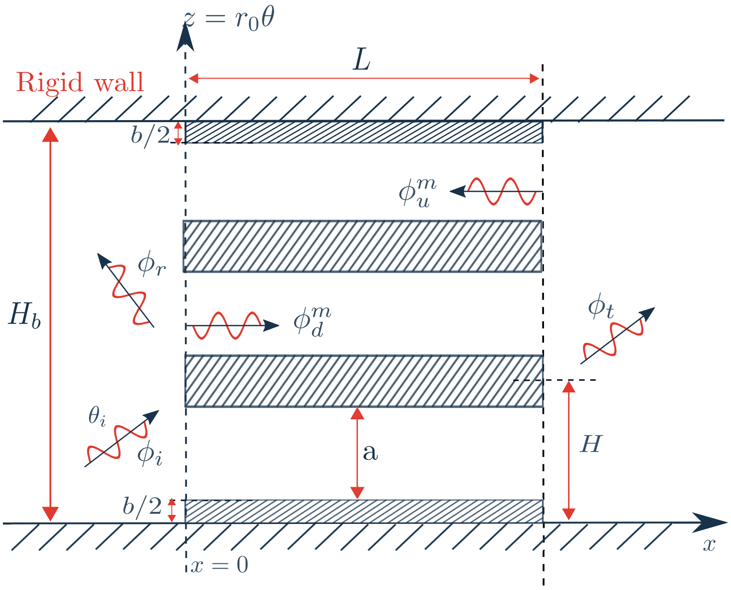

**Figure 1.41:** Unwrapped representation of a cylindrical cut at $r_0$

This excitation is given by

$$\phi_i(x, z) = A_n \cos(\alpha_i z)\, \mathrm{e}^{\mathrm{i}k_i^+ x} \tag{1.53}$$

where

$$\alpha_i = n\frac{\pi}{H_b}$$

The mathematical property of the cosine function allows the eigenfunction $\cos(\alpha_i z)$ to be decomposed into a sum of two exponential functions

$$\cos(\alpha_i z) = \frac{\mathrm{e}^{\mathrm{i}\alpha_i z} + \mathrm{e}^{-\mathrm{i}\alpha_i z}}{2} \tag{1.54}$$

The incident wave $\phi_i$ can therefore be expressed as a sum of two periodic waves with opposite propagation angles, as depicted in Figure 1.42

$$\phi_i(x,z) = \phi_{i+}(x,z) + \phi_{i-}(x,z) \tag{1.55}$$

where $\phi_{i+}$ and $\phi_{i-}$ represent respectively waves travelling in the positive and negative $z$ directions. They are given by:

$$\phi_{i+}(x,z) = \frac{A_n}{2} \mathrm{e}^{\mathrm{i}\alpha_i z} \mathrm{e}^{\mathrm{i}k_i^+ x} \tag{1.56}$$

$$\phi_{i-}(x,z) = \frac{A_n}{2} \mathrm{e}^{-\mathrm{i}\alpha_i z} \mathrm{e}^{\mathrm{i}k_i^+ x} \tag{1.57}$$

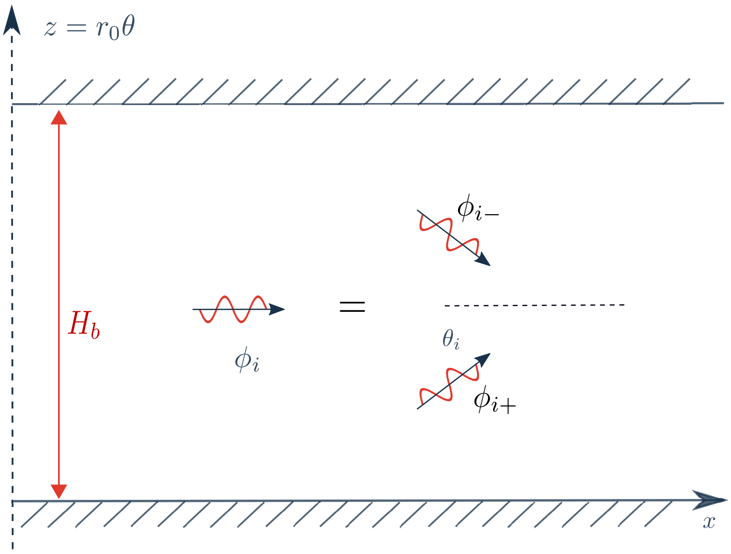

**Figure 1.42:** Decomposition of the incident wave

For example, Figure 1.43 shows the instantaneous acoustic potential fields of the different acoustic waves $\phi_i$, $\phi_{i+}$ and $\phi_{i-}$. Figure 1.43a is obtained after superposing Figures 1.43b and 1.43b.

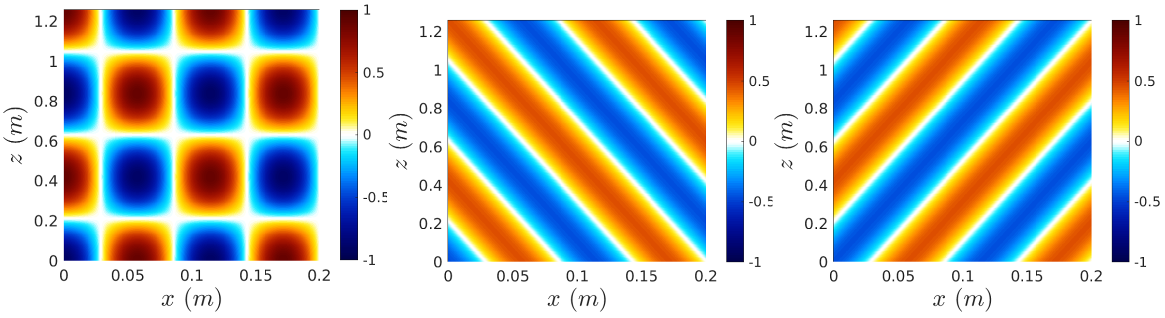

**(a)** **(b)** **(c)**

**Figure 1.43:** Instantaneous acoustic potential fields. (a) $\phi_i$, (b) $\phi_i^+$, (c) $\phi_i^-$.

After using this decomposition, the problem reduces to two diffraction sub-problems that can be studied independently. The scattering of each of these waves ($\phi_{i+}$ or $\phi_{i-}$) by the channels can be investigated in the same way as in Section 1.3. Within the framework of linear acoustics, the response of the system to the excitation $\phi_i$ is obtained by superposing the acoustic fields generated by the diffraction of $\phi_{i+}$ and $\phi_{i-}$. Four acoustic fields are produced by the diffraction of $\phi_i$. The reflected $\phi_r$ and transmitted fields $\phi_t$ read

$$\phi_r(x,z) = \phi_{r+}(x,z) + \phi_{r-}(x,z) = \sum_{s=-\infty}^{+\infty} \Big( R_{s_+} \mathrm{e}^{\mathrm{i}\alpha_{s_+} z} \mathrm{e}^{\mathrm{i}k^-_{s_+} x} + R_{s_-} \mathrm{e}^{\mathrm{i}\alpha_{s_-} z} \mathrm{e}^{\mathrm{i}k^-_{s_-} x} \Big) \tag{1.58}$$

$$\phi_t(x,z) = \phi_{t+}(x,z) + \phi_{t-}(x,z) = \sum_{s=-\infty}^{+\infty} \Big( T_{s_+} \mathrm{e}^{\mathrm{i}\alpha_{s_+} z} \mathrm{e}^{\mathrm{i}k^+_{s_+} (x-L)} + T_{s_-} \mathrm{e}^{\mathrm{i}\alpha_{s_-} z} \mathrm{e}^{\mathrm{i}k^+_{s_-} (x-L)} \Big) \tag{1.59}$$

where

$$\alpha_{s\pm} = \pm\alpha_i + \frac{2\pi}{H} \qquad , k^-_{s_\pm} = -\sqrt{k^2 - \alpha^2_{s_\pm}} \qquad , k^+_{s_\pm} = \sqrt{k^2 - \alpha^2_{s_\pm}}$$

To ensure the symmetry of the geometry, the first and the last channels must be offset by a height of $b/2$ from the walls $z = 0$ and $z = H_b$ (see Figure 1.41). The downstream and upstream acoustic potentials $\phi_d^{(m)}$ and $\phi_u^{(m)}$ in the $m^{th}$ channel can therefore be written as

$$\begin{aligned} \phi_d^{(m)}(x,z) &= \phi_{d+}^{(m)}(x,z) + \phi_{u-}^{(m)}(x,z) \\ &= \sum_{q=0}^{+\infty} \Big( D^0_{q_+} \mathrm{e}^{\mathrm{i}m\alpha_i H} + D^0_{q_-} \mathrm{e}^{-\mathrm{i}m\alpha_i H} \Big) \cos\Big( \alpha_q \Big[ z - mH - \frac{b}{2} \Big] \Big) \mathrm{e}^{\mathrm{i}k^+_q x} \end{aligned} \tag{1.60}$$

$$\begin{aligned} \phi_u^{(m)}(x,z) &= \phi_u^{+(m)}(x,z) + \phi_u^{-(m)}(x,z) \\ &= \sum_{q=0}^{+\infty} \Big( U^0_{q_+} \mathrm{e}^{\mathrm{i}m\alpha_i H} + U^0_{q_-} \mathrm{e}^{-\mathrm{i}m\alpha_i H} \Big) \cos\Big( \alpha_q \Big[ z - mH - \frac{b}{2} \Big] \Big) \mathrm{e}^{\mathrm{i}k^-_q (x-L)} \end{aligned} \tag{1.61}$$

The coefficients denoted by $R_{s_+}$, $T_{s_+}$, $D_{q_+}$ and $U_{q_+}$ represent the modal amplitudes of various acoustic fields generated by the scattering of $\phi_{i+}$ , and the coefficients $R_{s_-}$, $T_{s_-}$, $D_{q_-}$ and $U_{q_-}$ are the modal amplitudes of the fields produced by the scattering of $\phi_{i-}$. These coefficients are determined by the use of the mode-matching method, by imposing the continuity of the acoustic pressure and the axial velocity at the inlet and outlet interfaces of the channels. The matching equations describing the diffraction of $\phi_{i+}$ and $\phi_{i-}$ must be formulated independently.

### 1.5.2 Results

The analytical model is applied in this section to a configuration consisting of $V = 10$ channels. As explained previously, the incident wave should be divided into two oblique plane waves of the same amplitude $An/2$, and propagate with opposite angles of propagation. The parameters of the test case are listed in Table 1.2.

| $V$ | $L$ (m) | $H_b$ (m) | $f$ (Hz) | $n$ | $a/H$ | $A_n$ |
|---|---|---|---|---|---|---|
| 10 | 0.5 | 1.257 | 2500 | 7 | 0.6 | 1 |

**Table 1.2:** Test-case parameters

Figures 1.44a and 1.44b show respectively the instantaneous acoustic potential fields obtained by the scattering of $\phi_{i-}$ and $\phi_{i+}$, using the mode-matching method.

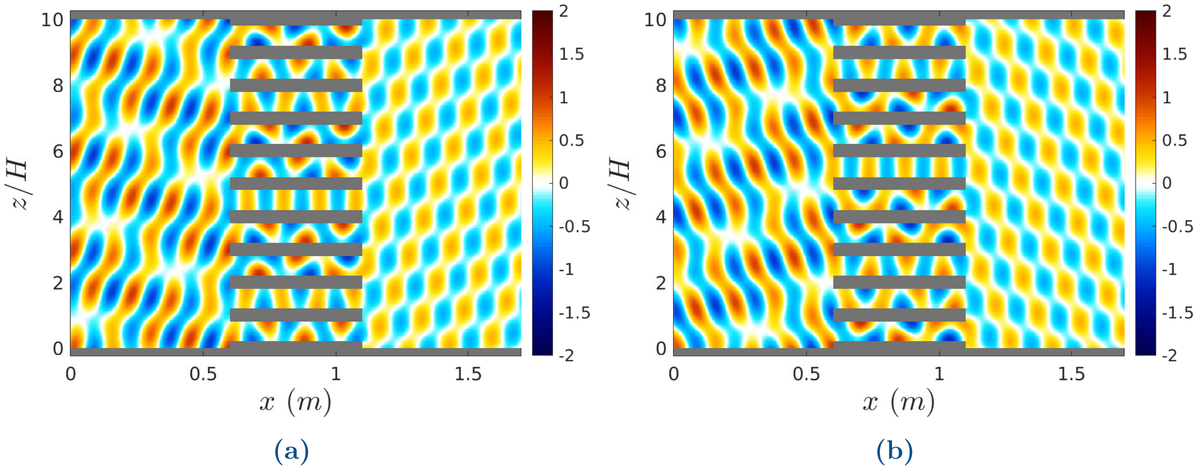

**Figure 1.44:** Instantaneous acoustic potential fields obtained by the mode-matching technique. ($a$) scattering of $\phi_{i-}$, ($b$) scattering of $\phi_{i+}$. $V = 10$, $L = 0.5$m, $H_b = 1.257$m, $f = 2700$Hz, $n = 7$, $a/H = 0.6$.

The instantaneous sound field obtained after the superposition of these two maps is shown in Figure 1.45a. In order to assess the relevance of the analytical model, a qualitative comparison with the finite element method was carried out. Figure 1.45b shows the acoustic potential field obtained by the finite element method. As can be seen, the results obtained by the methods are in a good agreement.

#### 1.5.2.1 Effect of walls

In order to quantify the effect of the walls situated at the bottom and at the top of the system, a comparison between two different configurations is presented in this section. The first one corresponds to a configuration connected to two unbounded mediums (Section 1.3), and the second one corresponds to a configuration connected to two bounded domains. The same dimensions are used for the two configurations (See Table 1.3).

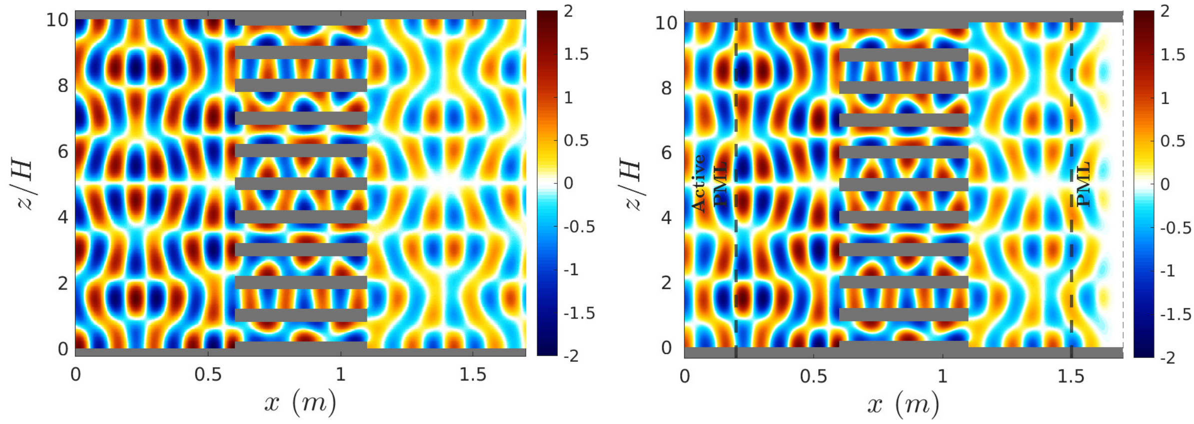

(a)

(b)

**Figure 1.45:** Instantaneous acoustic potential fields obtained by mode-matching method (Scattering of $\phi_{i+}$ and $\phi_{i-}$) $(a)$ and the finite element method $(b)$. $V = 10$, $L = 0.5$m, $H_b = 1.257$m, $f = 2700$Hz, $n = 7$, $a/H = 0.6$.

| $\boldsymbol{V}$ | $\boldsymbol{L}$ (m) | $\boldsymbol{H_b}$ (m) | $\boldsymbol{f}$ (Hz) | $\boldsymbol{n}$ | $\boldsymbol{a/H}$ | $\boldsymbol{A_n}$ |
|---|---|---|---|---|---|---|
| 10 | 0.5 | 1.257 | 3300 | 6 | 0.6 | 1 |

**Table 1.3:** Test-case parameters

A comparison between the acoustic potential fields of the two configurations is shown in Figure 1.46. The acoustic powers ($|\mathcal{P}_d|+|\mathcal{P}_u|$) inside each channel are shown in Figure 1.47 for the two configurations. In the first case (Figure 1.46a) the channels are periodically excited by the incident wave. The acoustic potential inside the channels remains the same, but phase-shifted by a factor $e^{imn/r_0H}$. The acoustic power inside channels is the same (see Figure 1.47a). In contrast, in the second configuration 1.46b, the acoustic potential inside each channel is different. Furthermore, no acoustic wave is transmitted in the third and the seventh channels ($m = 2$ and $m = 7$) as shown in Figure 1.47b.

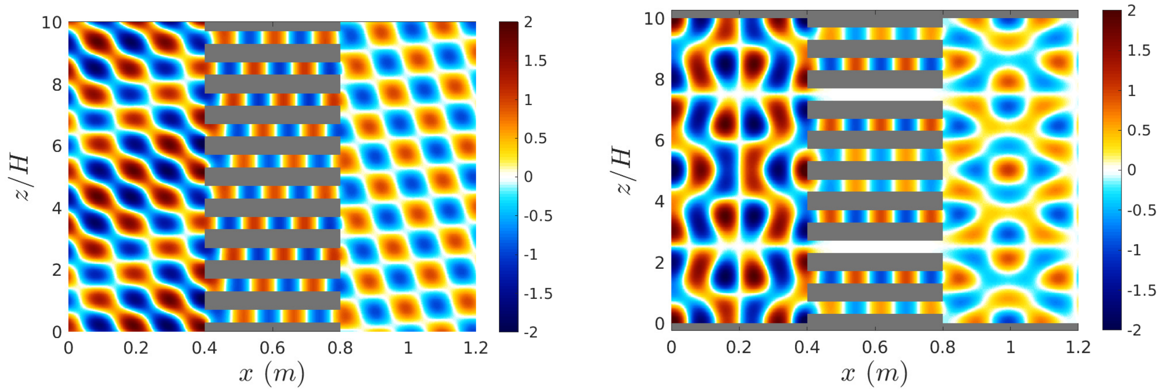

(a)

(b)

**Figure 1.46:** Instantaneous acoustic potential fields obtained for a periodic configuration $(a)$, and a truncated configuration $(b)$. $V = 10$, $L = 0.5$m, $H_b = 1.257$m, $f = 3300$Hz, $n = 6$, $a/H = 0.6$.

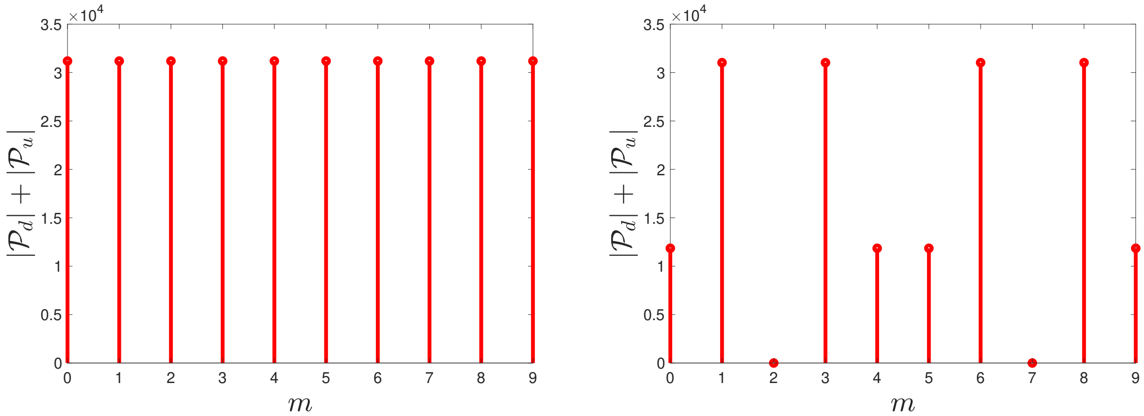

(a)

(b)

**Figure 1.47:** Acoustic powers inside each channel calculated for a periodic configuration ($a$) and a truncated configuration ($b$).

### 1.5.3 Coupled system

After studying the scattering of acoustic waves by a single row of channels connected to two bounded mediums, the transmission of sound through a complete block of the ventilation system, composed mainly of guide vanes and cooling channels can be investigated using an iterative procedure, as explained in Section 1.4. The simulation parameters are listed below in Table 1.4

| $V_1$ | $V_2$ | $L_1$ (m) | $L_2$ (m) | $H_b$ (m) | $d$ (m) | $f$ (Hz) | $n$ | $A_n$ |
|---|---|---|---|---|---|---|---|---|
| 9 | 19 | 0.1 | 0.35 | 0.9424 | 0.15 | 3000 | 4 | 1 |

**Table 1.4:** Test-case parameters

Figure 1.48 shows the instantaneous acoustic potential fields calculated by the mode-matching method and the finite element method for an incidence wave $n = 4$ at the frequency $f = 3000$Hz.

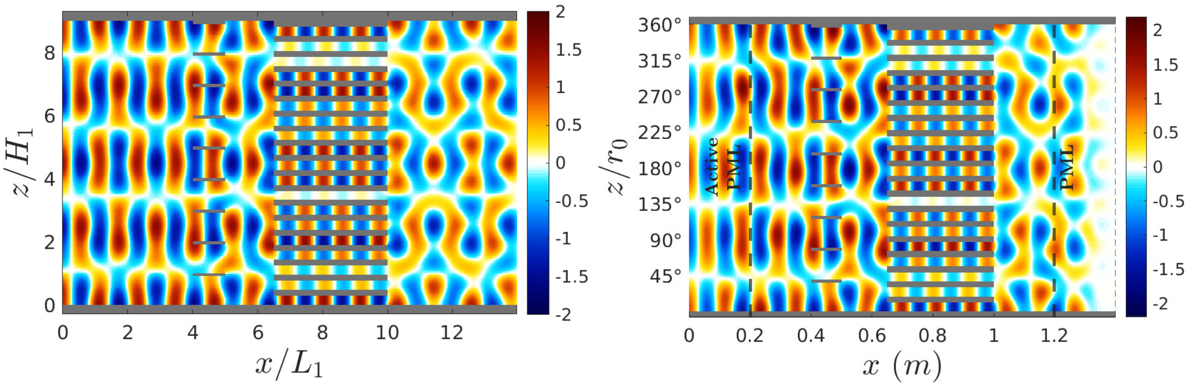

(a)

(b)

**Figure 1.48:** Instantaneous acoustic potential fields obtained by the mode-matching method ($a$), and the finite element method ($b$). $n = 4$, $f = 3000$ Hz, $V_1 = 9$, $V_2 = 19$

## 1.6 Sound generation

The present section is devoted to the sound generation mechanism. The impingement of the impeller wakes on the guide-vanes (see Figure 1.49) generates a noise at the blade passing frequency and its harmonics. The use of fans with uneven blade-spacing allows to reduce the annoyance related to this noise. But it induces new frequencies which are multiple of the rotational frequency. This noise is transmitted through all components of the ventilation system and it can be amplified by the presence of the cooling channels. This occurs when the rotational frequency harmonics coincide with the resonance frequencies of the cooling channels. The present work is based on the work of Roger & Bouley [92, 18].

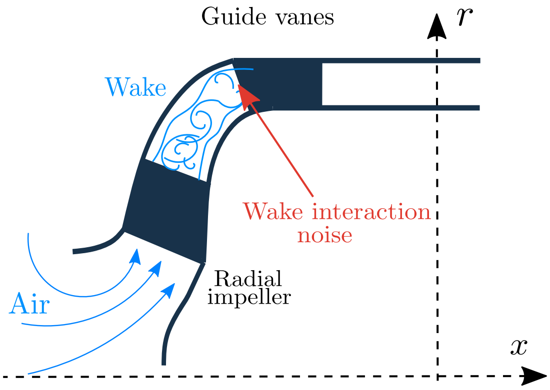

**Figure 1.49:** Impingement of impeller wakes on the guide vanes

The complete analytical modelling of the sound generation requires the description of the wake velocity deficit induced by the rotating blades of the impeller. In such a complex geometry, this parameter is not known and it needs to be extracted from an unsteady RANS simulation. Note here that the influence of this parameter is beyond the scope of this study. The aim is not to predict the absolute amplitude of the acoustic waves generated by the ventilation system, but to develop an analytical model to estimate relative variations, in order to optimise a cooling fan system. Furthermore, the model developed by Bouley et al [19] to predict the noise generated by the impingement of vortical waves on the guide vanes requires the definition of a mean flow. The hydrodynamic waves are convected by the flow. Roger *et al* [92, 18] suggest an alternative approach to describe the response to a hydrodynamic disturbance as a diffraction problem of equivalent dipoles placed very close to the leading edge of each vane as shown in figure 1.50. The use of this approach avoids the need for a mean-flow description, but it requires the description of the equivalent acoustic excitation $\phi_{\text{dip}}$. The latter is reproduced by the superposition of identical dipoles placed very close to the guide vanes. This excitation can be written as a sum of oblique plane waves having various propagation angles. The incident field $\phi_{\text{dip}}$ can be written as [18] :

$$\phi_{\text{dip}}(x,z) = V_1 \sum_{s=-\infty}^{+\infty} \frac{\alpha_s}{4\pi r_0 k_s} \mathrm{e}^{\mathrm{i}\alpha_s z} \mathrm{e}^{\mathrm{i}k_s(x-x_i)} \qquad , k_s = \sqrt{k_n^2 - \alpha_s^2} \qquad , k_n = \frac{n\Omega}{c_0} \tag{1.62}$$

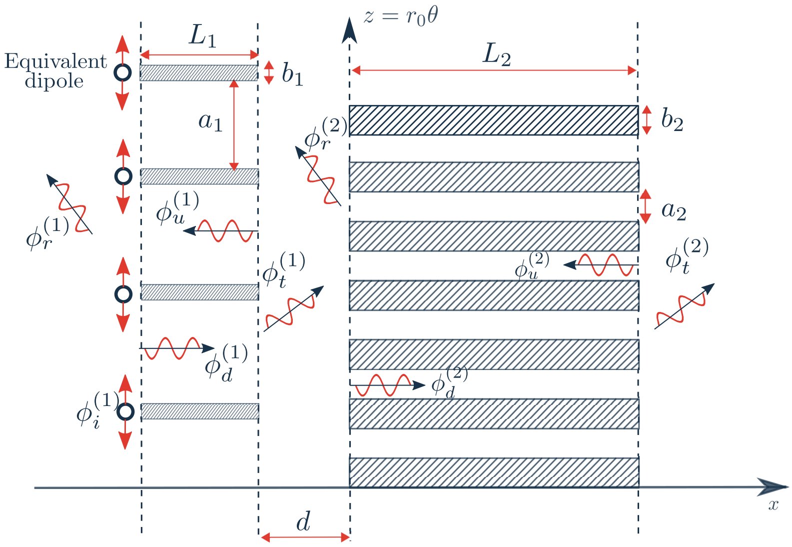

**Figure 1.50:** two-dimensional unwrapped representation. Propagation of waves generated by the diffraction of equivalent dipoles by the guide vanes

where $n$ is the order of the rotational frequency harmonics.

In practice the amplitude of the equivalent dipoles must be calibrated by the comparison with a reference solution [18]. It depends on the amplitude of the hydrodynamic waves $\phi_n \sim w_n$. The scattering of this excitation can be achieved by using the mode-matching technique [18, 19].

### 1.6.1 Blade modulation technique

The blade modulation technique consists in giving an irregular spacing of the impeller blades (see Figures 1.51). This technique is very useful for reducing the tonal annoyance of a given fan by modifying the noise spectrum and distributing the sound energy to rotational frequency harmonics [39, 35, 41, 67, 89].

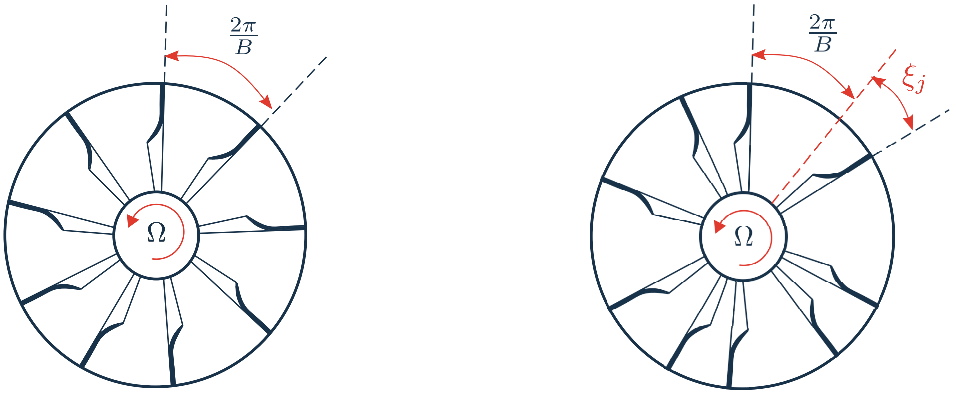

**(a)** **(b)**

**Figure 1.51:** (a) Radial impeller with regular blade spacing. (b) Radial impeller with irregular blade spacing.

The blade modulation effects have to be considered in a mathematical formulation of the hydrodynamic excitation. This was investigated, for instance, by Roger [89] who demonstrated that the mathematical expression of the hydrodynamic excitation is written as:

$$w_n = \Omega \Pi_{-n}(\xi)\mathcal{F}(n\Omega) \tag{1.63}$$

where $\mathcal{F}(n\Omega)$ is the Fourier transform of the velocity disturbance, and $\Pi_n(\xi)$ is an interference function, given by:

$$\Pi_n(\xi) = \sum_{j=0}^{B-1} \mathrm{e}^{\mathrm{i}n(2\pi j/B+\xi_j)} \tag{1.64}$$

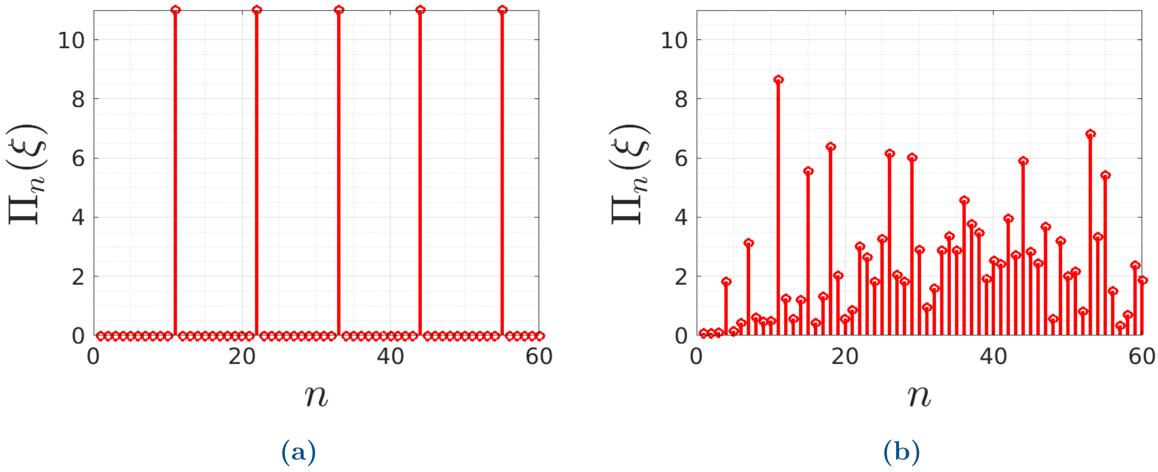

**(a)** **(b)**

**Figure 1.52:** (*a*) Interference function for a fan with regular blade spacing $\xi_j = 0$. (*b*) Interference function for a fan with irregular blade spacing $\xi_j \neq 0$

The modulus of the interference function may have a value between 0 and the number of blades $B$. The influence of modulation angles on the interference function is illustrated in Figure 1.52 for a 11-bladed impeller. It shows clearly that

- For an equally spaced impeller $\xi = 0$ (Figure 1.52a), $\Pi_n$ is equal to $B$ if $n = mB$ and 0 if $n \neq mB$, where $m$ is any integer.
- With unequal spacing of the fan blades (Figure 1.52b) the interference is not completely constructive when $n = mB$ and it is not completely destructive when $n \neq mB$. Therefore, compared to a fan with regular blade spacing, a decrease of the peak levels at multiples of the blade-passing frequency is expected, with regeneration of harmonics of the rotational frequency.

In the following, the interference function is used in order to select the most annoying harmonics to be studied.

### 1.6.2 Results

The analytical model is applied in this section to a ventilation system composed of 11-bladed impeller with circumferentially unsymmetrical blade-spacing, 8 guide vanes and

12 cooling channels. The test-case parameters are listed in Table 1.5.

| $V_1$ | $V_2$ | $L_1$ (m) | $L_2$ (m) | $r_0$ (m) | $B$ | $d$ (m) |
|---|---|---|---|---|---|---|
| 8 | 12 | 0.1 | 0.39 | 0.15 | 11 | 0.1 |

**Table 1.5:** Test-case parameters

The modulation angles $\xi$ are given in Table 1.6.

| $j$ | 0 | 1 | 2 | 3 | 4 | 5 | 6 | 7 | 8 | 9 | 10 |
|---|---|---|---|---|---|---|---|---|---|---|---|
| $\xi(j)$ | 3° | 2° | 1° | −5° | 2° | 3° | −4° | 5° | −1° | −6° | 7° |

**Table 1.6:** Modulation angles

The interference function for different values of n is shown in figure 1.53a. The dominant harmonics are $n = 11, 15, 18, 26, 29$. Each mode generates acoustic waves at the frequency $f_n = n\Omega/2\pi$. Figure 1.53b shows the variation of the transmitted powers as a function of rotational speed. It is found that all the dominant harmonics have no contribution in acoustic radiation when the fan speed is less than 1400rpm. Indeed, the acoustic waves generated by the ventilation system at this rotational speed are cut-off. These modes can be transmitted when the fan speed increases.

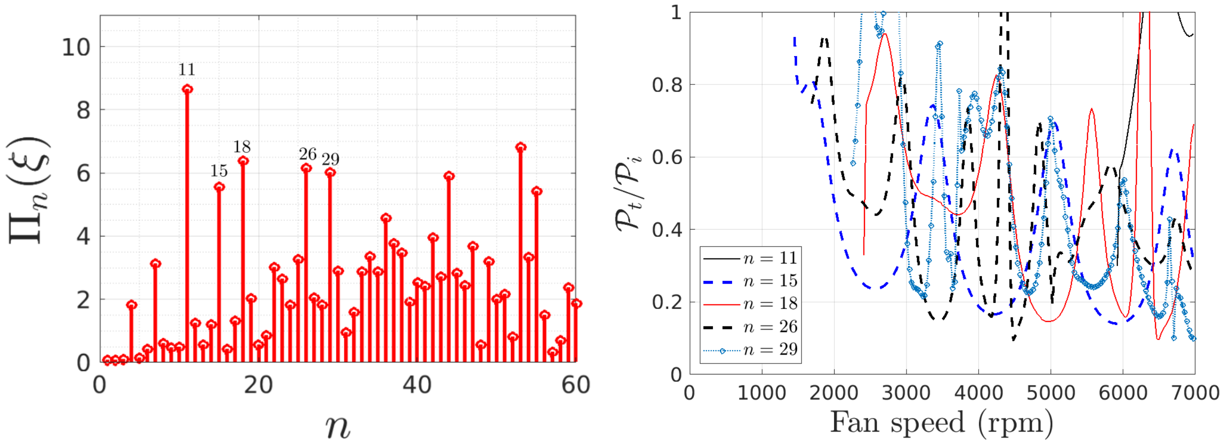

(a)

(b)

**Figure 1.53:** (*a*) Interference function. (*b*) Variation of transmitted acoustic powers as functions of fan speed

### 1.6.2.1 Influence of channel length

One of the most important aspects in this study, is the influence of the length of the cooling channels on sound transmission. The transmitted acoustic powers are plotted as functions of fan speed in Figure 1.54 for $n = 18$. Figures 1.55a and 1.55b show the instantaneous acoustic pressure fields for two different lengths of channels at 4200 rpm. The transmission peaks in Figure 1.54 are due to the acoustic resonances of the cooling

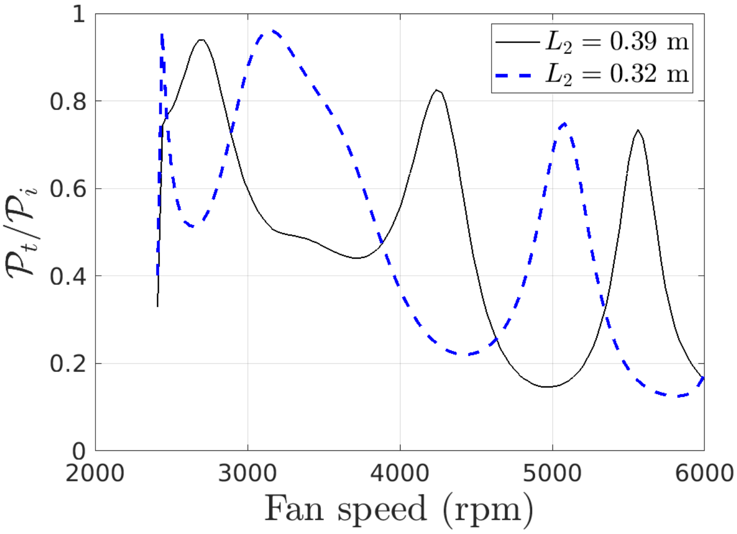

**Figure 1.54:** Variation of transmitted power as a function of rotational speed for two different lengths of channels. $L_2 = 0.32$m (- - - -), $L_2 = 0.39$m (——). $n = 18$, $L_1 = 0.1\ m$, $d = 0.1\ m$.

channels. These frequencies are characterised by a strong amplification of sound inside the cooling channels as shown in Figure 1.55a. It is therefore important to use channels having a length different from 0.39m at this rotational speed. The resonant frequencies of the channels must be different from the rotational frequency harmonics.

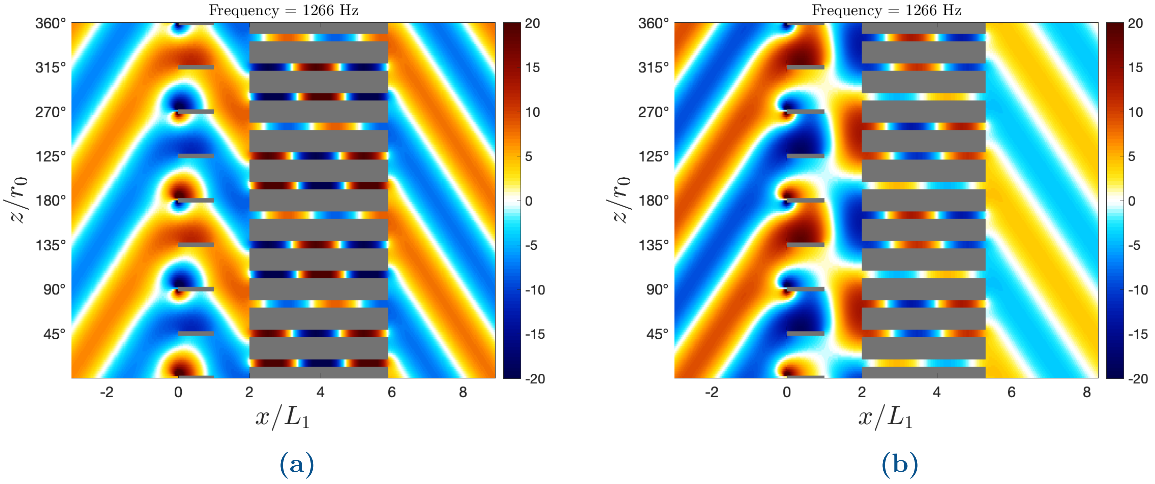

(a)

(b)

**Figure 1.55:** Instantaneous acoustic potential fields obtained for two different lengths. $(a)$ $L_2 = 0.39$m, $(b)$ $L_2 = 0.32$m. $n = 18$, $r_0 = 0.15$m, $V_1 = 8$, $V_2 = 12$, $\Omega = 441.91$ rad/s (4220rpm).

### 1.6.2.2 Effect of distance

Figure 1.57 shows the acoustic potential fields for 2 different configurations. The reference configuration in Figure 1.56 corresponds to the case without the cooling channels. The ventilation system emits upstream and downstream propagating waves. Figures 1.57a and 1.57b represent two configurations with different distances between the guide vanes and

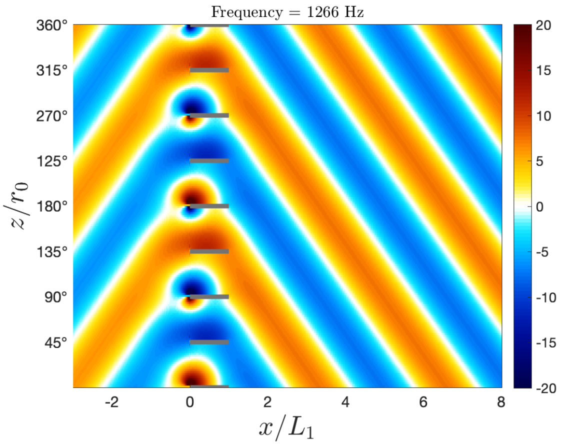

**Figure 1.56:** Instantaneous acoustic potential field for a configuration without cooling channels. $L_1 = 0.1\ m$, $n = 18$, $\Omega = 441.91$ rad/s

the cooling channels. Figure 1.57a shows that the acoustic field upstream the guide vanes has been amplified compared with the reference (Figure 1.56). This amplification is due to a constructive interference between the acoustic waves generated by the wake-interaction mechanism and those reflected by the cooling channels. Constructive interference occurs when two waves are in phase and propagate at the same frequency. The amplitude of the acoustic field is equal to the sum of the amplitudes of the two waves. In contrast, destructive interference occurs when the two waves are out of phase. This case is shown in Figure 1.57b. When the distance between the two subsystems changes, the acoustic waves reflected by the cooling channels are phase-shifted. The low amplitude of the acoustic field upstream the guide vanes is due to the superposition of the maximum amplitude of the first wave with the low amplitude of the second one. It should be noted that the

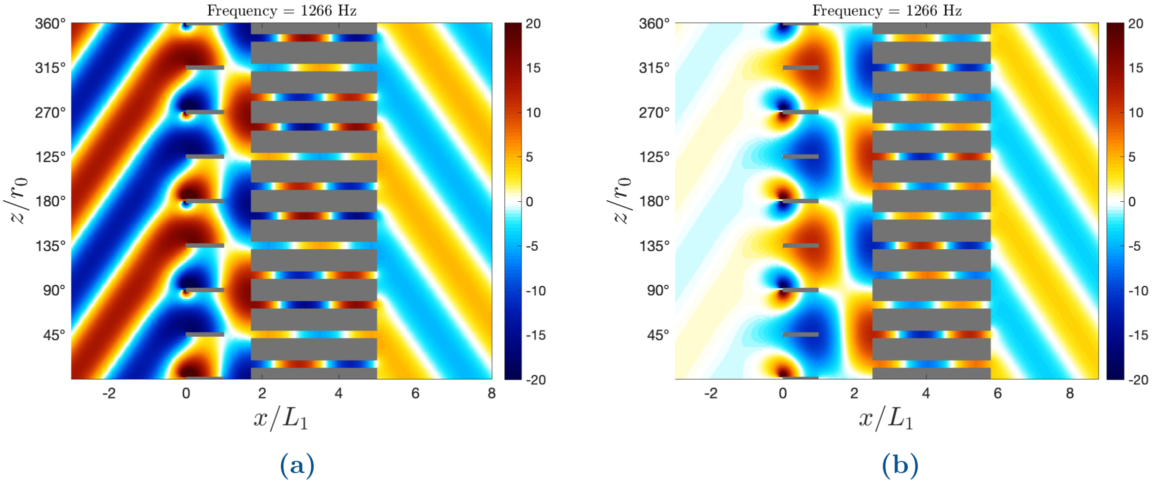

**(a)** **(b)**

**Figure 1.57:** Instantaneous acoustic potential fields. (a) $d = 0.07$m, (b) $d = 0.15$m. $L_1 = 0.1$m, $L_2 = 0.33$m, $n = 18$, $V_1 = 8$, $V_2 = 12$, $\Omega = 441.91$ rad/s.

same interferences can be observed in the space between the guide vanes and the channels, because of the multiple reflections of the acoustic waves as discussed in Section 1.4.

### 1.6.2.3 Effect of the number of vanes

The influence of the number of vanes on sound generation is discussed in this section for $n = 18$. Figure 1.58 shows the instantaneous acoustic pressure fields for three different numbers of vanes at the rotation speed 4200 rpm. In the first case (Figure 1.58a), the configuration is composed of $V_1 = 5$, it generates two propagative modes, given by: $n_s = n + sV_1 = 18 + s5 = [3, -2]$ . The acoustic field is dominated by the mode $n_s = 3$ and modulated by the mode $n_s = -2$. In the second case, for the configuration with $V_1 = 13$ vanes (Figure 1.58b), the modes generated by the system are cut-off, their amplitudes are attenuated exponentially from the interfaces. The sound can only propagate inside the inter-vane channels and the cooling channels. These acoustic modes can be considered as trapped modes [38, 34]. They do not contribute to the acoustic radiation. The last configuration with $V_1 = 16$ vanes is shown in Figure 1.58c, the ventilation system emits only one cut-on mode ($n_s = 2$). Among these configurations, the second one ($V_1 = 13$) is quieter, because the acoustic waves generated at this frequency are cut-off.

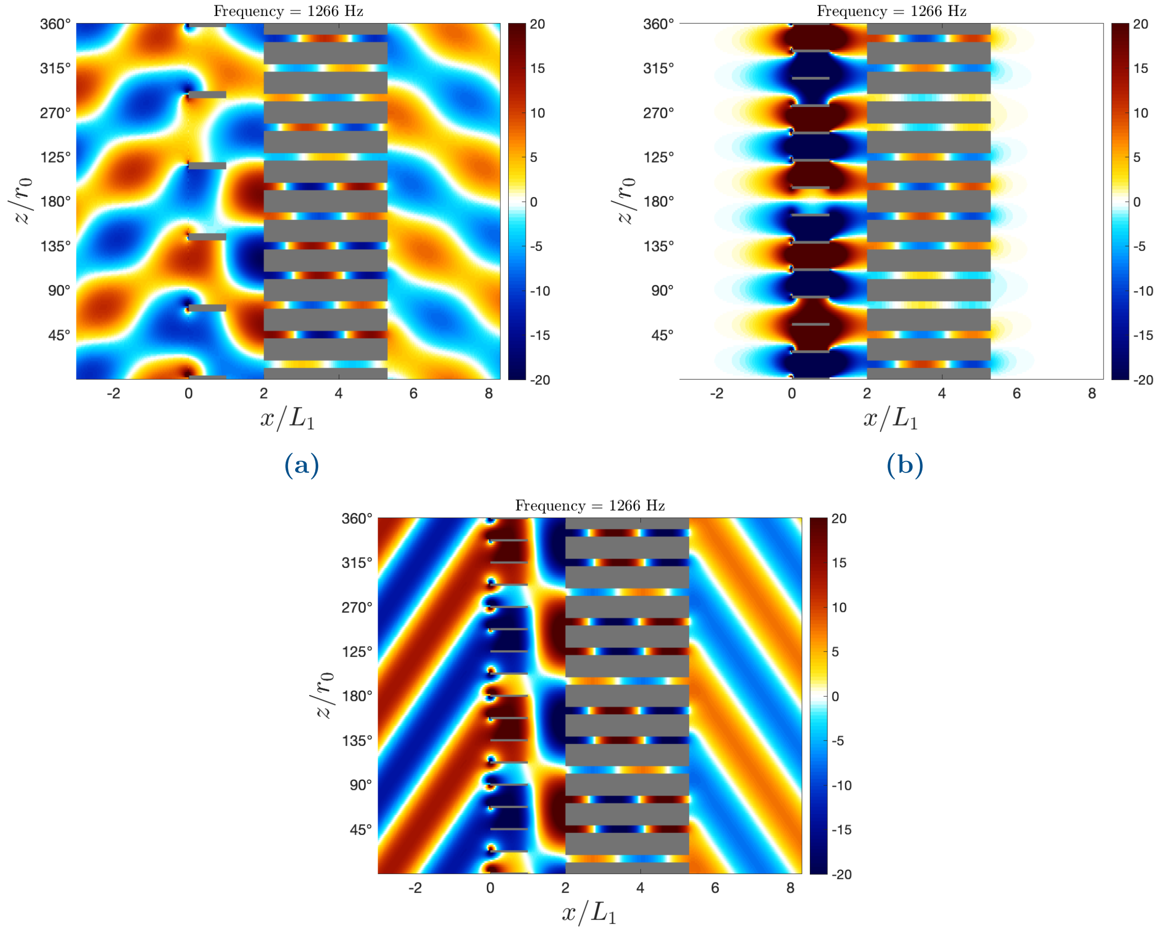

(a)

(b)

(c)

**Figure 1.58:** Instantaneous acoustic potential fields for different numbers of vanes, and with excitation by the mode 18. (a) $V_1 = 5$, (b) $V_1 = 13$, (c) $V_1 = 16$. $n = 18$, $V_2 = 12$, $L_1 = 0.1$m, $L_2 = 0.33$m, $r_0 = 0.15$m, $d = 0.1$m.

## 1.7 Conclusion

In this chapter, an analytical model of sound transmission through a system consisting of two periodic rows of thick-walled channels has been developed. The aim of this model is to investigate how the sound is transmitted through components of the ventilation system integrated in totally enclosed traction motors, in order to improve their design and reduce the aerodynamic noise. The first part of this work was devoted to the diffraction of an oblique plane wave by a periodic row of thick-walled channels using the mode-matching method. Then, this model was applied to the guide vanes and to the cooling channels to predict the sound propagation in this complex geometry. An iterative procedure was used to take into account the multiple diffractions of the acoustic waves between the two subsystems. At most frequencies of interest, the comparisons between the results obtained by the analytical model and the finite element method were in good agreement. The effect of various parameters such as the channel length, the wall-thickness and the distance between the guide-vanes and the cooling channels has been investigated in this chapter. The results obtained have shown that the acoustic response of the cooling channels is strongly affected by the presence of guide vanes. Acoustic resonances can take place in the space between the guide vanes and cooling channels due to the back-and-forth waves propagating in this space. These frequencies can be modulated by changing the distance between the two subsystems.

# Chapter 2

# Analytical modelling of sound propagation inside an open motor

## 2.1 Introduction

The previous chapter has dealt with sound generation and propagation inside the ventilation systems integrated in totally-enclosed motors, using a two-dimensional approach based on the mode-matching technique. The use of the latter was justified by the simplicity of the geometry. As previously mentioned, the performance of totally-enclosed motors is limited by their thermal performance, since the air passes only through the motor frame. In the case of an open motor, the air has a direct contact with the hottest parts of the motor such as the windings. The cooling process is more efficient in this case. A typical configuration of an open motor is illustrated by meridian and axial cuts in Figure 2.1. As can be seen, it is typically composed of various elements such as the flow deflector, windings, motor housing, motor shaft, stator cooling channels, rotor cooling channels, air gap, radial impeller and rigid bars placed at the air outlet of the motor. It should be kept in mind, that the stator and the rotor ventilation ducts are purely axial and they are respectively integrated in the stator and rotor cores. The noise generated by the radial impeller and the rotating parts is transmitted through all components of the motor. Therefore, investigating the propagation of acoustic waves inside this configuration using an analytical approach is much more complicated than in the case of a totally-enclosed motor. Thus, a two-dimensional approach cannot be selected to investigate how the sound can propagate inside this system, due to its large transverse dimensions compared to acoustic wavelengths, and also because of the radial dependencies between its different components. For this, a three-dimensional approach is used in this chapter to deal with this problem.

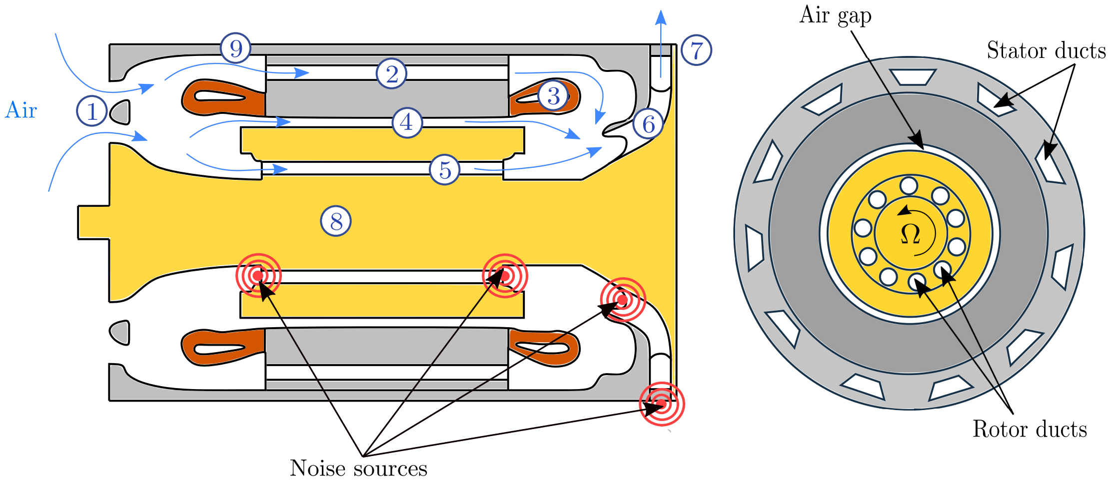

**(a)** **(b)**

**Figure 2.1:** A typical configuration of the ventilation system integrated in an open motor. Rotating part of the motor (yellow). Air flow (blue) (a) Meridian cut. (b) Axial cut. ① Deflector, ② Stator ducts, ③ End-windings, ④ Rotor stator gap, ⑤ Rotor ducts, ⑥ Radial impeller, ⑦ Motor outlet, ⑧ Motor shaft, ⑨ motor housing.

## 2.2 Geometrical approximations

In the first step of the present analysis, the geometry of the motor must be simplified for mathematical tractability. This step allows one to associate the realistic configuration of the ventilation system with a simplified configuration consisting only of generic elements of different transverse dimensions, in which the sound field can be expressed as a sum of orthogonal modes. On the other hand, the geometrical simplifications should not be too excessive in order to maintain the main parameters of the realistic configuration which can have a non-negligible influence on its acoustic response. For that, a meridian cut of the geometry suggested in this work is illustrated in Figure 2.2b. Comparing with the realistic configuration (Figure 2.2a), it is obvious to see that all the curved parts of the ventilation

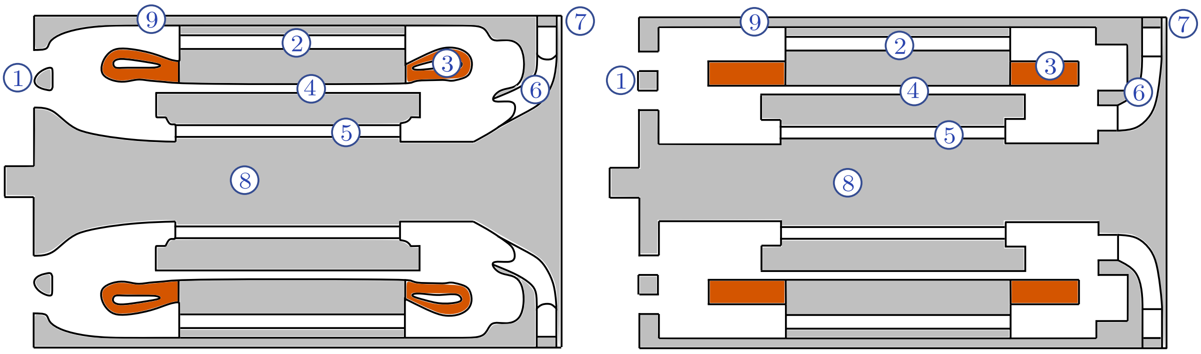

**(a)** Realistic configuration **(b)** Simplified configuration

**Figure 2.2:** Meridian cut of a typical configuration of an open motor of traction. (a) Realistic configuration. (b) Simplified configuration. ① Deflector, ② Stator ducts, ③ End-windings, ④ Rotor stator air gap, ⑤ Rotor ducts, ⑥ Radial impeller, ⑦ Motor outlet, ⑧ Motor shaft, ⑨ Casing.

system have been neglected. Note here that the influence of this parameter is beyond the scope of this study. However, taking into account the effects due to the variation of the duct cross-section or curvature requires a numerical or semi-analytical description of the sound field in the different regions where the curvature is strong, such as the finite element method or the multimodal method [81, 42, 40, 70]. A strong variation of the duct cross-section or curvature involves a coupling between the acoustic modes, and the use of the slowly varying approach [86, 80, 20, 60, 45] does not allow to take these coupling effects into account. Furthermore, the geometry of the stator end-winding is considerably complex (see Figure 2.3a), and it cannot be investigated analytically. In practice, the stator end-windings can be considered as either a rigid part when the space between two conductors is tool small, or a porous region, when this space becomes significant. In a fist approximation, only the rigid part is considered in this work (see Figure 2.3b).

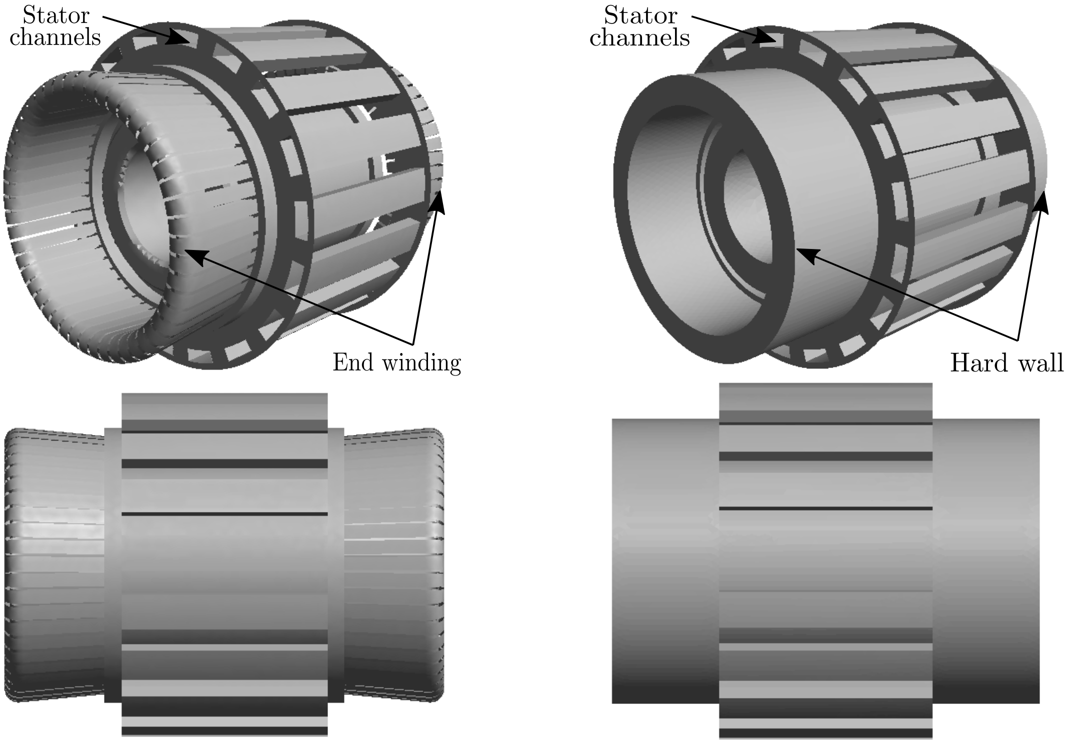

(a) (b)

**Figure 2.3:** Geometrical approximation of the end windings. (a) Realistic configuration. (b) Simplified configuration.

Various kinds of stator channels are commonly used in open motors: circular, rectangular and flat-oval cross-sections. However, the analytical solution of the Helmholtz equation is known only in the case of a duct of circular or rectangular cross-section [66]. In contrast, in the case of a waveguide of flat-oval cross-section, the Helmholtz equation is not separable, and the eigenfunctions need to be determined numerically. This was investigated, for instance, by Cummings *et al* [31, 24, 30]. Furthermore, the cooling channels are generally connected to two annular ducts. Thus, all acoustic fields must be described in the same coordinate system in order determine the matching equations. For the three cases mentioned here, a coordinate transformation is necessary to deal with this problem [94, 79, 54]. It is assumed here for simplicity that the stator channels have the same cross-section illustrated in Figure 2.3. It turns out that the influence of the channel cross-section becomes significant at relatively high frequencies, when several acoustic modes are cut-on. At most frequencies of interest, only plane waves can propagate inside the cooling channels. However, the use of the mode-matching technique in this problem requires a three-dimensional description of the sound field. For that, a multimodal propagation of sound inside the channels should be considered in the analytical formulation of the problem. The next step is to divide the simplified configuration into four interconnected blocks addressed separately as shown in figure 2.4.

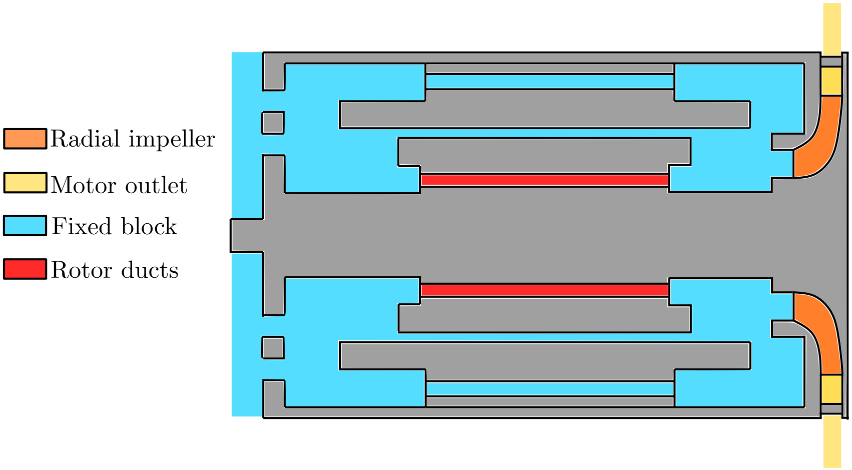

**Figure 2.4:** Dividing the simplified configuration into four interconnected blocks

As can be seen, the propagation of noise inside an open motor can be studied by using four propagation sub-models. Each model requires specific development:

1. Radial impeller: As what has been discussed in Chapter 1, the transmission of acoustic waves through a radial impeller is achieved by the use of three different sub-models.

2. Stationary part: this model deals with the propagation of the acoustic waves generated by the radial impeller and the rotor ducts in the stationary part of the motor. This model is presented in detail in the next section. The associated area is featured in blue in Figure 2.4.

3. Outlet guide vane: the diffraction of spiral waves generated by the radial impeller by the rigid bars located at the motor outlet (yellow area in Figure 2.4). The mathematical formulation of this problem is presented in the last part of this chapter.

4. Rotor ducts: diffraction of oblique plane waves by a periodic row of rotating channels (red area in Figure 2.4). This will be investigated in the next chapter.

The present chapter deals only with the propagation of sound in the stationary part of the motor.

## 2.3 Sound propagation in the stationary part of the motor

After splitting the complete configuration of the ventilation system into several generic elements, only its stationary part is studied in this section. The latter is illustrated in Figure 2.5. As can be seen, it is directly connected to the radial impeller and the rotor cooling channels, by means of three annular ducts, denoted by $(F)$, $(R_{d1})$ and $(R_{d2})$. It is worth noting that the motor shaft and the rotor core without the ventilating holes are axisymmetric. The propagation of sound inside this system is not affected by their rotation, because slip boundary conditions are assumed on all rigid surfaces in the formulation. Therefore, they can be considered fixed in this analysis, and included in the unmoving part of the ventilation system. Not here that in this specific part of the motor, the acoustic waves come from the radial impeller, and from both sides the rotor cooling channels (see Figure 2.5). However, the sound can be either generated or reflected by these components of the ventilation system. In the three cases, the acoustic excitation can be considered as a helical wave propagating in the negative or positive $x$ direction towards the stationary part of the motor. It is therefore important to consider the three incident waves together in the mathematical formulation of the problem. For practical purpose, these three incident waves $\phi_i^{(R_{d1})}$, $\phi_i^{(R_{d2})}$ and $\phi_i^{(F)}$ cannot be studied

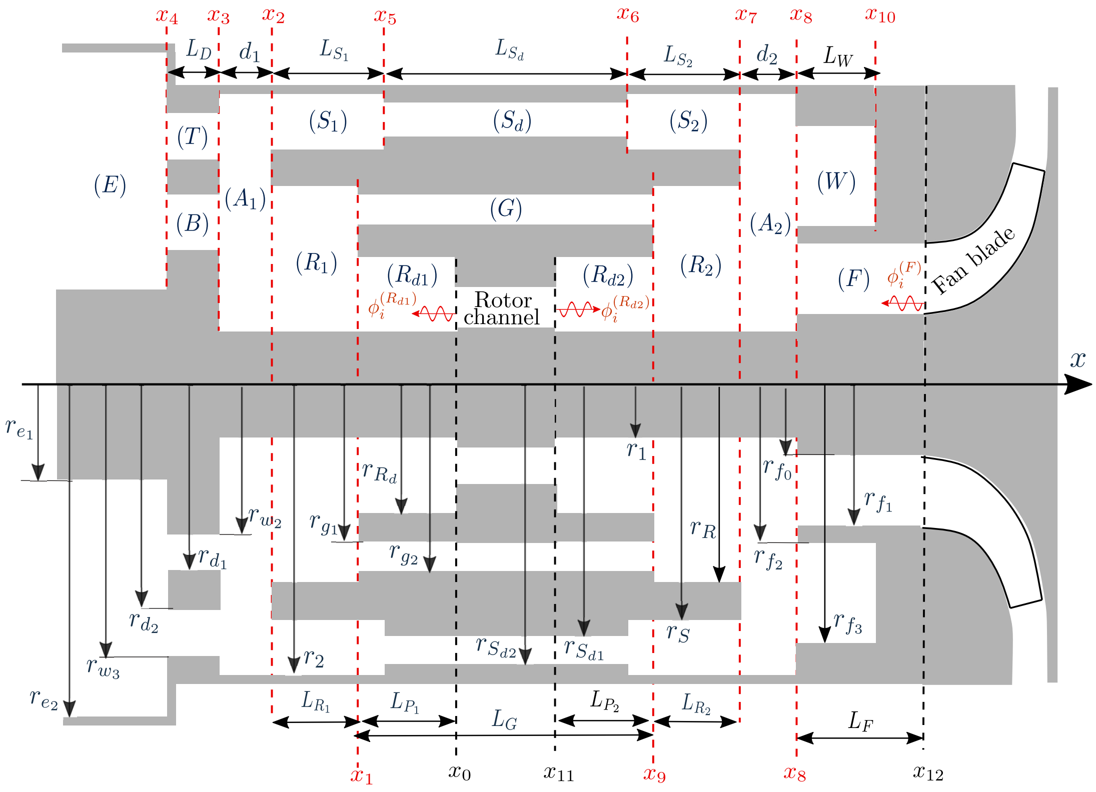

**Figure 2.5:** Diagram indicating the different subdomains of the fixed part of the motor. Incident waves (⟶). Interfaces between the different sub-domains (- - - -). Black dashed lines (- - - -) indicate the interfaces between the stationary part and the rotating parts of the motor.

simultaneously. For this, the diffraction of each of these waves can simply be addressed by setting the amplitude of the other two to zero.

### 2.3.1 Helmholtz equation

The geometry shown in Figure 2.5 can be divided into 15 subdomains denoted by $(R_{d1})$, $(R_1)$, $(A_1)$, $(S_1)$, $(T)$, $(B)$, $(E)$, $(S_d)$, $(S_2)$, $(A_2)$, $(R_2)$, $(R_{d2})$, $(W)$ and $(F)$, in which the sound field can be expressed as a sum of orthogonal modes. These subdomains mainly consist of 14 straight annular ducts and a periodic row of cooling channels as illustrated in Figures 2.6a and 2.6b respectively.

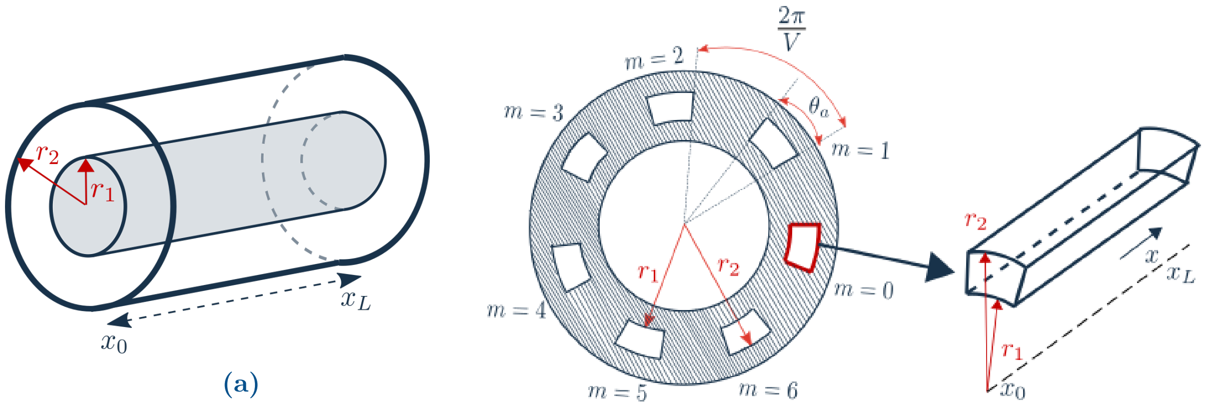

**(a)** **(b)**

**Figure 2.6:** Subdomains of the fixed part of an open motor. (a) Annular duct. (b) Periodic row of cooling channels.

For the same reasons mentioned previously, all acoustic fields must be expressed in terms of their acoustic potentials. They must satisfy the Helmholtz equation in a cylindrical coordinate system:

$$\frac{\partial^2 \phi}{\partial r^2} + \frac{1}{r^2}\frac{\partial^2 \phi}{\partial \theta^2} + \frac{\partial^2 \phi}{\partial x^2} + \frac{\partial \phi}{\partial r} + k_0^2 \phi = 0 \tag{2.1}$$

A general solution of the above equation can be found by separation of variables [84, 87]. The particular solutions of this equation are then obtained by applying the appropriate boundary conditions on the azimuthal and radial directions of each of these geometries (see Figure 2.6).

In the case of a duct of annular cross-section (see Figures 2.6a and 2.7a), a rigid-wall boundary condition must be imposed on the inner and outer radii of the duct. Moreover, since the latter is axisymmetric, a periodic boundary condition should be applied on its azimuthal direction. The acoustic potential inside an annular duct, can be expressed as

$$\phi(r, \theta, x, t) = \sum_{n=-\infty}^{+\infty} \sum_{j=0}^{+\infty} \left( B_{nj}^{+} \mathrm{e}^{\mathrm{i}k_{nj}^{+}(x - x_0)} + B_{nj}^{-} \mathrm{e}^{\mathrm{i}k_{nj}^{-}(x - x_L)} \right) f_{nj}(r) \mathrm{e}^{\mathrm{i}n\theta} \mathrm{e}^{-\mathrm{i}\omega t} \tag{2.2}$$

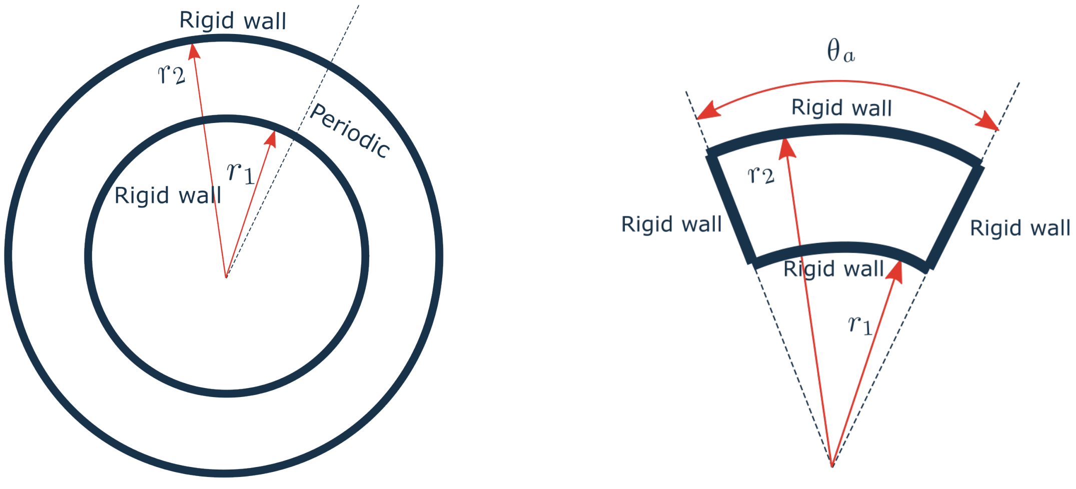

(a)

(b)

**Figure 2.7:** Cross sections of an annular duct (a) and an annular sector duct (b)

where $n \in \mathbb{Z}$ and $j \in \mathbb{N}$ are respectively the azimuthal and radial mode indices, and $f_{nj}(r)$ represent the radial shape functions, which are linear combinations of Bessel functions of the first and the second kinds. They are given by [87]:

$$f_{nj}(r) = \mathcal{N}_{nj} \left\{ \cos\left(\tau_{nj}\right) J_n(K_{nj} r) - \sin\left(\tau_{nj}\right) Y_n(K_{nj} r) \right\} \quad , \tau_{nj} = \arctan\left( \frac{J_n'(K_{nj})}{Y_n'(K_{nj})} \right) \tag{2.3}$$

The normalization constant $\mathcal{N}_{nj}$ is given by [87, 88]

$$N_{nj} = \frac{\frac{1}{2}\sqrt{2}\pi K_{nj} r_2}{\left( \dfrac{1 - n^2/(K_{nj}^2 r_2^2)}{J_n'(K_{nj} r_2)^2 + Y_n'(K_{nj} r_2)^2} - \dfrac{1 - n^2/(K_{nj}^2 r_1^2)}{J_n'(K_{nj} r_1)^2 + Y_n'(K_{nj} r_1)^2} \right)^{1/2}} \quad , \text{if } n \in \mathbb{R}, j \geq 0 \tag{2.4}$$

For a plane wave $n = 0, j = 0$, the normalization constant becomes:

$$N_{00} = \frac{\sqrt{2}}{\sqrt{1 - r_1/r_2}} \tag{2.5}$$

Note here that the radial shape functions are orthogonal according to the integral

$$\int_{r_1}^{r_2} f_{nj}(r) f_{n'j'}^{*}(r) r \mathrm{d}r = r_o \delta_{j'j}, \quad j' \in \mathbb{N},\ n' \in \mathbb{R} \tag{2.6}$$

where $f_{n'j'}^{*}(r)$ is the complex conjugate of the eigenfunction $f_{nj}(r)$.

For an annular sector duct (see Figures 2.6b and 2.7b), the rigid-wall boundary condition should be imposed on the inner and the outer radii of the duct ($r_1$ and $r_2$), and on the walls of channel separators (on $\theta = 0$ and $\theta = \theta_a$). The sound field can be expressed as

$$\phi(r,\theta,x,t) = \sum_{q=0}^{+\infty}\sum_{j=0}^{+\infty}\left(B_{nj}^{+}\mathrm{e}^{\mathrm{i}k_{nj}^{+}(x-x_0)} + B_{nj}^{-}\mathrm{e}^{\mathrm{i}k_{nj}^{-}(x-x_L)}\right) f_{nj}(r)\cos(n\theta)\,\mathrm{e}^{-\mathrm{i}\omega t} \tag{2.7}$$

with

$$n = q\frac{\pi}{\theta_a}$$

#### 2.3.1.1 Determination of eigenvalues $K_{nj}$

The use of Equations 2.2 and 2.7 requires the determination of the radial wavenumbers $K_{nj}$. They represent the eigenvalues of the problem. These depend only on the azimuthal index $n$ and the radial dimensions of the duct. Note here that $K_{nj}$ takes only discrete values (real and positive), and they must satisfy the following equation

$$J_n'(Kr_2)Y_n'(Kr_1) - J_n'(Kr_1)Y_n'(Kr_2) = 0 \tag{2.8}$$

The left-hand side of Equation 2.8 as a function of $K$ for the azimuthal index $n = 1$ is illustrated in Figure 2.8. The eigenvalues of the problem can directly be extracted graphically from Figure 2.8 by pointing the zeros, and numbered by the index $j \in \mathbb{N}$. From a practical point of view, it is not convenient to use this graphical method, especially when multiple calculations need to be performed. The most straightforward way to find them, is to use a numerical procedure. However, this non-linear equation can be solved, for instance, by the Newton-Raphson method [85]. It is interesting to note that when the radial index $j \to \infty$, the eigenvalues $K_{nj}$ can be approximated empirically by the use of the following equation [2]:

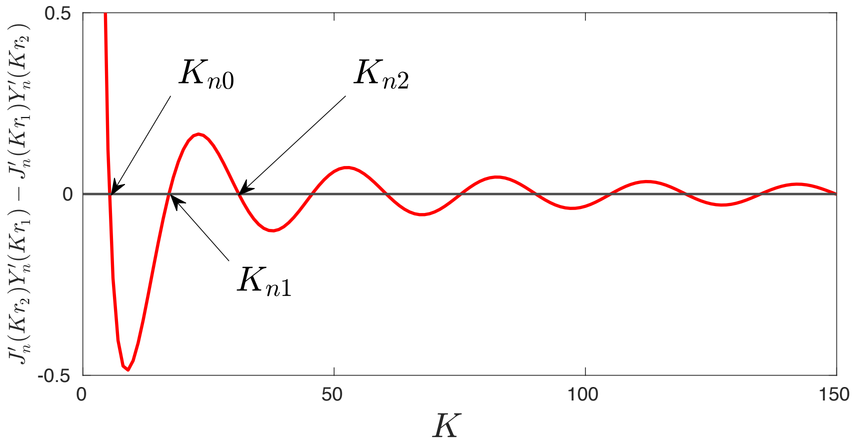

**Figure 2.8:** Determination of the eigenvalues. $n = 1$, $r_1/r_2 = 0.3$.

$$K_{nj} = \frac{1}{r_1}\left(\sigma_3 + \frac{\sigma_4}{\sigma_3} + \frac{\sigma_1 - \sigma_4^2}{\sigma_3^3} + \frac{\sigma_2 - 4\sigma_4\sigma_1 + 2\sigma_4^3}{\sigma_3^5}\right) \tag{2.9}$$

where

$$\sigma_1 = \frac{(\sigma_5 + 46\sigma_5 - 63)(\sigma_0^3 - 1)}{6(4\sigma_0)^3(\sigma_0 - 1)} \qquad , \sigma_2 = \frac{(\sigma_5^3 + 185\sigma_5^2 - 2053\sigma_5 + 1899)(\sigma_0^5 - 1)}{5(4A)^5(\sigma_0 - 1)}$$

$$\sigma_3 = \frac{j\pi}{\sigma_0 - 1} \qquad , \sigma_4 = \frac{\sigma_5 + 3}{8A} \qquad , \sigma_5 = 4n^2 \qquad , \sigma_0 = \frac{r_2}{r_1}$$

In order to evaluate the validity of the empirical formula, a comparison between the eigenvalues $K_{nj}$ calculated by the two methods (numerical and empirical) is illustrated in Figure 2.9. The index $j$ is increased incrementally from 0 to 40. As can be seen, Equation 2.9 is only valid for large values of $j$. The difference between the two methods can be seen to be significant for large values of the azimuthal order $n$ (see Figure 2.9a), and for low values of $r_1/r_2$ (see Figure 2.9b).

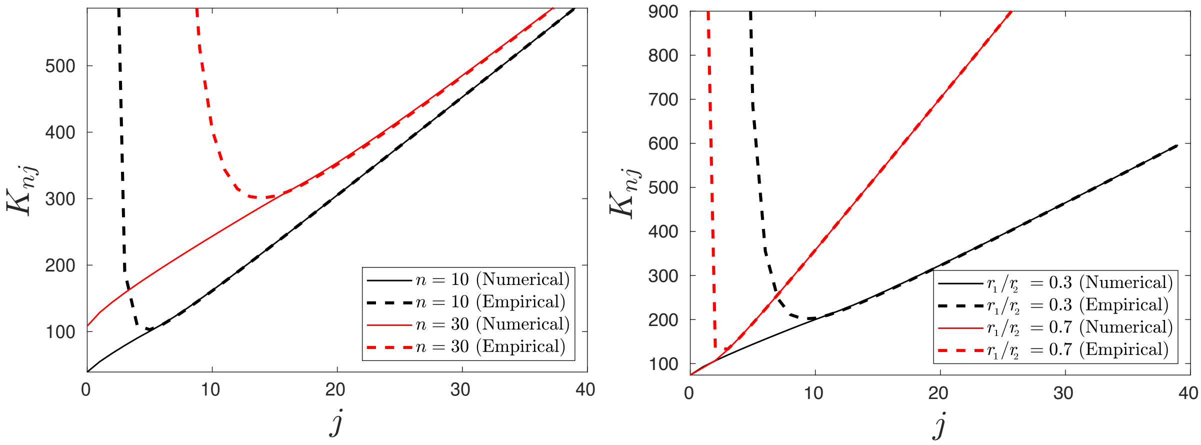

**(a)** **(b)**

**Figure 2.9:** Variation of the radial wave numbers $K_{nj}$ obtained by the numerical and empirical methods with the radial index $j$. (*a*) influence of azimuthal order $n$ for $r_1/r_2 = 0.3$: $n = 10$ numerical (——), $n = 10$ empirical (- - - -), $n = 30$ numerical (——), $n = 30$ empirical (- - - -). (*b*) Influence of $r_1/r_2$, for $n = 20$: $r_1/r_2 = 0.3$ numerical (——), $r_1/r_2 = 0.3$ empirical (- - - -), $r_1/r_2 = 0.7$ numerical (——), $r_1/r_2 = 0.7$ empirical (- - - -).

It should be kept in mind that the numerical calculation of the radial wavenumbers $K_{nj}$ can become prohibitive for large values of the azimuthal index $n$. The two calculation techniques can therefore be combined to reduce the computational time, by using the numerical method for low values of $j$ and the empirical formula for large values of $j$.

### 2.3.2 Acoustic potentials

The sound field generated by impingement of vortical waves on the impeller blades or on the rotor channels can be expanded into a sum of helical waves. The mathematical expressions of the incident excitations emitted by the rotor channels at the axial positions

$x_0$ (left-hand side) and $x_{11}$ (right-hand side) are written as

$$\phi_i^{(R_{d1})}(r,\theta,x,t) = A_{nj}^{(R_{d1})} f_{nj}^{(R_d)}(r) \mathrm{e}^{\mathrm{i}k_{nj}^{-}(x-x_0)} \mathrm{e}^{\mathrm{i}n\theta} \mathrm{e}^{-\mathrm{i}\omega t} \quad, x_1 \leq x \leq x_0 \quad, r_1 \leq x \leq r_{R_d} \tag{2.10}$$

$$\phi_i^{(R_{d2})}(r,\theta,x,t) = A_{nj}^{(R_{d2})} f_{nj}^{(R_d)}(r) \mathrm{e}^{\mathrm{i}k_{nj}^{+}(x-x_{11})} \mathrm{e}^{\mathrm{i}n\theta} \mathrm{e}^{-\mathrm{i}\omega t} \quad, x_{11} \leq x \leq x_9, r_1 \leq x \leq r_{R_d} \tag{2.11}$$

where

$$k_{nj}^{\pm} = \pm\sqrt{k_0^2 - K_{nj}^2}$$

The acoustic potential of a single acoustic excitation generated by the radial impeller is expressed as

$$\phi_i^{(F)}(r,\theta,x,t) = A_{nj}^{(F)} f_{nj}^{(F)}(r) \mathrm{e}^{\mathrm{i}k_{nj}^{-}(x-x_{12})} \mathrm{e}^{\mathrm{i}n\theta} \mathrm{e}^{-\mathrm{i}\omega t} \tag{2.12}$$

where

$$k_{nj}^{-} = -\sqrt{k_0^2 - K_{nj}^2}$$

The scattering of each of these incident waves by the different discontinuities of the geometry produces 26 acoustic fields, as illustrated in Figure 2.10. It should be noted that the azimuthal index $n$ of each incident wave is not scattered by the annular ducts because of their assumed axisymmetry. However, the sound field is only scattered in the radial direction. On the other hand, the presence of the stator cooling channels modifies the acoustic response of the system in both the radial and azimuthal directions. The azimuthal acoustic modes produced upstream and downstream the cooling channels are of orders $n_s = n + sV$. These are transmitted through all annular ducts of the system. It is therefore important to account for these modes in mathematical expressions of the different acoustic potentials.

- The acoustic field $\phi_u^{(R_d)}$ propagating in the sub-domain $(R_{d1})$ ($x_1 \leq x \leq x_0$ and $r_1 \leq x \leq r_{R_d}$) is expressed as

  $$\phi_u^{(R_d)}(r,\theta,x) = \sum_{s=-\infty}^{+\infty} \sum_{\gamma=0}^{+\infty} U_{n_s\gamma}^{(R_d)} f_{n_s\gamma}^{(R_d)}(r) \mathrm{e}^{\mathrm{i}k_{n_s\gamma}^{+}(x-x_1)} \mathrm{e}^{\mathrm{i}n_s\theta} \mathrm{e}^{-\mathrm{i}\omega t} \tag{2.13}$$

  where

  $$k_{n_s\gamma}^{+} = \sqrt{k_0^2 - K_{n_s\gamma}^2}$$

- The acoustic potentials of the downstream $\phi_d^{(G)}$ and upstream $\phi_u^{(G)}$ waves propagating in the air gap $(G)$ ($x_1 \leq x \leq x_9$ and $r_{g_1} \leq r \leq r_{g_2}$) can be written as

  $$\begin{pmatrix} \phi_d^{(G)}(r,\theta,x) \\ \phi_u^{(G)}(r,\theta,x) \end{pmatrix} = \sum_{s=-\infty}^{+\infty} \sum_{g=0}^{+\infty} \begin{pmatrix} D_{n_sg}^{(G)} \\ U_{n_sg}^{(G)} \end{pmatrix} f_{n_sg}^{(G)}(r) \mathrm{e}^{\mathrm{i}n_s\theta} \begin{pmatrix} \mathrm{e}^{\mathrm{i}k_{n_sg}^{-}(x-x_9)} \\ \mathrm{e}^{\mathrm{i}k_{n_sg}^{+}(x-x_1)} \end{pmatrix}, \quad \begin{matrix} x_1 \leq x \leq x_9 \\ r_{g_1} \leq r \leq r_{g_2} \end{matrix} \tag{2.14}$$

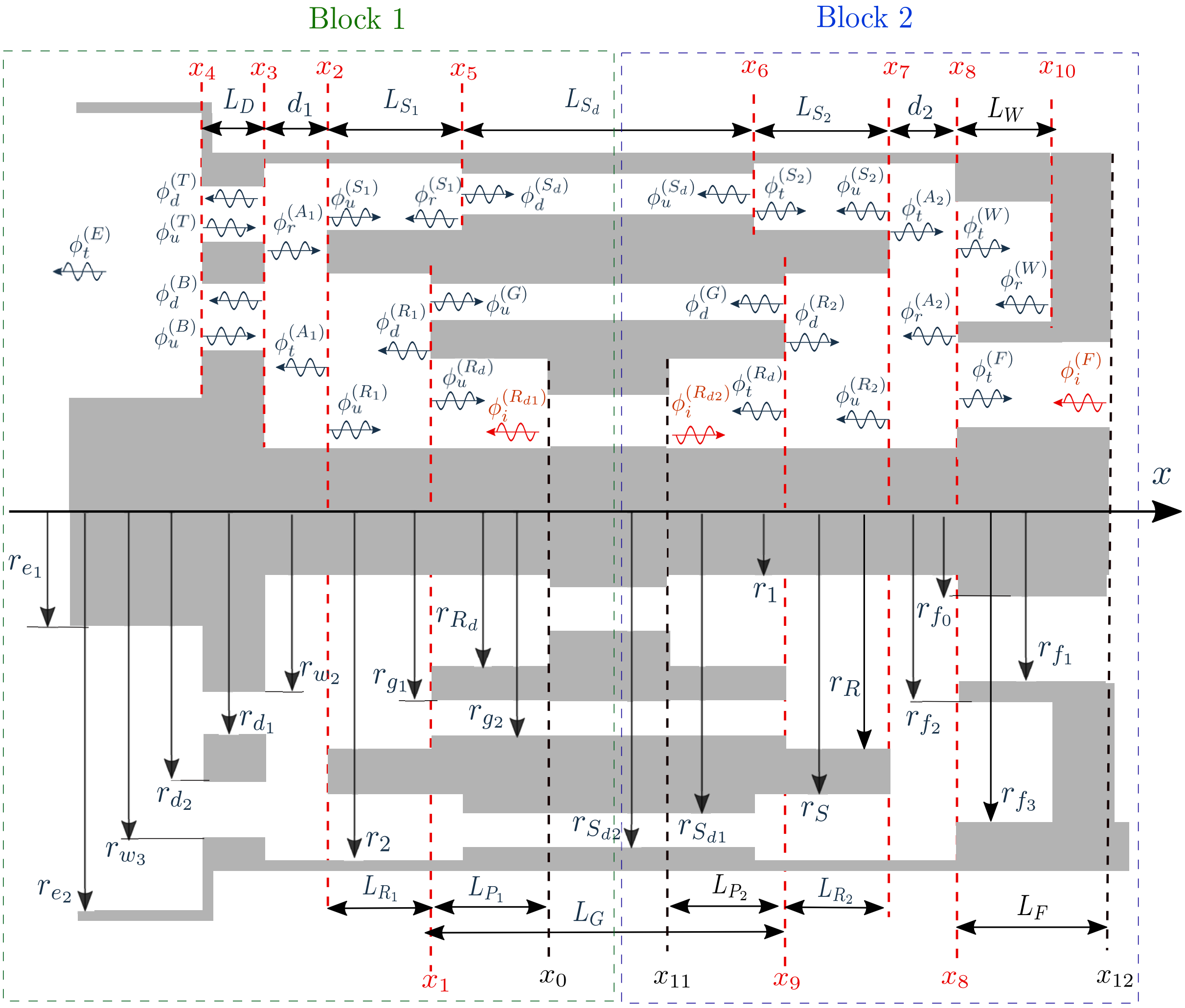

**Figure 2.10:** Acoustic potentials of the multiple waves generated in the fixed part of the motor. Incident waves (⟶), generated waves (⟶), Interfaces between the different sub-domains (- - - -). Black dashed lines (- - - -) indicate the interfaces between the stationary part and the rotating parts of the ventilation system.

where

$$k^{\pm}_{nsg} = \pm\sqrt{k_0^2 - K^2_{nsg}}$$

- The acoustic fields $\phi_d^{(R_1)}$ and $\phi_u^{(R_1)}$ propagating in the region limited by the end-windings and the motor shaft $(R_1)$ $(x_2 \leq x \leq x_1$ and $r_1 \leq r \leq r_R)$ read

$$\begin{pmatrix} \phi_d^{(R_1)}(r,\theta,x) \\ \phi_u^{(R_1)}(r,\theta,x) \end{pmatrix} = \sum_{s=-\infty}^{+\infty} \sum_{\xi=0}^{+\infty} \begin{pmatrix} D^{(R_1)}_{n_s\xi} \\ U^{(R_1)}_{n_s\xi} \end{pmatrix} f^{(R_1)}_{n_s\xi}(r) \mathrm{e}^{\mathrm{i}n_s\theta} \begin{pmatrix} \mathrm{e}^{\mathrm{i}k^-_{n_s\xi}(x-x_1)} \\ \mathrm{e}^{\mathrm{i}k^+_{n_s\xi}(x-x_2)} \end{pmatrix}, \quad \begin{matrix} x_2 \leq x \leq x_1 \\ r_1 \leq r \leq r_R \end{matrix} \tag{2.15}$$

where

$$k^{\pm}_{n_s\xi} = \pm\sqrt{k_0^2 - K^2_{n_s\xi}}$$

- The transmitted $\phi_t^{(A_1)}$ and reflected $\phi_r^{(A_1)}$ acoustic fields propagating in the space between the end-windings and the deflector $(x_3 \leq x \leq x_2$ and $r_1 \leq r \leq r_2)$ are expressed as

$$\begin{pmatrix} \phi_t^{(A_1)}(r,\theta,x,t) \\ \phi_r^{(A_1)}(r,\theta,x,t) \end{pmatrix} = \sum_{s=-\infty}^{+\infty} \sum_{\beta=0}^{+\infty} \begin{pmatrix} T_{n_s\beta}^{(A_1)} \\ R_{n_s\beta}^{(A_1)} \end{pmatrix} f_{n_s\beta}^{(A_1)}(r) \begin{pmatrix} \mathrm{e}^{\mathrm{i}k_{n_s\beta}^{-}(x-x_2)} \\ \mathrm{e}^{\mathrm{i}k_{n_s\beta}^{+}(x-z_3)} \end{pmatrix} \mathrm{e}^{\mathrm{i}n_s\theta}\mathrm{e}^{-\mathrm{i}\omega t} \tag{2.16}$$

where

$$k_{n_s\beta}^{\pm} = \pm\sqrt{k_0^2 - K_{n_s\beta}^2}$$

- The acoustic potentials of the downstream $\phi_d^{(T)}$ and upstream $\phi_u^{(T)}$ propagating waves in the region $(T)$ ($x_4 \leq x \leq x_3$ and $r_{d_2} \leq r \leq r_{w_3}$) can be expressed as:

$$\begin{pmatrix} \phi_d^{(T)}(r,\theta,x,t) \\ \phi_u^{(T)}(r,\theta,x,t) \end{pmatrix} = \sum_{s=-\infty}^{+\infty} \sum_{\mu=0}^{+\infty} \begin{pmatrix} D_{n_s\mu}^{(T)} \\ U_{n_s\mu}^{(T)} \end{pmatrix} f_{n_s\mu}^{(T)}(r) \begin{pmatrix} \mathrm{e}^{\mathrm{i}k_{n_s\mu}^{-}(x-z_3)} \\ \mathrm{e}^{\mathrm{i}k_{n_s\mu}^{+}(x-z_4)} \end{pmatrix} \mathrm{e}^{\mathrm{i}n_s\theta}\mathrm{e}^{-\mathrm{i}\omega t} \tag{2.17}$$

where

$$k_{n_s\mu}^{\pm} = \pm\sqrt{k_0^2 - K_{n_s\mu}^2}$$

- The acoustic potentials of the downstream $\phi_d^{(B)}$ and upstream $\phi_u^{(B)}$ propagating waves in the region $(B)$ ($x_4 \leq x \leq x_3$ and $r_{w_2} \leq r \leq r_{d_1}$) are given by:

$$\begin{pmatrix} \phi_d^{(B)}(r,\theta,x,t) \\ \phi_u^{(B)}(r,\theta,x,t) \end{pmatrix} = \sum_{s=-\infty}^{+\infty} \sum_{\nu=0}^{+\infty} \begin{pmatrix} D_{n_s\nu}^{(B)} \\ U_{n_s\nu}^{(B)} \end{pmatrix} f_{n_s\nu}^{(B)}(r) \begin{pmatrix} \mathrm{e}^{\mathrm{i}k_{n_s\nu}^{-}(x-x_2)} \\ \mathrm{e}^{\mathrm{i}k_{n_s\nu}^{+}(x-x_3)} \end{pmatrix} \mathrm{e}^{\mathrm{i}n_s\theta}\mathrm{e}^{-\mathrm{i}\omega t} \tag{2.18}$$

where

$$k_{n_s\nu}^{\pm} = \pm\sqrt{k_0^2 - K_{n_s\nu}^2}$$

- The acoustic potential transmitted outside the ventilation system $\phi_t^{(E)}$ ($x \leq x_4$, $r_{e_1} \leq r \leq r_{e_2}$) reads

$$\phi_t^{(E)}(r,\theta,x,t) = \sum_{m=0}^{+\infty} T_{nm}^{(E)} f_{nm}^{(E)}(r)\mathrm{e}^{\mathrm{i}k_{nm}^{-}(x-x_5)}\mathrm{e}^{\mathrm{i}n\theta}\mathrm{e}^{-\mathrm{i}\omega t} \tag{2.19}$$

where

$$k_{n_sm}^{-} = -\sqrt{k_0^2 - K_{n_sm}^2}$$

- The upstream $\phi_r^{(S_1)}$ and downstream $\phi_u^{(S_1)}$ waves propagating in the region $(S_1)$ ($x_2 \leq x \leq x_5$, $r_S \leq r \leq r_2$) can be expressed as:

$$\begin{pmatrix} \phi_r^{(S_1)}(r,\theta,x,t) \\ \phi_u^{(S_1)}(r,\theta,x,t) \end{pmatrix} = \sum_{s=-\infty}^{+\infty} \sum_{\eta=0}^{+\infty} \begin{pmatrix} R_{n_s\eta}^{(S_1)} \\ U_{n_s\eta}^{(S_1)} \end{pmatrix} f_{n_s\eta}^{(S_1)}(r) \begin{pmatrix} \mathrm{e}^{\mathrm{i}k_{n_s\eta}^{-}(x-x_5)} \\ \mathrm{e}^{\mathrm{i}k_{n_s\eta}^{+}(x-x_2)} \end{pmatrix} \mathrm{e}^{\mathrm{i}n_s\theta}\mathrm{e}^{-\mathrm{i}\omega t} \tag{2.20}$$

where

$$k_{n_s\eta}^{\pm} = \pm\sqrt{k_0^2 - K_{n_s\eta}^2}$$

- The downstream $\phi_d^{(S_d)}$ and upstream $\phi_u^{(S_d)}$ acoustic potentials propagating in the $m^{th}$ channel ($x_5 \leq x \leq x_6$, $r_{S_{d1}} \leq r \leq r_{S_{d2}}$) are given by:

$$\begin{pmatrix} \phi_d^{(S_d)}(r,\theta,x) \\ \phi_u^{(S_d)}(r,\theta,x) \end{pmatrix} = \sum_{s=-\infty}^{+\infty} \sum_{q=0}^{+\infty} \sum_{p=0}^{+\infty} \begin{pmatrix} D_{n_q p}^{(S_d)} \\ U_{n_q p}^{(S_d)} \end{pmatrix} \mathrm{e}^{\mathrm{i}n_s 2\pi m/V} f_{n_s p}^{(S_d)}(r) \begin{pmatrix} \mathrm{e}^{\mathrm{i}k_{n_q p}^{+}(x-x_5)} \\ \mathrm{e}^{\mathrm{i}k_{n_q p}^{-}(x-x_6)} \end{pmatrix} \\ \times \cos\left(n_q \left[\theta - \frac{2\pi m}{V}\right]\right) \quad (2.21)$$

with

$$k_{n_q p}^{\pm} = \pm\sqrt{k_0^2 - K_{n_q p}^2}$$

Note here that the phase-shift between the adjacent channels $\mathrm{e}^{\mathrm{i}n_s 2\pi m/V}$ is imposed by the propagation angle of each mode $n_s = n + sV$ propagating upstream and downstream of the channels. This can be written as

$$\mathrm{e}^{\mathrm{i}n_s 2\pi m/V} = \mathrm{e}^{\mathrm{i}n 2\pi m/V} \cancelto{1}{\mathrm{e}^{\mathrm{i}s 2\pi m}} \quad (2.22)$$

Therefore, the first sum can be ignored, and Equation 2.21 becomes

$$\begin{pmatrix} \phi_d^{(S_d)}(r,\theta,x) \\ \phi_u^{(S_d)}(r,\theta,x) \end{pmatrix} = \sum_{q=0}^{+\infty} \sum_{p=0}^{+\infty} \begin{pmatrix} D_{n_q p}^{(S_d)} \\ U_{n_q p}^{(S_d)} \end{pmatrix} \mathrm{e}^{\mathrm{i}n 2\pi m/V} f_{n_s p}^{(S_d)}(r) \begin{pmatrix} \mathrm{e}^{\mathrm{i}k_{n_q p}^{+}(x-x_5)} \\ \mathrm{e}^{\mathrm{i}k_{n_q p}^{-}(x-x_6)} \end{pmatrix} \\ \times \cos\left(n_q \left[\theta - \frac{2\pi m}{V}\right]\right) \quad (2.23)$$

- The acoustic potential of the acoustic fields $\phi_r^{(S_2)}$ and $\phi_u^{(S_2)}$ propagating in the sub-domain $(S_2)$ ($x_6 \leq x \leq x_7$, $r_S \leq r \leq r_{S2}$) are written as

$$\begin{pmatrix} \phi_t^{(S_2)}(r,\theta,x,t) \\ \phi_u^{(S_2)}(r,\theta,x,t) \end{pmatrix} = \sum_{s=-\infty}^{+\infty} \sum_{\eta=0}^{+\infty} \begin{pmatrix} T_{n_s \eta}^{(S_2)} \\ U_{n_s \eta}^{(S_2)} \end{pmatrix} f_{n_s \eta}^{(S_1)}(r) \begin{pmatrix} \mathrm{e}^{\mathrm{i}k_{n_s \eta}^{+}(x-x_6)} \\ \mathrm{e}^{\mathrm{i}k_{n_s \eta}^{-}(x-x_7)} \end{pmatrix} \mathrm{e}^{\mathrm{i}n_s\theta} \mathrm{e}^{-\mathrm{i}\omega t} \quad (2.24)$$

with

$$k_{n_s \eta}^{\pm} = \pm\sqrt{k_0^2 - K_{n_s \eta}^2}$$

- The acoustic waves transmitted and reflected ($\phi_t^{(A_2)}$ and $\phi_r^{(A_2)}$) in the space between located between the end-windings and the fan inlet ($x_7 \leq x \leq x_8$, $r_1 \leq r \leq r_2$) read

$$\begin{pmatrix} \phi_t^{(A_2)}(r,\theta,x,t) \\ \phi_r^{(A_2)}(r,\theta,x,t) \end{pmatrix} = \sum_{s=-\infty}^{+\infty} \sum_{\beta=0}^{+\infty} \begin{pmatrix} T_{n_s \beta}^{(A_2)} \\ R_{n_s \beta}^{(A_2)} \end{pmatrix} f_{n_s \beta}^{(A_1)}(r) \begin{pmatrix} \mathrm{e}^{\mathrm{i}k_{n_s \beta}^{+}(x-x_7)} \\ \mathrm{e}^{\mathrm{i}k_{n_s \beta}^{-}(x-x_8)} \end{pmatrix} \mathrm{e}^{\mathrm{i}n_s\theta} \mathrm{e}^{-\mathrm{i}\omega t} \quad (2.25)$$

with

$$k_{n_s \beta}^{\pm} = \pm\sqrt{k_0^2 - K_{n_s \beta}^2}$$

- The downstream $\phi_d^{(R_2)}$ and upstream $\phi_u^{(R_2)}$ propagating fields in the region $(R_2)$

($x_7 \leq x \leq x_8$ and $r_1 \leq r \leq r_2$) are expressed as:

$$\begin{pmatrix} \phi_d^{(R_2)}(r,\theta,x,t) \\ \phi_u^{(R_2)}(r,\theta,x,t) \end{pmatrix} = \sum_{s=-\infty}^{+\infty} \sum_{\xi=0}^{+\infty} \begin{pmatrix} D_{n_s\xi}^{(R_2)} \\ U_{n_s\xi}^{(R_2)} \end{pmatrix} f_{n_s\xi}^{(R_1)}(r) \begin{pmatrix} \mathrm{e}^{\mathrm{i}k_{n_s\xi}^{+}(x-x_{10})} \\ \mathrm{e}^{\mathrm{i}k_{n_s\xi}^{-}(x-x_7)} \end{pmatrix} \mathrm{e}^{\mathrm{i}n_s\theta}\mathrm{e}^{-\mathrm{i}\omega t} \tag{2.26}$$

where

$$k_{n_s\xi}^{\pm} = \pm\sqrt{k_0^2 - K_{n_s\xi}^2}$$

- The acoustic potentials of the different fields ($\phi_t^{(W)}$ and $\phi_r^{(W)}$) propagating inside the cavity located at $x_8 \leq x \leq x_{10}$ and $r_{f_2} \leq r \leq r_{f_3}$ are given by:

$$\begin{pmatrix} \phi_t^{(W)}(r,\theta,x,t) \\ \phi_r^{(W)}(r,\theta,x,t) \end{pmatrix} = \sum_{s=-\infty}^{+\infty} \sum_{w=0}^{+\infty} \begin{pmatrix} T_{n_s w}^{(W)} \\ R_{n_s w}^{(W)} \end{pmatrix} f_{n_s w}^{(W)}(r) \begin{pmatrix} \mathrm{e}^{\mathrm{i}k_{n_s w}^{+}(x-x_8)} \\ \mathrm{e}^{\mathrm{i}k_{n_s w}^{-}(x-x_{11})} \end{pmatrix} \mathrm{e}^{\mathrm{i}n_s\theta}\mathrm{e}^{-\mathrm{i}\omega t} \tag{2.27}$$

where

$$k_{n_s w}^{\pm} = \pm\sqrt{k_0^2 - K_{n_s w}^2}$$

- The sound field transmitted into the radial impeller $\phi_t^{(F)}$ ($x_8 \leq x \leq x_{12}$ and $r_{f_0} \leq r \leq r_{f_1}$) is written as:

$$\phi_t^{(F)}(r,\theta,x,t) = \sum_{n_s=-\infty}^{+\infty} \sum_{\alpha=0}^{+\infty} T_{n_s\alpha}^{(F)} f_{n_s\alpha}^{(F)}(r) \mathrm{e}^{\mathrm{i}k_{n_s\alpha}^{+}(x-x_8)} \mathrm{e}^{\mathrm{i}n_s\theta}\mathrm{e}^{-\mathrm{i}\omega t} \tag{2.28}$$

where

$$k_{n_s\alpha}^{+} = \sqrt{k_0^2 - K_{n_s\alpha}^2}$$

- The acoustic field $\phi_t^{(R_d)}$ transmitted into the sub-domain ($R_{d2}$) ($x_{11} \leq x \leq x_9$ and $r_1 \leq r \leq r_{R_d}$) reads:

$$\phi_t^{(R_d)}(r,\theta,x,t) = \sum_{n_s=-\infty}^{+\infty} \sum_{\gamma=0}^{+\infty} T_{n_s\gamma}^{(R_d)} f_{n_s\gamma}^{(R_d)}(r) \mathrm{e}^{\mathrm{i}k_{n_s\gamma}^{-}(x-x_9)} \mathrm{e}^{\mathrm{i}n_s\theta}\mathrm{e}^{-\mathrm{i}\omega t} \tag{2.29}$$

where

$$k_{n_s\gamma}^{-} = -\sqrt{k_0^2 - K_{n_s\gamma}^2}$$

The radial shape functions $f_{\varsigma\varrho}^{(\vartheta)}(r)$ of the different fields are given by

$$f_{\varsigma\varrho}^{(\vartheta)}(r) = \mathcal{N}_{\tau\varrho}\left\{\cos\left(\tau_{\varsigma\varrho}\right) J_n(K_{\varsigma\varrho}r) - \sin\left(\tau_{\varsigma\varrho}\right) Y_n(K_{\varsigma\varrho}r)\right\} \quad , \tau_{\varsigma\varrho} = \arctan\left(\frac{J_\varsigma'(K_{\varsigma\varrho})}{Y_\varsigma'(K_{\varsigma\varrho})}\right) \tag{2.30}$$

where $\varsigma = \{n_s, n_q\}$, $\varrho = \{\xi, g, \gamma, \beta, \alpha, \eta, p, w, \nu, \mu\}$, and $\mathcal{N}_{\varsigma\varrho}$ is a normalisation constant, given by

$$N_{\varsigma\varrho} = \frac{\frac{1}{2}\sqrt{2}\pi K_{\varsigma\varrho} r_o}{\left(\dfrac{1-\varsigma^2/(K_{\varsigma\varrho}^2 r_o^2)}{J'_\varsigma(K_{\varsigma\varrho} r_o)^2 + Y'_\varsigma(K_{\varsigma\varrho} r_o)^2} - \dfrac{1-\varsigma^2/(K_{\varsigma\varrho}^2 r_i^2)}{J'_\varsigma(K_{\varsigma\varrho} r_i)^2 + Y'_\varsigma(K_{\varsigma\varrho} r_i)^2}\right)^{1/2}} \quad \text{, if } \varsigma \in \mathbb{R}, \varrho \geq 0 \tag{2.31}$$

For a plane wave $\varsigma = 0, \varrho = 0$, the normalization constant becomes:

$$N_{00} = \frac{\sqrt{2}}{\sqrt{1 - r_i/r_o}} \tag{2.32}$$

where $r_i = \{r_1, r_{g1}, r_{w2}, r_{d2}, r_{f0}, r_{f2}, r_S, r_{S_{d1}}, r_{e1}\}$ and $r_o = \{r_R, r_{g2}, r_{d1}, r_{w3}, r_{f1}, r_{f3}, r_2, r_{S_{d2}}, r_{e2}\}$.

The orthogonality the radial eigenfunctions is written as

$$\int_{r_i}^{r_o} f^{(\vartheta)}_{\varsigma\varrho}(r) f^{*(\vartheta)}_{\varsigma'\varrho'}(r) r \mathrm{d}r = r_o \delta_{\varrho'\varrho}, \quad \varrho' \in \mathbb{N},\ \varsigma' \in \mathbb{R} \tag{2.33}$$

where $f^{*(\vartheta)}_{\varsigma'}(r)$ is complex conjugate of the eigenfunction $f^{(\vartheta)}_{\varsigma}(r)$.

In this section, the acoustic fields have been expressed only in the different sub-domains of geometry. To obtain a solution of the problem in the whole computational domain, it is necessary to join the different solutions found in each sub-domain. The relationship between the different acoustic fields can be obtained by using the mode-matching technique. This will be presented in details in the next section.

### 2.3.3 Mode-matching technique

The modal amplitudes of the different acoustic fields are the only unknowns in this problem. In order to determine them, the mode-matching technique must be applied at each interface separating two or more subdomains with different transverse dimensions. As mentioned before, the matching equations are derived from the continuity of the acoustic pressure and the axial velocity at each interface defined in Figure 2.10. However, two kinds of interfaces are investigated in the following sub-sections. The first one corresponds to an interface separating three annular ducts with different radial dimensions. This kind of interface is located at the positions $x_1$, $x_2$, $x_3$, $x_4$, $x_7$, $x_8$ and $x_9$. However, in order to avoid heavy mathematical developments, the different steps of the mode-matching method will be explained in detail for only the interface $x_1$. Then, the diffraction of sound at the other interfaces can be studied in the same manner. The second kind of interface studied in this section corresponds to the interfaces $x_5$ and $x_6$, which are located between an annular duct and a row of thick-walled channels.

#### 2.3.3.1 Matching equations at the interface $x = x_1$

The interface $x_1$ is a junction of three subdomains denoted by $(R_{d1})$, $(R_1)$ and $(G)$. As can be seen from Figure 2.11, the subdomain on the left-hand side $(R_1)$ is connected to the subdomain $(R_{d1})$ at $r_1 < r < r_{R_d}$, and also connected to the subdomain $(G)$ at $r_{g_1} < r < r_{R_{g_2}}$. At both interfaces, the continuity of the acoustic pressure and the axial velocity must be satisfied. In addition, the rigid-wall boundary condition must be imposed on the front side of the walls located at $r_1 < r < r_{R_{g_1}}$ and $r_{g_2} < r < r_R$, which corresponds to a vanishing normal velocity $v \cdot \mathbf{n} = v \cdot \mathbf{e_x} = 0$. In the following, the acoustic pressure and the axial velocity are gathered in a vector denoted by $\Xi$

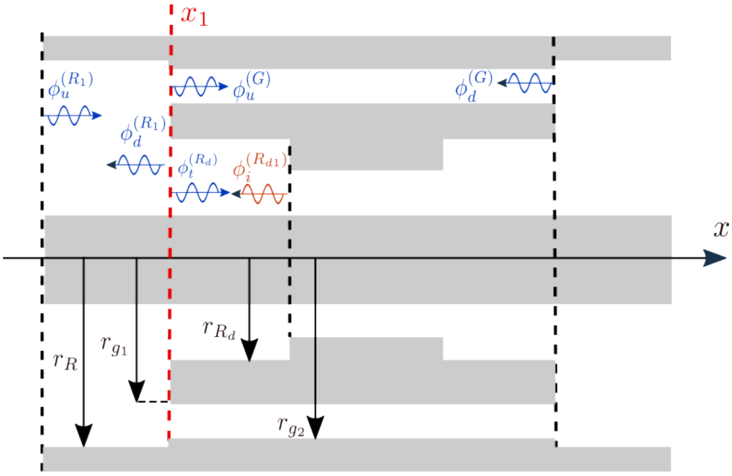

**Figure 2.11:** Acoustic fields generated at the interface $x_1$

$$\Xi_l^{(\vartheta)}(r,\theta,x) = \begin{pmatrix} p_l^{(\vartheta)}(r,\theta,x) \\ v_l^{(\vartheta)}(r,\theta,x)\cdot \mathbf{e_x} \end{pmatrix}$$

where $l = \{i,u,d,r,t\}\,,\quad \vartheta = \{R_{d1}, R_{d2}, R_1, R_2, S_1, S_2, A_1, A_2, G, W, F, E, T, B, S_d\}$

The matching equations at the interface $x_1$ read

$$\begin{cases} \Xi_{\mathbf{i}}^{(\mathbf{R_d})} + \Xi_{\mathbf{u}}^{(\mathbf{R_d})} = \Xi_{\mathbf{d}}^{(\mathbf{R_1})} + \Xi_{\mathbf{u}}^{(\mathbf{R_1})}, \quad x = x_1, \quad \forall\theta, \quad r \in [r_1; r_{R_d}] & (2.34a) \\ \Xi_{\mathbf{u}}^{(\mathbf{G})} + \Xi_{\mathbf{d}}^{(\mathbf{G})} = \Xi_{\mathbf{d}}^{(\mathbf{R_1})} + \Xi_{\mathbf{u}}^{(\mathbf{R_1})}, \quad x = x_1, \quad \forall\theta, \quad r \in [r_{g_1}; r_{g_2}] & (2.34b) \\ v_d^{(R_1)}\cdot \mathbf{e_x} + v_u^{(R_1)}\cdot \mathbf{e_x} = 0, \quad x = x_1, \quad \forall\theta, \quad r \in ]r_{R_d}; r_{g_1}[ \cup ]r_{g_2}; r_R] & (2.34c) \end{cases}$$

After replacing the expressions of the acoustic pressure and the axial velocity in Equation 2.34a, one obtains

$$A_{nj}^{(R_{d1})} \mathrm{e}^{-\mathrm{i}k_{nj}^{-} L_{P_1}} f_{nj}^{(R_d)}(r)\mathrm{e}^{\mathrm{i}n\theta} + \sum_{s=-\infty}^{+\infty}\sum_{\gamma=0}^{+\infty} U_{n_s\gamma}^{(R_d)} f_{n_s\gamma}^{(R_d)}(r)\mathrm{e}^{\mathrm{i}n_s\theta} \\ = \sum_{s=-\infty}^{+\infty}\sum_{\xi=0}^{+\infty}\left(D_{n_s\xi}^{(R_1)} + U_{n_s\xi}^{(R_1)}\mathrm{e}^{\mathrm{i}k_{n_s\xi}^{+} L_{R_1}}\right) f_{n_s\xi}^{(R_1)}(r)\mathrm{e}^{\mathrm{i}n_s\theta} \quad (2.35)$$

$$
\begin{aligned}
k^-_{nj} A^{(R_{d1})}_{nj} \mathrm{e}^{-\mathrm{i}k^-_{nj} L_{P_1}} f^{(R_d)}_{nj}(r) \mathrm{e}^{\mathrm{i}n\theta} + \sum_{s=-\infty}^{+\infty} \sum_{\gamma=0}^{+\infty} k^-_{n_s\gamma} U^{(R_d)}_{n_s\gamma} f^{(R_d)}_{n_s\gamma}(r) \mathrm{e}^{\mathrm{i}n_s\theta} & \\
= \sum_{s=-\infty}^{+\infty} \sum_{\xi=0}^{+\infty} \left( k^-_{n_s\xi} D^{(R_1)}_{n_s\xi} + k^+_{n_s\xi} U^{(R_1)}_{n_s\xi} \mathrm{e}^{\mathrm{i}k^+_{n_s\xi} L_{R_1}} \right) f^{(R_1)}_{n_s\xi}(r) \mathrm{e}^{\mathrm{i}n_s\theta} & \quad (2.36)
\end{aligned}
$$

In the same way, substituting the expressions of the acoustic pressure and the axial velocity in Equation 2.34b yields

$$
\begin{aligned}
\sum_{s=-\infty}^{+\infty} \sum_{g=0}^{+\infty} \left( U^{(G)}_{n_sg} + U^{(G)}_{n_sg} \mathrm{e}^{-\mathrm{i}k^-_{n_sg} L_G} \right) f^{(G)}_{n_sg}(r) \mathrm{e}^{\mathrm{i}n_s\theta} & \\
= \sum_{s=-\infty}^{+\infty} \sum_{\xi=0}^{+\infty} \left( D^{(R_1)}_{n_s\xi} + U^{(R_1)}_{n_s\xi} \mathrm{e}^{\mathrm{i}k^+_{n_s\xi} L_{R_1}} \right) f^{(R_1)}_{n_s\xi}(r) \mathrm{e}^{\mathrm{i}n_s\theta} & \quad (2.37)
\end{aligned}
$$

$$
\begin{aligned}
\sum_{s=-\infty}^{+\infty} \sum_{g=0}^{+\infty} \left( k^+_{n_sg} U^{(G)}_{n_sg} + k^-_{n_sg} D^{(G)}_{n_sg} \mathrm{e}^{-\mathrm{i}k^-_{n_sg} L_G} \right) f^{(G)}_{n_sg}(r) \mathrm{e}^{\mathrm{i}n_s\theta} & \\
= \sum_{s=-\infty}^{+\infty} \sum_{\xi=0}^{+\infty} \left( k^-_{n_s\xi} D^{(R_1)}_{n_s\xi} + k^+_{n_s\xi} U^{(R_1)}_{n_s\xi} \mathrm{e}^{\mathrm{i}k^+_{n_s\xi} L_{R_1}} \right) f^{(R_1)}_{n_s\xi}(r) \mathrm{e}^{\mathrm{i}n_s\theta} & \quad (2.38)
\end{aligned}
$$

The next step is to perform modal projections of Equations 2.35, 2.36, 2.37 and 2.38 using the orthogonality of the acoustic modes. As what has been discussed in Chapter 1, the pressure equations must be projected on the eigenfunctions related to the smaller ducts $(R_d)$ and $(G)$, while the velocity equations should be projected on the modal basis of the sound field propagating in the wider duct $(R_1)$.

Equations 2.35 and 2.37 are respectively projected on the eigenfunctions $f^{*(R_d)}_{n'_s\gamma'}(r)\mathrm{e}^{-\mathrm{i}n'_s\theta}$ and $f^{*(G)}_{n'_sg'}(r)\mathrm{e}^{-\mathrm{i}n'_s\theta}$

$$
\begin{aligned}
\int_0^{2\pi} \int_{r_1}^{r_{R_d}} \left( p^{(R_d)}_i + p^{(R_d)}_u \right) f^{*(R_d)}_{n'_s\gamma'}(r) \mathrm{e}^{-\mathrm{i}n'_s\theta} r \mathrm{d}r \mathrm{d}\theta & \\
= \int_0^{2\pi} \int_{r_1}^{r_{R_d}} \left( p^{(R_1)}_u + p^{(R_1)}_d \right) f^{*(R_d)}_{n'_s\gamma'}(r) \mathrm{e}^{-\mathrm{i}n'_s\theta} r \mathrm{d}r \mathrm{d}\theta & \quad (2.39)
\end{aligned}
$$

$$
\begin{aligned}
\int_0^{2\pi} \int_{r_{g_1}}^{r_{g_2}} \left( p^{(G)}_d + p^{(G)}_u \right) f^{*(G)}_{n'_sg'}(r) \mathrm{e}^{-\mathrm{i}n'_s\theta} r \mathrm{d}r \mathrm{d}\theta & \\
= \int_0^{2\pi} \int_{r_{g_1}}^{r_{g_2}} \left( p^{(R_1)}_d + p^{(R_2)}_u \right) f^{*(G)}_{n'_sg'}(r) \mathrm{e}^{-\mathrm{i}n'_s\theta} r \mathrm{d}r \mathrm{d}\theta & \quad (2.40)
\end{aligned}
$$

where $n'_s = n + s'V$, $s' \in \mathbb{Z}$, $g' \in \mathbb{N}$, $\gamma' \in \mathbb{N}$. $f^{*(R_d)}_{n'_s\gamma'}(r)\mathrm{e}^{-\mathrm{i}n'_s\theta}$ and $f^{*(G)}_{n'_sg'}(r)\mathrm{e}^{-\mathrm{i}n'_s\theta}$ represent respectively the complex conjugates of the eigenfunctions $f^{(R_d)}_{n_s\gamma}(r)\mathrm{e}^{\mathrm{i}n_s\theta}$ and $f^{(G)}_{n_sg}(r)\mathrm{e}^{\mathrm{i}n_s\theta}$.

In the same way, the projection of Equations 2.36 and 2.38 on the bases $f^{*(R_1)}_{n'_s\xi'}(r)\mathrm{e}^{-\mathrm{i}n'_s\theta}$

leads to

$$\begin{aligned}\int_0^{2\pi}\int_{r_1}^{r_{R_d}} &\left(v_i^{(R_d)}\cdot\mathbf{e}_{\boldsymbol{x}}+v_u^{(R_d)}\cdot\mathbf{e}_{\boldsymbol{x}}\right) f^{*(R_1)}_{n'_s\xi'}(r)\mathrm{e}^{-\mathrm{i}n'_s\theta}r\mathrm{d}r\mathrm{d}\theta\\&=\int_0^{2\pi}\int_{r_1}^{r_{R_d}}\left(v_d^{(R_1)}\cdot\mathbf{e}_{\boldsymbol{x}}+v_u^{(R_1)}\cdot\mathbf{e}_{\boldsymbol{x}}\right) f^{*(R_1)}_{n'_s\xi'}(r)\mathrm{e}^{-\mathrm{i}n'_s\theta}r\mathrm{d}r\mathrm{d}\theta\end{aligned}\tag{2.41}$$

$$\begin{aligned}\int_0^{2\pi}\int_{r_{g_1}}^{r_{g_2}} &\left(v_u^{(G)}\cdot\mathbf{e}_{\boldsymbol{x}}+v_d^{(G)}\cdot\mathbf{e}_{\boldsymbol{x}}\right) f^{*(A)}_{n'_s\xi'}(r)\mathrm{e}^{-\mathrm{i}n'_s\theta}r\mathrm{d}r\mathrm{d}\theta\\&=\int_0^{2\pi}\int_{r_{g1}}^{r_{g2}}\left(v_d^{(R_1)}\cdot\mathbf{e}_{\boldsymbol{x}}+v_u^{(R_1)}\cdot\mathbf{e}_{\boldsymbol{x}}\right) f^{*(R_1)}_{n'_s\xi'}(r)\mathrm{e}^{-\mathrm{i}n'_s\theta}r\mathrm{d}r\mathrm{d}\theta\end{aligned}\tag{2.42}$$

where $\xi'\in\mathbb{N}$, and $f^{*(R_1)}_{n'_s\xi'}(r)\mathrm{e}^{-\mathrm{i}n'_s\theta}$ being the complex conjugate of the eigenfunction $f^{(R_1)}_{n_s\xi}(r)\mathrm{e}^{\mathrm{i}n_s\theta}$.

On the other hand, the rigid-wall boundary condition (Equation 2.95d), is equivalent to

$$\begin{aligned}\int_0^{2\pi}\int_{r_1}^{r_R} &\left(v_d^{(R_1)}\cdot\mathbf{e}_{\boldsymbol{x}}+v_u^{(R_1)}\cdot\mathbf{e}_{\boldsymbol{x}}\right) f^{*(R_1)}_{n'_s\xi'}(r)\mathrm{e}^{-\mathrm{i}n'_s\theta}r\mathrm{d}r\mathrm{d}\theta\\&=\int_0^{2\pi}\int_{r_1}^{r_{R_d}}\left(v_d^{(R_1)}\cdot\mathbf{e}_{\boldsymbol{x}}+v_u^{(R_1)}\cdot\mathbf{e}_{\boldsymbol{x}}\right) f^{*(R_1)}_{n'_s\xi'}(r)\mathrm{e}^{-\mathrm{i}n'_s\theta}r\mathrm{d}r\mathrm{d}\theta\\&\quad+\int_0^{2\pi}\int_{r_{g_1}}^{r_{g_2}}\left(v_d^{(R_1)}\cdot\mathbf{e}_{\boldsymbol{x}}+v_u^{(R_1)}\cdot\mathbf{e}_{\boldsymbol{x}}\right) f^{*(R_1)}_{n'_s\xi'}(r)\mathrm{e}^{-\mathrm{i}n'_s\theta}r\mathrm{d}r\mathrm{d}\theta\end{aligned}\tag{2.43}$$

Thus, combining Equation 2.43 with Equations 2.41 and 2.42, we get

$$\begin{aligned}\int_0^{2\pi}\int_{r_1}^{r_{R_d}} &\left(v_i^{(R_d)}\cdot\mathbf{e}_{\boldsymbol{x}}+v_u^{(R_d)}\cdot\mathbf{e}_{\boldsymbol{x}}\right) f^{*(R_1)}_{n'_s\xi'}(r)\mathrm{e}^{-\mathrm{i}n'_s\theta}r\mathrm{d}r\mathrm{d}\theta\\&+\int_0^{2\pi}\int_{r_{g_1}}^{r_{g_2}}\left(v_u^{(G)}\cdot\mathbf{e}_{\boldsymbol{x}}+v_d^{(G)}\cdot\mathbf{e}_{\boldsymbol{x}}\right) f^{*(A)}_{n'_s\xi'}(r)\mathrm{e}^{-\mathrm{i}n'_s\theta}r\mathrm{d}r\mathrm{d}\theta\\&=\int_0^{2\pi}\int_{r_1}^{r_R}\left(v_d^{(R_1)}\cdot\mathbf{e}_{\boldsymbol{x}}+v_u^{(R_1)}\cdot\mathbf{e}_{\boldsymbol{x}}\right) f^{*(R_1)}_{n'_s\xi'}(r)\mathrm{e}^{-\mathrm{i}n'_s\theta}r\mathrm{d}r\mathrm{d}\theta\end{aligned}\tag{2.44}$$

After accounting for the orthogonality of the different modal bases, the matching equations become

$$\boxed{\begin{aligned}k^-_{nj}A^{(R_{d1})}_{nj}\mathrm{e}^{-\mathrm{i}k^-_{nj}L_{p1}}\mathcal{F}^{n'_s\xi'}_{nj}&+\sum_{s=-\infty}^{+\infty}\sum_{\gamma=0}^{+\infty}k^+_{n_s\gamma}U^{(R_d)}_{n_s\gamma}\mathcal{F}^{n'_s\xi'}_{n_s\gamma}\delta_{ss'}\\&+\sum_{s=-\infty}^{+\infty}\sum_{g=0}^{+\infty}\left(k^+_{n_sg}U^{(G)}_{n_sg}+k^-_{n_sg}D^{(G)}_{n_sg}\mathrm{e}^{-\mathrm{i}k^-_{n_sg}L_G}\right)\mathcal{W}^{n'_s\xi'}_{n_sg}\delta_{ss'}\\&=k^-_{n'_s\xi'}D^{(R_1)}_{n'_s\xi'}r_R^2+k^+_{n'_s\xi'}U^{(R_1)}_{n'_s\xi'}\mathrm{e}^{\mathrm{i}k^+_{n'_s\xi'}L_{R_1}}r_R^2\end{aligned}}\tag{2.45}$$

$$\boxed{\begin{aligned} A^{(R_{d1})}_{nj} \mathrm{e}^{-\mathrm{i}k^{-}_{nj}L_{p1}} \delta_{\gamma' j} r^2_{R_d} &+ U^{(R_d)}_{n'_s\gamma'} r^2_{R_d} \\ &= \sum_{s=-\infty}^{+\infty} \sum_{\xi=0}^{+\infty} \left( D^{(R_1)}_{n_s\xi} + U^{(R_1)}_{n_s\xi} \mathrm{e}^{\mathrm{i}k^{+}_{n_s\xi}L_{R_1}} \right) \mathcal{F}^{n'_s\gamma'[T]}_{n_s\xi} \delta_{ss'} \end{aligned}} \tag{2.46}$$

$$\boxed{U^{(G)}_{n'_s g'} r^2_{g_2} + D^{(G)}_{n'_s g'} \mathrm{e}^{-\mathrm{i}k^{-}_{n'_s g'}L_G} r^2_{g_2} = \sum_{s=-\infty}^{+\infty} \sum_{\xi=0}^{+\infty} \left( D^{(R_1)}_{n_s\xi} + U^{(R_1)}_{n_s\xi} \mathrm{e}^{\mathrm{i}k^{+}_{n_s\xi}L_{R_1}} \right) \mathcal{W}^{n'_s g'[T]}_{n_s\xi} \delta_{ss'}} \tag{2.47}$$

where $\mathcal{F}^{n'_s\xi'}_{nj}$, $\mathcal{F}^{n'_s\xi'}_{n_s\gamma}$, $\mathcal{F}^{n'_s\gamma'[T]}_{n_s\xi}$, $\mathcal{W}^{n'_s\xi'}_{n_s g}$ and $\mathcal{W}^{n'_s g'[T]}_{n_s\xi}$ represent the projection matrices. They are defined as

$$\mathcal{F}^{n'_s\xi'}_{nj} = \int_{r_1}^{r_{R_d}} f^{*(R_1)}_{n'_s\xi'}(r) f^{(R_d)}_{nj}(r) r dr \qquad , \mathcal{F}^{n'_s\xi'}_{n_s\gamma} = \int_{r_1}^{r_{R_d}} f^{*(R_1)}_{n'_s\xi'}(r) f^{(R_d)}_{n_s\gamma}(r) r dr$$

$$\mathcal{F}^{n'_s\gamma'[T]}_{n_s\xi} = \int_{r_1}^{r_{R_d}} f^{*(R_d)}_{n'_s\gamma'}(r) f^{(R_1)}_{n_s\xi}(r) r dr$$

$$\mathcal{W}^{n'_s\xi'}_{n_s g} = \int_{r_{g_1}}^{r_{g_2}} f^{*(R_1)}_{n'_s\xi'}(r) f^{(G)}_{n_s g}(r) r dr \qquad , \mathcal{W}^{n'_s g'[T]}_{n_s\xi} = \int_{r_{g_1}}^{r_{g_2}} f^{*(G)}_{n'_s g'}(r) f^{(R_1)}_{n_s\xi}(r) r dr$$

The matrices $\mathcal{F}^{n'_s\gamma'[T]}_{n_s\xi}$ and $\mathcal{W}^{n'_s g'[T]}_{n_s\xi}$ are respectively the transpose of the matrices $\mathcal{F}^{n'_s\xi'}_{n_s\gamma}$ and $\mathcal{W}^{n'_s\xi'}_{n_s g}$. It is important to note that the projection integrals of the radial eigenfunctions are significantly more complex than the azimuthal functions. They cannot be integrated analytically. In this work, these integrals are evaluated numerically, by using the Trapezoidal method [85].

#### 2.3.3.2 Matching equations at the interface $x = x_2$

The interface $x_2$ separates three different subdomains ($(R_1)$, $(A_1)$ and $(S_1)$) as shown in Figure 2.12. The modal amplitudes of the acoustic fields $\phi^{(R_1)}_u$, $\phi^{(A_1)}_t$ and $\phi^{(S_1)}_u$ are determined at this interface.

The matching equations are derived in the same manner as for the interface $x_1$.

$$\begin{cases} \boldsymbol{\Xi}^{(\mathbf{R_1})}_{\mathbf{d}} + \boldsymbol{\Xi}^{(\mathbf{R_1})}_{\mathbf{u}} = \boldsymbol{\Xi}^{(\mathbf{A_1})}_{\mathbf{t}} + \boldsymbol{\Xi}^{(\mathbf{A_1})}_{\mathbf{r}}, \quad x = x_2, \quad \forall\theta, \quad r \in [r_1; r_R] & \text{(2.48a)} \\ \boldsymbol{\Xi}^{(\mathbf{S_1})}_{\mathbf{u}} + \boldsymbol{\Xi}^{(\mathbf{S_1})}_{\mathbf{r}} = \boldsymbol{\Xi}^{(\mathbf{A_1})}_{\mathbf{t}} + \boldsymbol{\Xi}^{(\mathbf{A_1})}_{\mathbf{r}}, \quad x = x_2, \quad \forall\theta, \quad r \in [r_S; r_2] & \text{(2.48b)} \\ v^{(A_1)}_t \cdot \mathbf{e_x} + v^{(A_1)}_r \cdot \mathbf{e_x} = 0, \quad x = x_2, \quad \forall\theta, \quad r \in ]r_R; r_S[ & \text{(2.48c)} \end{cases}$$

In the same way, these equations should be projected on the three sets of eigenfunctions. After accounting for the orthogonality of the modal bases and the rigid wall-

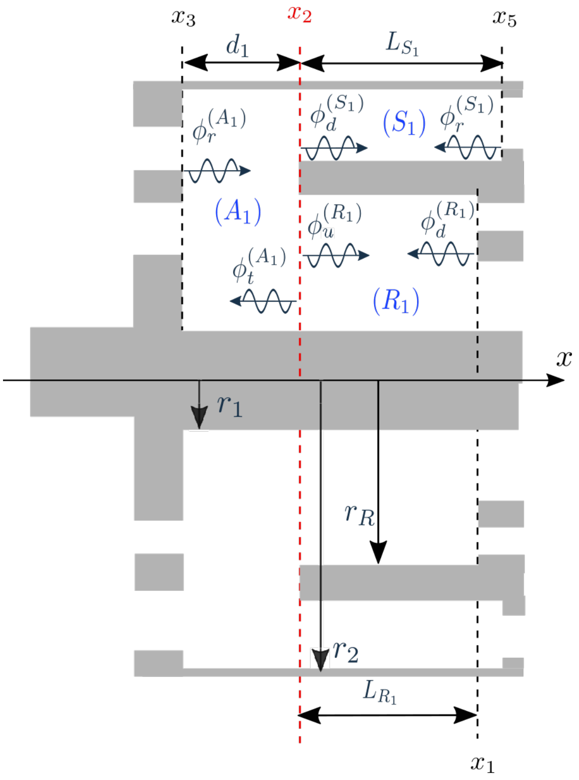

**Figure 2.12:** Acoustic fields generated at the interface $x_2$. Matching interface (----).

boundary condition, this system becomes

$$\boxed{\begin{aligned}&\sum_{s=-\infty}^{+\infty}\sum_{\xi=0}^{+\infty}\left(k^{+}_{n_s\xi}U^{(R_1)}_{n_s\xi}+k^{-}_{n_s\xi}D^{(R_1)}_{n_s\xi}\mathrm{e}^{-\mathrm{i}k^{-}_{n_s\xi}L_{R_1}}\right)\mathcal{K}^{n'_s\beta'}_{n_s\xi}\,\delta_{s's}\\&\qquad+\sum_{s=-\infty}^{+\infty}\sum_{\eta=0}^{+\infty}\left(k^{+}_{n_s\eta}U^{(S_1)}_{n_s\eta}+k^{-}_{n_s\eta}R^{(S_1)}_{n_s\eta}\mathrm{e}^{-\mathrm{i}k^{-}_{n_s\eta}L_{S_1}}\right)\mathcal{X}^{n'_s\beta'}_{n_s\eta}\,\delta_{s's}\\&\qquad\qquad=k^{-}_{n'_s\beta'}T^{(A_1)}_{n'_s\beta'}r_2^2+k^{+}_{n'_s\beta'}R^{(A_1)}_{n'_s\beta'}\mathrm{e}^{\mathrm{i}k^{+}_{n'_s\beta'}d_1}r_2^2\end{aligned}}\tag{2.49}$$

$$\boxed{U^{(R_1)}_{n'_s\xi'}r_R^2+D^{(R_1)}_{n'_s\xi'}\mathrm{e}^{-\mathrm{i}k^{-}_{n'_s\xi'}L_{R_1}}r_R^2=\sum_{s=-\infty}^{+\infty}\sum_{\beta=0}^{+\infty}\left(T^{(A_1)}_{n_s\beta}+R^{(A_1)}_{n_s\beta}\mathrm{e}^{\mathrm{i}k^{+}_{n_s\beta}d_1}\right)\mathcal{K}^{n'_s\xi'[T]}_{n_s\beta}\delta_{s's}}\tag{2.50}$$

$$\boxed{U^{(S_1)}_{n'_s\eta'}r_2^2+R^{(S_1)}_{n'_s\eta'}\mathrm{e}^{-\mathrm{i}k^{-}_{n'_s\eta'}L_{S_1}}r_2^2=\sum_{s=-\infty}^{+\infty}\sum_{\beta=0}^{+\infty}\left(T^{(A_1)}_{n_s\beta}+R^{(A_1)}_{n_s\beta}\mathrm{e}^{\mathrm{i}k^{+}_{n_s\beta}d_1}\right)\mathcal{X}^{n'_s\eta'[T]}_{n_s\beta}\delta_{s's}}\tag{2.51}$$

where

$$\mathcal{K}^{n'_s\beta'}_{n_s\xi}=\int_{r_1}^{r_R}f^{*(A)}_{n'_s\beta'}(r)f^{(R_1)}_{n_s\xi}(r)rdr\qquad,\mathcal{K}^{n'_s\xi'[T]}_{n_s\beta}=\int_{r_1}^{r_R}f^{*(R_1)}_{n'_s\xi'}(r)f^{(A)}_{n_s\beta}(r)rdr$$

$$\mathcal{X}_{n_s\eta}^{n'_s\beta'} = \int_{r_S}^{r_2} f_{n'_s\beta'}^{*(A)}(r) f_{n_s\eta}^{(S_1)}(r) r dr \qquad , \mathcal{X}_{n_s\beta}^{n'_s\eta'[T]} = \int_{r_S}^{r_2} f_{n'_s\eta'}^{*(S_1)}(r) f_{n_s\beta}^{(A)}(r) r dr$$

#### 2.3.3.3 Matching equations at the interface $x = x_3$

The acoustic field $\phi_t^{(A_1)}$ transmitted in the space $(A_1)$ is diffracted by the flow deflector, which is located at the interface $x_3$ (see Figure 2.13). The matching equations at this interface can be expressed as

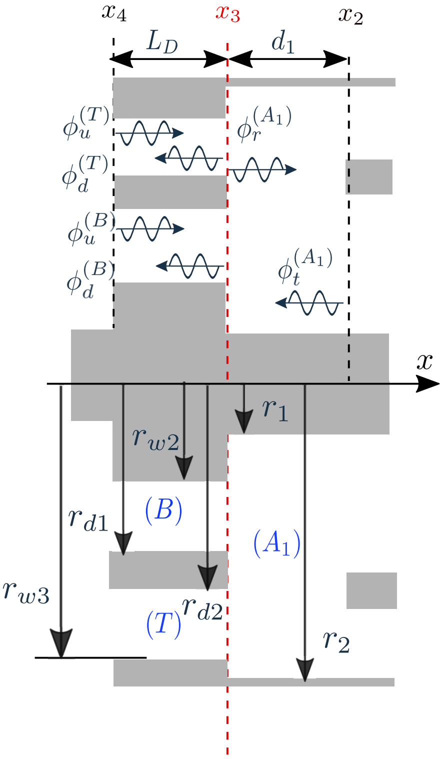

**Figure 2.13:** Acoustic fields generated at the interface $x_3$. Matching interface (- - - -).

$$\begin{cases} \quad \boldsymbol{\Xi}_{\mathbf{t}}^{(\mathbf{A_1})} + \boldsymbol{\Xi}_{\mathbf{r}}^{(\mathbf{A_1})} = \boldsymbol{\Xi}_{\mathbf{d}}^{(\mathbf{T})} + \boldsymbol{\Xi}_{\mathbf{u}}^{(\mathbf{T})}, \quad x = x_3, \quad \forall\theta, \quad r \in [r_{w2}; r_{d_1}] & (2.52a) \\ \quad \boldsymbol{\Xi}_{\mathbf{t}}^{(\mathbf{A_1})} + \boldsymbol{\Xi}_{\mathbf{r}}^{(\mathbf{A_1})} = \boldsymbol{\Xi}_{\mathbf{d}}^{(\mathbf{B})} + \boldsymbol{\Xi}_{\mathbf{u}}^{(\mathbf{B})}, \quad x = x_3, \quad \forall\theta, \quad r \in [r_{d_2}; r_{w3}] & (2.52b) \\ v_t^{(A_1)} \cdot \mathbf{e_x} + v_r^{(A_1)} \cdot \mathbf{e_x} = 0, \quad x = x_3, \quad \forall\theta, \quad r \in ]r_1; r_{w_2}[ \cup ]r_{d_1}; r_{d_2}[ \cup ]r_{w_2}; r_2] & (2.52c) \end{cases}$$

Using the same procedure as for the interfaces $x_1$ and $x_2$, one obtains

$$\boxed{\begin{aligned} & k_{n'_s\beta'}^{-} T_{n'_s\beta'}^{(A)} \mathrm{e}^{-\mathrm{i}k_{n'_s\beta'}^{-} d_1} r_2^2 + k_{n'_s\beta'}^{+} R_{n'_s\beta'}^{(A)} r_2^2 \\ & \qquad = \sum_{s=-\infty}^{+\infty} \sum_{\mu=0}^{+\infty} \left( k_{n_s\mu}^{-} D_{n_s\mu}^{(T)} + k_{n_s\mu}^{+} U_{n_s\mu}^{(T)} \mathrm{e}^{\mathrm{i}k_{n_s\mu}^{+} L_D} \right) \mathcal{Q}_{n_s\mu}^{n'_s\beta'} \delta_{ss'} \\ & \qquad\qquad + \sum_{s=-\infty}^{+\infty} \sum_{\nu=0}^{+\infty} \left( k_{n_s\mu}^{-} D_{n_s\mu}^{(B)} + k_{n_s\nu}^{+} U_{n_s\nu}^{(B)} \mathrm{e}^{\mathrm{i}k_{n_s\nu}^{+} L_D} \right) \mathcal{Y}_{n_s\nu}^{n'_s\beta'} \delta_{ss'} \end{aligned}} \tag{2.53}$$

$$\boxed{\sum_{s=-\infty}^{+\infty}\sum_{\beta=0}^{+\infty}\left(T^{(A)}_{n_s\beta}\mathrm{e}^{-\mathrm{i}k^{-}_{n_s\beta}d_1}+R^{(A)}_{n_s\beta}\right)\mathcal{Q}^{n'_s\mu'[T]}_{n_s\beta}\delta_{ss'}=D^{(T)}_{n'_s\mu'}r^2_{w_3}+U^{(T)}_{n'_s\mu'}\mathrm{e}^{\mathrm{i}k^{+}_{n'_s\mu'}L_D}r^2_{w_3}} \tag{2.54}$$

$$\boxed{\sum_{s=-\infty}^{+\infty}\sum_{\beta=0}^{+\infty}\left(T^{(A)}_{n_s\beta}\mathrm{e}^{-\mathrm{i}k^{-}_{n_s\beta}d_1}+R^{(A)}_{n_s\beta}\right)\mathcal{Y}^{n'_s\nu'[T]}_{n_s\beta}\delta_{ss'}=D^{(B)}_{n'_s\nu'}r^2_{d_1}+U^{(B)}_{n'_s\nu'}\mathrm{e}^{\mathrm{i}k^{+}_{n'_s\nu'}L_D}r^2_{d_1}} \tag{2.55}$$

where

$$\mathcal{Q}^{n'_s\beta'}_{n_s\mu}=\int_{r_{d_2}}^{r_{w_3}}f^{*(A)}_{n'_s\beta'}(r)f^{(T)}_{n_s\mu}(r)rdr \qquad ,\mathcal{Q}^{n'_s\mu'[T]}_{n_s\beta}=\int_{d_2}^{r_{w_3}}f^{*(T)}_{n'_s\mu'}(r)f^{(A)}_{n_s\beta}(r)rdr$$

$$\mathcal{Y}^{n'_s\beta'}_{n_s\nu}=\int_{r_{w_2}}^{r_{d_1}}f^{*(A)}_{n'_s\beta'}(r)f^{(B)}_{n_s\nu}(r)rdr \qquad ,\mathcal{Y}^{n'_s\nu'[T]}_{n_s\beta}=\int_{w_2}^{r_{d_1}}f^{*(B)}_{n'_s\nu'}(r)f^{(A)}_{n_s\beta}(r)rdr$$

#### 2.3.3.4 Matching equations at the interface $x = x_4$

The different acoustic fields transmitted ($\phi_d^{(B)}$ and $\phi_d^{(T)}$) into the subdomains $(B)$ and $(T)$ are scattered at the interface $x_4$, generating transmitted and reflected acoustic fields (see Figure 2.14).

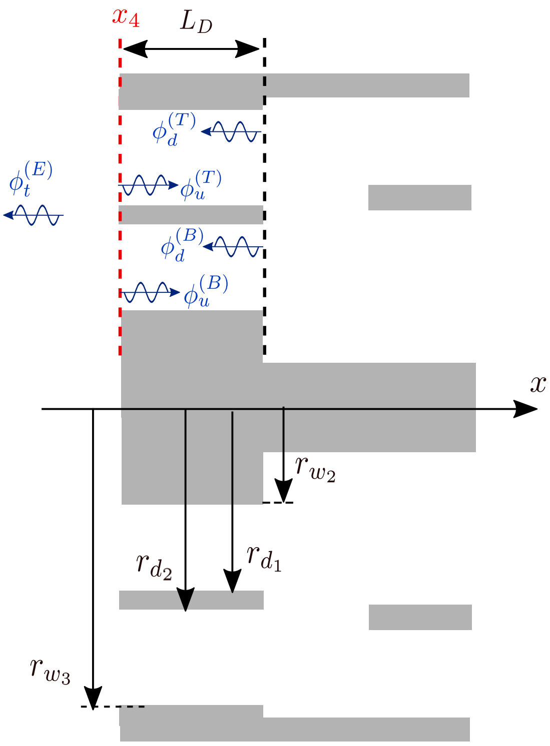

**Figure 2.14:** Scattering of the sound field at the matching interface $x_4$

The matching equations can be written as

$$\begin{cases} \mathbf{\Xi_d^{(T)}} + \mathbf{\Xi_u^{(T)}} = \mathbf{\Xi_t^{(E)}}, \quad x = x_4, \quad \forall\theta, \quad r \in [r_{w2}; r_{d_1}] & (2.56a) \\ \mathbf{\Xi_d^{(B)}} + \mathbf{\Xi_u^{(B)}} = \mathbf{\Xi_t^{(E)}}, \quad x = x_4, \quad \forall\theta, \quad r \in [r_{d_2}; r_{w_3}] & (2.56b) \\ \quad v_t^{(E)} \cdot \mathbf{e}_{\boldsymbol{x}} = 0, \quad x = x_4, \quad \forall\theta, \quad r \in ]r_{e_1}; r_{w_2}[ \cup ]r_{d_1}; r_{d_2}[ \cup ]r_{w_2}; r_{e_2}] & (2.56c) \end{cases}$$

The projection of these equations on the different modal bases gives

$$\boxed{\begin{aligned} &\sum_{s=-\infty}^{+\infty} \sum_{\mu=0}^{+\infty} \left( k_{n_s\mu}^- D_{n_s\mu}^{(T)} \mathrm{e}^{-\mathrm{i}k_{n_s\mu}^- L_D} + k_{n_s\mu}^+ U_{n_s\mu}^{(T)} \right) \mathcal{A}_{n_s\mu}^{n_s'm'} \delta_{ss'} \\ &\qquad + \sum_{s=-\infty}^{+\infty} \sum_{\nu=0}^{+\infty} \left( k_{n_s\nu}^- D_{n_s\nu}^{(B)} \mathrm{e}^{-\mathrm{i}k_{n_s\nu}^- L_D} + k_{n_s\nu}^+ U_{n_s\nu}^{(B)} \right) \mathcal{G}_{n_s\nu}^{n_s'm'} \delta_{ss'} = T_{n_s'm'}^{(E)} r_{e_2}^2 \end{aligned}} \tag{2.57}$$

$$\boxed{D_{n_s'\mu'}^{(T)} \mathrm{e}^{-\mathrm{i}k_{n_s'\mu'}^- L_D} r_{w_3}^2 + U_{n_s'\mu'}^{(T)} r_{w_3}^2 = \sum_{s=-\infty}^{+\infty} \sum_{m=0}^{+\infty} T_{n_sm}^{(E)} \mathcal{A}_{n_sm}^{n_s'\mu'[T]} \delta_{ss'}} \tag{2.58}$$

$$\boxed{D_{n_s'\nu'}^{(B)} \mathrm{e}^{-\mathrm{i}k_{n_s'\nu'}^- L_D} r_{d_1}^2 + U_{n_s'\nu'}^{(B)} r_{d_1}^2 = \sum_{s=-\infty}^{+\infty} \sum_{m=0}^{+\infty} T_{n_sm}^{(E)} \mathcal{G}_{n_sm}^{n_s'\nu'[T]} \delta_{ss'}} \tag{2.59}$$

where

$$\mathcal{Q}_{n_s\mu}^{n_s'\beta'} = \int_{r_{d_2}}^{r_{w3}} f_{n_s'\beta'}^{*(A)}(r) f_{n_s\mu}^{(T)}(r) r dr \qquad , \mathcal{Q}_{n_s\beta}^{n_s'\mu'[T]} = \int_{d_2}^{r_{w3}} f_{n_s'\mu'}^{*(T)}(r) f_{n_s\beta}^{(A)}(r) r dr$$

$$\mathcal{Y}_{n_s\nu}^{n_s'\beta'} = \int_{r_{w_2}}^{r_{d_1}} f_{n_s'\beta'}^{*(A)}(r) f_{n_s\nu}^{(B)}(r) r dr \qquad , \mathcal{Y}_{n_s\beta}^{n_s'\nu'[T]} = \int_{w_2}^{r_{d_1}} f_{n_s'\nu'}^{*(B)}(r) f_{n_s\beta}^{(A)}(r) r dr$$

#### 2.3.3.5 Channel inlet $x = x_5$

Sound transmission through the stator channels can be investigated in the same way as for the previous interfaces. The only difference is that the sound field is scattered in both azimuthal and radial directions, because of the presence of the stator ventilating holes (see Figure 2.15). The diffraction of a helical wave by three-dimensional rigid flat plates of zero thickness has been already reported by Ingenito *et al* [59] and Bouley *et al* [17], by using the mode-matching technique. However, in the case of an open motor, the ventilating holes are integrated in the stator core. The front face and the back face of the walls may have a significant influence on the sound propagation. Therefore, the cooling channels cannot be considered as flat plates in this analysis. In the following, the mode-matching method will be extended to the transmission of helical waves through a periodic row of thick-walled channels. As mentioned in Chapter **??**, the cooling channels are periodically excited by the incident waves, therefore, the matching equations need only to be formulated for the

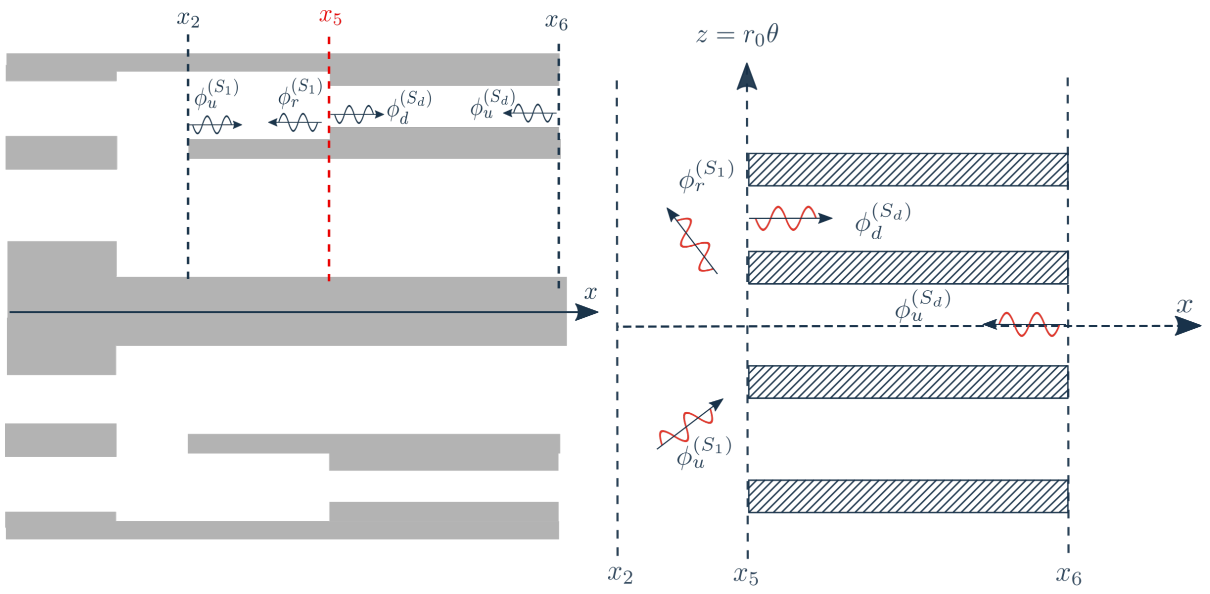

**(a)** **(b)**

**Figure 2.15:** Scattering of the sound field at the matching interface $x_5$. (a) Meridian cut, (b) cylindrical cut

reference channel $m = 0$. For this, the continuity of pressure and axial velocity must be imposed at the channel cross-section ($0 < \theta < \theta_a$ and $r_{S_{d1}} < r < r_{S_{d2}}$). The rigid-wall boundary condition corresponding to a vanishing normal velocity $v.\mathbf{n} = v.\mathbf{e_x} = 0$ must imposed on the front face of the channel walls.

$$\begin{cases} \Xi_{\mathbf{u}}^{(\mathbf{S_1})} + \Xi_{\mathbf{r}}^{(\mathbf{S_1})} = \Xi_{\mathbf{d}}^{(\mathbf{S_d})} + \Xi_{\mathbf{u}}^{(\mathbf{S_d})}, \quad x = x_5, \quad \theta \in [0;\theta_a], \quad r \in [r_{S_{d1}}; r_{S_{d2}}] & \text{(2.60a)} \\ v_u^{(S_1)} \cdot \mathbf{e}_{\boldsymbol{x}} + v_r^{(S_1)} \cdot \mathbf{e}_{\boldsymbol{x}} = 0, \quad x = x_5, \quad \theta \in \left[\theta_a; \dfrac{2\pi}{V}\right], \quad r \in ]r_S; r_{S_{d1}}[ \cup ]r_{S_{d2}}; r_2[ & \text{(2.60b)} \end{cases}$$

The modal projection must be carried out using the two modal bases, associated with the waves propagating in the annular duct and in the reference channel. The projection of the pressure equation on the eigenfunctions related to the reference channel leads to

$$\int_0^{\theta_a} \int_{r_{S_{d1}}}^{r_{S_{d2}}} \left(p_u^{(S_1)} + p_r^{(S_1)}\right) f_{n'_q p'}^{(S_d)}(r) \cos\left(n'_q \theta\right) r \mathrm{d}r \mathrm{d}\theta = \int_0^{\theta_a} \int_{r_{S_{d1}}}^{r_{S_{d2}}} \left(p_d^{(S_d)} + p_u^{(S_d)}\right) f_{n'_q p'}^{(S_d)}(r) \cos\left(n'_q \theta\right) r \mathrm{d}r \mathrm{d}\theta \tag{2.61}$$

Projection of the velocity equation on the eigenfunctions related to the annular duct yields

$$\int_0^{\theta_a} \int_{r_{S_{d1}}}^{r_{S_{d2}}} \left(v_u^{(S_1)} \cdot \mathbf{e}_{\boldsymbol{x}} + v_r^{(S_1)} \cdot \mathbf{e}_{\boldsymbol{x}}\right) f_{n'_s \eta'}^{(S_1)}(r) \mathrm{e}^{-\mathrm{i} n'_s \theta} r \mathrm{d}r \mathrm{d}\theta = \int_0^{\theta_a} \int_{r_{S_{d1}}}^{r_{S_{d2}}} \left(v_d^{(S_d)} \cdot \mathbf{e}_{\boldsymbol{x}} + v_u^{(S_d)} \cdot \mathbf{e}_{\boldsymbol{x}}\right) f_{n'_s \eta'}^{(S_1)}(r) \mathrm{e}^{-\mathrm{i} n'_s \theta} r \mathrm{d}r \mathrm{d}\theta \tag{2.62}$$

The rigid-wall boundary condition (Equation 2.60b) is equivalent to

$$\begin{aligned}\int_0^{2\pi/V}\int_{r_S}^{r_2}\left(v_u^{(S_1)}\cdot\mathbf{e}_{\boldsymbol{x}}+v_r^{(S_1)}\cdot\mathbf{e}_{\boldsymbol{x}}\right)f^{*(S_1)}_{n'_s\eta'}(r)\mathrm{e}^{-\mathrm{i}n'_s\theta}r\mathrm{d}r\mathrm{d}\theta \\ =\int_0^{\theta_a}\int_{r_{S_{d1}}}^{r_{S_{d2}}}\left(v_u^{(S_1)}\cdot\mathbf{e}_{\boldsymbol{x}}+v_r^{(S_1)}\cdot\mathbf{e}_{\boldsymbol{x}}\right)f^{*(S_1)}_{n'_s\eta'}(r)\mathrm{e}^{-\mathrm{i}n'_s\theta}r\mathrm{d}r\mathrm{d}\theta\end{aligned} \tag{2.63}$$

Combining Equations 2.62 and 2.63 one gets

$$\begin{aligned}\int_0^{2\pi/2}\int_{r_S}^{r_2}\left(v_u^{(S_1)}\cdot\mathbf{e}_{\boldsymbol{x}}+v_r^{(S_1)}\cdot\mathbf{e}_{\boldsymbol{x}}\right)f^{(S_1)}_{n'_s\eta'}(r)\mathrm{e}^{-\mathrm{i}n'_s\theta}r\mathrm{d}r\mathrm{d}\theta \\ =\int_0^{\theta_a}\int_{r_{S_{d1}}}^{r_{S_{d2}}}\left(v_d^{(S_d)}\cdot\mathbf{e}_{\boldsymbol{x}}+v_u^{(S_d)}\cdot\mathbf{e}_{\boldsymbol{x}}\right)f^{(S_1)}_{n'_s\eta'}(r)\mathrm{e}^{-\mathrm{i}n'_s\theta}r\mathrm{d}r\mathrm{d}\theta\end{aligned} \tag{2.64}$$

Equations 2.64 and 2.61 are reduced by using the orthogonality of radial and azimuthal modes. After accounting for the orthogonality, the matching equations become

$$\boxed{\begin{aligned}\sum_{s=-\infty}^{+\infty}\sum_{\eta=0}^{+\infty}\left(U^{(S_1)}_{n_s\eta}\mathrm{e}^{\mathrm{i}k^+_{n_s\eta}L_{S_1}}+R^{(S_1)}_{n_s\eta}\right)\Lambda_{q'n_s}\Upsilon^{n'_qp'}_{n_s\eta} \\ =\left(D^{(S_d)}_{n'_qp'}+U^{(S_d)}_{n'_qp'}\mathrm{e}^{-\mathrm{i}k^-_{n'_qp'}L_d}\right)\frac{\theta_a}{2}r_3^2\left(1+\delta_{q'0}\right)\end{aligned}} \tag{2.65}$$

$$\boxed{\begin{aligned}\frac{2\pi}{V}r_2^2k^+_{n'_s\eta'}U^{(S_1)}_{n'_s\eta'}\mathrm{e}^{\mathrm{i}k^+_{n_s\eta}L_{S_1}}+\frac{2\pi}{V}r_2^2k^-_{n'_s\eta'}R^{(S_1)}_{n'_s\eta'} \\ =\sum_{q=0}^{+\infty}\sum_{p=0}^{+\infty}\left(D^{(S_d)}_{n_qp}+U^{(S_d)}_{n_qp}\mathrm{e}^{-\mathrm{i}k^-_{n_qq}L_{S_d}}\right)\varphi_{n'_sq}\Upsilon^{n'_s\eta'[T]}_{n_qp}\end{aligned}} \tag{2.66}$$

The projection matrices $\Lambda_{q',s}$ and $\varphi_{s',q}$ are evalutaed analytically:

$$\Lambda_{q's}=\int_0^{\theta_a}\mathrm{e}^{\mathrm{i}n_s\theta}\cos(n'_q\theta)d\theta=\begin{cases}\dfrac{\mathrm{i}n_s\left[1-(-1)^{q'}\mathrm{e}^{-\mathrm{i}n_s\theta_a}\right]}{n_s^2-n_q'^2} & ,\text{if } n_{q'}\neq n_s\\ \dfrac{a}{2}(1+\delta_{q'0}) & ,\text{if } n'_q=n_s\end{cases} \tag{2.67}$$

$$\varphi_{s'q}=\int_0^{\theta_a}\cos(n_q\theta)\mathrm{e}^{-\mathrm{i}n'_s\theta}d\theta=\begin{cases}\dfrac{\mathrm{i}n'_s\left[(-1)^{q}\mathrm{e}^{-\mathrm{i}n'_s\theta_a}+1\right]}{n_s'^2-n_q^2} & ,\text{if } n_q\neq n'_s\\ \dfrac{a}{2}(1+\delta_{q0}) & ,\text{if } n_q=n'_s\end{cases} \tag{2.68}$$

The projection integrals of the radial eigenfunctions $\Upsilon^{n_s\eta}_{n'_qp'}$ and $\Upsilon^{n_qp[T]}_{n'_s\eta'}$ are evaluated numerically.

$$\Upsilon_{n_s\eta}^{n'_q p'} = \int_{r_{S_{d1}}}^{r_{S_{d2}}} f_{n_s\eta}^{(S_1)}(r) f_{n'_q p'}^{*(S_d)}(r) r dr \qquad , \Upsilon_{n_q p}^{n'_s\eta'[T]} = \int_{r_{S_{d1}}}^{r_{S_{d2}}} f_{n_q p}^{(S_d)}(r) f_{n'_s\eta'}^{*(S_1)}(r) r dr$$

#### 2.3.3.6 Channel outlet $x = x_6$

As before, the continuity of acoustic pressure and axial velocity must be imposed on the channel cross-section ($0 < \theta < \theta_a$ and $r_{S_{d1}} < r < r_{S_{d2}}$) (see Figure 2.16). The rigid-wall boundary condition is imposed on the front face of the channel walls. the matching equations read

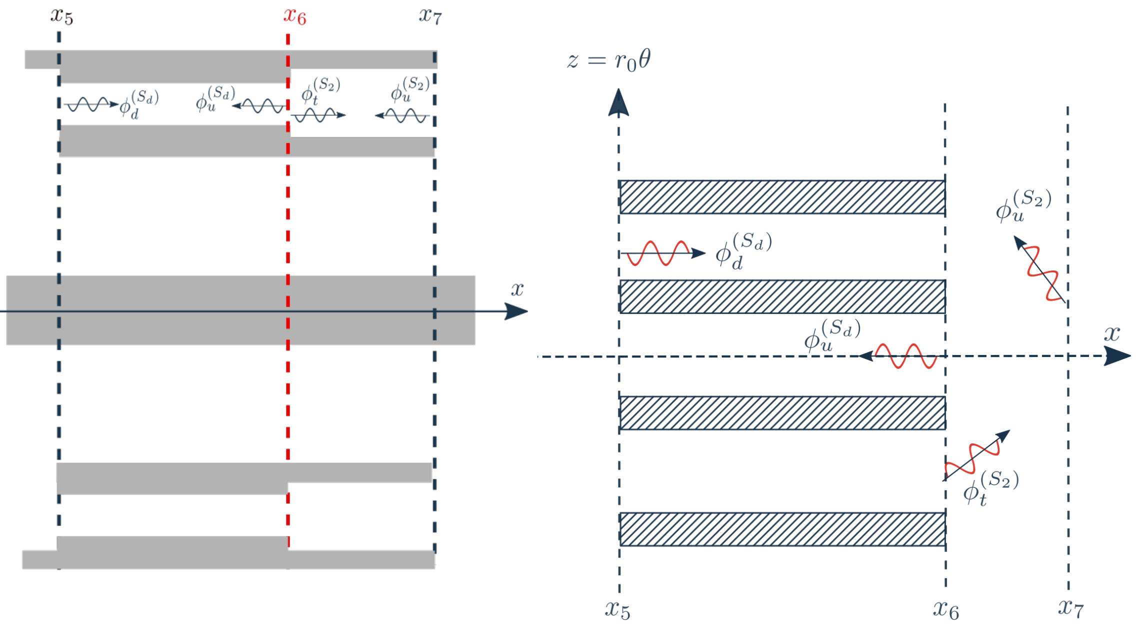

(a) (b)

**Figure 2.16:** Scattering of the sound field at the matching interface $x_6$. (a) Meridian cut, (b) Unwrapped representation of a cylindrical cut at $r = (r_{S_{d1}} + r_{S_{d2}})/2$

$$\begin{cases} \boldsymbol{\Xi}_{\mathbf{d}}^{(\mathbf{S_d})} + \boldsymbol{\Xi}_{\mathbf{u}}^{(\mathbf{S_d})} = \boldsymbol{\Xi}_{\mathbf{t}}^{(\mathbf{S_2})} + \boldsymbol{\Xi}_{\mathbf{u}}^{(\mathbf{S_2})}, \quad x = x_6, \quad \theta \in [0; \theta_a], \quad r \in [r_{S_{d1}}; r_{S_{d2}}] & (2.69\text{a}) \\ v_t^{(S_2)} \cdot \mathbf{e}_{\boldsymbol{x}} + v_u^{(S_2)} \cdot \mathbf{e}_{\boldsymbol{x}} = 0, \quad x = x_6, \quad \theta \in \left[\theta_a; \dfrac{2\pi}{V}\right], \quad r \in ]r_S; r_{S_{d1}}[ \cup ]r_{S_{d2}}; r_2[ & (2.69\text{b}) \end{cases}$$

As before, the matching equations can be reduced by using the orthogonality of the radial and azimuthal eigenfunctions. After accounting for the orthogonality, we get

$$\boxed{\begin{aligned} &\left(D_{n'_q p'}^{(S_d)} \mathrm{e}^{\mathrm{i}k_{n'_q p'}^{+} L_{S_d}} + U_{n'_q p'}^{(S_d)}\right) \frac{\theta_a}{2} r_{S_{d2}}^2 \left(1 + \delta_{q'0}\right) \\ &\qquad = \sum_{s=-\infty}^{+\infty} \sum_{\eta=0}^{+\infty} \left(U_{n_s\eta}^{(S_2)} \mathrm{e}^{-\mathrm{i}k_{n_s\eta}^{-} L_{S_2}} + T_{n'_s\eta'}^{(S_2)}\right) \Lambda_{q' n_s} \Upsilon_{n_s\eta}^{n'_q p'} \end{aligned}} \tag{2.70}$$

$$\boxed{\sum_{q=0}^{+\infty}\sum_{p=0}^{+\infty}\left(D_{n_qp}^{(S_d)}\mathrm{e}^{\mathrm{i}k^+_{n_qq}L_{S_d}} + U_{n_qp}^{(S_d)}\right)\varphi_{n'_sq}\Upsilon_{n_qp}^{n'_s\eta'[T]} = \frac{2\pi}{V} r_2^2 k^+_{n'_s\eta'} T^{(S_2)}_{n'_s\eta'} + \frac{2\pi}{V} r_2^2 k^-_{n'_s\eta'} U^{(S_2)}_{n'_s\eta'} \mathrm{e}^{-\mathrm{i}k^-_{n_s\eta}L_{S_2}}} \tag{2.71}$$

#### 2.3.3.7 Matching equations at the interface $x = x_7$

The matching equations at the interface $x_7$ (see Figure 2.17) can be expressed as

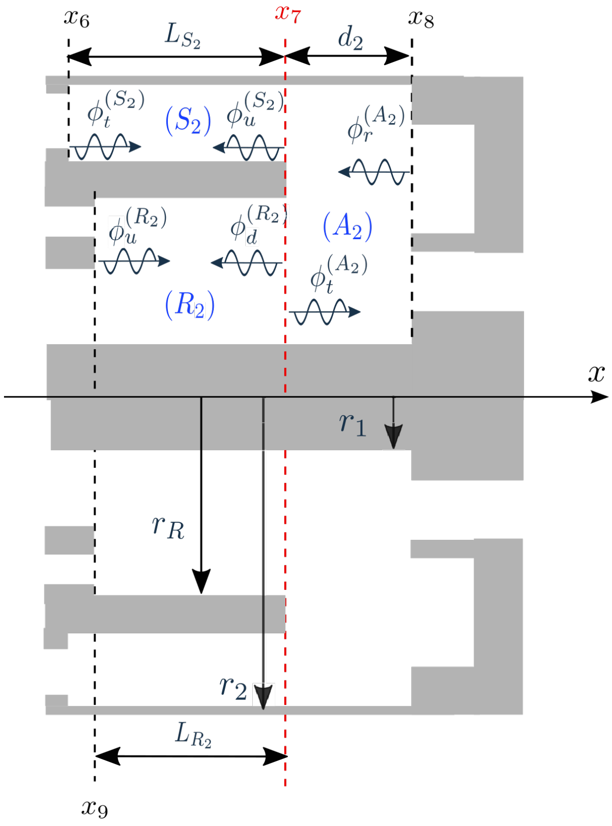

**Figure 2.17:** Scattering of the sound field at the matching interface $x_7$

$$\begin{cases} \mathbf{\Xi_d^{(R_2)}} + \mathbf{\Xi_u^{(R_2)}} = \mathbf{\Xi_t^{(A_2)}} + \mathbf{\Xi_r^{(A_2)}}, \quad x = x_7, \quad \forall\theta, \quad r \in [r_1; r_R] & \text{(2.72a)} \\ \mathbf{\Xi_t^{(S_2)}} + \mathbf{\Xi_u^{(S_2)}} = \mathbf{\Xi_t^{(A_2)}} + \mathbf{\Xi_r^{(A_2)}}, \quad x = x_7, \quad \forall\theta, \quad r \in [r_S; r_2] & \text{(2.72b)} \\ v_t^{(A_2)} \cdot \mathbf{e}_x + v_r^{(A_2)} \cdot \mathbf{e}_x = 0, \quad x = x_7, \quad \forall\theta, \quad r \in ]r_R; r_S[ & \text{(2.72c)} \end{cases}$$

In the same way, these equations should be projected on the three sets of eigenfunctions. After accounting for the orthogonality of the modal bases and the rigid wall boundary condition, this system becomes

$$\boxed{\begin{aligned}&\sum_{s=-\infty}^{+\infty}\sum_{\xi=0}^{+\infty}\left(k^-_{n_s\xi}U^{(R_2)}_{n_s\xi}+k^+_{n_s\xi}D^{(R_2)}_{n_s\xi}\mathrm{e}^{\mathrm{i}k^+_{n_s\xi}L_{R_2}}\right)\mathcal{K}^{n'_s\beta'}_{n_s\xi}\,\delta_{s's}\\&\qquad+\sum_{s=-\infty}^{+\infty}\sum_{\eta=0}^{+\infty}\left(k^-_{n_s\eta}U^{(S_2)}_{n_s\eta}+k^+_{n_s\eta}T^{(S_2)}_{n_s\eta}\mathrm{e}^{\mathrm{i}k^+_{n_s\eta}L_{S_2}}\right)\mathcal{X}^{n'_s\beta'}_{n_s\eta}\,\delta_{s's}\\&\qquad\qquad=k^+_{n'_s\beta'}T^{(A_2)}_{n'_s\beta'}r_2^2+k^-_{n'_s\beta'}R^{(A_2)}_{n'_s\beta'}\mathrm{e}^{-\mathrm{i}k^-_{n'_s\beta'}d_2}r_2^2\end{aligned}}\tag{2.73}$$

$$\boxed{U^{(R_2)}_{n'_s\xi'}r_R^2+D^{(R_2)}_{n'_s\xi'}\mathrm{e}^{\mathrm{i}k^+_{n'_s\xi'}L_{R_2}}r_R^2=\sum_{s=-\infty}^{+\infty}\sum_{\beta=0}^{+\infty}\left(T^{(A_2)}_{n_s\beta}+R^{(A_2)}_{n_s\beta}\mathrm{e}^{-\mathrm{i}k^-_{n_s\beta}d_2}\right)\mathcal{K}^{n'_s\xi'[T]}_{n_s\beta}\delta_{s's}}\tag{2.74}$$

$$\boxed{U^{(S_2)}_{n'_s\eta'}r_2^2+T^{(S_2)}_{n'_s\eta'}\mathrm{e}^{\mathrm{i}k^+_{n'_s\eta'}L_{S_2}}r_2^2=\sum_{s=-\infty}^{+\infty}\sum_{\beta=0}^{+\infty}\left(T^{(A_2)}_{n_s\beta}+R^{(A_2)}_{n_s\beta}\mathrm{e}^{-\mathrm{i}k^-_{n_s\beta}d_2}\right)\mathcal{X}^{n'_s\eta'[T]}_{n_s\beta}\delta_{s's}}\tag{2.75}$$

#### 2.3.3.8 Matching equations at the interface $x = x_8$

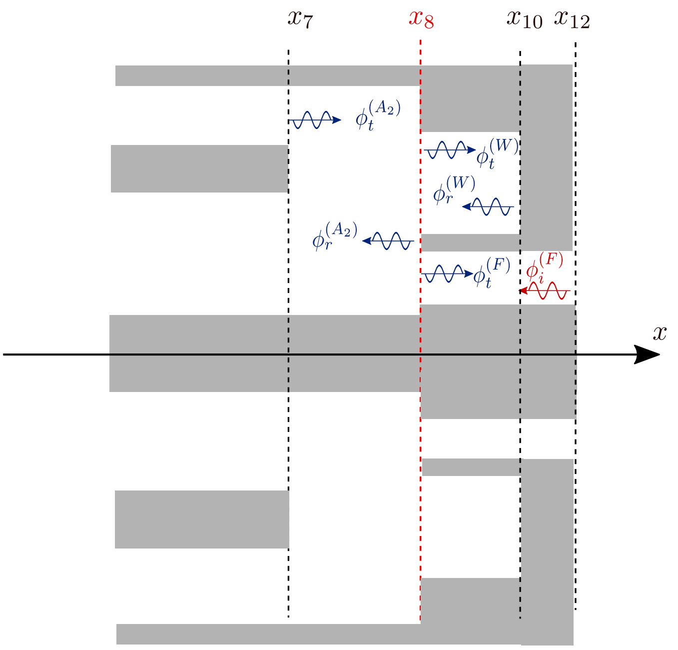

**Figure 2.18:** Scattering of the sound field at the matching interface $x_8$

The continuity of the sound field at the interface $x_8$ (see Figure 2.18) can be written as

$$\begin{cases} \mathbf{\Xi_t^{(A_2)}} + \mathbf{\Xi_r^{(A_2)}} = \mathbf{\Xi_t^{(W)}} + \mathbf{\Xi_r^{(W)}}, \quad x = x_8, \quad \forall\theta, \quad r \in [r_{f_2}; r_{f_3}] & (2.76a) \\ \mathbf{\Xi_t^{(A_2)}} + \mathbf{\Xi_r^{(A_2)}} = \mathbf{\Xi_t^{(F)}} + \mathbf{\Xi_i^{(F)}}, \quad x = x_8, \quad \forall\theta, \quad r \in [r_{f_0}; r_{f_1}] & (2.76b) \\ v_t^{(A_1)} \cdot \mathbf{e_x} + v_r^{(A_1)} \cdot \mathbf{e_x} = 0, \quad x = x_8, \quad \forall\theta, \quad r \in ]r_1; r_{f_0}[ \cup ]r_{f_1}; r_{f_2}[ \cup ]r_{f_3}; r_2] & (2.76c) \end{cases}$$

The system of equations obtained after projecting Equations 2.76a, 2.76b and 2.76c on the different eigenfunctions, is given by:

$$\boxed{\begin{aligned} & k^+_{n'_s\beta'} T^{(A_2)}_{n'_s\beta'} \mathrm{e}^{\mathrm{i}k^+_{n'_s\beta'} d_2} r_2^2 + k^-_{n'_s\beta'} R^{(A_2)}_{n'_s\beta'} r_2^2 \\ & \qquad = \sum_{s=-\infty}^{+\infty} \sum_{\mu=0}^{+\infty} \left( k^+_{n_s w} T^{(W)}_{n_s w} + k^-_{n_s w} R^{(W)}_{n_s w} \mathrm{e}^{-\mathrm{i}k^-_{n_s w} L_W} \right) \mathcal{B}^{n'_s\beta'}_{n_s w} \delta_{s's} \\ & \qquad\qquad + \sum_{s=-\infty}^{+\infty} \sum_{\nu=0}^{+\infty} k^+_{n_s\alpha} T^{(F)}_{n_s\mu} \mathcal{O}^{n'_s\beta'}_{n_s\alpha} \delta_{ss'} + k^-_{nj} A^{(F)}_{nj} \mathrm{e}^{\mathrm{i}k^-_{nj} L_F} \mathcal{O}^{n'_s\beta'}_{nj} \delta_{ss'} \end{aligned}} \tag{2.77}$$

$$\boxed{\sum_{s=-\infty}^{+\infty} \sum_{\beta=0}^{+\infty} \left( T^{(A_2)}_{n_s\beta} \mathrm{e}^{\mathrm{i}k^+_{n_s\beta} d_2} + R^{(A_2)}_{n_s\beta} \right) \mathcal{B}^{n'_s w' [T]}_{n_s\beta} \delta_{s's} = T^{(W)}_{n'_s w'} r_{f_3}^2 + R^{(W)}_{n'_s w'} \mathrm{e}^{-\mathrm{i}k^-_{n'_s w'} L_W} r_{f_3}^2} \tag{2.78}$$

$$\boxed{\sum_{s=-\infty}^{+\infty} \sum_{\beta=0}^{+\infty} \left( T^{(A_2)}_{n_s\beta} \mathrm{e}^{\mathrm{i}k^+_{n_s\beta} d_2} + R^{(A_2)}_{n_s\beta} \right) \mathcal{O}^{n'_s \alpha' [T]}_{n_s\beta} \delta_{s's} = T^{(F)}_{n'_s \nu'} r_{f_1}^2 + A^{(F)}_{nj} \mathrm{e}^{-\mathrm{i}k^-_{nj} L_F} r_{f_1}^2 \delta_{s'0}} \tag{2.79}$$

where

$$\mathcal{B}^{n'_s\beta'}_{n_s w} = \int_{r_{f_2}}^{r_{f_3}} f^{*(A)}_{n'_s\beta'}(r) f^{(W)}_{n_s w}(r) r dr \qquad , \mathcal{B}^{n'_s w' [T]}_{n_s\beta} = \int_{r_{f_2}}^{r_{f_3}} f^{*(T)}_{n'_s\mu'}(r) f^{(A)}_{n_s w}(r) r dr$$

$$\mathcal{O}^{n'_s\beta'}_{n_s\alpha} = \int_{r_{f_0}}^{r_{f_1}} f^{*(A)}_{n'_s\beta'}(r) f^{(F)}_{n_s\alpha}(r) r dr \qquad , \mathcal{O}^{n'_s\alpha' [T]}_{n_s\beta} = \int_{f_0}^{r_{f_1}} f^{*(F)}_{n'_s\alpha'}(r) f^{(A)}_{n_s\beta}(r) r dr,$$

$$\mathcal{O}^{n'_s\beta'}_{nj} = \int_{r_{f_0}}^{r_{f_1}} f^{*(A)}_{n'_s\beta'}(r) f^{(F)}_{nj}(r) r dr$$

#### 2.3.3.9 Matching equations at the interface $x = x_{10}$

The interface $x_{10}$ consists only of a rigid wall (see Figure 2.19). Only one equation is required to determine the amplitude of the reflected field $\phi_r^{(W)}$. The hard-wall boundary condition is imposed at right wall of the motor $x_{10}$. This condition corresponds to a

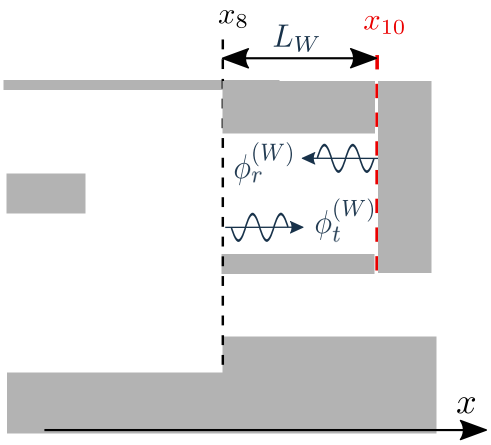

**Figure 2.19:** Scattering of the sound field at the matching interface $x_{10}$

vanishing normal velocity.

$$v_t^{(W)} \cdot \mathbf{e}_{\boldsymbol{x}} + v_r^{(W)} \cdot \mathbf{e}_{\boldsymbol{x}} = 0, \quad x = x_{10}, \quad \forall\theta, \quad r \in [r_{f_2}; r_{f_3}] \tag{2.80}$$

Multiplying this equation by $f_{n_s'w'}^{(W)}(r)\mathrm{e}^{-\mathrm{i}n_{s'}\theta}$ and integrating over the cross-section of the wall, yields

$$\boxed{k_{n_s'w'}^{+} T_{n_s'w'}^{(W)} \mathrm{e}^{\mathrm{i}k_{n_s'w'}^{+} L_W} r_{f3}^2 + k_{n_s'w'}^{-} R_{n_s'w'}^{(W)} r_{f3}^2 = 0} \tag{2.81}$$

#### 2.3.3.10 Matching equations at the interface $x = x_9$

The modal coefficients of the acoustic fields $\phi_d^{(G)}$, $\phi_d^{(R2)}$ and $\phi_t^{(R_d)}$ are determined at the interface $x_9$ (see Figure 2.20). The matching equations can be expressed as

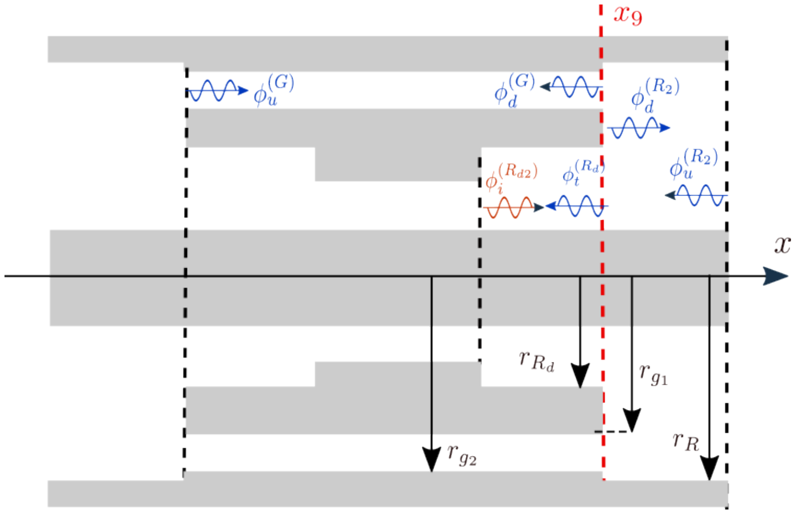

**Figure 2.20:** Scattering of the sound field at the matching interface $x_9$

$$\left\{\begin{aligned} \boldsymbol{\Xi}_{\mathbf{i}}^{(\mathbf{R_{d2}})} + \boldsymbol{\Xi}_{\mathbf{t}}^{(\mathbf{R_d})} &= \boldsymbol{\Xi}_{\mathbf{d}}^{(\mathbf{R_2})} + \boldsymbol{\Xi}_{\mathbf{u}}^{(\mathbf{R_2})}, \quad x = x_9, \quad \forall\theta, \quad r \in [r_1; r_{R_d}] && (2.82a) \\ \boldsymbol{\Xi}_{\mathbf{u}}^{(\mathbf{G})} + \boldsymbol{\Xi}_{\mathbf{d}}^{(\mathbf{G})} &= \boldsymbol{\Xi}_{\mathbf{d}}^{(\mathbf{R_2})} + \boldsymbol{\Xi}_{\mathbf{u}}^{(\mathbf{R_2})}, \quad x = x_9, \quad \forall\theta, \quad r \in [r_{g_1}; r_{g_2}] && (2.82b) \\ v_d^{(R_2)} \cdot \mathbf{e}_{\boldsymbol{x}} + v_u^{(R_2)} \cdot \mathbf{e}_{\boldsymbol{x}} = 0, &\quad x = x_9, \quad \forall\theta, \quad r \in \,]r_{R_d}; r_{g_1}[\, \cup \,]r_{g_2}; r_R] && (2.82c) \end{aligned}\right.$$

After projecting the above equations on the different modal bases and accounting for their orthogonality, one obtains

$$\boxed{\begin{aligned} &k_{nj}^{+} A_{nj}^{(R_{d2})} \mathrm{e}^{\mathrm{i}k_{nj}^{+} L_{p2}} \mathcal{F}_{nj}^{n_s'\xi'} + \sum_{s=-\infty}^{+\infty} \sum_{\gamma=0}^{+\infty} k_{n_s\gamma}^{-} T_{n_s\gamma}^{(R_d)} \mathcal{F}_{n_s\gamma}^{n_s'\xi'} \delta_{ss'} \\ &\qquad + \sum_{s=-\infty}^{+\infty} \sum_{g=0}^{+\infty} \left( k_{n_sg}^{-} D_{n_sg}^{(G)} + k_{n_sg}^{+} U_{n_sg}^{(G)} \mathrm{e}^{\mathrm{i}k_{n_sg}^{+} L_G} \right) \mathcal{W}_{n_sg}^{n_s'\xi'} \delta_{ss'} \\ &\qquad\qquad = k_{n_s'\xi'}^{+} D_{n_s'\xi'}^{(R_2)} r_R^2 + k_{n_s'\xi'}^{+} U_{n_s'\xi'}^{(R_2)} \mathrm{e}^{-\mathrm{i}k_{n_s'\xi'}^{-} L_{R_2}} r_R^2 \end{aligned}} \tag{2.83}$$

$$\boxed{\begin{aligned} &A_{nj}^{(R_{d2})} \mathrm{e}^{\mathrm{i}k_{nj}^{+} L_{p2}} \delta_{\gamma' j} r_{R_d}^2 + U_{n_s'\gamma'}^{(R_d)} r_{R_d}^2 \\ &\qquad = \sum_{s=-\infty}^{+\infty} \sum_{\xi=0}^{+\infty} \left( D_{n_s\xi}^{(R_2)} + U_{n_s\xi}^{(R_2)} \mathrm{e}^{-\mathrm{i}k_{n_s\xi}^{-} L_{R_2}} \right) \mathcal{F}_{n_s\xi}^{n_s'\gamma'[T]} \delta_{ss'} \end{aligned}} \tag{2.84}$$

$$\boxed{D_{n_s'g'}^{(G)} r_{g_2}^2 + U_{n_s'g'}^{(G)} \mathrm{e}^{\mathrm{i}k_{n_s'g'}^{+} L_G} r_{g_2}^2 = \sum_{s=-\infty}^{+\infty} \sum_{\xi=0}^{+\infty} \left( D_{n_s\xi}^{(R_2)} + U_{n_s\xi}^{(R_2)} \mathrm{e}^{-\mathrm{i}k_{n_s\xi}^{-} L_{R_2}} \right) \mathcal{W}_{n_s\xi}^{n_s'g'[T]} \delta_{ss'}} \tag{2.85}$$

## 2.3.4 Solving procedure

The system of linear equations obtained after the projection of the matching equations can be solved either by a direct method or an iterative method. In the direct method, the 26 matching equations are written in a matrix form $\underline{\boldsymbol{\mathcal{M}}}\mathbf{X} = \boldsymbol{\mathcal{N}}$, where $\mathbf{X}$ represents the modal coefficients vector. The determination of the latter is achieved by a direct matrix inversion $\mathbf{X} = \underline{\boldsymbol{\mathcal{M}}}^{-1}\boldsymbol{\mathcal{N}}$. It should be kept in mind that the use of this technique can lead to some problems related to the conditioning of the global matrix $\underline{\boldsymbol{\mathcal{M}}}$ when the number of modes increases. In order to avoid this problem, the two solving procedures are used in this section. In the first step, the system composed of 26 equations is divided into two sub-systems consisting of 14 and 12 equations $\underline{\boldsymbol{\mathcal{C}}}\mathbf{X_1} = \boldsymbol{\mathcal{V}}$ and $\underline{\boldsymbol{\mathcal{H}}}\mathbf{X_2} = \boldsymbol{\mathcal{S}}$, in which the direct method can be applied. These sets of equations correspond respectively to the blocks 1 and 2 of the stationary part of the ventilation system (see Figure 2.10). The iterative method can finally be used to couple the two sub-systems of linear equations, by taking the outputs of one block as inputs for the other one.

### 2.3.4.1 System of linear equations related to the block 1

The block 1 in Figure 2.10 contains all the interfaces located in the left-hand side of the fixed part: $x_1$, $x_2$, $x_3$, $x_4$ and $x_5$. The matrix $\underline{\boldsymbol{\mathcal{C}}}$, the vector $\boldsymbol{\mathcal{S}}$ and the modal amplitudes vector $\boldsymbol{X_1}$ are built up from Equations 2.45, 2.46, 2.47, 2.49, 2.50, 2.51, 2.53, 2.54, 2.55, 2.57, 2.58, 2.59, 2.65 and 2.66.

$$\underline{\boldsymbol{\mathcal{C}}}\mathbf{X_1} = \boldsymbol{\mathcal{V}} \tag{2.86}$$

with

$$\underline{\boldsymbol{\mathcal{C}}} = \begin{pmatrix}
\boldsymbol{\mathcal{C}}_1^1 & \boldsymbol{\mathcal{C}}_1^2 & \boldsymbol{\mathcal{C}}_1^3 & \boldsymbol{\mathcal{C}}_1^4 & 0 & 0 & 0 & 0 & 0 & 0 & 0 & 0 & 0 & 0 \\
\boldsymbol{\mathcal{C}}_2^1 & 0 & \boldsymbol{\mathcal{C}}_2^3 & \boldsymbol{\mathcal{C}}_2^4 & 0 & 0 & 0 & 0 & 0 & 0 & 0 & 0 & 0 & 0 \\
0 & \boldsymbol{\mathcal{C}}_3^2 & \boldsymbol{\mathcal{C}}_3^3 & \boldsymbol{\mathcal{C}}_3^4 & 0 & 0 & 0 & 0 & 0 & 0 & 0 & 0 & 0 & 0 \\
0 & 0 & \boldsymbol{\mathcal{C}}_4^3 & \boldsymbol{\mathcal{C}}_4^4 & \boldsymbol{\mathcal{C}}_4^5 & \boldsymbol{\mathcal{C}}_4^6 & \boldsymbol{\mathcal{C}}_4^7 & \boldsymbol{\mathcal{C}}_4^8 & 0 & 0 & 0 & 0 & 0 & 0 \\
0 & 0 & \boldsymbol{\mathcal{C}}_5^3 & \boldsymbol{\mathcal{C}}_5^4 & 0 & 0 & \boldsymbol{\mathcal{C}}_5^7 & \boldsymbol{\mathcal{C}}_5^8 & 0 & 0 & 0 & 0 & 0 & 0 \\
0 & 0 & 0 & 0 & \boldsymbol{\mathcal{C}}_6^5 & \boldsymbol{\mathcal{C}}_6^6 & \boldsymbol{\mathcal{C}}_6^7 & \boldsymbol{\mathcal{C}}_6^8 & 0 & 0 & 0 & 0 & 0 & 0 \\
0 & 0 & 0 & 0 & 0 & 0 & \boldsymbol{\mathcal{C}}_7^7 & \boldsymbol{\mathcal{C}}_7^8 & \boldsymbol{\mathcal{C}}_7^9 & \boldsymbol{\mathcal{C}}_7^{10} & \boldsymbol{\mathcal{C}}_7^{11} & \boldsymbol{\mathcal{C}}_7^{12} & 0 & 0 \\
0 & 0 & 0 & 0 & 0 & 0 & \boldsymbol{\mathcal{C}}_8^7 & \boldsymbol{\mathcal{C}}_8^8 & \boldsymbol{\mathcal{C}}_8^9 & \boldsymbol{\mathcal{C}}_8^{10} & 0 & 0 & 0 & 0 \\
0 & 0 & 0 & 0 & 0 & 0 & \boldsymbol{\mathcal{C}}_9^7 & \boldsymbol{\mathcal{C}}_9^8 & 0 & 0 & \boldsymbol{\mathcal{C}}_9^{11} & \boldsymbol{\mathcal{C}}_9^{12} & 0 & 0 \\
0 & 0 & 0 & 0 & 0 & 0 & 0 & 0 & \boldsymbol{\mathcal{C}}_{10}^9 & \boldsymbol{\mathcal{C}}_{10}^{10} & \boldsymbol{\mathcal{C}}_{10}^{11} & \boldsymbol{\mathcal{C}}_{10}^{12} & \boldsymbol{\mathcal{C}}_{10}^{13} & 0 \\
0 & 0 & 0 & 0 & 0 & 0 & 0 & 0 & \boldsymbol{\mathcal{C}}_{11}^9 & \boldsymbol{\mathcal{C}}_{11}^{10} & 0 & 0 & \boldsymbol{\mathcal{C}}_{11}^{13} & 0 \\
0 & 0 & 0 & 0 & 0 & 0 & 0 & 0 & 0 & 0 & \boldsymbol{\mathcal{C}}_{12}^{11} & \boldsymbol{\mathcal{C}}_{12}^{12} & \boldsymbol{\mathcal{C}}_{12}^{13} & 0 \\
0 & 0 & 0 & 0 & \boldsymbol{\mathcal{C}}_{13}^5 & \boldsymbol{\mathcal{C}}_{13}^6 & 0 & 0 & 0 & 0 & 0 & 0 & 0 & \boldsymbol{\mathcal{C}}_{13}^{14} \\
0 & 0 & 0 & 0 & \boldsymbol{\mathcal{C}}_{14}^5 & \boldsymbol{\mathcal{C}}_{14}^6 & 0 & 0 & 0 & 0 & 0 & 0 & 0 & \boldsymbol{\mathcal{C}}_{14}^{14}
\end{pmatrix}$$

$$\boldsymbol{X_1} = \left\{\boldsymbol{U^{R_d}}, \boldsymbol{U^{G}}, \boldsymbol{D^{R_1}}, \boldsymbol{U^{R_1}}, \boldsymbol{U^{S_1}}, \boldsymbol{R^{S_1}}, \boldsymbol{T^{A_1}}, \boldsymbol{R^{A_1}}, \boldsymbol{D^{T}}, \boldsymbol{U^{T}}, \boldsymbol{D^{B}}, \boldsymbol{U^{B}}, \boldsymbol{T^{E}}, \boldsymbol{D^{S_d}}\right\}$$

$$\boldsymbol{\mathcal{V}} = \{\boldsymbol{\mathcal{V}_1}, \boldsymbol{\mathcal{V}_2}, 0, 0, 0, 0, 0, 0, 0, 0, 0, 0, \boldsymbol{\mathcal{V}_{13}}, \boldsymbol{\mathcal{V}_{14}}\}$$

The matrix $\underline{\boldsymbol{\mathcal{C}}}$ and the vector $\boldsymbol{\mathcal{V}}$ terms are given in Appendix A.1. Thus, the modal amplitudes vector is found by a direct matrix inversion $\boldsymbol{X_1} = \underline{\boldsymbol{\mathcal{C}}}^{-1}\boldsymbol{\mathcal{V}}$.

#### 2.3.4.2 System of linear equations related to the block 2

The second block in Figure 2.10 corresponds to all the interfaces located in the right side of the ventilation system : $x_6$, $x_7$, $x_8$, $x_9$ and $x_{10}$. In the same way, Equations 2.70, 2.71, 2.73, 2.74, 2.75, 2.77, 2.78, 2.79, 2.81, 2.83, 2.84 and 2.85 are written in a matrix form

$$\underline{\boldsymbol{\mathcal{H}}}\mathbf{X_2} = \boldsymbol{\mathcal{S}} \tag{2.87}$$

with

$$\underline{\boldsymbol{\mathcal{H}}} = \begin{pmatrix}
\boldsymbol{\mathcal{H}_1^1} & \boldsymbol{\mathcal{H}_1^2} & \boldsymbol{\mathcal{H}_1^3} & \boldsymbol{\mathcal{H}_1^4} & 0 & 0 & 0 & 0 & 0 & 0 & 0 & 0 \\
\boldsymbol{\mathcal{H}_2^1} & 0 & \boldsymbol{\mathcal{H}_2^3} & \boldsymbol{\mathcal{H}_2^4} & 0 & 0 & 0 & 0 & 0 & 0 & 0 & 0 \\
0 & \boldsymbol{\mathcal{H}_3^2} & \boldsymbol{\mathcal{H}_3^3} & \boldsymbol{\mathcal{H}_3^4} & 0 & 0 & 0 & 0 & 0 & 0 & 0 & 0 \\
0 & 0 & \boldsymbol{\mathcal{H}_4^3} & \boldsymbol{\mathcal{H}_4^4} & \boldsymbol{\mathcal{H}_4^5} & \boldsymbol{\mathcal{H}_4^6} & \boldsymbol{\mathcal{H}_4^7} & \boldsymbol{\mathcal{H}_4^8} & 0 & 0 & 0 & 0 \\
0 & 0 & \boldsymbol{\mathcal{H}_5^3} & \boldsymbol{\mathcal{H}_5^4} & 0 & 0 & \boldsymbol{\mathcal{H}_5^7} & \boldsymbol{\mathcal{H}_5^8} & 0 & 0 & 0 & 0 \\
0 & 0 & 0 & 0 & \boldsymbol{\mathcal{H}_6^5} & \boldsymbol{\mathcal{H}_6^6} & \boldsymbol{\mathcal{H}_6^7} & \boldsymbol{\mathcal{H}_6^8} & 0 & 0 & 0 & 0 \\
0 & 0 & 0 & 0 & 0 & 0 & \boldsymbol{\mathcal{H}_7^7} & \boldsymbol{\mathcal{H}_7^8} & \boldsymbol{\mathcal{H}_7^9} & \boldsymbol{\mathcal{H}_7^{10}} & \boldsymbol{\mathcal{H}_7^{11}} & 0 \\
0 & 0 & 0 & 0 & 0 & 0 & \boldsymbol{\mathcal{H}_8^7} & \boldsymbol{\mathcal{H}_8^8} & \boldsymbol{\mathcal{H}_8^9} & \boldsymbol{\mathcal{H}_8^{10}} & 0 & 0 \\
0 & 0 & 0 & 0 & 0 & 0 & \boldsymbol{\mathcal{H}_9^7} & \boldsymbol{\mathcal{H}_9^8} & 0 & 0 & \boldsymbol{\mathcal{H}_9^{11}} & 0 \\
0 & 0 & 0 & 0 & 0 & 0 & 0 & 0 & \boldsymbol{\mathcal{H}_{10}^9} & \boldsymbol{\mathcal{H}_{10}^{10}} & 0 & 0 \\
0 & 0 & 0 & 0 & \boldsymbol{\mathcal{H}_{11}^5} & \boldsymbol{\mathcal{H}_{11}^6} & 0 & 0 & 0 & 0 & 0 & \boldsymbol{\mathcal{H}_{11}^{12}} \\
0 & 0 & 0 & 0 & \boldsymbol{\mathcal{H}_{12}^5} & \boldsymbol{\mathcal{H}_{12}^6} & 0 & 0 & 0 & 0 & 0 & \boldsymbol{\mathcal{H}_{12}^{12}}
\end{pmatrix}$$

$$\boldsymbol{X_2} = \left\{\boldsymbol{U^{R_{d2}}}, \boldsymbol{D^{G}}, \boldsymbol{D^{R_2}}, \boldsymbol{U^{R_2}}, \boldsymbol{U^{S_2}}, \boldsymbol{T^{S_2}}, \boldsymbol{T^{A_2}}, \boldsymbol{R^{A_2}}, \boldsymbol{T^{W}}, \boldsymbol{R^{W}}, \boldsymbol{T^{F}}, \boldsymbol{U^{S_d}}\right\}$$

$$\boldsymbol{S} = \{\boldsymbol{\mathcal{S}_1}, \boldsymbol{\mathcal{S}_2}, 0, 0, 0, 0, 0, 0, 0, 0, \boldsymbol{\mathcal{S}_{11}}, \boldsymbol{\mathcal{S}_{12}}\}$$

The matrix $\underline{\boldsymbol{\mathcal{H}}}$ and the vector $\boldsymbol{\mathcal{S}}$ terms are given in Appendix A.2. The modal coefficients vector $\mathbf{X_2}$ is obtained by a direct matrix inversion $\boldsymbol{X_2} = \underline{\boldsymbol{\mathcal{H}}}^{-1}\boldsymbol{\mathcal{S}}$.

#### 2.3.4.3 Coupling strategy

The next step consists in coupling the two sub-systems of linear equations 2.86 and 2.87 together to determine the modal amplitudes of the different acoustic fields. It is clear that the solving of Equation 2.86 requires prior knowledge of the modal coefficients $\mathbf{U^G}$ and $\mathbf{U^{S_d}}$ stored in vector $\boldsymbol{\mathcal{V}}$, and solving Equation 2.87 also requires prior knowledge of the coefficients $\mathbf{D^G}$ and $\mathbf{D^{S_d}}$ stored in the vector $\boldsymbol{\mathcal{S}}$. To solve this problem, it is necessary to use an iterative procedure to account for the multiple reflections of the acoustic waves in the air gap and inside the stator cooling channels. For the initialization step of the iterative procedure $g = 0$ , the modal amplitudes of the acoustic waves propagating inside the stator cooling channels and the air gap are considered to be zero ($\mathbf{U^{S_d(g=0)}} = \mathbf{U^{G(g=0)}} = \mathbf{D^{S_d(g=0)}} = \mathbf{D_G^{(g=0)}} = 0$). Therefore, solving Equation 2.86 allows one to determine the modal amplitudes of the fields $D^{S_d(g=0)}$ and $D_G^{(g=0)}$. These are used in Equation 2.87 to compute the new values of $\mathbf{U^{S_d(g=1)}}$ and $\mathbf{U_G^{(g=1)}}$. This procedure must be repeated until convergence.

It is important to note here that the matrices $\underline{\boldsymbol{\mathcal{C}}}$ and $\underline{\boldsymbol{\mathcal{H}}}$ depend only on the transverse dimensions of the geometry, the number of stator ducts and the modal order of the incident wave $n$. In practice, these matrices must be calculated only once, when several frequencies or lengths need to be tested. Therefore, a parametric study on the transverse dimensions is more expensive than a parametric study on the longitudinal dimensions. This augmentation in computational time is explained by the fact that the radial wavenumbers and the modal projections are computed each time the transverse dimensions change. Furthermore, the size of the matrices increases drastically with the number of modes. In order to optimize the memory storage, the matrices $\underline{\boldsymbol{\mathcal{C}}}$ and $\underline{\boldsymbol{\mathcal{H}}}$ can be declared as sparse matrices in the `MATLAB` code, using the intrinsic function "`sparse()`".

#### 2.3.4.4 Number of modes

As what has been discussed in Chapter 1, the infinite sets of linear equations must be truncated in order to have a finite number of modes. The latter depends on both radial and azimuthal dimensions of each subsystem. The numbers of radial modes needed in each subdomain are given by

$$N_\xi \approx \frac{r_R - r_1}{r_{R_d} - r_1} N_\gamma + 1, \quad N_g \approx \frac{r_{g_2} - r_{g_1}}{r_{R_d} - r_1} N_\gamma + 1, \quad N_\beta \approx \frac{r_2 - r_1}{r_{R_d} - r_1} N_\gamma + 1$$

$$N_m \approx \frac{r_{e2} - r_{e1}}{r_{R_d} - r_1} N_\gamma + 1, \quad N_w \approx \frac{r_{f_2} - r_{f_3}}{r_{R_d} - r_1} N_\gamma + 1, \quad N_\alpha \approx \frac{r_2 - r_1}{r_{R_d} - r_1} N_\gamma + 1$$

$$N_\alpha \approx \frac{r_{f0} - r_{f1}}{r_{R_d} - r_1} N_\gamma + 1, \quad N_\nu \approx \frac{r_{w_2} - r_{d_1}}{r_{R_d} - r_1} N_\gamma + 1, \quad N_\mu \approx \frac{r_{d_2} - r_{w_3}}{r_{R_d} - r_1} N_\gamma + 1$$

The number of azimuthal modes required inside stator channels, is given by

$$N_q \approx \frac{\theta_a}{2\pi/V}(2N_s + 1)$$

### 2.3.5 Numerical validation

In order to assess the relevance of the analytical model, a comparison with the finite element method has been performed. As a first step, both methods are applied to a simplified configuration of an open motor for mathematical validation. Consider a test-case of a ventilation system consisting of 18 stator cooling channels. The transverse and the longitudinal dimensions of the ventilation system are listed in Table 2.1. In this test-case, an incident mode of order $(n = 2, j = 0)$ and amplitude $A_{nj}^{(F)} = 1$ is imposed in the annular duct located upstream the radial impeller $(F)$ at a frequency $f = 3500$ Hz. Note here that the incident waves generated by the rotor ducts are not considered in this specific test-case $(A_{nj}^{(R_{d1})} = A_{nj}^{(R_{d2})} = 0$ and $A_{nj}^{(F)} = 1)$.

| $r_1$ | $r_{R_d}$ | $r_{g1}$ | $r_{g2}$ | $r_R$ | $r_S$ | $r_{w2}$ | $r_{d1}$ | $r_{d2}$ | $r_{w3}$ | $r_{e1}$ | $r_{e2}$ |
|---|---|---|---|---|---|---|---|---|---|---|---|
| 0.065 | 0.09 | 0.14 | 0.145 | 0.16 | 0.21 | 0.18 | 0.20 | 0.22 | 0.25 | 0.10 | 0.30 |
| $r_2$ | $r_{f_0}$ | $r_{f_1}$ | $r_{f_2}$ | $r_{f_3}$ | $r_{S_{d1}}$ | $r_{S_{d2}}$ | $V$ | $\theta_a V/2\pi$ | | | |
| 0.28 | 0.09 | 0.13 | 0.145 | 0.24 | 0.245 | 0.265 | 18 | 0.7 | | | |
| $L_{P_1}$ | $L_{P_2}$ | $d_1$ | $d_2$ | $L_{S_1}$ | $L_{S_2}$ | $L_{S_d}$ | $L_D$ | $L_W$ | $L_F$ | $L_G$ | $L_E$ |
| 0.03 | 0.03 | 0.1 | 0.1 | 0.15 | 0.15 | 0.35 | 0.05 | 0.07 | 0.095 | 0.38 | 0.15 |

**Table 2.1:** Dimensions of the ventilation system used in the test case.

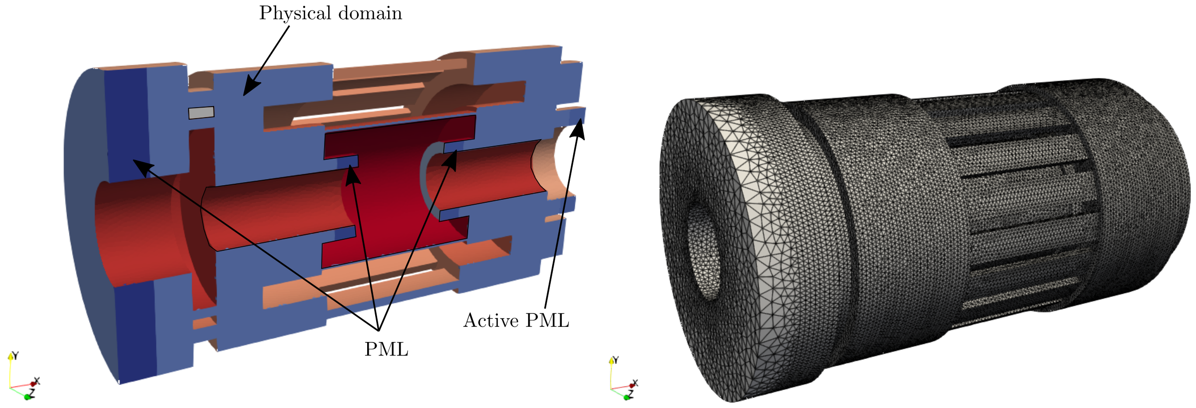

(a)

(b)

**Figure 2.21:** (a) Different regions of the finite element simulation, (b) Finite element mesh

For the same reasons mentioned in Chapter 1, the computational domain used in the finite element method needs to be divided into 5 different regions, as illustrated in Figure 2.21a:

- The physical domain $\Omega_{\text{phy}}$, in which the solution of the problem must be found.
- Three perfectly matched layers (PML) denoted by $\Omega^1_{\text{pml}}$, $\Omega^2_{\text{pml}}$ and $\Omega^3_{\text{pml}}$ to absorb all the acoustic waves coming from the physical domain $\Omega_{\text{phy}}$ and avoid their reflection.
- An active perfectly matched layer $\Omega^4_{\text{pml}}$ in which the incident wave must be imposed without being attenuated.

The variational formulation of the Helmholtz equation is described in a three-dimensional cartesian coordinate system (see Appendix B). As before, the problem is solved by using the open source solver `FreeFem++`. It is important to note that the corresponding finite element mesh is composed of about $8.10^5$ tetrahedral elements, as illustrated in Figure 2.21b. At this frequency, the use of a second-order interpolation is necessary to obtain the desired precision. The acoustic potential field calculated by the finite element method is shown in Figure 2.22. This was obtained after about 20 minutes of calculation on a personal computer with a single core. Before comparing the results obtained by the two methods, a convergence study on the number of iterations has been carried out, by estimating that the results of the analytical model are converged when the relative variation of the modal amplitudes between two successive iterations is less than $\epsilon_{max} \approx 10^{-3}$. The variations of the modal amplitudes of the downstream and upstream propagating waves

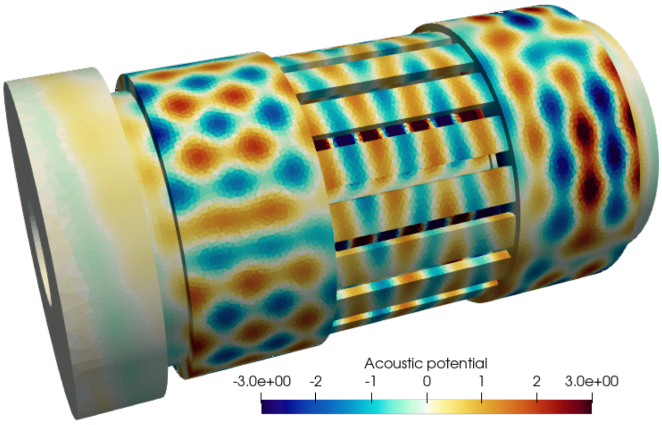

**Figure 2.22:** Acoustic potential field obtained by the finite element method. $f$ = 3500 Hz, n=2, j=0

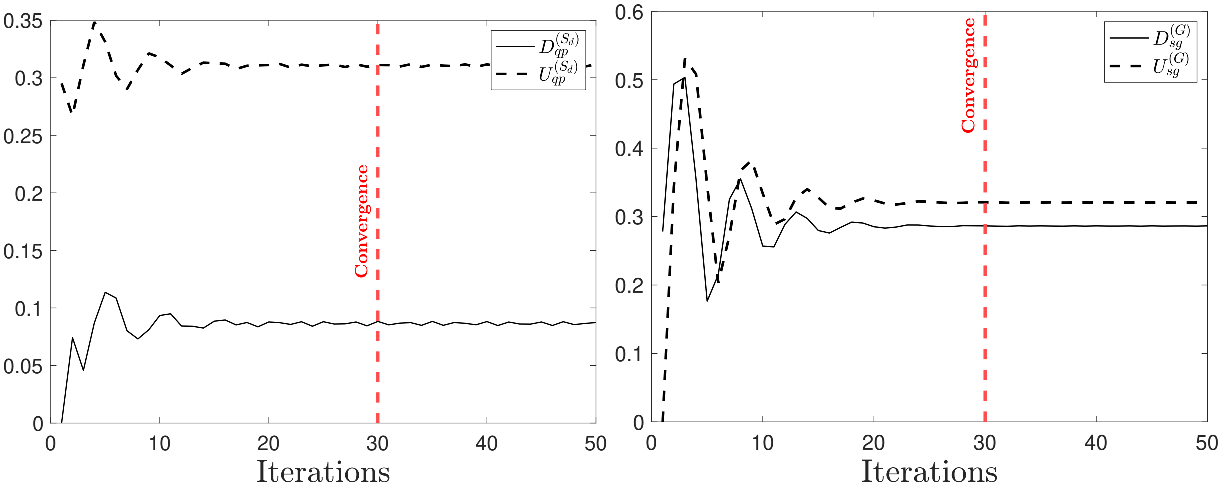

**(a)** **(b)**

**Figure 2.23:** Modal amplitudes of the upstream and downstream propagating acoustic modes in the air gap (a) and inside the stator cooling channels (b) as functions of the number of iterations.

in the air gap and inside the stator channels as functions of the number of iterations are shown in Figure 2.23. It is found that the convergence is reached after only 30 iterations. The instantaneous acoustic potential fields obtained by the mode-matching technique and the finite element method are first illustrated by a meridian cut at a constant angle ($\theta = 0$ in the upper region $r/r_2 > 0$ and $\theta = \pi$ in the lower region $r/r_2 < 0$) in Figures 2.24a and 2.24b respectively. Qualitatively, a very good agreement is found between the two results. This meridian cut shows clearly the radial variations of the sound field in the

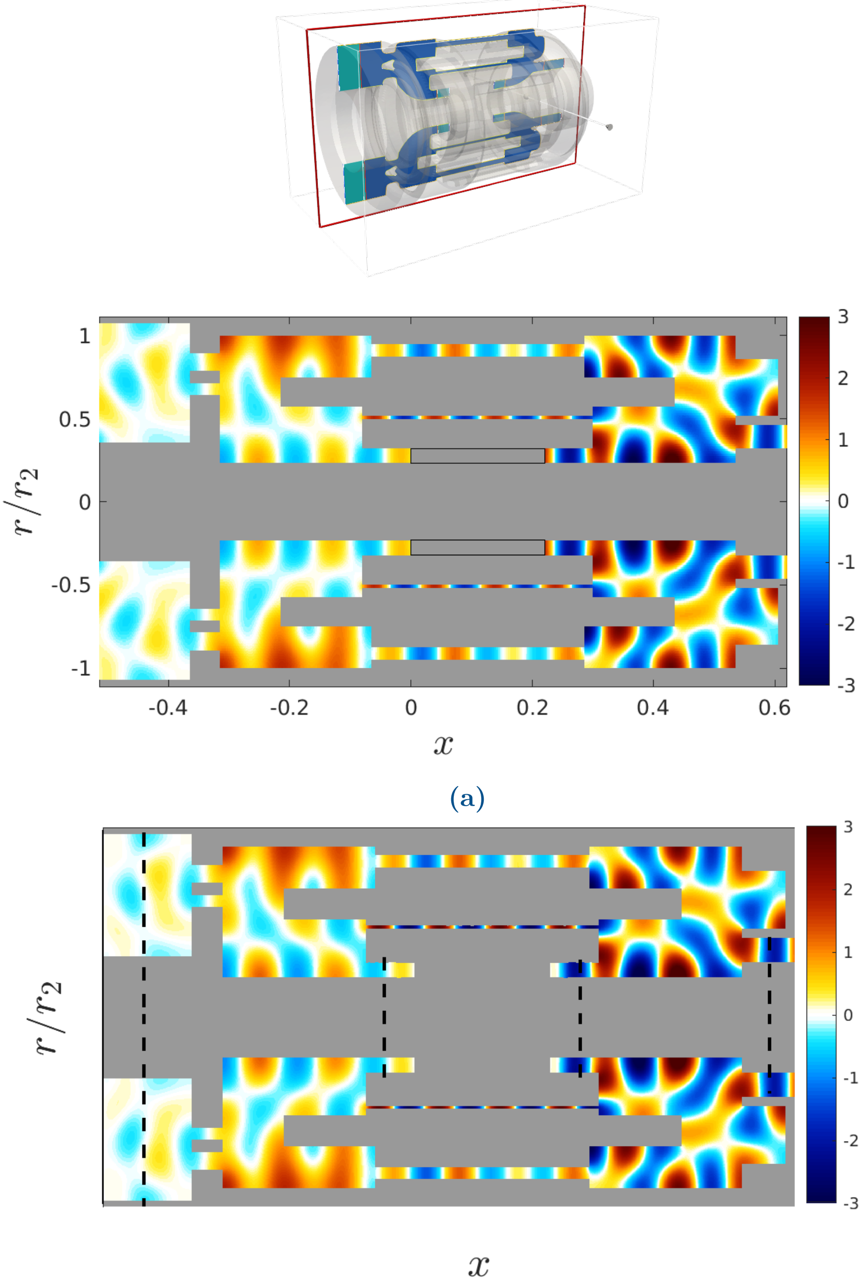

(a)

(b)

**Figure 2.24:** Meridian cut of the instantaneous acoustic potential field at $\theta = 0$. Mode-matching technique (a). Finite element method (b). Physical domain limits (- - - -) . $n = 2$, $f = 3500$.

ventilation system, due to the propagation of several radial higher-order modes generated by the diffraction of the incident wave. On the other hand, a continuity of the sound field is observed at all the interfaces located between the different sub-domains defined in the analytical model (see Figure 2.24a). Note here that the use of a large number of cut-off modes is necessary to ensure this continuity. Figure 2.25 shows axial cuts of the instantaneous acoustic potential fields obtained by the mode-matching technique (Figures 2.25a, 2.25b and 2.25c) and the finite element method (Figures 2.25d, 2.25e and 2.25f) at three

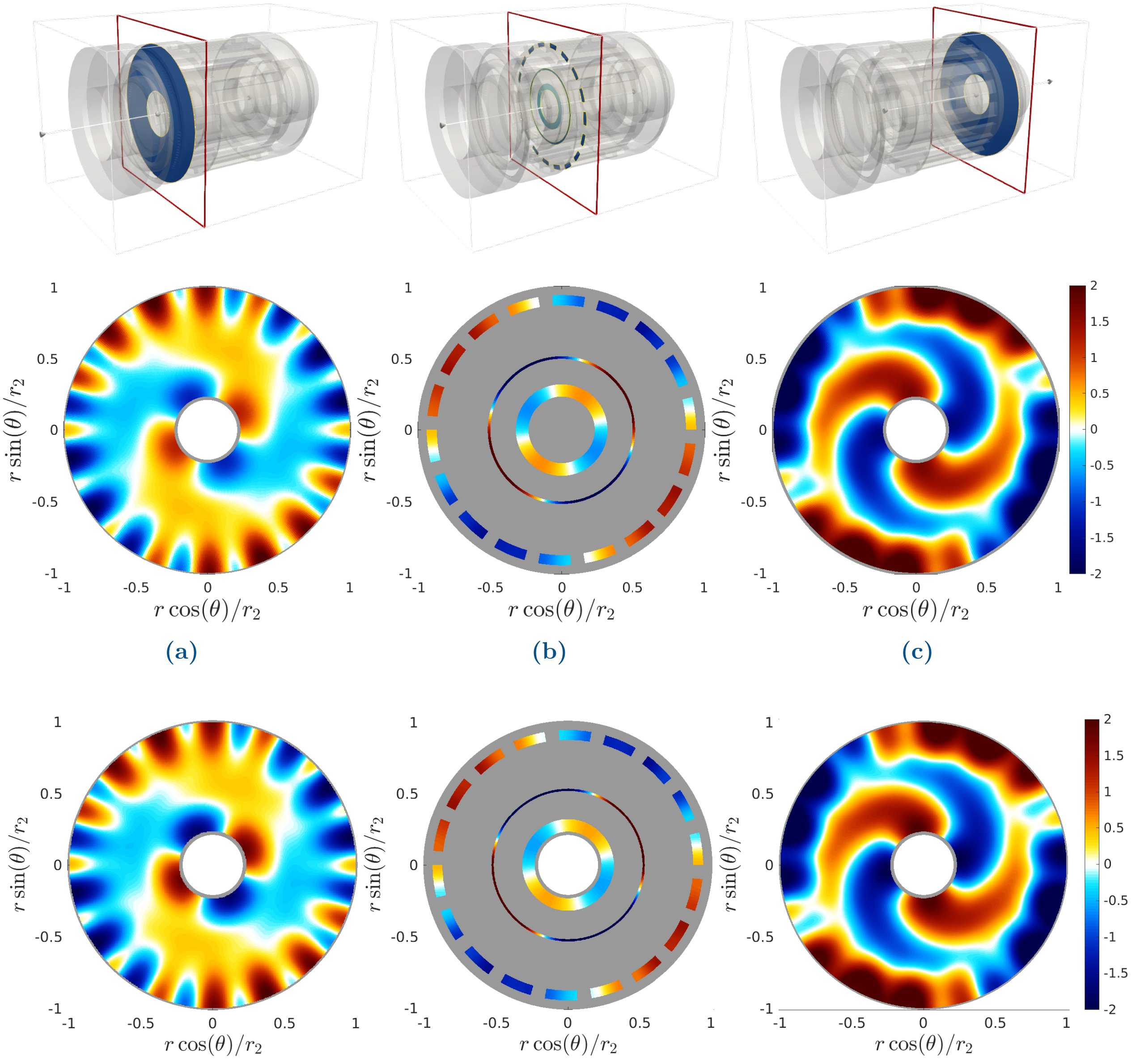

(a) (b) (c)

(d) (e) (f)

**Figure 2.25:** Instantaneous acoustic potential fields obtained by the mode-matching technique (a-b-c) and the finite element method (d-e-f). Axial cut at $x = 0$ (a-d), axial cut at $x = (x_2 + x_3)/2$ (b-e), axial cut at $x = (x_7 + x_8)/2$ (c-f). $f = 3500$ Hz, $n = 2$.

different axial positions $x = (x_2 + x_3)/2$ (Figures 2.25a and 2.25d), $x = -0.05$m (Figures 2.25a and 2.25d) and $x = (x_7 + x_8)/2$ (Figures 2.25a and 2.25d). There is obviously a perfect agreement between the results obtained by the two methods. The moduli of the complex-valued modal coefficients of the different acoustic fields illustrated in Figures 2.25a, 2.25b and 2.25c are shown in Figure 2.26. Figures 2.26e and 2.26f indicate that

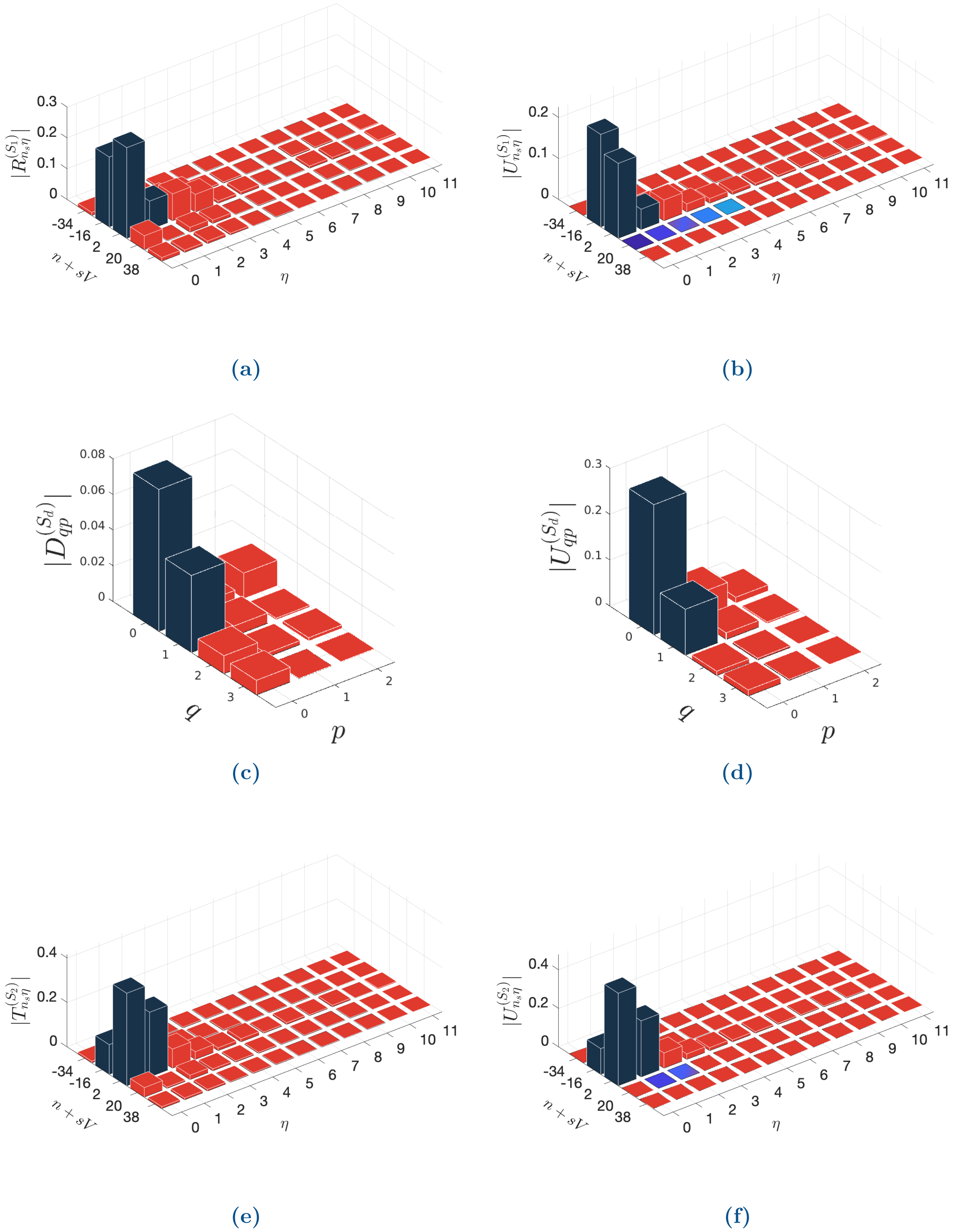

(a) (b) (c) (d) (e) (f)

**Figure 2.26:** Modal amplitudes of the different acoustic fields. (a) $R_{s\eta}^{(S_1)}$, (b) $U_{s\eta}^{(S_1)}$, (c) $D_{qp}^{(S_d)}$, (d) $U_{qp}^{(S_d)}$, (e) $T_{s\eta}^{(S_2)}$, (f) $U_{s\eta}^{(S_2)}$, Cut-off modes (bars 🟥 ), Cut-on modes (bars ■ ).

upstream of the stator channels (see Figure 2.25c), the sound field is dominated by the modes $(2, 0)$, $(2, 1)$, and slightly modulated by the mode $(-16, 0)$. Note here that the 16 azimuthal lobes of the latter are rotating clockwise. However, this mode is generated by the diffraction of the azimuthal mode $n = 2$ by the stator channels, as expected from the equation $n_s = n + sV = 2 + s18 = -16$. The effect of the latter seems to be significant downstream of the stator channels (see Figures 2.26a and 2.26b). Typically, the acoustic field is dominated by the mode $(-16, 0)$ near the outer wall of the duct, and by the modes $(2, 0)$ and $(2, 1)$ near the inner wall of the duct (see Figures 2.25a and 2.25d).

It may be observed from Figures 2.25b and 2.25e that the sound field distribution inside the stator channels is not homogeneous. This is explained by the propagation of two cut-on modes $(0, 0)$ and $(1, 0)$ inside each channel, as indicated in Figures 2.26c and 2.26d. In the same way, to illustrate the variation of the acoustic field in the azimuthal direction, cylindrical cuts have been made at three different radii. These have been taken at the center of the stator channels $r = 0.5(r_{S_{d1}} + r_{S_{d2}})$, the air gap $r = 0.5(r_{g_1} + r_{g_2})$ and the rotor annular duct $r = 0.5(r_1 + r_{R_d})$. Their unwrapped representations are respectively illustrated in Figures 2.27a, 2.27b and 2.27c. As can be seen, the mode $n_s = -16$ can only propagate in the region located near the outer wall of the duct (see Figure 2.27a), and only the mode $n_s = 2$ can be transmitted into the air gap (Figure 2.27b) and the rotor (Figure 2.27c).

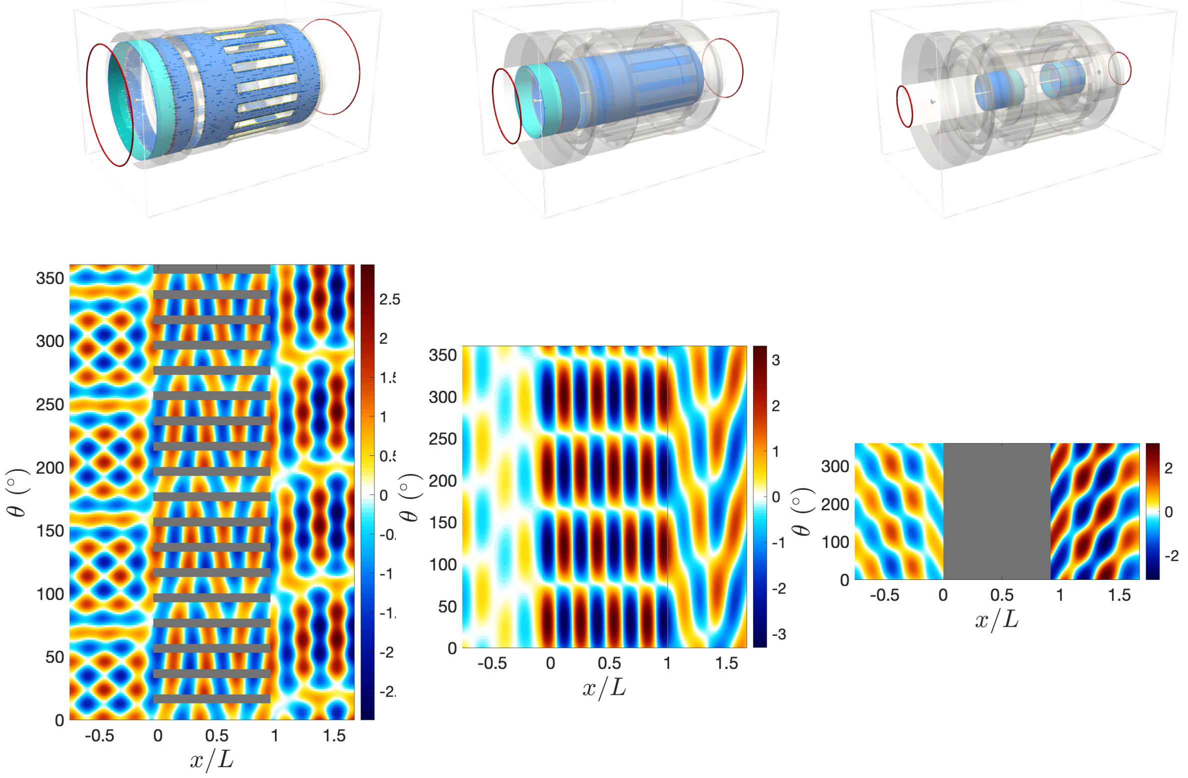

(a) (b) (c)

**Figure 2.27:** Instantaneous acoustic potential fields obtained by the mode-matching method for three cylindrical cuts. $r = (r_{S_{d2}} + r_{S_{d1}})/2$ (a), $r = (r_{g_2} + r_{g_1})/2$ (b), $r = (r_1 + r_{R_d})/2$ (c).

#### 2.3.5.1 Comparison with a realistic configuration

The finite element method is applied in this section to a realistic configuration of an open motor, in order to evaluate the limitations of the analytical model. In fact, one of the advantages of the finite element method is to provide a solution of the problem in a complex geometry, by taking into account the influence of various parameters neglected in the simplified configuration, such as the curvature and the end-windings. It is important to note that only the effect of curvature is investigated in this work. In fact, the end-windings are still assumed to be perfectly rigid, and the influence of their real geometry on sound propagation is beyond the scope of this study. The geometry investigated in this work is shown in Figure 2.28. Both methods are applied in this section to the diffraction of an incident mode of order $(2, 0)$ and of amplitude $A_{nj}^{(F)} = 0$. The dimensions of the ventilation system are given in Table 2.2. In the finite element method, the incident mode was imposed in the active perfectly matched layer (see Figure 2.28).

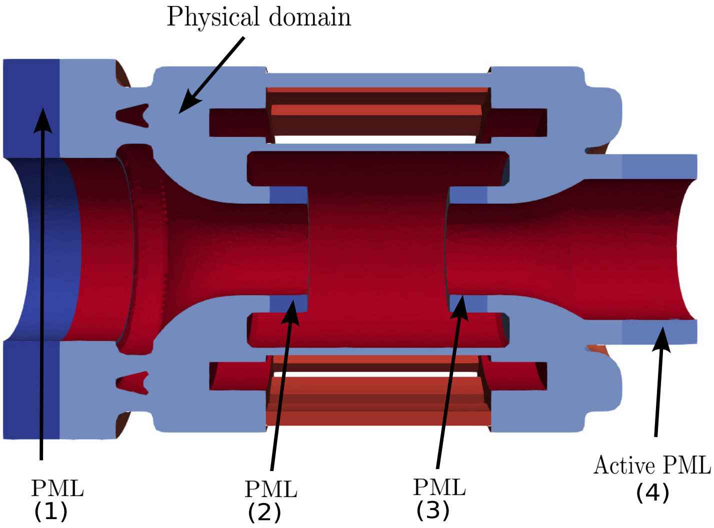

**Figure 2.28:** Meridian cut of the realistic configuration, showing the different regions of the finite element simulation

| $r_1$ | $r_{R_d}$ | $r_{g1}$ | $r_{g2}$ | $r_R$ | $r_S$ | $r_{w2}$ | $r_{d1}$ | $r_{d2}$ | $r_{w3}$ | $r_{e1}$ | $r_{e2}$ |
|---|---|---|---|---|---|---|---|---|---|---|---|
| 0.065 | 0.09 | 0.14 | 0.145 | 0.16 | 0.21 | 0.18 | 0.20 | 0.22 | 0.25 | 0.10 | 0.30 |
| $r_2$ | $r_{f_0}$ | $r_{f_1}$ | $r_{f_2}$ | $r_{f_3}$ | $r_{S_{d1}}$ | $r_{S_{d2}}$ | $V$ | $\theta_a V/2\pi$ | | | |
| 0.28 | 0.09 | 0.13 | 0.145 | 0.24 | 0.245 | 0.265 | 18 | 0.7 | | | |
| $L_{P_1}$ | $L_{P_2}$ | $d_1$ | $d_2$ | $L_{S_1}$ | $L_{S_2}$ | $L_{S_d}$ | $L_D$ | $L_W$ | $L_F$ | $L_G$ | $L_E$ |
| 0.08 | 0.08 | 0.075 | 0.05 | 0.075 | 0.075 | 0.30 | 0.05 | 0.05 | 0.15 | 0.35 | 0.15 |

**Table 2.2:** Dimensions of the ventilation system used in the test case

The instantaneous acoustic potential fields obtained by the two methods are illustrated in Figure 2.29 by a meridian cut at a constant azimuthal angle ($\theta = 0$ when $r/r_2 > 0$ and $\theta = \pi$ when $r/r_2 < 0$) for three different frequencies $f = 1000$ Hz (Figures 2.29b and 2.29a), $f = 2000$ Hz (Figures 2.29d and 2.29c) and $f = 3000$ Hz (Figures 2.29f and 2.29e).

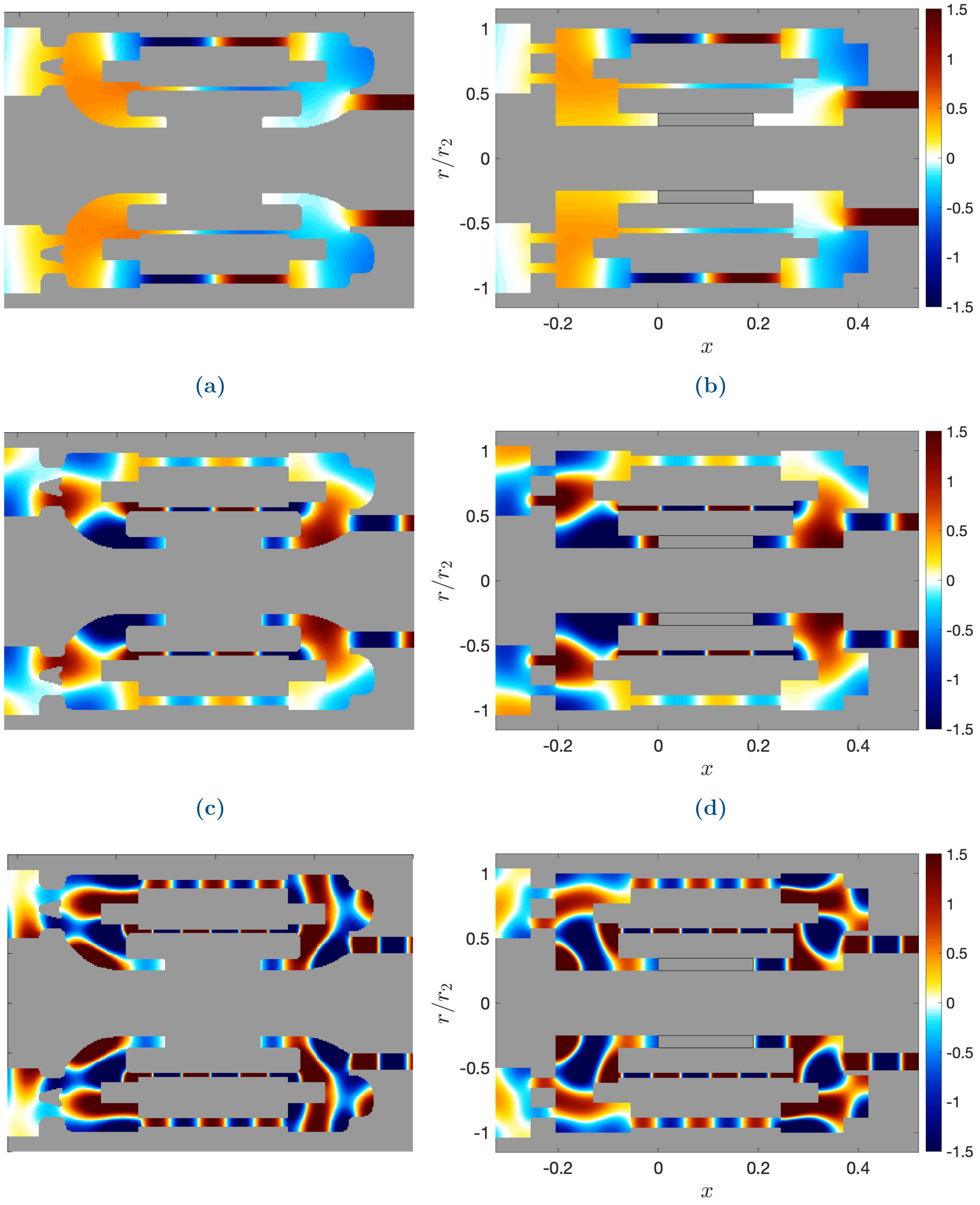

(a) (b) (c) (d) (e) (f)

**Figure 2.29:** Instantaneous acoustic potential fields obtained by the finite element method applied to a realistic configuration (a-c-e), and the mode-matching method (b-d-f), at three different frequencies. $f = 1000$ Hz (a-b), $f = 2000$ Hz (c-d), $f = 3000$ Hz (e-f). $n = 2$, $j = 0$, $A_{nj}^{(F)} = 1$, $A_{nj}^{(R_1)} = 0$, $A_{nj}^{(R_2)} = 0$.

It can be noticed from Figure 2.29 that the results obtained by two methods agree well at particularly low and medium frequencies of interest. This can be explained by the fact that the acoustic wavelengths are large enough with respect to the characteristic dimensions of the curved parts of the ventilation system in these frequency ranges. The sound waves are eventually not affected by the variation of the duct cross-section. This can readily be seen at the first frequency ($f = 1000$Hz) in Figures 2.29a and 2.29b. It is obvious that the acoustic response of the two configurations is almost the same. In fact, when the frequency increases, the acoustic response of each of these configurations remains nearly the same with a slight difference near the motor shaft, as illustrated in Figures 2.29c and 2.29d. However, the difference between the two configurations seems to be significant at relatively high frequencies, as shown in Figures 2.29e and 2.29f. The wave motion in the right part of the domain appears as dominantly axial in the numerical solution and dominantly radial in the analytical one. The effects due to the axial variation of the duct cross-section become too important and they cannot be neglected in the analysis.

It is interesting to note that the analytical model can obviously be improved by using the multimodal method [81, 42, 40, 43, 70, 71] to account for the variation of the duct cross-section. This method makes it possible to account for the coupling between the different acoustic modes propagating in the ventilation system. Its implementation could be considered for a future extension of the work but it is beyond the scope of the present study.

### 2.3.6 Parametric studies

#### 2.3.6.1 Effect of frequency

One of the most important aspects in the present investigation is the influence of frequency on the acoustic response of the ventilation system. The analytical model is applied in this section to the same configuration investigated in Section 2.3.5 (see Table 2.1), by imposing an incident mode of azimuthal and radial orders ($n = 4, j = 0$) in the annular duct located upstream the radial impeller (sub-domain $(F)$). The variations of the different acoustic powers as functions of frequency are shown in Figure 2.30. The acoustic powers have been evaluated analytically as follows

$$\left\{\begin{aligned}
\mathcal{P}_i^{(F)} &= -\pi k_0 r_{f_1}^2 Z_0 A_{nj}^{(F)} \left|k_{n,j}\right|^2, \quad k_{nj}^- \in \mathbb{R} && \text{(2.88a)}\\
\mathcal{P}_t^{(F)} &= \pi k_0 r_{f_1}^2 Z_0 \sum_{s=-\infty}^{+\infty} \sum_{\alpha=0}^{+\infty} T_{n_s\alpha} \left|k_{n_s\alpha}^-\right|^2, \quad k_{n_s\alpha}^+ \in \mathbb{R} && \text{(2.88b)}\\
\mathcal{P}_u^{(R_d)} &= -\pi k_0 r_{R_d}^2 Z_0 \sum_{s=-\infty}^{+\infty} \sum_{\gamma=0}^{+\infty} T_{n_s\gamma} \left|k_{n_s\gamma}^-\right|^2, \quad k_{n_s\gamma}^+ \in \mathbb{R} && \text{(2.88c)}\\
\mathcal{P}_t^{(R_d)} &= \pi k_0 r_{R_d}^2 Z_0 \sum_{s=-\infty}^{+\infty} \sum_{\gamma=0}^{+\infty} U_{n_s\gamma} \left|k_{n_s\gamma}^-\right|^2, \quad k_{n_s\gamma}^+ \in \mathbb{R} && \text{(2.88d)}\\
\mathcal{P}_t^{(E)} &= -\pi k_0 r_{e_2}^2 Z_0 \sum_{s=-\infty}^{+\infty} \sum_{m=0}^{+\infty} T_{n_sm} \left|k_{n_sm}^-\right|^2, \quad k_{n_sm}^- \in \mathbb{R} && \text{(2.88e)}
\end{aligned}\right.$$

Computing a complete spectrum with 500 frequencies using the analytical model takes

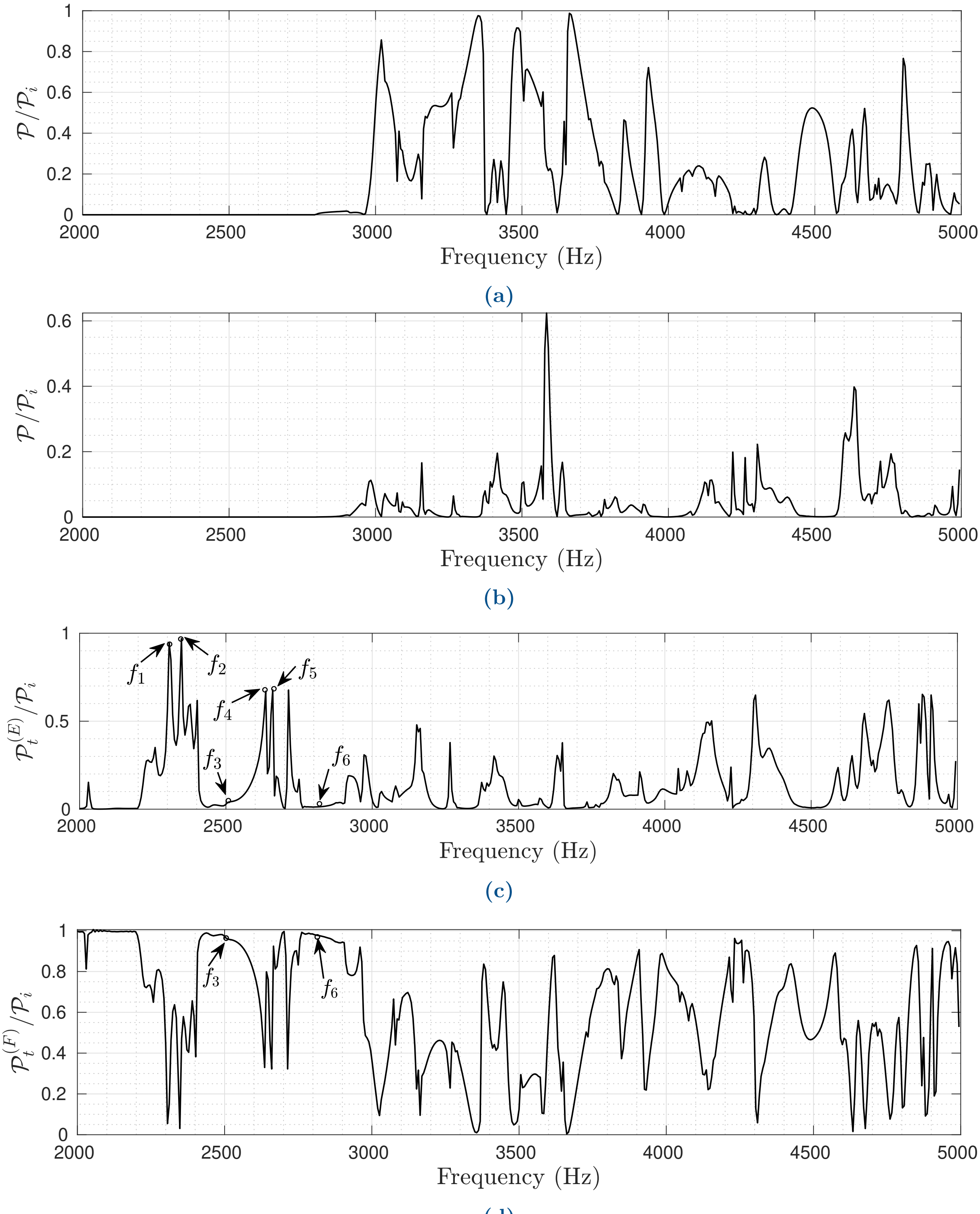

(a)

(b)

(c)

(d)

**Figure 2.30:** Variations of acoustic powers as functions of frequency. (a) $\mathcal{P}_u^{(R_{d1})}/\mathcal{P}_i^{(F)}$. (b) $\mathcal{P}_t^{(R_{d2})}/\mathcal{P}_i^{(F)}$. (c) $\mathcal{P}_t^{(E)}/\mathcal{P}_i^{(F)}$. (d) $\mathcal{P}_t^{(F)}/\mathcal{P}_i^{(F)}$. $n = 4$, $f_1 = 2306$Hz, $f_2 = 2348$Hz, $f_3 = 2504$Hz, $f_4 = 2636$Hz, $f_5 = 2660$Hz, $f_6 = 2816$Hz.

about 9 minutes on a personal computer. In this specific test case, the time required to calculate the radial wavenumbers and the projection integrals of the radial eigenfunctions is about 20 seconds. Using the iterative procedure at each frequency of the spectrum to calculate the modal coefficients takes on average only 1 seconds. As can be seen from Figure 2.30, the acoustic power distribution depends strongly on the excitation frequency. It is found that no acoustic wave can be transmitted to the rotor cooling channels ($\mathcal{P}_u^{(R_d)} = \mathcal{P}_t^{(R_d)} = 0$) when the excitation frequency is lower than 2797 Hz (see Figures 2.30b and 2.30a). This frequency limit represents the cut-off frequency of the

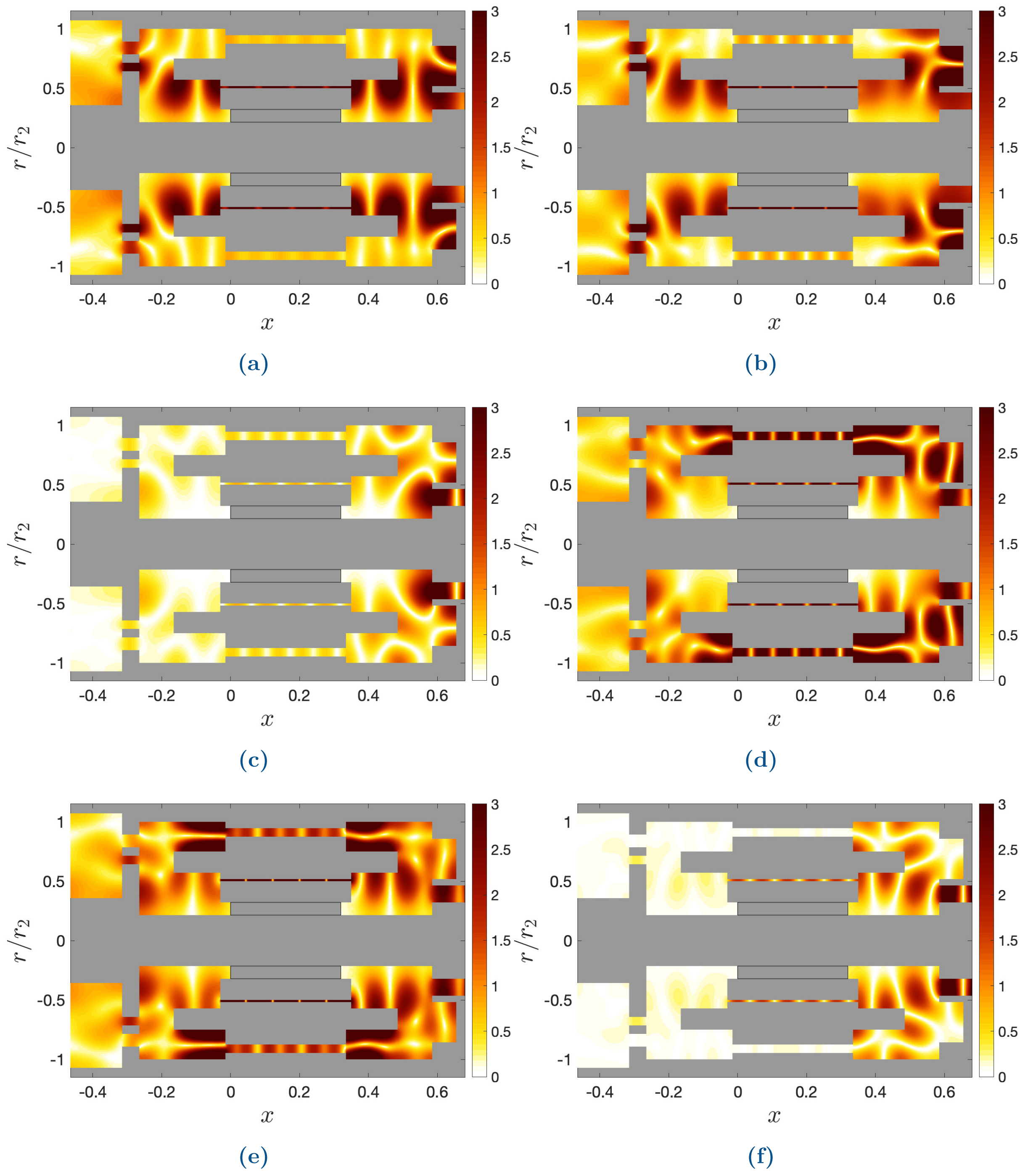

**Figure 2.31:** Acoustic potential modulus $|\phi|$ at 6 different frequencies form Figure 2.30. $(a)$ $f_1 = 2306$ Hz, $(b)$ $f_2 = 2348$ Hz, $(c)$ $f_3 = 2504$ Hz, $(d)$ $f_4 = 2636$ Hz, $(e)$ $f_5 = 2660$ Hz, $(f)$ $f_6 = 2816$ Hz. $n = 4$, $A_{nj}^{(F)} = 1$, $A_{nj}^{(R_1)} = 0$, $A_{nj}^{(R_2)} = 0$.

mode ($n = 4, j = 0$) in the sub-domains located upstream and downstream the rotor channels (($R_{d1}$) and ($R_{d2}$)). It is defined by $f_{(4,0)} = K_{40}^{(R_d)} c_0/2\pi = 2797$ Hz. For certain frequencies below this value, the sound can only be transmitted through the air gap and the stator cooling channels. Note here that this mode becomes cut-on when the frequency increases. In the following, considerable attention is paid to the variation of the acoustic power emitted outside the ventilation system $\mathcal{P}_t^{(E)}$. The aim is to predict the resonance frequencies of the ventilation system. To better understand the origin of the transmission peaks $\mathcal{P}_t^{(E)}$ in Figure 2.30c, it is important to visualize the sound field at different frequencies of the spectrum. It should be emphasized here that the real part of the instantaneous acoustic potential field is not the best indicator for observing interference between sound waves. In such a complex geometry, multiple interferences may appear in different regions of the ventilation system, requiring visualization of the sound field over a complete time period. For this, it is more convenient to use the modulus of the acoustic potential field (absolute value) instead of its real part for comparison purposes. Figure 2.31 shows the modulus of the acoustic potential fields (amplitudes) for 6 different frequencies extracted from Figure 2.30. The first frequency (Figure 2.31a) corresponds to the first transmission peak $f_1$ in Figure 2.30. It is clear to see that the amplitude of the acoustic field was amplified in the region located below the end windings. The same behaviour is observed at the second frequency $f_2 = 2366$ Hz (see Figure 2.31a), which corresponds to the second transmission peak. In both cases, the peak levels are maximum, and therefore the incident wave is almost totally transmitted outside the motor.

However, other constructive interferences between acoustic waves can be observed in the stator core as shown in Figures 2.31d and 2.31e. These correspond respectively to the transmission peaks at $f_4 = 2636$Hz and $f_5 = 2660$Hz in Figure 2.30c. On the other hand, the interferences are less marked for the frequencies in which the transmitted power $\mathcal{P}_t^{(E)}$ is very low, as shown in Figures 2.31c and 2.31f. At these frequencies ($f_3$ and $f_6$), the incident wave is almost totally reflected back to the cooling fan, as shown in the Figure 2.30d. This analysis confirms that acoustic resonances involve high transmission levels. These frequencies should not coincide with the characteristic frequencies of the cooling fan in order to improve the acoustic performance of the ventilation system of the motor.

#### 2.3.6.2 Influence of channel length

A large number of geometrical parameters could be examined to find the most suitable dimensions of the ventilation system to reduce its overall noise. Such a configuration possesses 33 geometrical parameters that can be used for parametric studies. Each parameter has a more or less significant influence on the acoustic response of the system. In this section, only the influence of the length of the stator ventilating holes is discussed. For this, two configurations with different channel lengths are compared in the rest of this section. Both configurations have the same transverse dimensions, given in Table 2.1. Their longitudinal dimensions are listed in Table 2.3. Note here that changing the length of the

| | $L_{P_1}$ | $L_{P_2}$ | $d_1$ | $d_2$ | $L_{S_1}$ | $L_{S_2}$ | $L_{S_d}$ | $L_D$ | $L_W$ | $L_F$ | $L_G$ | $L_E$ |
|---|---|---|---|---|---|---|---|---|---|---|---|---|
| **Config 1** | 0.03 | 0.03 | 0.1 | 0.1 | 0.15 | 0.15 | 0.33 | 0.05 | 0.07 | 0.095 | 0.38 | 0.15 |
| **Config 2** | 0.03 | 0.03 | 0.1 | 0.1 | 0.15 | 0.15 | 0.39 | 0.05 | 0.07 | 0.095 | 0.38 | 0.15 |

**Table 2.3:** Different lengths used in the two configurations (meter)

channels without affecting other parameters of the ventilation system leads to a change in the size of the motor. The comparison between the two configurations has been performed on the acoustic power transmitted outside the ventilation system $\mathcal{P}_t^{(E)}$. Figure 2.30 shows the variations of the transmitted powers obtained for the two configurations as functions of frequency. As expected, a significant difference is found between the results obtained in the two configurations. All transmission peaks appear at different frequencies in the two spectra. This may be attributed to the modification of the resonance frequencies of the two configurations. In fact, these frequencies are directly affected by the dimensions of the ventilation system. A qualitative comparison between the moduli of the acoustic potential fields obtained for the two configurations at three different frequencies denoted $f_1$, $f_2$ and $f_3$ in the spectra is shown in Figure 2.33.

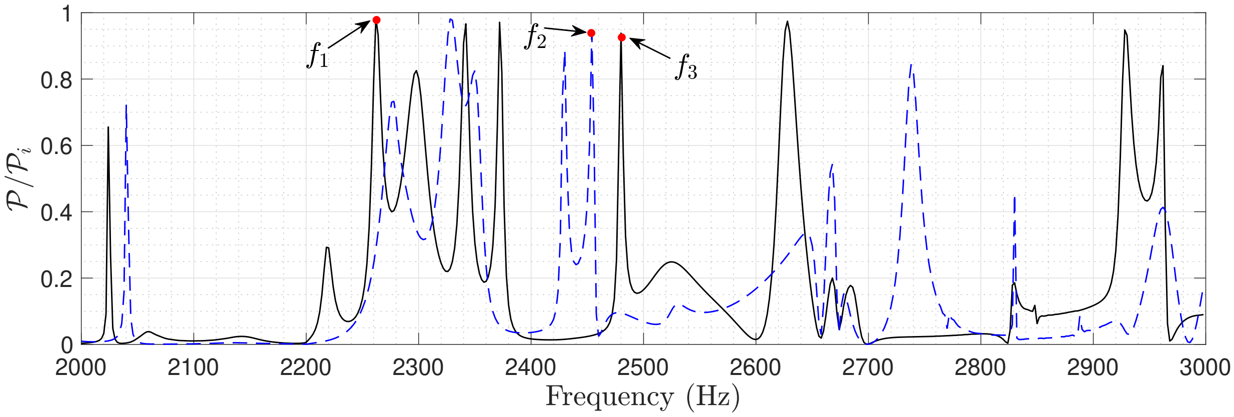

**Figure 2.32:** Variation of acoustic powers as functions of frequency. $L_{S_d} = 0.33$m (- - - -), $L_{S_d} = 0.39$m (——). $n = 4$, $f_1 = 2262$ Hz, $f_2 = 2454$ Hz, $f_3 = 2480$ Hz.

At the first frequency $f = f_1$, an important transmission peak appears in the first configuration (see Figure 2.32), which is mainly caused by the amplification of sound in the system, as illustrated in Figure 2.33a. This peak disappears in the second configuration, because no constructive interference between the acoustic waves can take place in the cooling system at this frequency (see Figure 2.33b). The second frequency $f = f_2$ corresponds to the resonance frequency of the cooling channels used in the second configuration (see Figure 2.33d). A strong amplification of sound can clearly be observed inside the channels, which is responsible for the transmission peak at the frequency $f_2$. It should be noted that the same behavior is observed in the first configuration when it is excited by the frequency $f = f_3$ (see Figure 2.33e).

This section has shown that the acoustic response of the stationary part of the ven-

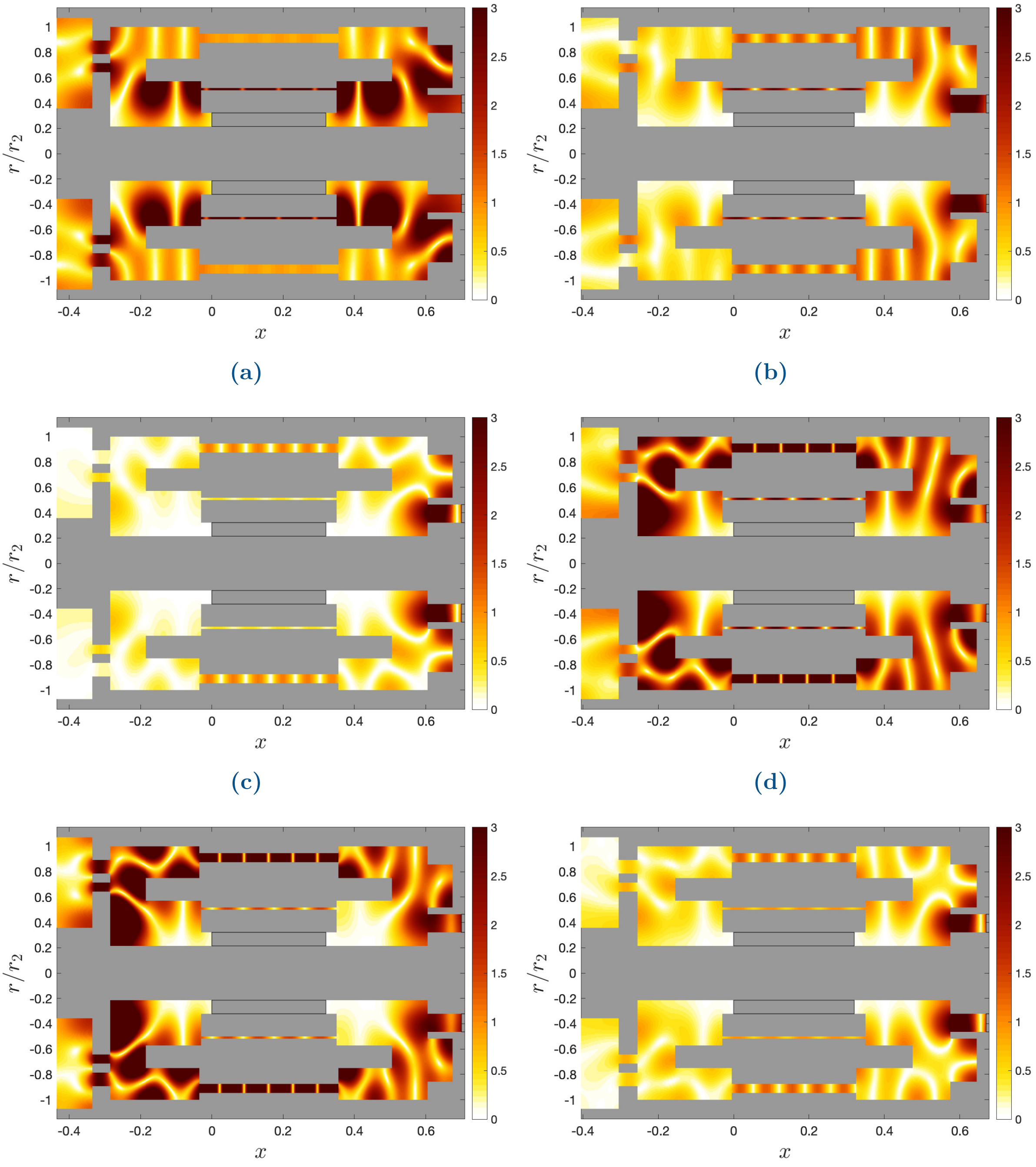

**(a)** **(b)** **(c)** **(d)** **(e)** **(f)**

**Figure 2.33:** Acoustic potential modulus $|\phi|$. $(a)$ $L_{S_d} = 0.39\ m$, $f = f_1$. $(b)$ $L_{S_d} = 0.33\ m$, $f = f_1$. $(c)$ $L_{S_d} = 0.39\ m$, $f = f_2$. $(d)$ $L_{S_d} = 0.33\ m$, $f = f_2$. $(e)$ $L_{S_d} = 0.39\ m$, $f = f_3$. $(f)$ $L_{S_d} = 0.33\ m$, $f = f_3$. $n = 4$.

tilation system is strongly affected by the variation of the channel length. Consequently, the resonance frequencies can be shifted by decreasing or increasing this parameter. In contrast, in most practical applications the size of the motor cannot change too much because of its allocated space in the train. For this reason, when the length of the stator channels changes, other parameters of the ventilation system must be modified to maintain the same motor size.

#### 2.3.6.3 Scattering of evanescent waves

In the previous sections, the acoustic response of the ventilation system to an incident excitation generated by the fan has been presented. Up to now, all incident modes considered in this work have been assumed to be cut-on. In practice, the sound field generated by a ducted fan is composed of both cut-on and cut-off modes. It is instructive to examine how evanescent waves can excite the stationary part of the ventilation system. In the following, particular attention will be paid to cut-off modes. It should be recalled here that the tonal noise generated by a ducted fan can be controlled by generating higher order modes at the blade passing frequency and its first harmonics. The aim is to generate only cut-off modes at these frequencies. In fact, when an acoustic mode of order $(n, j)$ is generated at a frequency below its cut-off frequency $f < f_{cutoff}$, its amplitude decays exponentially along the distance, with a decay rate defined by

$$\tau_{nj} = \exp\left(-\sqrt{K_{nj}^2 - k_0^2}\Delta x\right), \quad \Delta x = |x - x_{12}| \tag{2.89}$$

where $x_{12}$ corresponds to the axial position of the leading edges of the fan blades (see Figure 2.10). Equation 2.89 shows clearly that the amplitude of the decaying field goes to zero when the axial distance $\Delta x$ is large enough. In practical applications, the duct in which the incident wave is generated is not semi-infinite. More precisely, in the case of an open motor, this duct is connected to another duct of larger transverse dimensions. To explain the propagation mechanism of a cut-off mode generated by an upstream fan through the ventilation system, a comparison between two configurations with different distances between the impeller leading edge and the discontinuity interface $L_F = x_{12} - x_8$ has been carried out. Both configurations have the same dimensions listed in Table 2.1, except for the distance between the two interfaces $L_F$. In the first configuration, the impeller blades are placed at a distance of $L_F = 0.08\ m$ from the discontinuity interface $x_8$, whereas the second configuration has a smaller distance given by $L_F = 0.01\ m$. It should be noted here that the second configuration is more realistic than the first one ($L_F \approx 0$). First of all, an incident mode of order $(8, 0)$ is imposed in the annular duct located upstream of the radial impeller at a frequency $f = 2000$Hz. The cut-off frequency of the latter is given by $f_{(8,0)}^{(F)} = K_{(8,0)}^{(F)} c_0/2\pi = 3886.8$ Hz ($K_{(8,0)}^{(F)} = 71.82$). The variation of the amplitude of the incident wave with distance is shown in Figure 2.34. A meridian cut of the instantaneous acoustic potential fields, corresponding to the two configurations are illustrated in Figure 2.35. As can be seen, in the first configuration (Figure 2.35a), no acoustic wave can propagate inside the ventilation system. This is due to the fact that the amplitude of the incident wave decays completely along the axis before reaching the discontinuity interface $x_8$, as indicated in Figure 2.34. In contrast, when the distance $L_F$ is relatively small as in the second configuration (Figure 2.35b), the incident wave can be transmitted into the ventilation system. Figure 2.34 shows clearly that the amplitude of the incident wave does not decay to zero at the interface $x_8$. It reaches about 54% of

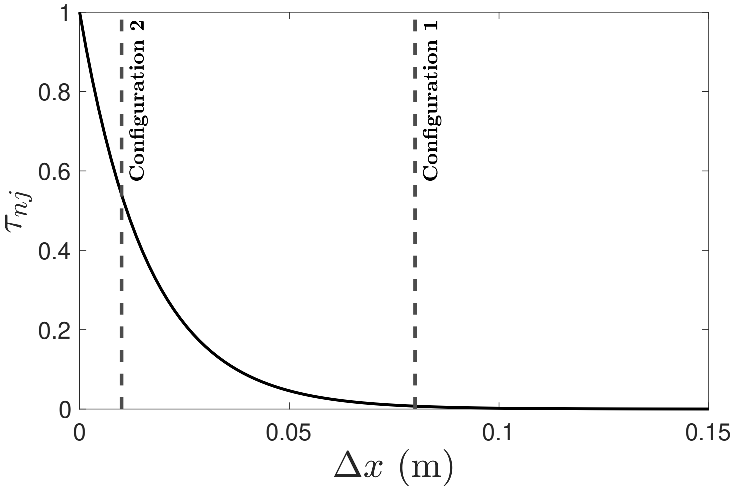

**Figure 2.34:** Variation of amplitude factor $\tau_{nj}$ with distance $|x - x_{12}|$ (——). Discontinuity interface (- - - -).

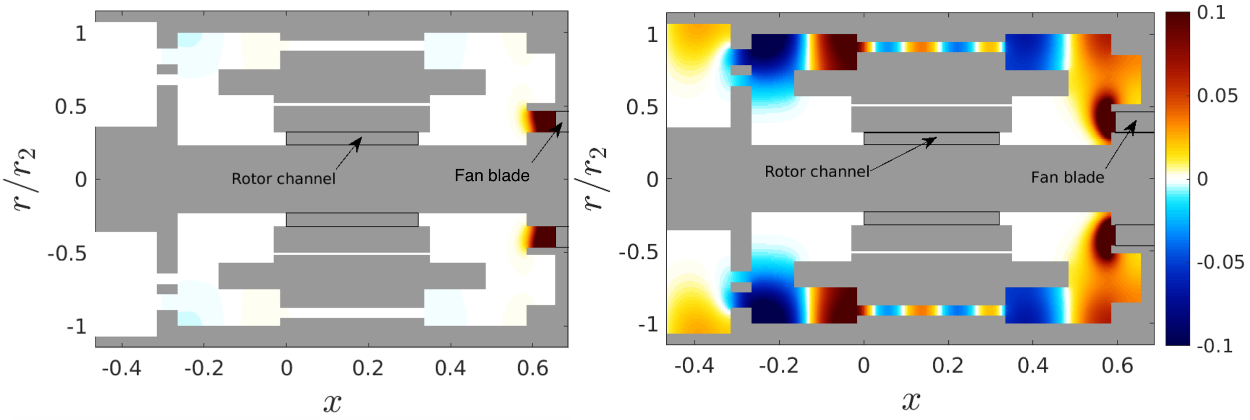

(a)

(b)

**Figure 2.35:** Instantaneous acoustic potential fields obtained by the mode-matching technique applied to the diffraction of an evanescent wave emitted at two different positions. (*a*) $L_F = 0.08$m, (*b*) $L_F = 0.01$m. $f = 2000$ Hz, $n = 8$, $A_{nj}^{(F)} = 1$, $A_{nj}^{(R_1)} = 0$, $A_{nj}^{(R_2)} = 0$

its maximum value. Axial cuts of the acoustic potential fields ($\phi_t^{(A_2)} + \phi_r^{(A_2)}$) and their associated modal amplitudes are illustrated in Figure 2.36 at two different positions $x = x_8$ and $x = (x_7 + x_8)/2$. At the interface $x_8$ (Figure 2.36a), a strong variation of the sound field is observed in the radial direction. Basically, the sound field remains concentrated at the junction interface located between the two ducts. This is explained by the presence of a large number of cut-off modes at this interface with relatively high amplitudes, as indicated in Figure 2.36c. The amplitude of these modes decreases rapidly with distance, as shown in Figure 2.36b. It is found that only the mode of order $(8, 0)$ is cut-on at this frequency. This propagates outwards in the radial direction to the stator block before being diffracted by the different components of the ventilation system, and then transmitted outside the ventilation system. To give a more comprehensive interpretation of the sound propagation mechanism in this specific case, an axial cut of the acoustic

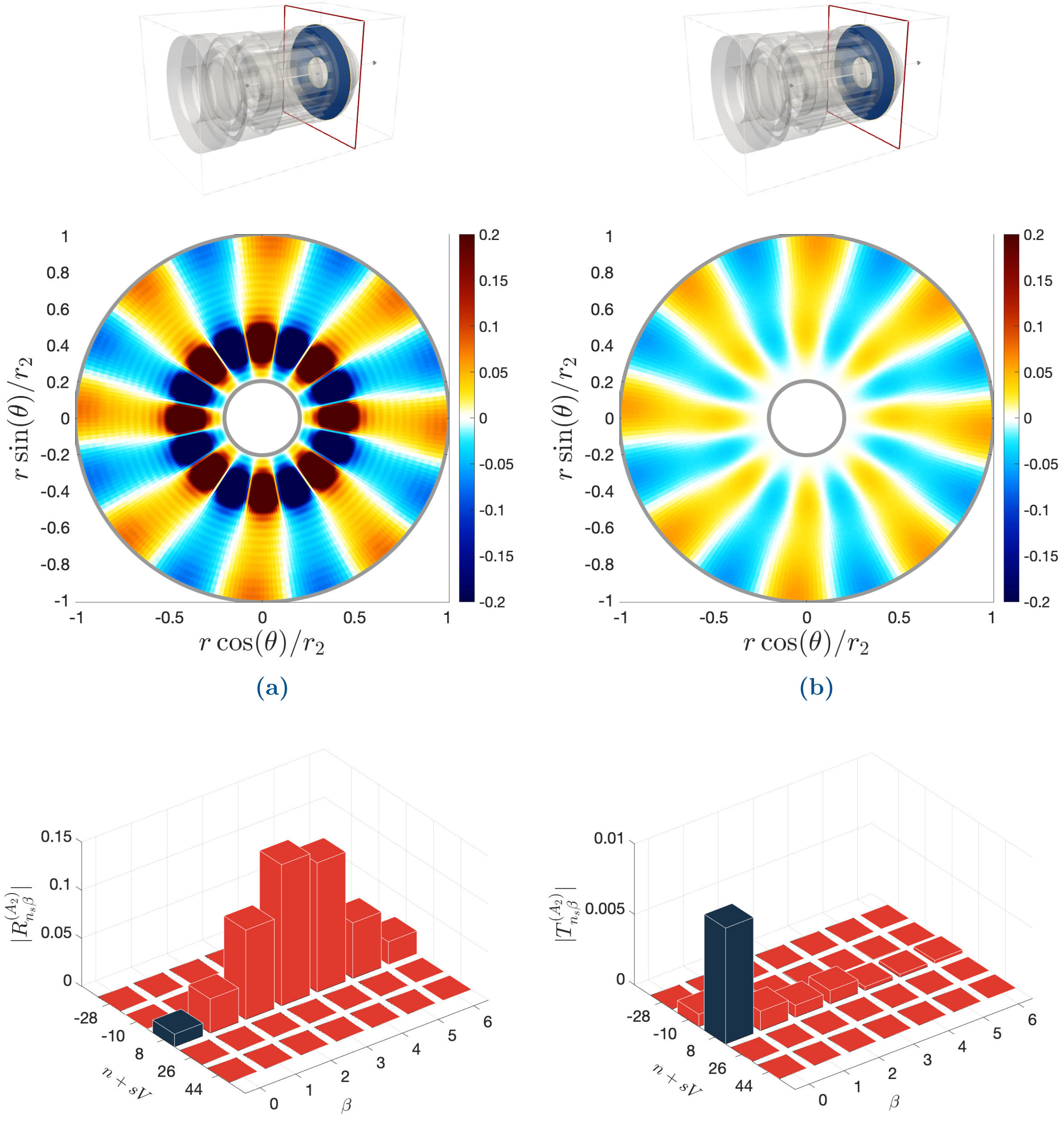

**(a)** **(b)**

**(c)** **(d)**

**Figure 2.36:** Instantaneous acoustic potential fields obtained by the mode-matching technique. (a) Axial cut at $x_8 = 0.585\ m$. (b) Axial cut at $(x_7 + x_8)/2 = 0.535\ m$. (c) Modal amplitudes $|R_{n_s\beta}^{(A_2)}|$. (d) Modal amplitudes $|T_{n_s\beta}^{(A_2)}|$. Cut-off modes (bars 🟥 ), Cut-on modes (bars ■ ). $L_F = 0.01\ m$, $f = 2000$ Hz, $n = 8$, $A_{nj}^{(F)} = 1$

potential field was made at a position located between the end-windings and the flow deflector $x = (x_3 + x_2)/2$ (see Figure 2.37a). The corresponding modal amplitudes are shown in Figures 2.37b and 2.37b. They indicate that only the mode of order $(8, 0)$ was transmitted downstream the cooling channels. It may be observed from Figure 2.37a, that the acoustic field is highly concentrated near the outer wall of the annular duct. This is the so-called the skin effect [25]. It appears when the azimuthal modal order is sufficiently

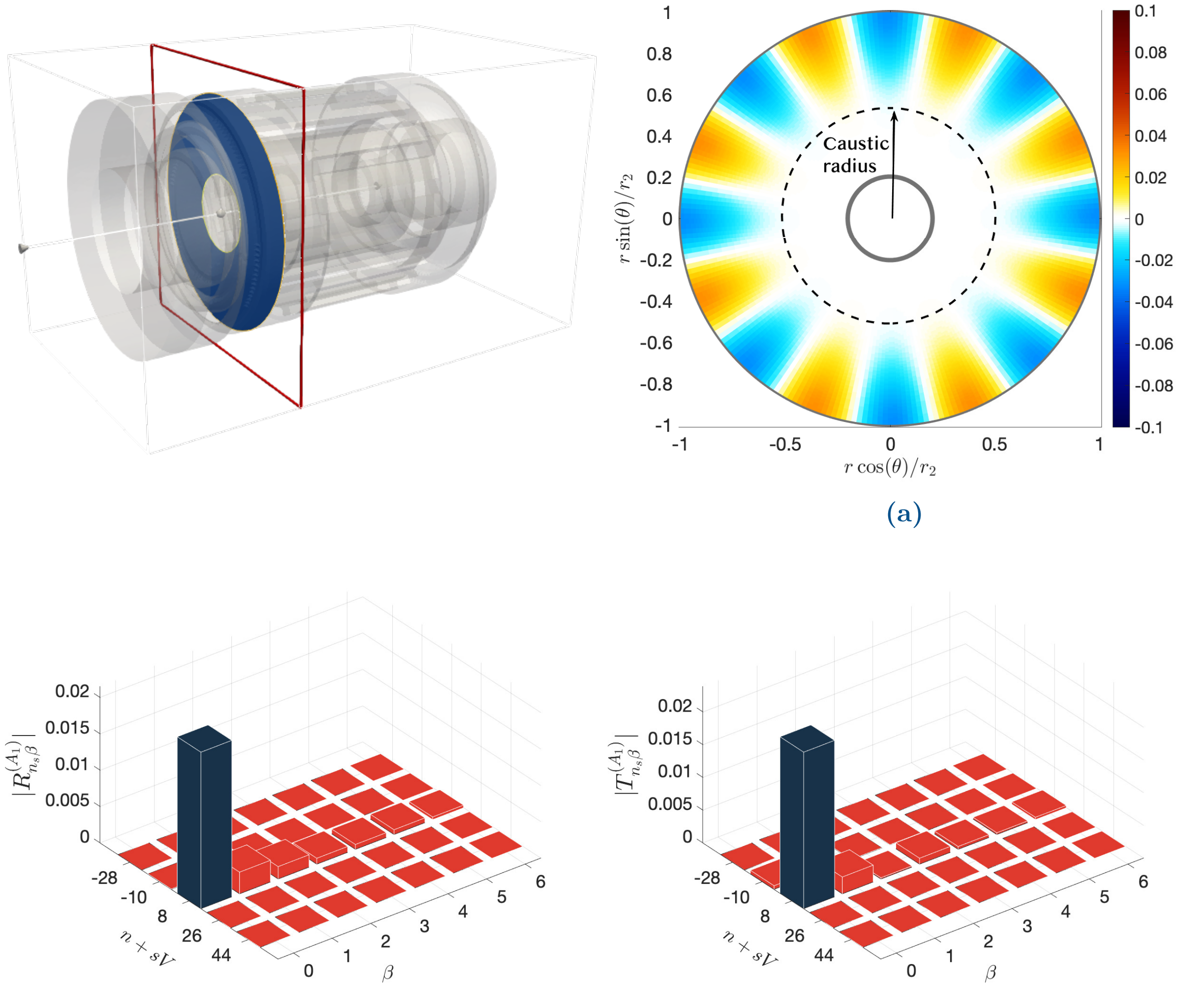

**(a)**

**(b)**

**(c)**

**Figure 2.37:** Instantaneous acoustic potential fields obtained by the mode-matching technique. (b) Axial cut at $(x_2 + x_3)/2 = -0.215\ m$. (c) Modal amplitudes $|R^{(A_1)}_{n_s\beta}|$. (d) Modal amplitudes $|T^{(A_1)}_{n_s\beta}|$. Cut-off modes (bars 🟥 ), Cut-on modes (bars ■ ). $L_F = 0.01\ m$, $f = 2000$ Hz, $n = 8$, $A^{(F)}_{nj} = 1$

high. As can be seen from Figure 2.37a, the sound field can be divided into two main regions, separated by a radius $r_c$ called the caustic radius [25]. The sound field varies only in the outer annulus $r_c \leq r \leq r_2$, and decays to zero in the inlet annulus $r_1 \leq r < r_c$. Hence, the wave is only reflected by the outer wall of the duct. Figure 2.38 shows the variation of the radial shape function of the mode $(8, 0)$ as a function of radius. As can be seen, it decays rapidly when $r$ decreases. This may explain why the sound field is almost zero in the region near the motor shaft ( $r_1 < r < r_c$).

In fact, the basic reason why sound cannot be transmitted through the air gap and rotor channels is that their external radii are lower than the caustic radius $r_{R_d} < r_{g2} < r_c$ of the mode $(8, 0)$. Note here that the influence of the distance $L_F$ becomes less important when the mode $(8, 0)$ is generated at a frequency very close to its cut-off frequency ($k_0 \approx$

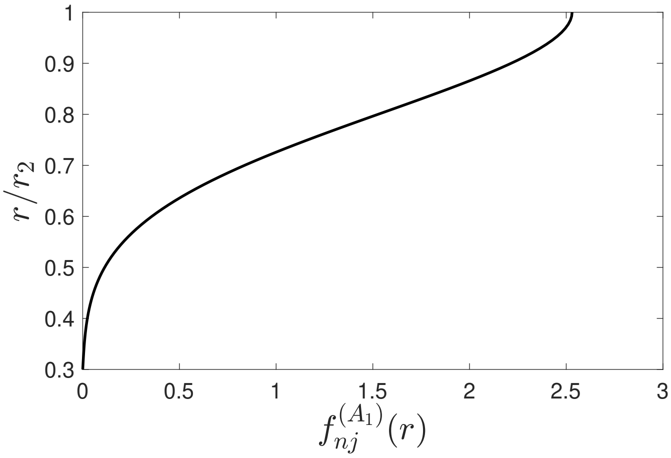

**Figure 2.38:** Variation of radial shape function with radius. $(n = 8, j = 0)$

$K_{nj}$). The attenuation becomes very slow and the decaying amplitude goes to zero for very long distances. The acoustic potential fields obtained for the two configurations studied previously at a frequency slightly lower than the cut-off frequency of the mode $(8, 0)$ $f = 3885$ Hz are shown in Figure 2.39. As can be seen, the same behavior is observed in both configurations.

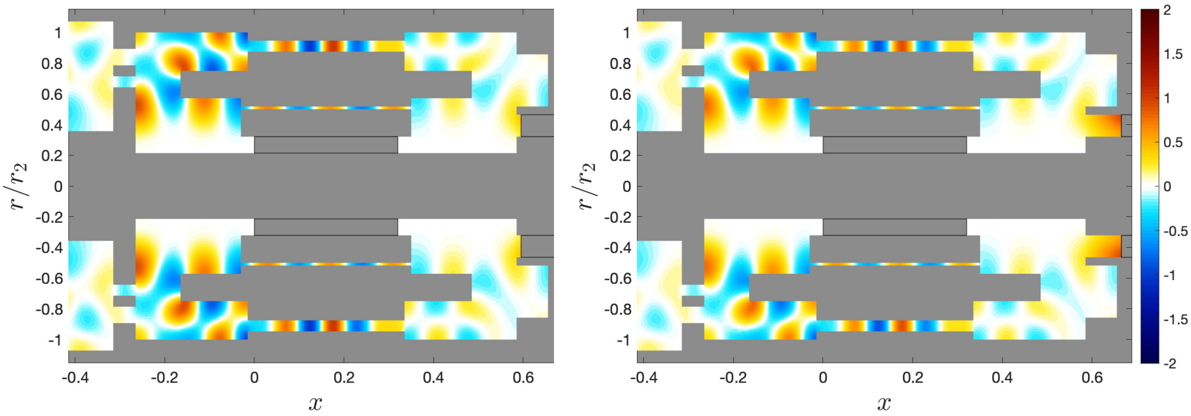

**(a)** **(b)**

**Figure 2.39:** Instantaneous acoustic potential fields obtained by the mode-matching technique applied to the diffraction of an evanescent wave emitted at two different positions. $(a)$ $L_F = 0.01$ m, $(b)$ $L_F = 0.08$ m. $f = 3885$ Hz, $n = 8$, $A_{nj}^{(F)} = 1$, $A_{nj}^{(R_1)} = 0$, $A_{nj}^{(R_2)} = 0$

It should be emphasized that the cut-off modes with relatively high azimuthal orders cannot be transmitted through the components of the ventilation system even if the distance $L_F$ is too small. This is due to the fact that the cut-off frequency increases with the modal order. In practical application, care should be taken when choosing the dimensions of the cooling fan, in order to avoid generating acoustic modes able to be transmitted into the ventilation system. It is worth noting that the same analysis can be applied to the rotor cooling channels and the rotor slots.

## 2.4 Air outlet

The last part of this chapter addresses the downstream transmission of impeller noise through the rigid bars located at the motor outlet. The typical representation of the latter is illustrated in Figure 2.40a. Up to now, only the noise transmitted into the stationary part of the ventilation system has been investigated (see Section 2.3.3). In reality, a part of impeller noise can propagate radially from the impeller trailing-edge towards the air outlet of the motor, as illustrated in Figure 2.40b. However, the sound field emitted downstream the radial impeller can be expanded into a sum of diverging spinning modes having various propagation angles. Each incident mode of order $n$ is scattered by the rigid bars into several spinning modes of orders $n_s = n + sV$. In the rest of this section, a three-dimensional mode-matching technique is applied to the diffraction of a single spiral wave by the rigid bars.

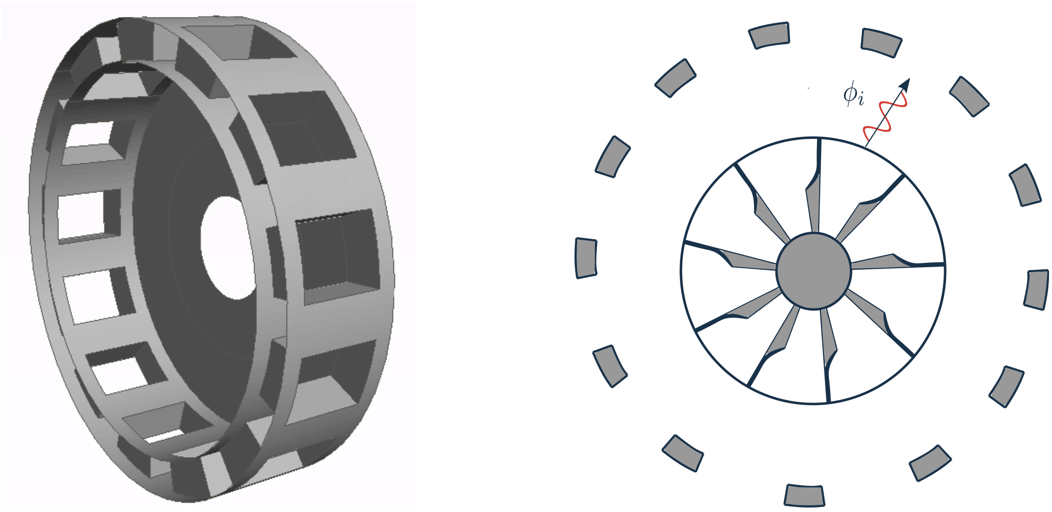

(a) (b)

**Figure 2.40:** (a) Typical configuration of an open motor. (b) Typical configuration of the rigid bars located at the air outlet of the motor. (c) Downstream propagation of the noise generated by the radial impeller.

### 2.4.1 Acoustic potentials

As a first step, the geometry is divided into three different sub-domains, corresponding to the upstream and the downstream annular volumes and the inter-bars channels, as depicted in Figure 2.41. Four acoustic fields are generated by the impingement of the incident wave on the rigid bars. Without further change of notation, the same indices considered for the case of a single row of channels (see Chapter 1) are used in this section. The mathematical expressions of the different acoustic fields can readily be found by solving the Helmholtz equation in cylindrical coordinates with the appropriate boundary conditions. The only difference compared to the problems investigated so far, is the direction of propagation of the different acoustic fields. In this specific problem, the

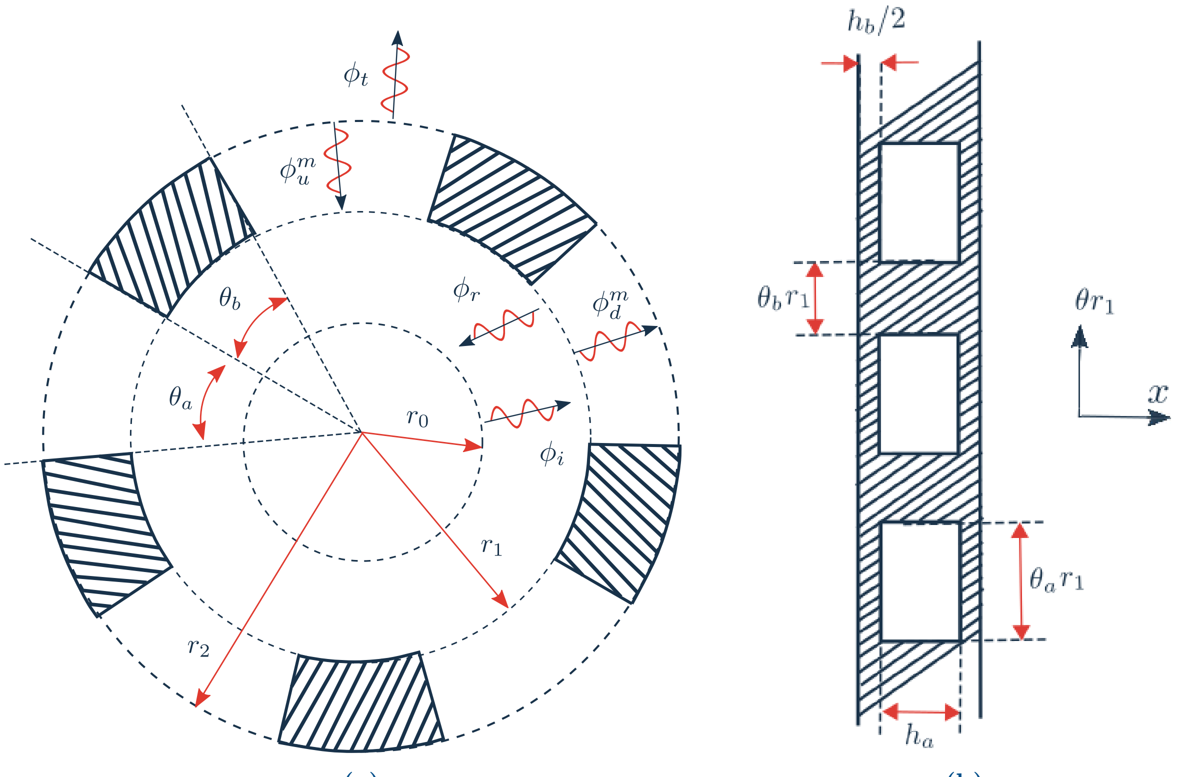

(a) (b)

**Figure 2.41:** Different acoustic fields generated by the diffraction of the incident wave. (a) Axial cut. (b) Unwrapped representation of a cylindrical cut at $r = r_1$

rigid wall boundary condition must be applied on the azimuthal $\theta$ and axial $x$ directions. Therefore, the radial direction represents the main direction of propagation of the different acoustic fields. These fields can be described in each sub-domain by a sum of converging or diverging spiral modes. The incident wave $\phi_i$ is considered as a single diverging spinning mode traveling form the impeller trailing-edge $r = r_0$ to the inlet interface of the rigid bars $r = r_1$. It can be expressed as

$$\boxed{\phi_i(r,\theta,x) = A_{nj} H_n^{(1)}\left(K_j r\right) \cos\left(k_j x\right) \mathrm{e}^{\mathrm{i}n\theta}, \quad k_j = j\frac{\pi}{h_a + h_b} \quad , K_j = \sqrt{k^2 - k_j^2}} \tag{2.90}$$

where $K_j$ and $k_j$ represent respectively the radial and the axial wave numbers, and $H_n^{(1)}$ is the Hankel function of the first kind $(H_n^{(1)}(K_j r) = J_n(K_j r) + \mathrm{i}Y_n(K_j r))$. It should be recalled here that this function is typically used to describe the radial propagation of diverging waves, as in the case of the incident wave.

The reflected field $\phi_r$ is considered as a converging spiral wave emitted at the inlet interface of the rigid bars $r_1$. The radial propagation of this wave can be described by the Hankel function of the second kind $H_{n_s}^{(2)}(K_t r) = J_{n_s}(K_t r) - \mathrm{i}Y_{n_s}(K_t r)$. In contrast, this function has no physical meaning for small arguments $K_t r$. It becomes infinite $(H_{n_s}^{(2)}(K_t r) \rightarrow \infty)$ when $K_t r \rightarrow 0$ because of the Bessel function of the second kind ($Y_{n_s}(K_t r) \to \infty$). Furthermore, the phase velocity of each converging mode $v_{ph} = k_0 r_0 c_0 / n_s$ varies with the radius $r$, and the mode is cut-on only if this velocity is supersonic $v_{ph} > c_0$. In fact, when the propagation radius decreases the local phase velocity also decreases, and it can reach a subsonic value $v_{ph} \leq c_0$. If this condition is fulfilled, the mode becomes cut-off, and it cannot be transmitted to the annular volume located bellow the cut-off radius. Therefore, the converging mode is totally reflected back towards the rigid bars as illustrated in Figure 2.42. Consequently, a standing wave is established between the cut-off radius and the inlet interface of the rigid bars, due to the interference between the two waves. In this condition, it is more convenient to use the Bessel function of the first kind $J_{ns}(K_t r)$ rather than the Hankel function of the second kind $H^{(2)}_{n_s}(K_t r)$ to account for the radial reversal of converging modes. The condition that can be used to switch from the Hankel function of the second kind to the Bessel function of the first kind is deduced from the phase velocity of each mode $n_s$. It is given by

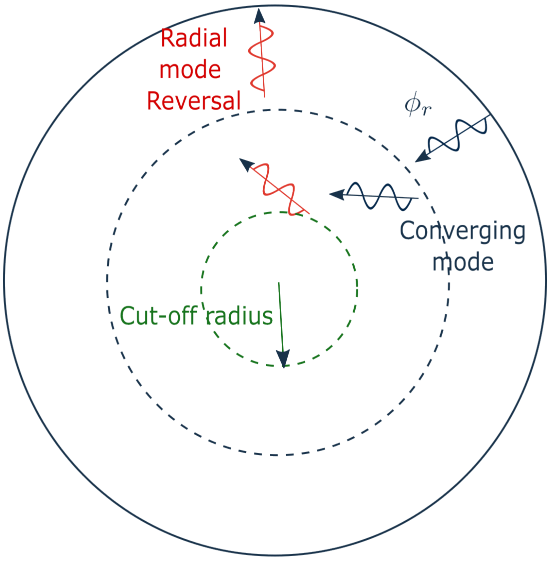

**Figure 2.42:** Radial mode reversal

$$\frac{v_{ph}}{c_0} = \frac{k r_0}{n_s} \leq 1 \tag{2.91}$$

The reflected field can therefore be expressed as

$$\boxed{\phi_r(r, \theta, x) = \sum_{s=-\infty}^{+\infty} \sum_{t=0}^{+\infty} R_{n_s t} \Phi_{n_s}\left(K_t r\right) \cos\left(k_t x\right) \mathrm{e}^{\mathrm{i} n_s \theta}} \tag{2.92}$$

where

$$n_s = n + sV \qquad , k_t = t\frac{\pi}{h_a + h_b} \qquad , K_t = \sqrt{k^2 - k_t^2}$$

$$\Phi_{n_s}(K_t r) = \begin{cases} J_{n_s}(K_t r) & \text{, if } kr_0/n_s \leq 1 \\ H_{n_s}^{(2)}(K_t r) & \text{, if } kr_0/n_s > 1 \end{cases}$$

The mathematical expressions of the downstream $\phi_d^{(m)}$ and upstream $\phi_u^{(m)}$ acoustic fields in the $m^{\text{th}}$ inter-bar channel are given by:

$$\boxed{\begin{pmatrix}\phi_d^{(m)}(r,\theta,x)\\ \phi_u^{(m)}(r,\theta,x)\end{pmatrix} = \sum_{q=0}^{+\infty}\sum_{p=0}^{+\infty}\begin{pmatrix}D_{qp}^m\\ U_{qp}^m\end{pmatrix}\begin{pmatrix}H_{n_q}^{(1)}\left(K_p r\right)\\ \Phi_{n_q}\left(K_p r\right)\end{pmatrix}\cos\left(k_p\left[x-\frac{h_b}{2}\right]\right)\cos\left(n_q\Big[\theta-\frac{2\pi m}{V}\Big]\right)} \tag{2.93}$$

with

$$n_q = q\frac{V}{2}\frac{\theta_a+\theta_b}{\theta_a} \quad , k_p = p\frac{\pi}{h_a} \quad , K_p = \sqrt{k^2-k_p^2} \quad , D_q^m = D_q^0 \mathrm{e}^{\mathrm{i}m2\pi n/V}, \quad U_q^m = U_q^0 \mathrm{e}^{\mathrm{i}m2\pi n/V}$$

$$\Phi_{n_q}(K_p r) = \begin{cases} J_{n_q}(K_p r) & \text{, if } kr_1/n_q \leq 1 \\ H_{n_q}^{(2)}(K_p r) & \text{, if } kr_1/n_q > 1 \end{cases}$$

The transmitted acoustic field is considered as a diverging wave emitted at the outlet interface of the rigid bars $r = r_2$. It can be expressed as

$$\boxed{\phi_t(r,\theta,x) = \sum_{s=-\infty}^{+\infty}\sum_{t=0}^{+\infty} T_{n_s t} H_{n_s}^{(1)}\left(K_t r\right)\cos\left(k_t x\right)\mathrm{e}^{\mathrm{i}n_s\theta}} \tag{2.94}$$

### 2.4.2 Matching equations

The mode-matching method is used in this section to calculate the modal coefficients of the different acoustic fields. In this particular configuration, the different sub-domains are joined at different radial positions. However, the matching equations can be obtained, by imposing the continuity of acoustic pressure and radial velocity at the interfaces $r_1$ and $r_2$. Moreover, the rigid-wall boundary condition corresponding to a vanishing normal velocity $v \cdot \mathbf{n} = v \cdot \mathbf{e_r} = 0$ must be imposed on the front face and the back face of the rigid bars. As mentioned earlier, the inter-bar channels are excited periodically by the incident wave, therefore the matching equations need to be written for only the reference channel $m = 0$. The acoustic pressure and the radial velocity are gathered into a vector $\mathbf{\Gamma}$, defined by

$$\mathbf{\Gamma}_\zeta(r,\theta,x) = \begin{pmatrix} p(r,\theta,x) \\ v(r,\theta,x)\cdot\mathbf{e_r} \end{pmatrix}, \quad \zeta = \{i, r, t, u, d\}$$

The matching equations result as

$$\begin{cases} \boldsymbol{\Gamma}_i + \boldsymbol{\Gamma}_u = \boldsymbol{\Gamma}_d + \boldsymbol{\Gamma}_u, \quad r = r_1, \quad \theta \in [0; \theta_a], \quad x \in [h_b/2; h_b/2 + h_a] & (2.95a) \\ (v_i + v_r) \cdot \mathbf{e}_{\boldsymbol{r}} = 0, \quad r = r_2, \quad \theta \in [\theta_a; 2\pi/V], \quad x \in ]0; h_b/2[ \cup ]h_a; h_a + h_b/2[ & (2.95b) \\ \boldsymbol{\Gamma}_u + \boldsymbol{\Gamma}_d = \boldsymbol{\Gamma}_t, \quad r = r_2, \quad \theta \in [0; \theta_a], \quad x \in [h_b/2; h_b/2 + h_a] & (2.95c) \\ v_t \cdot \mathbf{e}_{\boldsymbol{r}} = 0, \quad r = r_2, \quad \theta \in [\theta_a; 2\pi/V], \quad x \in ]0; h_b/2[ \cup ]h_a; h_a + h_b/2[ & (2.95d) \end{cases}$$

### 2.4.2.1 Inlet interface $r = r_1$

The continuity of acoustic pressure at the interface $r = r_1$ yields :

$$\begin{aligned} &A_{nj} H_n^{(1)}(K_j r_1) \cos(k_j x)\, \mathrm{e}^{\mathrm{i}n\theta} + \sum_{s=-\infty}^{+\infty} \sum_{t=0}^{+\infty} R_{n_s t} H_{n_s}^{(2)}(K_t r_1) \cos(k_t x)\, \mathrm{e}^{\mathrm{i}n_s\theta} \\ &\qquad = \sum_{q=0}^{+\infty} \sum_{p=0}^{+\infty} \left[ D_{qp}^0 H_{n_q}^{(1)}(K_p r_1) + U_{qp}^0 H_{n_q}^{(2)}(K_p r_1) \right] \cos\left( k_p \left[ x - \frac{h_b}{2} \right] \right) \cos(n_q \theta) \end{aligned} \tag{2.96}$$

The continuity of the radial velocity gives:

$$\begin{aligned} &A_{nj} H_n^{(1)\prime}(K_j r_1) \cos(k_j x)\, \mathrm{e}^{\mathrm{i}n\theta} + \sum_{s=-\infty}^{+\infty} \sum_{t=0}^{+\infty} R_{n_s t} H_{n_s}^{(2)\prime}(K_t r_1) \cos(k_t x)\, \mathrm{e}^{\mathrm{i}n_s\theta} \\ &\qquad = \sum_{q=0}^{+\infty} \sum_{p=0}^{+\infty} \left[ D_{qp}^0 H_{n_q}^{(1)\prime}(K_p r_1) + U_{qp}^0 H_{n_q}^{(2)\prime}(K_p r_1) \right] \cos\left( k_p \left[ x - \frac{h_b}{2} \right] \right) \cos(n_q \theta) \end{aligned} \tag{2.97}$$

Equations 2.96 and 2.97 must be projected on the two sets of eigenfunctions. The projection of the pressure equation on the transverse modes of inter-bar channels is written as

$$\begin{aligned} &\int_{h_b/2}^{h_a+h_b/2} \int_0^{\theta_a} (p_i + p_r) \cos\left( n'_p \left[ z - \frac{h_b}{2} \right] \right) \cos\left( n'_q \theta \right) \mathrm{d}z \mathrm{d}\theta \\ &\qquad = \int_{h_b/2}^{h_a+h_b/2} \int_0^{\theta_a} (p_d + p_d) \cos\left( n'_p \left[ z - \frac{h_b}{2} \right] \right) \cos\left( n'_q \theta \right) \mathrm{d}z \mathrm{d}\theta \end{aligned} \tag{2.98}$$

where

$$n'_p = p' \frac{\pi}{h_a} \qquad , n'_q = q' \frac{B}{2} \frac{\theta_a + \theta_b}{\theta_a}$$

The projection of the radial velocity equation on the transveres modes of the annular volume, is written as

$$\begin{aligned} &\int_0^{h_a+h_b} \int_0^{\theta_a+\theta_b} (v_i \cdot \mathbf{e}_{\boldsymbol{r}} + v_r \cdot \mathbf{e}_{\boldsymbol{r}}) \cos(n'_t z)\, \mathrm{e}^{-\mathrm{i}n'_s\theta} \mathrm{d}z \mathrm{d}\theta \\ &\qquad = \int_{h_b/2}^{h_a+h_b/2} \int_0^{\theta_a} (v_d \cdot \mathbf{e}_{\boldsymbol{r}} + v_u \cdot \mathbf{e}_{\boldsymbol{r}}) \cos(n'_t z)\, \mathrm{e}^{-\mathrm{i}n'_s\theta} \mathrm{d}z \mathrm{d}\theta \end{aligned} \tag{2.99}$$

where

$$n'_t = t'\frac{\pi}{h_a + h_b} \qquad , n'_s = n + s'V$$

Using the orthogonality of the different modal bases, the matching equations become:

$$\boxed{\begin{aligned} &A_{nj} H_n^{(1)}\left(K_j r_1\right) \Lambda^{(\theta)}_{q'n} \Lambda^{(z)}_{p'j} + \sum_{s=-\infty}^{+\infty} \sum_{t=0}^{+\infty} R_{n_s t} H_{n_s}^{(2)}\left(K_t r_1\right) \Lambda^{(\theta)}_{q's} \Lambda^{(z)}_{p',t} \\ &\qquad = \left[D^0_{q'p'} H_{n'_q}^{(1)}\left(K_{p'} r_1\right) + U^0_{q'p'} H_{n'_q}^{(2)}\left(K_{p'} r_1\right)\right] \frac{\theta_a}{2}\left(1 + \delta_{q'0}\right) \frac{h_a}{2}\left(1 + \delta_{p',0}\right) \end{aligned}} \tag{2.100}$$

$$\boxed{\begin{aligned} &\left[A_{nj} H_n^{(1)\prime}\left(K_j r_1\right) \delta_{s'0} \delta_{jt'} + R_{n'_s t'} H_{n'_s}^{(2)\prime}\left(K_{t'} r_1\right)\right] \left(\theta_a + \theta_b\right) \frac{h_a + h_b}{2}\left(1 + \delta_{t'0}\right) \\ &\qquad = \sum_{q=0}^{+\infty} \sum_{p=0}^{+\infty} \left[D^0_{qp} H_{n_q}^{(1)\prime}\left(K_p r_1\right) + U^0_{qp} H_{n_q}^{(2)\prime}\left(K_p r_1\right) \varphi^{(\theta)}_{s'q} \varphi^{(z)}_{t'p}\right] \end{aligned}} \tag{2.101}$$

where the matrices $\Lambda^{(z)}_{p'j}$, $\Lambda^{(z)}_{p't}$ and $\varphi^{(z)}_{t'p}$ represent the projection integrals of the axial eigenfunctions

$$\Lambda^{(z)}_{p'j} = \int_{h_b/2}^{h_a + h_b/2} \cos\left(k'_p\left[x - \frac{h_b}{2}\right]\right) \cos\left(k_j x\right) \mathrm{d}x$$

$$\Lambda^{(z)}_{p't} = \int_{h_b/2}^{h_a + h_b/2} \cos\left(k'_p\left[x - \frac{h_b}{2}\right]\right) \cos\left(k_t x\right) \mathrm{d}x$$

$$\varphi^{(z)}_{t'p} = \int_{h_b/2}^{h_a + h_b/2} \cos\left(k'_t x\right) \cos\left(k_p\left[x - \frac{h_b}{2}\right]\right) \mathrm{d}x$$

and $\Lambda^{(\theta)}_{q'n}$, $\Lambda^{(\theta)}_{q's}$ and $\varphi^{(\theta)}_{s'q}$ are the projection integrals of the azimuthal eigenfunctions

$$\Lambda^{(\theta)}_{q'n} = \int_0^{\theta_a} \cos\left(n'_q \theta\right) \mathrm{e}^{\mathrm{i}n\theta} \mathrm{d}\theta$$

$$\Lambda^{(\theta)}_{q's} = \int_0^{\theta_a} \cos\left(n'_q \theta\right) \mathrm{e}^{\mathrm{i}n_s\theta} \mathrm{d}\theta$$

$$\varphi^{(\theta)}_{s'q} = \int_0^{\theta_a} \mathrm{e}^{-\mathrm{i}n'_s\theta} \cos\left(n_q \theta\right) \mathrm{d}\theta$$

### 2.4.2.2 Channel outlet $r = r_2$

The matching equations at the outlet interface $r_2$ are derived in the same way as for the inlet interface. The continuity equations of acoustic pressure and radial vecolity at the outlet interface of the bars $r = r_2$ read

$$\begin{aligned}\sum_{q=0}^{+\infty}\sum_{p=0}^{+\infty}\left[D_{qp}^{0}H_{n_q}^{(1)}\left(K_p r_2\right)+U_{qp}^{0}H_{n_q}^{(2)}\left(K_p r_2\right)\right]\cos\left(k_p\left[x-\frac{h_b}{2}\right]\right)\cos\left(n_q\theta\right)\\ =\sum_{s=-\infty}^{+\infty}\sum_{t=0}^{+\infty}T_{n_s t}H_{n_s}^{(1)}\left(K_t r_2\right)\cos\left(k_t x\right)\mathrm{e}^{\mathrm{i}n_s\theta}\end{aligned}\qquad(2.102)$$

$$\begin{aligned}\sum_{q=0}^{+\infty}\sum_{p=0}^{+\infty}\left[D_{qp}^{0}H_{n_q}^{(1)\prime}\left(K_p r_2\right)+U_{qp}^{0}H_{n_q}^{(2)\prime}\left(K_p r_2\right)\right]\cos\left(k_p\left[x-\frac{h_b}{2}\right]\right)\cos\left(n_q\theta\right)\\ =\sum_{s=-\infty}^{+\infty}\sum_{t=0}^{+\infty}T_{n_s t}H_{n_s}^{(1)\prime}\left(K_t r_2\right)\cos\left(k_t x\right)\mathrm{e}^{\mathrm{i}n_s\theta}\end{aligned}\qquad(2.103)$$

After projecting Equations 2.102 and 2.103 on the two sets of eigenfunctions, and accounting for their orthogonality, we obtain

$$\boxed{\begin{aligned}\left[D_{q'p'}^{0}H_{n'_q}^{(1)}\left(K_{p'}r_2\right)+U_{q'p'}^{0}H_{n'_q}^{(2)}\left(K_{p'}r_2\right)\right]\frac{\theta_a}{2}\left(1+\delta_{q'0}\right)\frac{h_a}{2}\left(1+\delta_{p'0}\right)\\ =\sum_{s=-\infty}^{+\infty}\sum_{t=0}^{+\infty}T_{n_s t}H_{n_s}^{(1)}\left(K_t r_2\right)\Lambda_{q's}^{(\theta)}\Lambda_{p't}^{(z)}\end{aligned}}\qquad(2.104)$$

$$\boxed{\begin{aligned}\sum_{q=0}^{+\infty}\sum_{p=0}^{+\infty}\left[D_{qp}^{0}H_{n_q}^{(1)\prime}\left(K_p r_2\right)+U_{qp}^{0}\;H_{n_q}^{(2)\prime}\left(K_p r_2\right)\right]\varphi_{s',q}^{(\theta)}\varphi_{t'p}^{(z)}\\ =T_{n'_s t'}H_{n'_s}^{(1)\prime}\left(K_{t'}r_2\right)\left(\theta_a+\theta_b\right)\frac{h_a+h_b}{2}\left(1+\delta_{t'0}\right)\end{aligned}}\qquad(2.105)$$

#### 2.4.2.3 Solving procedure

As explained previously, these matching equations are solved by a direct matrix inversion. The matrix form of Equations 2.100, 2.101, 2.104 and 2.105 is given by:

$$\begin{pmatrix}\underline{\mathbf{E_p^1}} & \underline{\mathbf{F_p^1}} & \underline{\mathbf{X_p^1}} & \mathbf{0}\\ \underline{\mathbf{E_v^1}} & \underline{\mathbf{F_v^1}} & \underline{\mathbf{X_v^1}} & \mathbf{0}\\ \mathbf{0} & \underline{\mathbf{F_p^2}} & \underline{\mathbf{X_p^2}} & \underline{\mathbf{E_p^2}}\\ \mathbf{0} & \underline{\mathbf{F_v^2}} & \underline{\mathbf{X_v^2}} & \underline{\mathbf{E_v^2}}\end{pmatrix}\begin{pmatrix}\mathbf{R}\\ \mathbf{D^0}\\ \mathbf{U^0}\\ \mathbf{T}\end{pmatrix}\begin{pmatrix}\mathbf{H_p^1}\\ \mathbf{H_v^1}\\ \mathbf{0}\\ \mathbf{0}\end{pmatrix}\qquad(2.106)$$

with

$$\begin{aligned}
\underline{\mathbf{E}}^{\mathbf{1}}_{\mathbf{p}}(\beta,\alpha) &= \Phi_{n_s}\left(K_t r_1\right) \Lambda^{(\theta)}_{q's} \Lambda^{(z)}_{p't} \\
\underline{\mathbf{F}}^{\mathbf{1}}_{\mathbf{p}}(\beta,\beta) &= -H^{(1)}_{n'_q}\left(K_{p'} r_1\right) \frac{\theta_a}{2}\left(1+\delta_{q'0}\right) \frac{h_a}{2}\left(1-\delta_{p'0}\right) \\
\underline{\mathbf{X}}^{\mathbf{1}}_{\mathbf{p}}(\beta,\beta) &= -\Phi_{n'_q}\left(K_{p'} r_1\right) \frac{\theta_a}{2}\left(1+\delta_{q'0}\right) \frac{h_a}{2}\left(1-\delta_{p'0}\right) \\
\mathbf{H}^{\mathbf{1}}_{\mathbf{p}}(\beta,\mathbf{1}) &= -A_{n,j} H^{(1)}_{n}\left(K_j r_1\right) \Lambda^{(\theta)}_{q'n} \Lambda^{(z)}_{p'j} \\
\underline{\mathbf{E}}^{\mathbf{1}}_{\mathbf{v}}(\alpha,\alpha) &= \Phi'_{n'_s}\left(K_{t'} r_1\right) \left(\theta_a+\theta_b\right) \frac{h_a+h_b}{2}\left(1+\delta_{t'0}\right) \\
\underline{\mathbf{F}}^{\mathbf{1}}_{\mathbf{v}}(\alpha,\beta) &= -H^{(1)\prime}_{n_q}\left(K_p r_1\right) \varphi^{(\theta)}_{s'q} \varphi^{(z)}_{t'p}
\end{aligned}$$

$$\begin{aligned}
\underline{\mathbf{X}}^{\mathbf{1}}_{\mathbf{v}}(\alpha,\beta) &= -\Phi'_{n_q}\left(K_p r_1\right) \varphi^{(\theta)}_{s'q} \varphi^{(z)}_{t'p} \\
\mathbf{H}^{\mathbf{1}}_{\mathbf{v}}(\alpha,\mathbf{1}) &= -A_{n,j} H^{(1)\prime}_{n}\left(K_j r_1\right) \delta_{s'0}\delta_{jt'} \left(\theta_a+\theta_b\right) \frac{h_a+h_b}{2}\left(1+\delta_{t'0}\right) \\
\underline{\mathbf{F}}^{\mathbf{2}}_{\mathbf{p}}(\beta,\beta) &= H^{(1)}_{n'_q}\left(K_{p'} r_2\right) \frac{\theta_a}{2}\left(1+\delta_{q'0}\right) \frac{h_a}{2}\left(1-\delta_{p'0}\right) \\
\underline{\mathbf{X}}^{\mathbf{2}}_{\mathbf{p}}(\beta,\beta) &= \Phi_{n'_q}\left(K_{p'} r_2\right) \frac{\theta_a}{2}\left(1+\delta_{q'0}\right) \frac{h_a}{2}\left(1-\delta_{p'0}\right) \\
\underline{\mathbf{E}}^{\mathbf{2}}_{\mathbf{p}}(\beta,\alpha) &= -H^{(1)}_{n_s}\left(K_t r_2\right) \Lambda^{(\theta)}_{q's} \Lambda^{(z)}_{p't} \\
\underline{\mathbf{F}}^{\mathbf{2}}_{\mathbf{v}}(\alpha,\beta) &= H^{(1)\prime}_{n_q}\left(K_p r_2\right) \varphi^{(\theta)}_{s'q} \varphi^{(z)}_{t'p} \\
\underline{\mathbf{X}}^{\mathbf{2}}_{\mathbf{v}}(\alpha,\beta) &= \Phi'_{n_q}\left(K_p r_2\right) \varphi^{(\theta)}_{s'q} \varphi^{(z)}_{t'p} \\
\underline{\mathbf{E}}^{\mathbf{2}}_{\mathbf{v}}(\alpha,\alpha) &= -H^{(1)\prime}_{n'_s}\left(K_{t'} r_2\right) \left(\theta_a+\theta_b\right) \frac{h_a+h_b}{2}\left(1+\delta_{t'0}\right)
\end{aligned}$$

where

$$\alpha = (s,t) \qquad ,\beta = (q,p)$$

## 2.4.3 Results

### 2.4.3.1 Sample results

Sample results are presented in this section for the diffraction of a single incident mode of order $(n = 5, j = 2)$ by $V = 13$ rigid bars. The parameters used in the test-case are listed in Table 2.4. The instantaneous acoustic potential field obtained by the mode-matching method is illustrated in Figure 2.43 by an axial cut at $x = (h_a + h_b)/2$ (Figure 2.43a) and a cut at a constant azimuthal angle at $\theta = \theta_a/2$ (Figure 2.43b). These figures confirm that the incident wave is scattered in both directions of propagation (azimuthal and axial). Figure 2.43a shows a typical diverging spiral wave front composed mainly of

| $r_0$ | $r_1$ | $r_2$ | $V$ | $H$ | $h_b/(h_b+h_a)$ | $\theta_b V/2\pi$ | $A_{nj}$ | $f$ | $n$ | $j$ |
|---|---|---|---|---|---|---|---|---|---|---|
| 0.10 | 0.25 | 0.30 | 13 | 0.4 | 0.2 | 0.2 | 1 | 4000 | 5 | 2 |

**Table 2.4:** Test case parameters. Diffraction of a spiral wave by the rigid bars

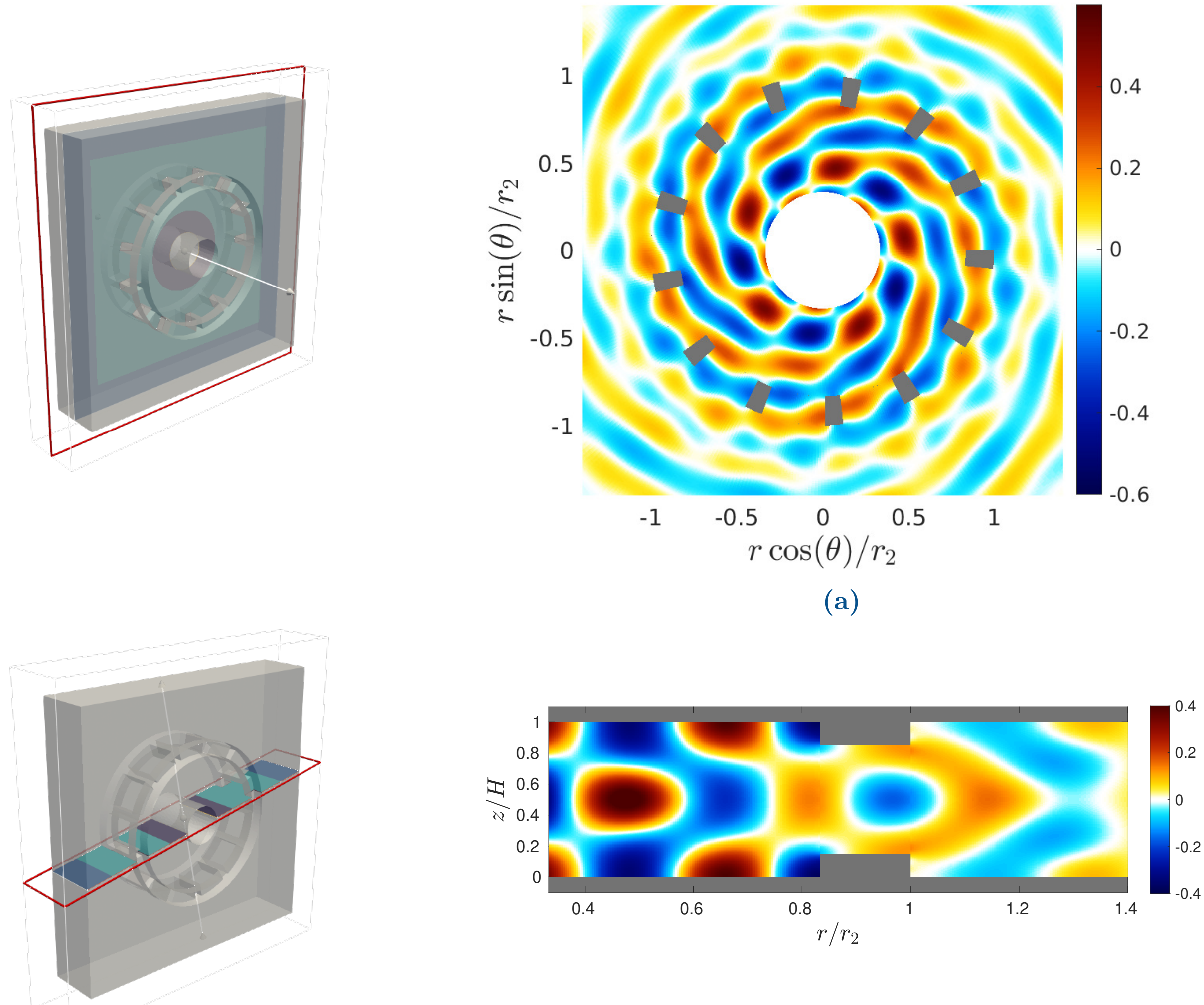

(a)

(b)

**Figure 2.43:** Instantaneous acoustic potential field obtained by the mode-matching technique (a) Axial cut at $x = H/2$. (b) Cut at a constant azimuthal angle $\theta = \theta_a/2$. $f = 4000$Hz, $n = 3$, $j = 2$, $V = 13$

5 lobes and rotating in the counter-clockwise direction. This field is modulated by the presence of several axial and azimuthal modes generated by the diffraction. The effect of the rigid-wall boundary condition applied to the parallel discs can be seen in Figure 2.43b.

### 2.4.3.2 Effect of thickness

To further investigate the influence of the bar thickness on sound transmission at the motor air outlet, a comparative study between four configurations with different bar thicknesses has been carried out. Note here that the step discontinuity in the axial direction is ignored in this section $h_b = 0$, in order to quantify only the influence of the thickness of bar separators $\theta_b$. In this case, the diffraction of the incident wave occurs only in the azimuthal direction. The thickness values of the different configurations are given in Table 2.5. The impeller trailing edge, the inlet and the outlet interfaces of the

| **Configuration** | 1 | 2 | 3 | 4 |
|---|---|---|---|---|
| $\boldsymbol{\theta_a V/2\pi}$ | 0 | 0.2 | 0.5 | 0.8 |

**Table 2.5:** Thickness values of the different configurations

rigid bars are respectively located at the radii $r_0 = 0.1$m, $r_1 = 0.25$m and $r_2 = 0.3$m. The instantaneous acoustic potential fields obtained for the diffraction of a single incident

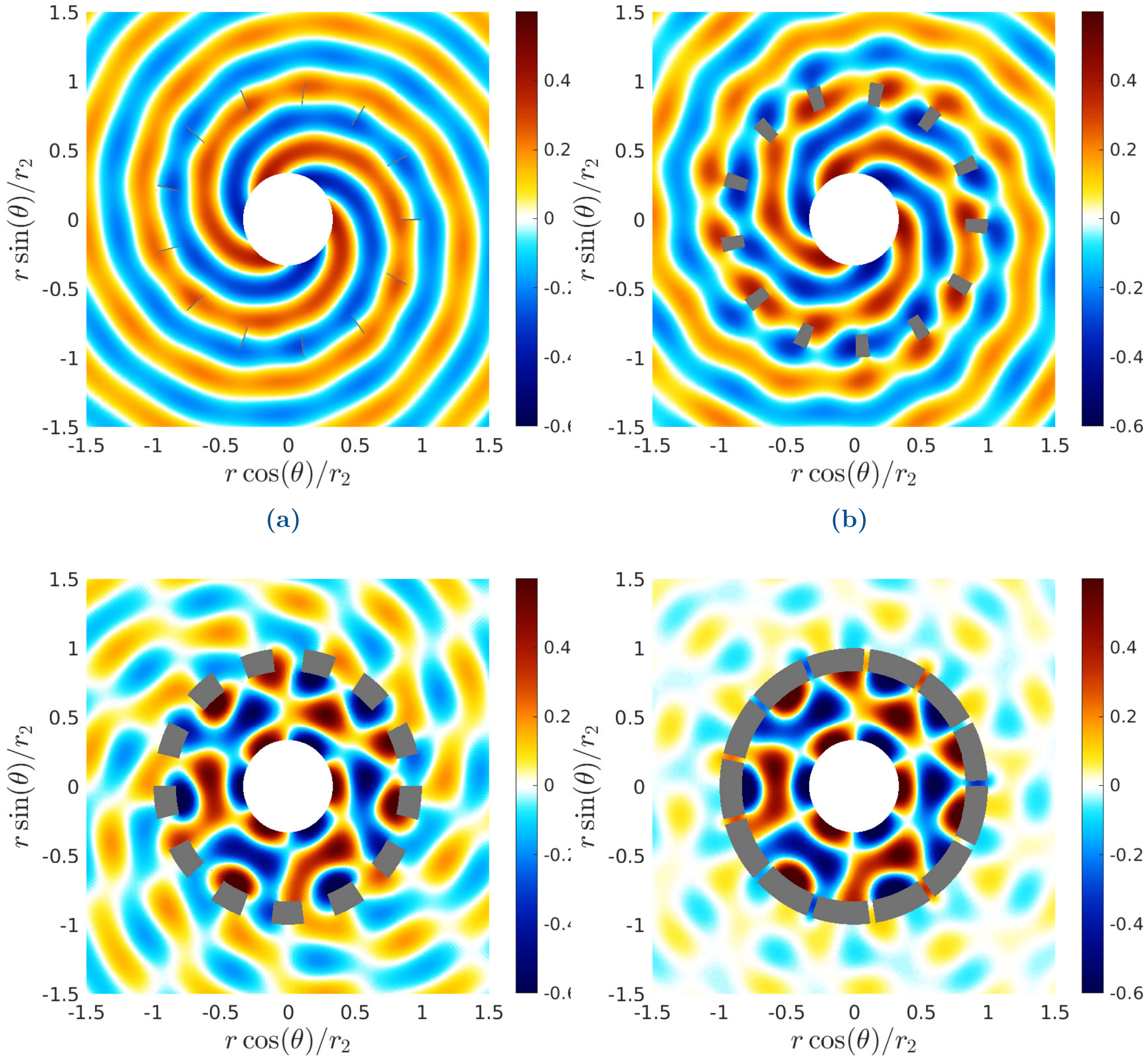

(a)

(b)

(c)

(d)

**Figure 2.44:** Instantaneous acoustic potential field for four thickness values. (a) $\theta_b V/2\pi = 0$, (b) $\theta_b V/2\pi = 0.2$, (c) $\theta_b V/2\pi = 0.5$, (d) $\theta_b V/2\pi = 0.9$. $f = 2500$ Hz, $j = 0$, $n = 3$

diverging mode of order $(3, 0)$, at the frequency $f = 2500$ Hz are shown in Figure 2.44 for the different configurations. Figures 2.44a and 2.44b clearly confirm that small wall-thicknesses generally yield only small reflections. In both configurations, the incident wave is almost totally transmitted downstream the rigid bars. As can be seen, the transmitted acoustic field is typically dominated by the mode $(3, 0)$ and slightly modulated by other modes generated by the diffraction $(n_s, 0)$. The effect of these, is less marked in the first configuration (Figure 2.44a), compared to the second one (Figure 2.44a). However, the effect of the rigid bars seems to be significant when the wall-thickness increases, as illustrated in Figures 2.44c and 2.44d. It can readily be seen from Figure 2.44c that upstream of the rigid bars, the interference between the incident and reflected fields becomes more complex, due to the increased bar thickness. Furthermore, it is found that the transmitted field is no longer dominated by the mode $(3, 0)$. It is dominated by the mode $(-10, 0)$ generated by the combination $n_s = n + sV = 3 + (-1)13 = -10$, where the 10 azimuthal lobes are rotating in clockwise direction. In the case of very thick bars (Figure 2.44d), the incident wave is strongly reflected back towards the radial impeller, causing more interference between the different acoustic waves, compared to the other configurations. Consequently, this involves a low noise transmission to the external environment.

Acoustically, the most straightforward way to reduce the transmission of motor noise to the external environment, is to use the last configuration (see Figure 2.44d). In contrast, the aerodynamic performance of the ventilation system must also be considered. It is worth noting that this configuration would not be encountered in practice because of its unacceptable flow blockage effect.

## 2.5 Conclusion

Three-dimensional analytical models based on the mode-matching method have been proposed in this chapter in order to investigate how sound can propagate in the stationary part of the ventilation system integrated in an open motor. The aim was to predict acoustic resonances in the ventilation system, in order to avoid them during the design stage. In the first step, the realistic configuration of the motor was substituted by a simplified configuration, composed only of several interconnected generic elements. Then, the acoustic field was expressed in each element as a sum of orthogonal modes. The modal amplitudes of the different acoustic fields have been determined by the use of the mode-matching method. The system of linear equations obtained by matching equations has been divided into two subsystems because of the important number of unknowns. Each subsystem has been solved by direct matrix inversion. Then, an iterative procedure was employed to couple the two subsystems. The results obtained by the analytical model have been validated by comparison with the finite element method. In the first step, both methods were applied to a simplified configuration of an open motor, specifically for mathematical validation purposes. A very good agreement was found between the results obtained by the two methods. Following this successful validation, the finite element method was then applied to the realistic configuration of an open motor, including all the curvatures present in the stationary part of the motor. The comparison of the results obtained by the two methods indicated a good agreement particularly at low and medium frequencies of interest. However, the difference between the two results seems to be significant at relatively high frequencies.

Throughout this chapter, various parametric studies were conducted, highlighting the fact that the acoustic resonances are not only caused by the stator cooling channels. The results obtained by this model have indicated that acoustic resonances can occur at different locations in the ventilation system. However this confirms that the use of a model encompassing all motor components is necessary to accurately predict the resonant frequencies of the ventilation system.

# Chapter 3

# Sound transmission through periodic rows of rotating channels

## 3.1 Introduction

The present chapter is dealing with sound transmission through two rotating rows of thick-walled channels. As what has been already discussed in the previous chapters, all ventilation systems integrated in electrical machines possess both a stationary part and a rotating part. The latter can either be the cooling fan and/or the ventilating holes integrated in the rotor core. So far in this work, only the propagation of acoustic waves inside the stationary part of the two types of motors has been addressed. In reality, the effects due to rotation have a considerable influence on the propagation of sound waves in the ventilation system, and they cannot be neglected in the analysis. Analytical modelling of sound transmission through systems consisting of both rotating and stationary parts is of considerable practical interest. In an industrial context, this can be seen, for instance, as a rotor/stator stage of a turbomachine [99, 50, 36] or a system composed of the two parts such as a traction motor used in railway applications. However, the use of numerical methods to take into account rotational effects requires the use of both fixed and moving meshes [36, 52, 96]. Each mesh represents a separate computational subdomain in which the wave equation must be satisfied. The transmission of acoustic waves between the fixed and moving meshes is then achieved by performing a simple interpolation between the grids of these meshes. On the other hand, the acoustic power of the scattered field is distributed not only over several modes but also over several frequencies [50]. Consequently, this requires solving the wave equation in the time domain and not in the frequency domain.

In this chapter, an analytical model based on a two-dimensional mode-matching technique is proposed to deal with this problem. Two kinds of coupled systems are investigated, mainly composed of two periodic rows of thick-walled channels. In the first configuration, one row rotates at constant rotational speed denoted $\Omega$, and the other row is considered fixed. The second configuration corresponds to two rows of channels rotating with different rotational speeds. This last configuration can be used to give a first understanding of the propagation mechanism inside new technology motors, known as autonomous motors, where the radial impeller does not rotate in the same direction and at the same rotational speed as the motor.

## 3.2 Scattering of an oblique plane wave by the rotor channels

As explained in Chapter 1, the coupled system can be divided into two sub-systems addressed separately. This section addresses only the diffraction of a single oblique plane wave by a single row of rotating channels, in order to investigate how the sound can be transmitted through the cooling channels integrated in the rotor core. The typical configuration of the latter is shown in Figure 3.1. It consists of $V$ channels of circular cross-section and length $L$. Since the radial dimensions of this geometry are smaller than acoustic wavelengths $r_{R_d} - r_1 << \lambda$, the problem can simply be addressed by using a two-dimensional approach. For that, an unwrapped representation of a cylindrical cut of the rotor ducts at $r = r_0$ is described in a two-dimensional Cartesian coordinates system, as sketched in Figure 3.2b. The channels have a width denoted by $a$, and separated by rigid walls of thickness $b$. In this analysis, the cooling channels are rotating counter-clockwise at a constant rotational speed denoted by $\Omega$. This effect can be reproduced by a translational motion of the channels in the direction of increasing $z$ at the speed $\Omega r_0$ (see Figure 3.2b). An incident wave $\phi_i^{(a)}$ composed of $n$ azimuthal lobes, propagates in the positive $x$ direction towards the channels with a certain angle $\theta_i$. The scattering of this wave by the channels generates four acoustic fields denoted by $\phi_r^{(a)}$, $\phi_d^{(a)}$, $\phi_u^{(a)}$ and

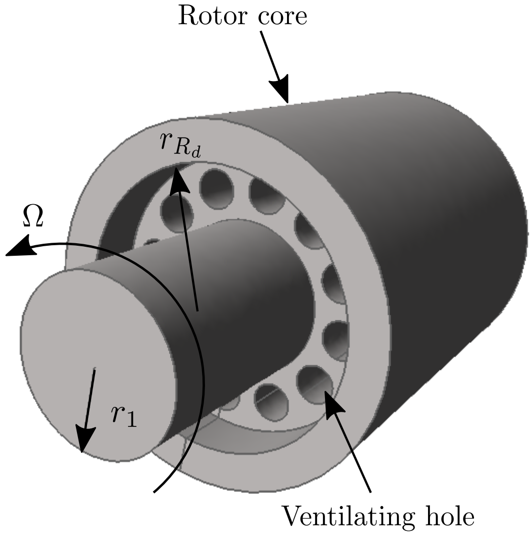

**Figure 3.1:** Typical configuration of the ventilating holes (cooling channels) integrated in the rotor core.

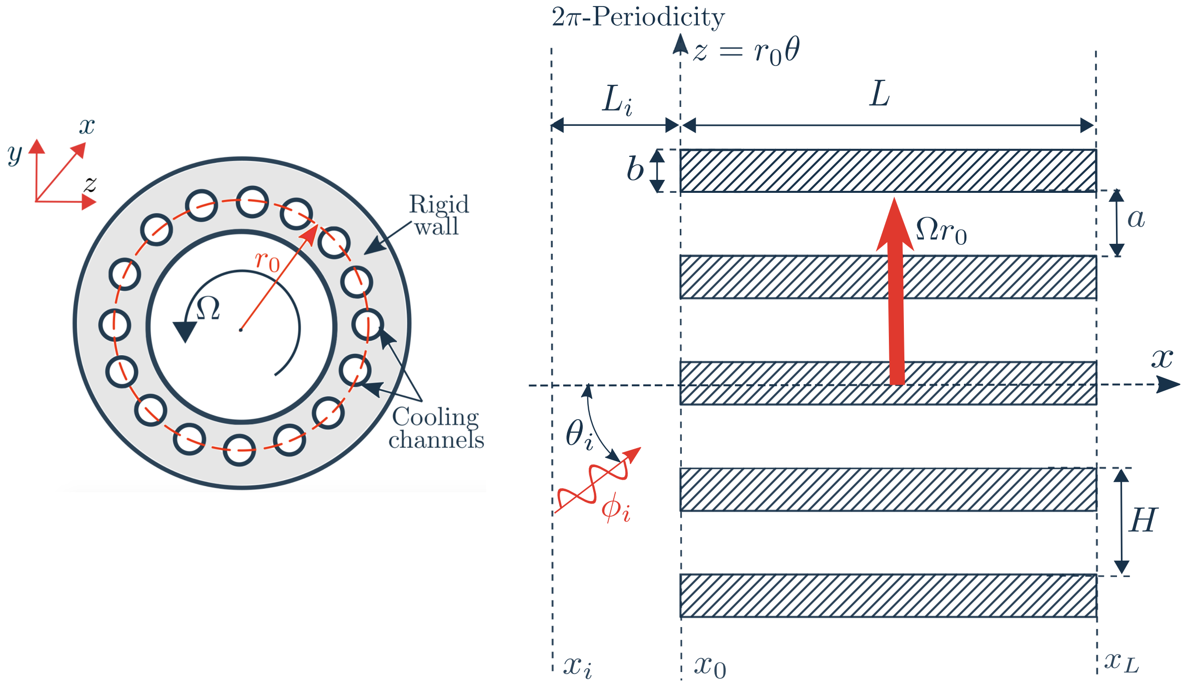

(a)

(b)

**Figure 3.2:** ($a$) Axial cut representation of the rotor channels. ($b$) Unwrapped representation of a cylindrical cut at $r = r_0$

$\phi_t^{(a)}$ at different frequencies, where the superscript $(a)$ refers to the waves expressed in the stationary reference frame (observer at rest). The downstream and upstream propagating acoustic fields inside the cooling channels $\phi_d^{(a)}$ and $\phi_u^{(a)}$ propagate at a relative frequency given by $\omega_r = \omega_0 - n\Omega$. On the other hand, the frequency of each reflected $\phi_r^{(a)}$ and transmitted $\phi_t^{(a)}$ acoustic mode is modulated by the rotation of the channels. However, each mode of order $n_s = n+sV$ propagates at a modulated frequency given $\omega_s = n+sV\Omega$. It is important to note that it will be more practical to express the different acoustic fields in the stationary reference frame, in the case where the rotor channels must be coupled with a stationary part such as the stator channels. But, since the different fields are not at the same frequency, the matching equations cannot be formulated in this reference frame. The procedure adopted in this work to deal with this problem, can be divided into three successive steps:

1. Express the incident wave in the reference frame related to the cooling channels by changing the frequency $\omega \rightarrow \omega_r$.
2. Writing the matching equations in the relative frame of reference at the same frequency $\omega_r$, by imposing the continuity of physical quantities at both ends of channels. This allows to determine the modal coefficients of the different fields.
3. Express all acoustic fields in the reference frame related to an observer at rest, by performing a change of coordinates and frequencies.

### 3.2.1 Acoustic potentials in the relative reference frame (observer attached to the channels)

As a first step, the incident excitation needs to be expressed in the reference frame attached to the rotating channels $\phi_i^{(a)} \to \phi_i^{(r)}$, by modifying its angular frequency $\omega \to \omega_r = \omega - n\Omega$. The scattering of $\phi_i^{(r)}$ generates four acoustic fields denoted by $\phi_r^{(r)}$, $\phi_d^{(r)}$, $\phi_u^{(r)}$ and $\phi_t^{(r)}$, where the superscript $(r)$ denotes wave expressed in the relative reference frame (observer attached to the rotating channels). Note here that all the acoustic fields generated in this reference frame propagate at the same angular frequency $\omega_r$ (see Figure 3.3). In addition, an observer moving with the rotor channels would observe a grazing flow in the unbounded domains located upstream and downstream of channels, which moves in the opposite direction of rotation (see Figure 3.3). Therefore, the incident $\phi_i^{(r)}$, reflected $\phi_r^{(r)}$ and transmitted $\phi_t^{(r)}$ fields must satisfy the convected Helmholtz equation with a uniform flow in the direction of decreasing $z$. It is given by

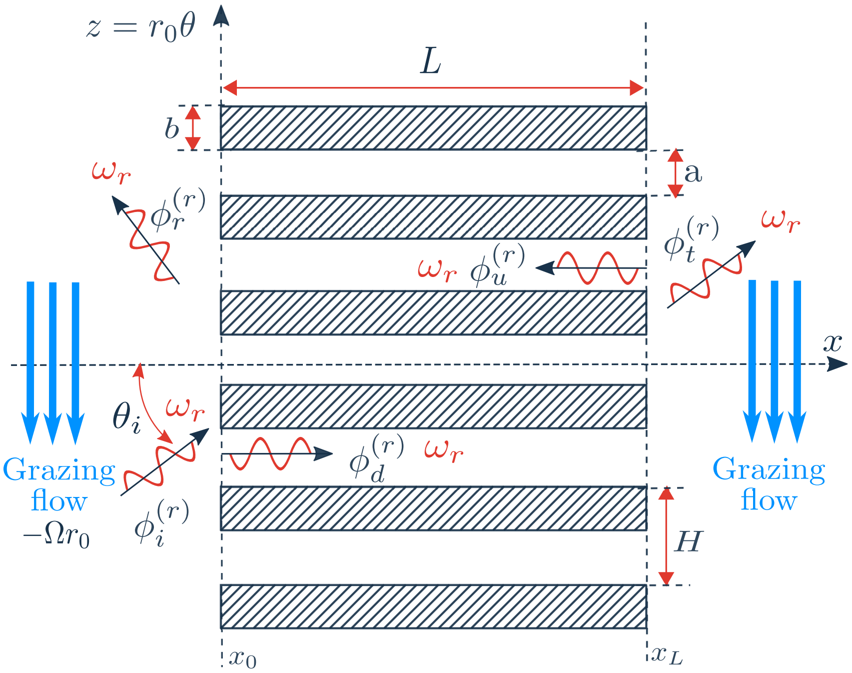

**Figure 3.3:** Two-dimensional unwrapped representation of the scattering of an incident wave by a row of rotating channels described in the relative reference frame. Grazing flow (blue)

$$(1 - M_z^2)\frac{\partial^2 \phi}{\partial z^2} + \frac{\partial \phi}{\partial x} - 2\mathrm{i}k_r M_z^2 \frac{\partial \phi}{\partial z} + k_r^2 \phi = 0, \qquad k_r = k_0 - \frac{n\Omega}{c_0} \tag{3.1}$$

where $M_z = -\Omega r_0/c_0$ is the tangential Mach number of the flow, and $k_r$ is the acoustic wavenumber expressed in the relative reference frame.

The acoustic pressure of the upstream and downstream acoustic fields can be deduced from their acoustic potentials:

$$\begin{aligned} p^{(r)}(x,z,t) &= -\rho\left(\frac{\partial\phi^{(r)}(x,z,t)}{\partial t} - \Omega r_0\frac{\partial\phi^{(r)}(x,z,t)}{\partial z}\right) \\ &= \mathrm{i}c_0\rho\left(k_r - M_z\alpha\right)\phi^{(r)}(x,z,t) \\ &= \mathrm{i}c_0\rho\left(k_r + \frac{\Omega r_0}{c_0}\alpha\right)\phi^{(r)}(x,z,t), \quad \text{if } x<0 \text{ or } x>L \end{aligned} \tag{3.2}$$

The axial velocity is calculated by

$$\begin{aligned} v(x,z,t)\cdot\mathbf{e}_{\boldsymbol{x}} &= \frac{\partial\phi(x,z,t)}{\partial z} \\ &= \mathrm{i}k^{\pm}\phi(x,z,t) \end{aligned} \tag{3.3}$$

The acoustic potential of the incident wave $\phi_i^{(r)}$ expressed in the frame of reference attached to the cooling channels reads

$$\phi_i^{(r)}(x,z,t) = A_n \mathrm{e}^{\mathrm{i}k_i^{(r)+}(x-x_i)}\mathrm{e}^{\mathrm{i}\alpha_i z}\mathrm{e}^{-\mathrm{i}\omega_r t}, \quad k_i^{(r)+} = \sqrt{k_r^2-(1-M_z^2)\alpha_i^2+2k_rM_z\alpha_i} \tag{3.4}$$

The reflected $\phi_r^{(r)}$ and transmitted $\phi_t^{(r)}$ fields are given by

$$\begin{pmatrix}\phi_r^{(r)}(x,z,t)\\ \phi_t^{(r)}(x,z,t)\end{pmatrix} = \sum_{s=-\infty}^{+\infty}\begin{pmatrix}R_s\\ T_s\end{pmatrix}\begin{pmatrix}\mathrm{e}^{\mathrm{i}k_s^{(r)+}(x-x_0)}\\ \mathrm{e}^{\mathrm{i}k_s^{(r)-}(x-x_L)}\end{pmatrix}\mathrm{e}^{\mathrm{i}\alpha_i z}\mathrm{e}^{-\mathrm{i}\omega_r t} \tag{3.5}$$

with

$$k_s^{(r)\pm} = \pm\sqrt{k_r^2-(1-M_z^2)\alpha_s^2+2k_rM_z\alpha_s}$$

The upstream $\phi_u^{(r)}$ and downstream $\phi_d^{(r)}$ fields in the $m^{\text{th}}$ channel must satisfy the Helmholtz equation without grazing flow. They are given by:

$$\begin{pmatrix}\phi_d^{(r)}(x,z,t)\\ \phi_u^{(r)}(x,z,t)\end{pmatrix} = \sum_{q=0}^{+\infty}\begin{pmatrix}D_q^0\\ U_q^0\end{pmatrix}\mathrm{e}^{imn2\pi/V}\begin{pmatrix}\mathrm{e}^{\mathrm{i}k_q^{(r)+}(x-x_0)}\\ \mathrm{e}^{\mathrm{i}k_q^{(r)-}(x-x_L)}\end{pmatrix}\cos\left(\alpha_q\left[z-m\frac{2\pi r_0}{V}\right]\right)\mathrm{e}^{-\mathrm{i}\omega_r t} \tag{3.6}$$

with

$$k_q^{(r)\pm} = \pm\sqrt{k_r^2-\alpha_q^2}$$

The acoustic pressure inside the channels can be obtained by

$$p^{(r)}(x,z,t) = -\rho\frac{\partial\phi^{(r)}(x,z,t)}{\partial t}, \quad \text{if } x_0 \le x \le x_L \tag{3.7}$$

### 3.2.2 Matching equations

In the next step, it is necessary to match the different fields expressed in the relative reference frame at both ends of the channels, in order to determine their modal amplitudes. As mentioned earlier, the matching conditions are derived form the conservation of physical quantities on each interface separating two sub-domains with different physical or geometrical properties, as illustrated in Figure 3.4. It is important to note that these conditions do not reduce to the continuity of the acoustic pressure and the axial velocity, because of the presence of the grazing flow in the azimuthal direction. Ingenito *et al* [59, 58] have demonstrated that only the acoustic pressure and the normal displacement are continuous at the junction interface:

$$p_2(x_0, z) = p_1(x_0, z)$$

$$v_2(x_0, z) \cdot \mathbf{e}_{\boldsymbol{x}} = v_1 \cdot \mathbf{e}_{\boldsymbol{x}} \left(1 - \frac{\Omega r_0 \alpha_s}{\omega_s}\right)$$

These have been used to address the problem of sound transmission through the inter-blade channels of a centrifugal fan, by considering the impeller inlet as a cascade of semi-infinite channels. However, in the literature, these matching conditions are typically applied on the surface of liners in the presence of a grazing flow [9].

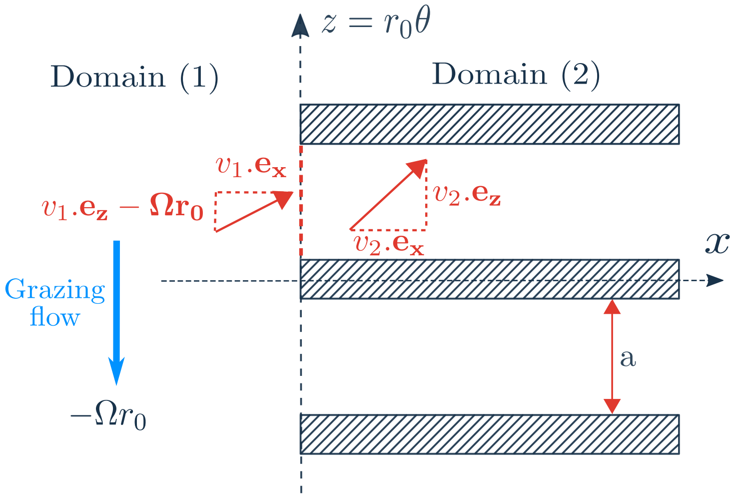

**Figure 3.4:** Unwrapped representation of a cylindrical cut at $r_0$

In the following, the continuity of the acoustic pressure and the normal displacement are written at both interfaces $x = x_0$ and $x = x_L$ (see figure 3.3).

#### 3.2.2.1 Channel inlet $x = x_0$

The continuity of the acoustic pressure at the inlet interface gives

$$A_n \mathrm{e}^{\mathrm{i}\alpha_i z} \mathrm{e}^{\mathrm{i}k_i^+ L_i} \left(k_r + \frac{\Omega r_0}{c_0}\alpha_i\right) + \sum_{s=-\infty}^{+\infty} R_s \mathrm{e}^{\mathrm{i}\alpha_s z} \left(k_r + \frac{\Omega r_0}{c_0}\alpha_s\right) \\ = \sum_{q=0}^{+\infty} \left(D_q^0 + U_q^0 \mathrm{e}^{-\mathrm{i}k_q^- L}\right) \cos(\alpha_q z), \quad x = x_0, \quad 0 \le z \le a \quad (3.8)$$

The continuity of the normal displacement is written as

$$A_n k_i^{(r)+} \mathrm{e}^{\mathrm{i}\alpha_i z} \mathrm{e}^{\mathrm{i}k_i^{(r)+}L_i} \left(1 - \frac{\Omega r_0}{\omega}\alpha_i\right) + \sum_{s=-\infty}^{+\infty} R_s k_s^{(r)-} \mathrm{e}^{\mathrm{i}\alpha_s z} \left(1 - \frac{\Omega r_0}{\omega_s}\alpha_s\right)$$
$$= \sum_{q=0}^{+\infty} \left(k_q^{(r)+} D_q^0 + k_q^{(r)-} U_q^0 \mathrm{e}^{-\mathrm{i}k_q^{(r)-}L}\right) \cos(\alpha_q z), \quad x = x_0, \quad 0 \le z \le a \quad (3.9)$$

The rigid wall boundary condition must be applied on the front face of the channel separators. This corresponds to a vanishing axial velocity

$$A_n k_i^{(r)+} \mathrm{e}^{\mathrm{i}\alpha_i z} \mathrm{e}^{\mathrm{i}k_i^{(r)+}L_i} \sum_{s=-\infty}^{+\infty} R_s k_s^{(r)-} \mathrm{e}^{\mathrm{i}\alpha_s z} = 0, \quad x = x_0, \quad a \le z \le H \quad (3.10)$$

The projection of Equation 3.8 on the eigenfunction related the reference channel $\cos(\alpha_\mu z)$, gives

$$\boxed{\begin{aligned} A_n \mathrm{e}^{\mathrm{i}k_i^{(r)+}L_i} \Lambda_{\mu i} \left(k_r + \frac{\Omega r_0}{c_0}\alpha_i\right) + \sum_{s=-\infty}^{+\infty} R_s \Lambda_{\mu s} \left(k_r + \frac{\Omega r_0}{c_0}\alpha_s\right) \\ = \left(D_\mu^0 + U_\mu^0 \mathrm{e}^{-\mathrm{i}k_\mu^{(r)-}L}\right) \frac{a}{2}(1 + \delta_{\mu 0}) \end{aligned}} \quad (3.11)$$

After projecting Equation 3.9 on the eigenfunction of the unbounded medium $\mathrm{e}^{-\mathrm{i}\alpha_\nu z}$, and taking into account the rigid wall boundary condition, one obtains

$$\boxed{\begin{aligned} A_n k_i^{(r)+} \mathrm{e}^{\mathrm{i}k_i^{(r)+}L_i} \left(1 - \frac{\Omega r_0}{\omega}\alpha_i\right) H + R_\nu k_\nu^{(r)-} \left(1 - \frac{\Omega r_0}{\omega_\nu}\alpha_\nu\right) H \\ = \sum_{q=0}^{+\infty} \left(D_q^0 k_q^{(r)+} + k_q^{(r)-} U_q^0 \mathrm{e}^{-\mathrm{i}k_q^{(r)-}L}\right) \varphi_{\nu q} \end{aligned}} \quad (3.12)$$

### 3.2.2.2 Channel outlet $x = x_L$

The continuity of the acoustic pressure at the outlet interface, gives

$$\sum_{q=0}^{+\infty} \left(D_q^0 \mathrm{e}^{\mathrm{i}k_q^{(r)+}L} + U_q^0\right) \cos(\alpha_q z) = \sum_{s=-\infty}^{+\infty} T_s \mathrm{e}^{\mathrm{i}\alpha_s z} \left(k_r + \frac{\Omega r_0}{c_0}\alpha_s\right), \quad x = x_L, \ 0 \le z \le a \quad (3.13)$$

The continuity of the normal displacement is written as

$$\sum_{q=0}^{+\infty} \left(k_q^{(r)+} D_q^0 \mathrm{e}^{\mathrm{i}k_q^{(r)+}L} + k_q^{(r)-} U_q^0\right) \cos(\alpha_q z)$$
$$= \sum_{s=-\infty}^{+\infty} T_s k_s^{(r)+} \mathrm{e}^{\mathrm{i}\alpha_s z} \left(1 - \frac{\Omega r_0}{\omega_s}\alpha_s\right), \quad x = x_L, \quad 0 \le z \le a \quad (3.14)$$

The rigid wall boundary condition imposed on the back face of the channel separators is written as

$$\sum_{s=-\infty}^{+\infty} T_s k_s^{(r)+} \mathrm{e}^{\mathrm{i}\alpha_s z} = 0, \quad x = x_L, \quad a \leq z \leq H \tag{3.15}$$

In the same way, Equations 3.13 and 3.14 are respectively projected on the eigenfunctions of the reference channel $\cos(\alpha_\mu z)$ and the unbounded domain $\mathrm{e}^{-\mathrm{i}\alpha_\nu z}$

$$\boxed{\left(D_\mu^0 \mathrm{e}^{\mathrm{i}k_\mu^{(r)+}L} + U_\mu^0\right)\frac{a}{2}(1+\delta_{\mu 0}) = \sum_{s=-\infty}^{+\infty} T_s \Lambda_{\mu s}\left(k_r + \frac{\Omega r_0}{c_0}\alpha_s\right)} \tag{3.16}$$

$$\boxed{\sum_{q=0}^{+\infty}\left(k_q^{(r)+} D_q^0 \mathrm{e}^{\mathrm{i}k_q^{(r)}L} + k_q^{(r)-} U_q^0\right)\varphi_{\nu q} = T_\nu k_\nu^{(r)-}\left(1 - \frac{\Omega r_0}{\omega_\nu}\alpha_\nu\right) H} \tag{3.17}$$

As before, Equations 3.11, 3.12, 3.16 and 3.17 are truncated and solved by direct matrix inversion. Their matrix form can be written as

$$\underbrace{\begin{pmatrix} \underline{\boldsymbol{\mathcal{A}}_{\mathbf{11}}} & \underline{\boldsymbol{\mathcal{A}}_{\mathbf{11}}} & \underline{\boldsymbol{\mathcal{A}}_{\mathbf{11}}} & \mathbf{0} \\ \underline{\boldsymbol{\mathcal{A}}_{\mathbf{21}}} & \underline{\boldsymbol{\mathcal{A}}_{\mathbf{22}}} & \underline{\boldsymbol{\mathcal{A}}_{\mathbf{23}}} & \mathbf{0} \\ \mathbf{0} & \underline{\boldsymbol{\mathcal{A}}_{\mathbf{32}}} & \underline{\boldsymbol{\mathcal{A}}_{\mathbf{33}}} & \underline{\boldsymbol{\mathcal{A}}_{\mathbf{34}}} \\ \mathbf{0} & \underline{\boldsymbol{\mathcal{A}}_{\mathbf{42}}} & \underline{\boldsymbol{\mathcal{A}}_{\mathbf{43}}} & \underline{\boldsymbol{\mathcal{A}}_{\mathbf{44}}} \end{pmatrix}}_{\underline{\boldsymbol{\mathcal{A}}}} \underbrace{\begin{pmatrix} \mathbf{R} \\ \mathbf{D} \\ \mathbf{U} \\ \mathbf{T} \end{pmatrix}}_{\boldsymbol{\mathcal{X}}} = \underbrace{\begin{pmatrix} \boldsymbol{\mathcal{H}}_\mathbf{1} \\ \boldsymbol{\mathcal{H}}_\mathbf{2} \\ \mathbf{0} \\ \mathbf{0} \end{pmatrix}}_{\boldsymbol{\mathcal{H}}} \tag{3.18}$$

where $\boldsymbol{\mathcal{X}}$ represents the modal amplitude vector. The matrix $\underline{\boldsymbol{\mathcal{A}}}$ terms are given by

$$\underline{\boldsymbol{\mathcal{A}}_{\mathbf{11}}}(\nu,\nu) = \mathrm{diag}\left\{H k_\nu^{(r)-}\left(1 - \frac{\Omega r_0}{\omega_\nu}\alpha_\nu\right)\right\},$$

$$\underline{\boldsymbol{\mathcal{A}}_{\mathbf{12}}}(\nu,q) = -k_q^{(r)+}\varphi_{\nu q},$$

$$\underline{\boldsymbol{\mathcal{A}}_{\mathbf{13}}}(\nu,q) = -k_q^{(r)-}\mathrm{e}^{-\mathrm{i}k_q^{(r)-}L}\varphi_{\nu q},$$

$$\underline{\boldsymbol{\mathcal{A}}_{\mathbf{21}}}(\mu,s) = \Lambda_{\mu s}\left(k_r + \frac{\Omega r_0}{c_0}\alpha_s\right),$$

$$\underline{\boldsymbol{\mathcal{A}}_{\mathbf{22}}}(\mu,\mu) = -\mathrm{diag}\left\{\frac{a}{2}(1+\delta_{\mu 0})\right\},$$

$$\underline{\boldsymbol{\mathcal{A}}_{\mathbf{23}}}(\mu,\mu) = -\mathrm{diag}\left\{\mathrm{e}^{-\mathrm{i}k_q^- L}\frac{a}{2}(1+\delta_{\mu 0})\right\},$$

$$\underline{\boldsymbol{\mathcal{A}}_{\mathbf{32}}}(\nu,q) = \mathrm{e}^{\mathrm{i}k_q^+ L}k_q^+\varphi_{\nu q},$$

$$\underline{\boldsymbol{\mathcal{A}}_{\mathbf{33}}}(\nu,q) = k_q^-\varphi_{\nu q},$$

$$\underline{\boldsymbol{\mathcal{A}}_{\mathbf{34}}}(\nu,\nu) = -\mathrm{diag}\left\{H k_\nu^+\left(1 - \frac{\Omega r_0}{\omega_\nu}\alpha_\nu\right)\right\}$$

$$\underline{\boldsymbol{\mathcal{A}}_{\mathbf{42}}}(\mu,\mu) = \mathrm{diag}\left\{\mathrm{e}^{\mathrm{i}k_q^+ L}\frac{a}{2}(1+\delta_{\mu 0})\right\},$$

$$\underline{\boldsymbol{\mathcal{A}}_{\mathbf{43}}}(\mu,\mu) = \mathrm{diag}\left\{\frac{a}{2}(1+\delta_{\mu 0})\right\},$$

$$\underline{\boldsymbol{\mathcal{A}}_{\mathbf{44}}}(\mu,s) = -\Lambda_{\mu s}\left(k_r + \frac{\Omega r_0}{c_0}\alpha_s\right)$$

The vector $\mathcal{H}$ terms are given by

$$\boldsymbol{\mathcal{H}}_{\mathbf{1}}(\mu,\mu) = -A_n H k_i^+ \mathrm{e}^{\mathrm{i}k_i^+ L_i}\left(1 - \frac{\Omega r_0}{\omega}\alpha_i\right),$$

$$\boldsymbol{\mathcal{H}}_{\mathbf{2}}(\mu,\mu) = -A_n \mathrm{e}^{\mathrm{i}k_i^+ L_i}\Lambda_{\mu i}\left(k_r + \frac{\Omega r_0}{c_0}\alpha_i\right)$$

### 3.2.3 Scattered field in the stationary reference frame (observer at rest)

Once the modal amplitudes of the different acoustic fields have been determined in the relative frame of reference, it is necessary to describe their acoustic potentials in the reference frame attached to an observer at rest. Up to now, the incident wave is scattered into several modes propagating at the same frequency, which corresponds to that of the different waves propagating inside the channels $\omega_r$. However, to describe the different acoustic fields in the stationary reference frame, it is necessary to take into account the frequency scattering. It should be recalled here that the frequency of each mode propagating upstream or downstream the channels is modulated by an amount defined

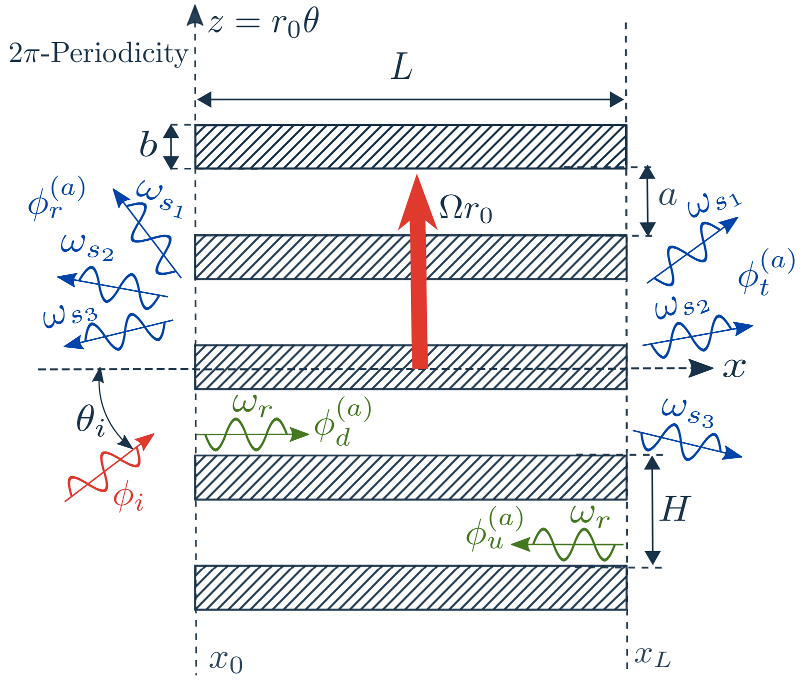

**Figure 3.5:** Two-dimensional unwrapped representation of the scattering of an incident wave by a row of rotating channels described in the stationary reference frame.

by its modal order and the rotational speed of the channels $\omega_s = \omega + sV\Omega$ (see Figure 3.5). This effect becomes more pronounced when the modal order increases. On the other hand, the reflected $\phi_r^{(a)}$ and transmitted $\phi_t^{(a)}$ acoustic potentials are solutions of the Helmholtz equation at rest. They are given by

$$\begin{pmatrix} \phi_r^{(a)}(x,z,t) \\ \phi_t^{(a)}(x,z,t) \end{pmatrix} = \sum_{s=-\infty}^{+\infty} \begin{pmatrix} R_s \\ T_s \end{pmatrix} \begin{pmatrix} \mathrm{e}^{\mathrm{i}k_s^{+(a)}(x-x_0)} \\ \mathrm{e}^{\mathrm{i}k_s^{-(a)}(x-x_L)} \end{pmatrix} \mathrm{e}^{\mathrm{i}\alpha_s z}\mathrm{e}^{-\mathrm{i}\omega_s t} \tag{3.19}$$

where

$$k_s^{(a)\pm} = \pm\sqrt{\left(\frac{\omega_s}{c_0}\right)^2 - \alpha_s^2}$$

In the same way, the acoustic potentials of the upstream $\phi_u^{(a)}$ and downstream $\phi_d^{(a)}$ propagating waves inside each channel, must satisfy the Helmholtz equation at rest. Note here that the their azimuthal function must be shifted of an amount of $\Omega r_0 t$ at each time step due to the relative motion of the channels in the stationary reference frame. The expressions of the different fields propagating inside the $m^{th}$ channel, read

$$\begin{pmatrix} \phi_d^{(a)}(x,z,t) \\ \phi_u^{(a)}(x,z,t) \end{pmatrix} = \sum_{q=0}^{+\infty} \begin{pmatrix} D_q^0 \\ U_q^0 \end{pmatrix} \mathrm{e}^{\mathrm{i}m\alpha_i H} \begin{pmatrix} \mathrm{e}^{\mathrm{i}k_q^{(r)+}(x-x_0)} \\ \mathrm{e}^{\mathrm{i}k_q^{(r)-}(x-x_L)} \end{pmatrix} \cos\left(\alpha_q\left[z - m\frac{2\pi r_0}{V} - \Omega r_0 t\right]\right)\mathrm{e}^{-\mathrm{i}\omega_r t} \tag{3.20}$$

### 3.2.4 Results

#### 3.2.4.1 Sample results

The mode-matching technique is applied in this section to the diffraction of an incident oblique plane wave composed of $n = 4$ azimuthal lobes by a periodic row of $V = 9$ rotating channels of length $L = 0.2$m and relative width $a/H = 0.6$. In this specific test case, the channels rotate clockwise (negative $z$ direction) with a negative tangential Mach number $M_z = \Omega r_0/c_0 = -0.5$. The test case parameters are listed in Table 3.1. In the following, it is instructive to compare the results obtained for this specific test-case with and without channel rotation. Figure 3.6 shows the normalized acoustic pressure fields obtained by the diffraction of the incident wave in the presence (Figure 3.6a) and the absence (Figure 3.6b) of rotation. It can readily be seen that the acoustic response of both configurations is not the same. To get further understanding of the origin of this difference, the moduli of the complex-valued modal coefficients of the various acoustic fields obtained with and without channel rotation are compared in Figure 3.7. As can be seen, without channel rotation $M_z = 0$, only one cut-on mode can be transmitted into the channels (see Figures 3.7b and

| $r_0$ (m) | $V$ | $L$ (m) | $a/H$ | $f$ (Hz) | $\Omega$ (rad/s) | $n$ | $A_n$ |
|---|---|---|---|---|---|---|---|
| 0.2 | 9 | 0.2 | 0.6 | 2000 | -850 | 4 | 1 |

**Table 3.1:** Test-case parameters

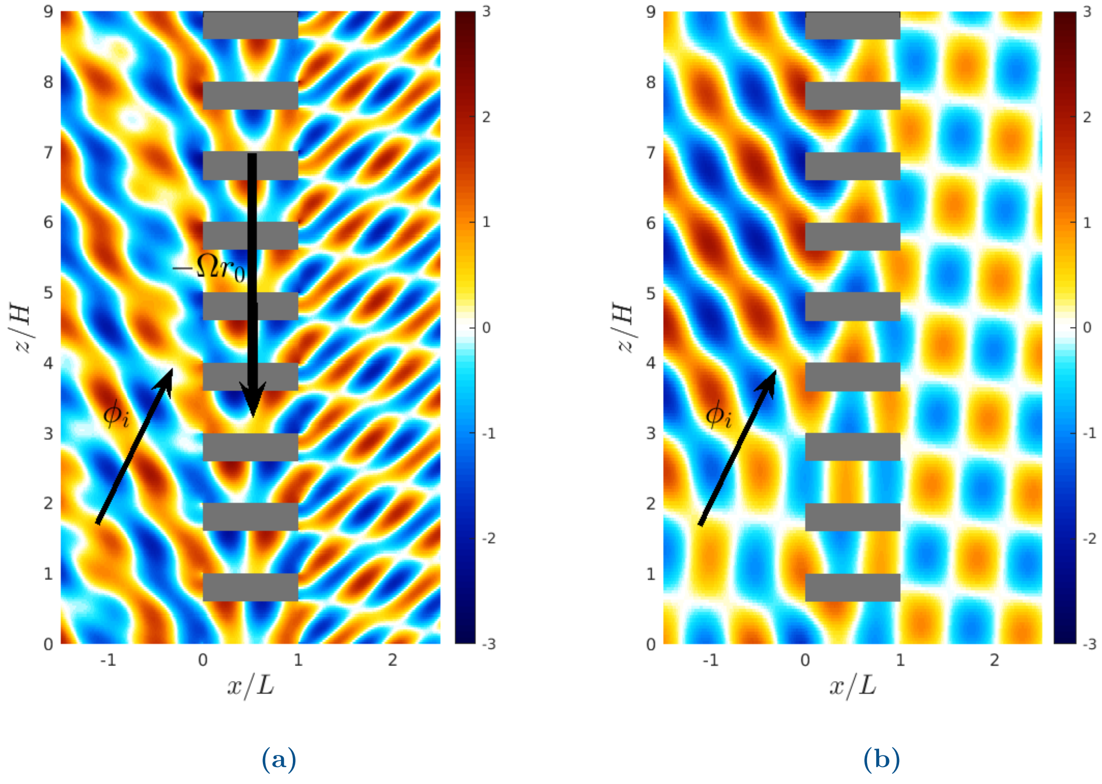

**(a)** **(b)**

**Figure 3.6:** Instantaneous acoustic pressure fields obtained by the mode-matching method. (a) $M_z = 0.5$, (b) $M_z = 0$. $r_0 = 0.2$, $V = 9$, $L = 0.2$m, $a/H = 0.6$, $f = 2000$Hz, $n = 4$, $A_n = 1$.

3.7d). All higher order modes $q > 0$ are cut-off. Their amplitudes decay exponentially from both ends of the channels. The cut-off frequencies of these modes $\omega^c_{q>0} = q\pi c_0/a$ are higher than the excitation frequency $\omega_r = \omega = 12570$ rad/s ($\omega^c_{q>0} > \omega_r$). In contrast, when the channels rotate in the negative $z$ direction with a negative tangential Mach number $M_z = -0.5$, two cut-on modes ($q = 0$ and $q = 1$) are transmitted into the channels (see Figures 3.7a and 3.7c). This is attributed to the increase in the frequency of the different acoustic waves propagating inside the channels. In fact, the frequency in the relative reference frame varies from $\omega_r = 12570$ rad/s ($f_r = 2000$Hz) without rotation to $\omega_r = \omega + n\Omega = 15970$ rad/s ($f_r = 2544$Hz) with rotation. Additionally, the cut-off frequency of the first higher order mode propagating inside the channels ($q = 1$) is given by $\omega^c_{q=1} = 12750$ rad/s ($f_c = 2029$Hz). The latter is lower than the relative frequency ($\omega^c_{q=1} < \omega_r$), and hence, it becomes cut-on. Figures 3.7f and 3.7h indicate that without rotation, the reflected and transmitted fields are dominated by the modes $n_s = 4$ and $-5$. These modes are respectively rotating counter-clockwise and clockwise. All other modes generated upstream and downstream the channels are cut-off. However, in the case of rotating channels (see Figures 3.7e and 3.7g), three cut-on modes are generated by the diffraction $n_s = 4$, $-5$ and $-14$. This is attributed to the variation of the frequency of each mode produced upstream and downstream the system. It should be reminded here, that only the mode $n_s = 4$ has the same frequency as the incident wave. The other modes

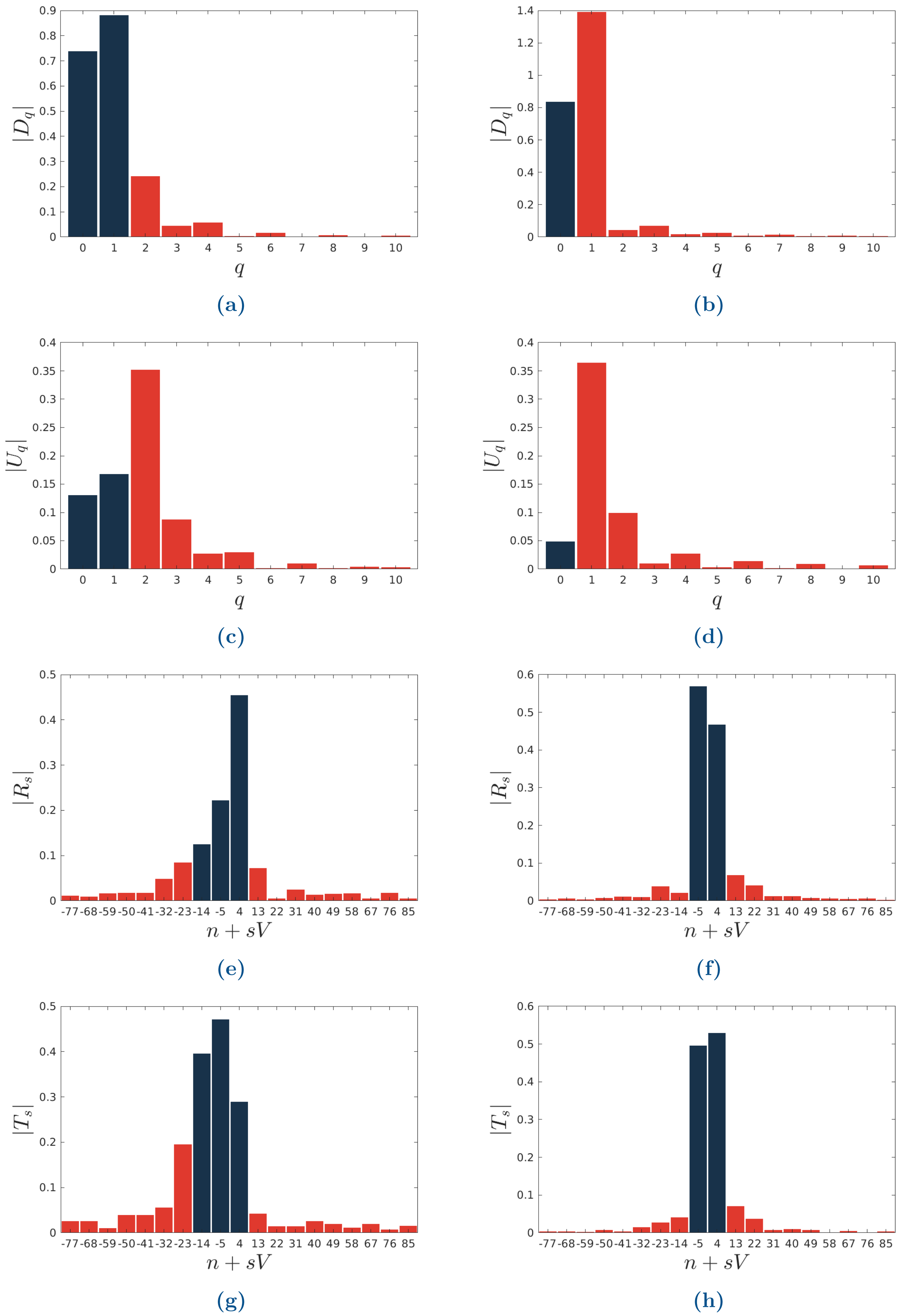

**(a)** **(b)**

**(c)** **(d)**

**(e)** **(f)**

**(g)** **(h)**

**Figure 3.7:** Modulus of the modal coefficients of the different acoustic fields generated by the diffraction of the incident wave. $M_z = 0.5$ (a-c-e-g), $M_z = 0$ (b-d-f-h), Cut-off modes (bars 🟥 ), Cut-on modes (bars ■ ).

may have higher or lower frequencies. Additionally, these modes do not propagate with the same angle $\theta_s$ in the two configurations, even if they possess the same modal order. In fact, the propagation angle of each mode depends on its modal order $n_s = n + sV$ and its frequency:

$$\Theta_s = \arcsin\left(\frac{\alpha_s}{k_0 + sV\Omega}\right) \tag{3.21}$$

The variation of the angle of propagation of each mode $n_s$ is illustrated in Figure 3.8 for three different rotational speeds $M_z = 0$, $M_z = -0.5$ and $M_z = -0.7$. The real part

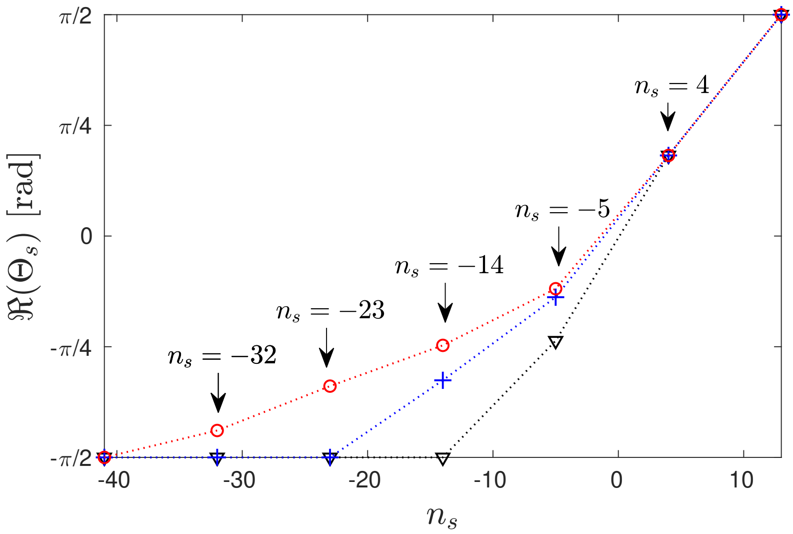

**Figure 3.8:** Variation of the angle of propagation as a function of the azimuthal order for three different rotational speeds. $M_z = 0$ (··▽··), $M_z = -0.5$ (··+··), $M_z = -0.7$ (··⊙··). $V = 9$, $n = 4$, $f = 2000$Hz, $r_0 = 0.2$m.

of the propagation angle of an oblique wave varies from $-\pi/2$ to $\pi/2$. These two limits corresponds respectively to the cut-off conditions of the co-rotating (when rotating in the same direction as the channels) and counter-rotating modes (when rotating in the opposite direction of the channels). The propagation angles become complex numbers if the cut-off condition is fulfilled. Figure 3.8 indicates that the propagation angles of the co-rotating modes $n_s < 0$ decrease with rotational speed.

### 3.2.4.2 Acoustic powers

In this section a considerable attention is paid to the modal acoustic powers of the reflected and transmitted fields. It should be reminded here that in the absence of rotation, the incident power can be distributed only on cut-on modes, which all propagate at the same frequency. The problem in this case is said to be monochromatic. The reflected and transmitted acoustic powers obtained for this test-case without rotation are respectively given by $\mathcal{P}_r/\mathcal{P}_i = 0.5024$ and $\mathcal{P}_t/\mathcal{P}_i = 0.4976$. These have been obtained by the superposition of the modal acoustic powers of the different cut-on modes generated by the diffraction. In the presence of rotation, the reflected and transmitted powers are not only distributed over several modes but also over various frequencies. The acoustic power associated with each mode of order $n_s$ can be evaluated in the two reference frames as follows [46]:

$$\text{Relative reference frame} \begin{cases} \mathcal{P}_{r,s}^{(r)} = \omega_r \rho \pi r_0 k_s^{(r)-} |R_s|^2, & \text{if} \quad (k_s^{(r)-})^2 > 0 \\ \mathcal{P}_{t,s}^{(r)} = \omega_r \rho \pi r_0 k_s^{(r)+} |T_s|^2, & \text{if} \quad (k_s^{(r)+})^2 > 0 \end{cases} \tag{3.22}$$

$$\text{Stationary reference frame} \begin{cases} \mathcal{P}_{r,s}^{(a)} = \omega_s \rho \pi r_0 k_s^{(a)-} |R_s|^2, & \text{if} \quad (k_s^{(a)-})^2 > 0 \\ \mathcal{P}_{t,s}^{(a)} = \omega_s \rho \pi r_0 k_s^{(a)+} |T_s|^2, & \text{if} \quad (k_s^{(a)+})^2 > 0 \end{cases} \tag{3.23}$$

Figure 3.9 illustrates the spectra of the transmitted and reflected powers obtained for a tangential Mach number $M_z = -0.5$. The angular frequency $\omega_s$ is scaled by dividing it by the radian frequency of the incident wave $\omega$. As can be seen, the acoustic powers are distributed only over three frequencies, corresponding to the frequencies of the azimuthal modes $n_s = 4, -5, -14$. It is observed from Figure 3.9a that the reflected power is dominated by the frequency of the incident excitation $\omega_s/\omega = 1$. The contribution of the other frequencies ($\omega_s/\omega = 1.61$ and $\omega_s/\omega = 2.22$) is less important. However, these frequencies contribute significantly in the transmitted power (see Figure 3.9b). It is important to note that the sum of the different modal acoustic powers is higher than the incident power, which means that the acoustic power is not conserved in the stationary frame. This was pointed out by Hanson [50] in a similar study of rotor-stator interaction noise in turbofan engines. The total acoustic power in the stationary reference frame is increased by the motion of the channels.

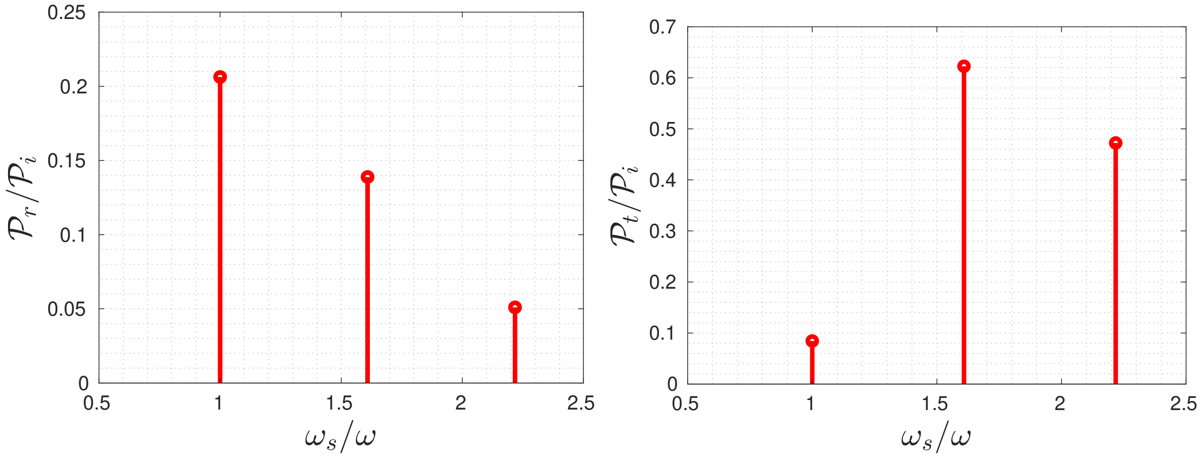

**(a)** **(b)**

**Figure 3.9:** Modal acoustic powers as functions of frequency in the stationary frame. (*a*) Reflected power. (*b*) Transmitted power

### 3.2.4.3 Resonant frequencies of the rotor channels

In order to get further understanding of the influence of the channel rotation on the acoustic resonances of the rotor ventilating holes, a comparison between three different rotational speeds has been carried out. The configuration investigated in this section consists of 17 cooling channels of length $L = 0.4$m and relative width $a/H = 0.3$. The channels are placed at a radius $r_0 = 0.2$m. The mode-matching technique is applied to the diffraction of an incident mode of order $n = 4$ by the rotating channels at three different tangential Mach numbers $M_z = 0$, $M_z = 0.2$ and $M_z = 0.3$. The comparison has been made on the acoustic powers evaluated upstream and downstream the channels. These are respectively plotted as functions of the Helmholtz number $k_0a$, corresponding to the excitation frequency (of the incident wave) in Figures 3.10a and 3.10b. As explained previously, the transmission peaks, correspond to the resonant frequencies of the cooling channels. Comparing the different spectra, it is observed that the resonant frequencies are shifted compared to the case without rotation $M_z = 0$. As previously explained, this is due to the fact that the frequency of the acoustic waves propagating inside the channels is shifted by an amount of $n\Omega$. It is obvious that the resonant frequencies in the reference frame attached to the channels are the same. They depend only on the length and width of the channels ($L$ and $a$) in the absence of mean flow. Therefore, the mathematical expression of these frequencies in the reference frame attached to an observer at rest is written as

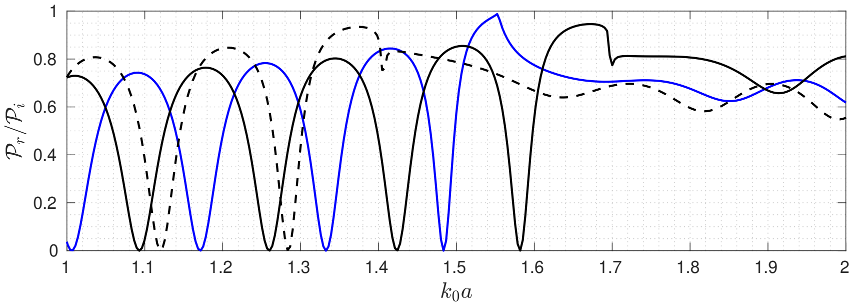

**(a)**

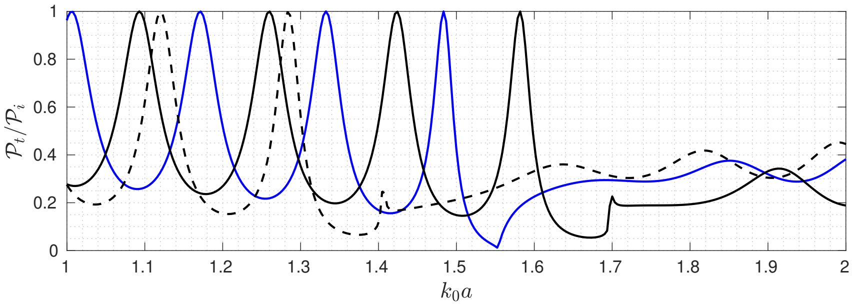

**(b)**

**Figure 3.10:** Variations of reflected (a) and transmitted (b) acoustic powers as functions of the Helmholtz number. $M_z = 0$ (——) $M_z = 0.2$ (——), $M_z = 0.3$ (- - - -),

$$\boxed{\omega_{n_r} = 2\pi \frac{n_r c_0}{2(L + \delta_L)} + n\Omega} \tag{3.24}$$

where $n_r$ and $\delta_L$ are respectively the resonant mode and the end-corrections (see Section 1.4).

## 3.3 Diffraction of sound by a system composed of a rotor and a stator

This section is dealing with the problem of sound propagation in a system consisting of both a stationary and a rotating parts. The aim is to understand how the acoustic waves are scattered by the ventilating holes integrated in the rotor and the stator cores (Figure 3.11a). As already mentioned, the rotor and the stator channels are connected by means of several interconnected annular ducts (see Chapter 2). Therefore, the problem of propagation inside this configuration have to be formulated in a three-dimensional context, due to the variations of the sound field in both azimuthal and radial directions. It should be kept in mind that the azimuthal orders of the different acoustic fields are not modified by the fact that the rotor and stator radii are different. Thus, the various frequencies induced by the interaction between stator and rotor ducts will not be affected by the annular character of the geometry. For a first insight into the underlying physics, it is assumed here for simplicity that the rotor and the stator channels are located at the same radial position. The system can be considered as two periodic rows of thick-walled channels separated by a distance denoted $d$. The first row is rotating in the clockwise direction, and the second row is considered fixed. The unwrapped representation of a cylindrical cut of this system at a radius $r_0$ is illustrated in Figure 3.11b. The configuration must be considered as an exercise, aimed at emphasizing on basic features.

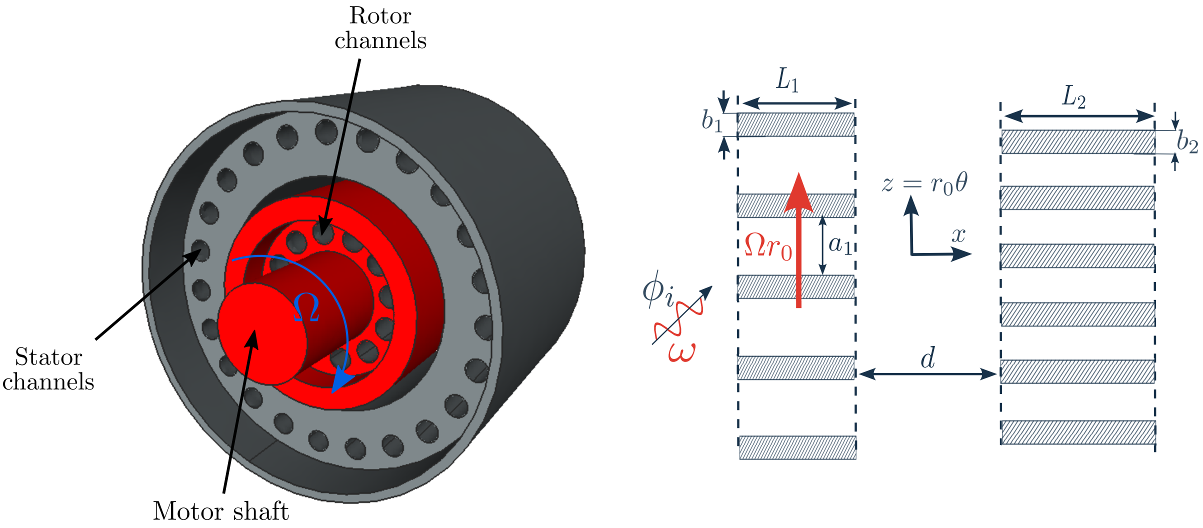

**(a)** **(b)**

**Figure 3.11:** (a) Typical configuration of the ventilating holes integrated in the rotor and stator cores. (b) Unwrapped representation of a simplified cut at common radius $r = r_0$

In the following considerable attention will be paid to the propagation of the multiple frequencies generated by the rotor channels in this coupled system.

## 3.3.1 Coupling strategy

The methodology used in this section is based on the different steps presented in Chapter 1 (see Section 1.4), to deal with the problem of transmission of an oblique plane wave through a system consisting of two periodic rows of channels. The main difficulty of this problem is how to handle the propagation of several frequencies in this system. The coupling strategy can be divided into three successive steps.

### 3.3.1.1 Scattering of the incident wave $\phi_i$ by the rotor channels (First step)

In the first step, the incident wave $\phi_i$ is scattered by the rotating channels, generating four acoustic fields, as shown in Figure 3.12.

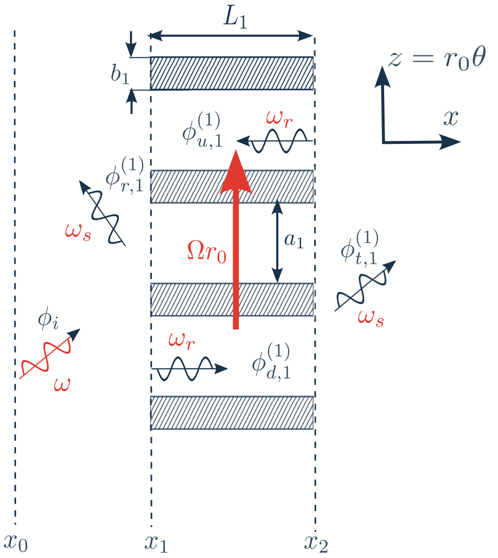

**Figure 3.12:** Scattering of the incident wave $\phi_i$ by the rotor channels.

The incident wave is considered as an oblique plane wave emitted at the interface $x_0$, and propagating in the positive $x$ direction with an angular frequency denoted $\omega$. The acoustic potential of the latter is given by

$$\phi_i(x,z,t) = A_n \mathrm{e}^{\mathrm{i}\alpha_i z}\mathrm{e}^{\mathrm{i}k_i(x-x_0)}\mathrm{e}^{-\mathrm{i}\omega t}, \quad \alpha_i = k\sin(\theta_i) = \frac{n}{r_0}, \quad k_i^+ = \sqrt{k^2-\alpha_i^2} \tag{3.25}$$

The acoustic potentials of the different acoustic fields generated upstream and downstream the rotating channels are expressed as

$$\begin{pmatrix} \phi^{(1)}_{r,1}(x,z,t) \\ \phi^{(1)}_{t,1}(x,z,t) \end{pmatrix} = \sum_{s=-\infty}^{+\infty} \begin{pmatrix} R_s^{(1)} \\ T_s^{(1)} \end{pmatrix} \mathrm{e}^{\mathrm{i}\alpha_s z} \begin{pmatrix} \mathrm{e}^{\mathrm{i}k_s^{(1)-}(x-x_1)} \\ \mathrm{e}^{\mathrm{i}k_s^{(1)+}(x-x_2)} \end{pmatrix} \mathrm{e}^{-\mathrm{i}\omega_s t} \tag{3.26}$$

with

$$\alpha_s = \frac{n+sV_1}{r_0}, \quad k_s^{(1)\pm} = \pm\sqrt{\left(\frac{\omega_s}{c_0}\right)^2 - \alpha_s^2}$$

The downstream and upstream propagating waves in the $m_1^{\text{th}}$ channel are given by

$$\begin{pmatrix} \phi_{d,1}^{(1)}(x,z,t) \\ \phi_{u,1}^{(1)}(x,z,t) \end{pmatrix} = \sum_{q=0}^{+\infty} \begin{pmatrix} D_q^{(1)} \\ U_q^{(1)} \end{pmatrix} \mathrm{e}^{\mathrm{i}m_1 H_1 \alpha_i} \cos\Big(\alpha_q \left[z - m_1 H_1 - \Omega r_0 t\right]\Big) \begin{pmatrix} \mathrm{e}^{\mathrm{i}k_q^{(1)+}(x-x_1)} \\ \mathrm{e}^{\mathrm{i}k_q^{(1)-}(x-x_2)} \end{pmatrix} \mathrm{e}^{-\mathrm{i}\omega_r t} \tag{3.27}$$

where

$$\alpha_q = q\frac{\pi}{a_1}, \quad k_q^{(1)\pm} = \pm\sqrt{k_0^2 - \alpha_q^2}$$

In this analysis the superscript (1) refers to the acoustic field produced by the rotor channels and the subscript 1 represents the index of iteration (step). The use of the analytical model developed in the previous section, allows to determine the modal amplitudes of the different fields.

#### 3.3.1.2 Scattering of $\phi_{t,1}^{(1)}$ by the stator channels (Second step)

The downstream acoustic waves generated by the rotor ducts $\phi_{t,1}^{(1)}$ are transmitted through the stator channels, generating four new acoustic fields, denoted by $\phi_{r,2}^{(2)}$, $\phi_{d,2}^{(2)}$, $\phi_{u,2}^{(2)}$ and $\phi_{t,2}^{(2)}$ as illustrated in Figure 3.13. The transmitted field $\phi_{t,1}^{(1)}$ must be expanded into a sum of incident excitations having various propagation angles. Each of these waves is characterized by its modal amplitude $T_s^{(1)}$, its modal order $n_s = n + sV_1$ and its angular frequency $\omega_s = \omega + sV_1\Omega$. The expression of a single excitation $\phi_{t,1,s}^{(1)}$ of order $n_s = n + sV_1$ at the inlet interface of the stator channels $x = x_3$, can be written as

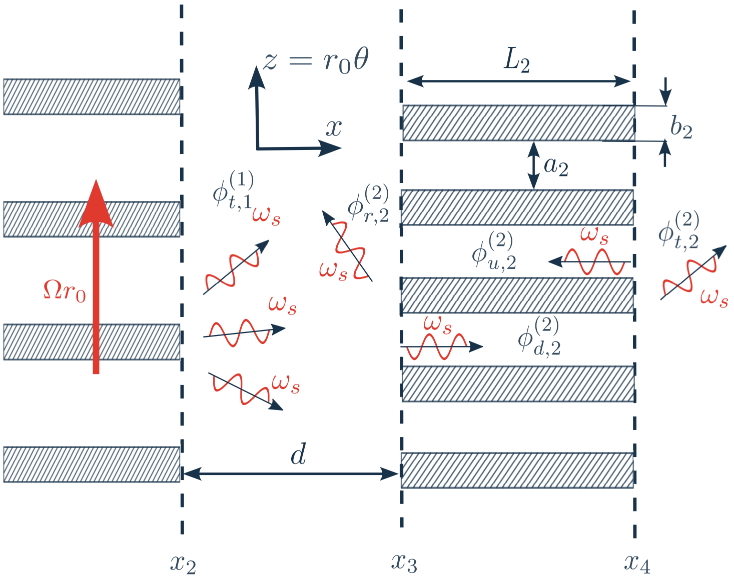

**Figure 3.13:** Scattering of the transmitted modes $\phi_{t,1}^{(1)}$ by the cooling channels in the second step.

$$\phi_{t,1,s}^{(1)}(x_3,z,t) = T_s^{(1)} \mathrm{e}^{\mathrm{i}\alpha_s z} \mathrm{e}^{\mathrm{i}k_s^{(1)+} d} \mathrm{e}^{-\mathrm{i}\omega_s t} \tag{3.28}$$

It is worth noting that each excitation $\phi^{(1)}_{t,1,s}$ of order $n_s$ is scattered by the stator channels into several azimuthal modes of orders $n_{s\nu} = n_s + \nu V_2$. These propagate at the frequency imposed by the incident excitations $\omega_s$.

The modal amplitudes of the different fields generated by each excitation can be obtained by the use of the same model developed in Section 3.2 by setting the rotational frequency to zero. After applying this model to all the incident excitations, the sound field can be constructed by the superposition of all the acoustic modes generated at this step:

$$\begin{pmatrix} \phi^{(2)}_{r,2}(x,z,t) \\ \phi^{(2)}_{t,2}(x,z,t) \end{pmatrix} = \sum_{s=-\infty}^{+\infty} \sum_{\nu=-\infty}^{+\infty} \begin{pmatrix} R^{(2)}_{s\nu} \\ T^{(2)}_{s\nu} \end{pmatrix} \mathrm{e}^{\mathrm{i}\alpha_{s\nu} z} \begin{pmatrix} \mathrm{e}^{\mathrm{i}k^{(2)+}_{s\nu}(x-x_3)} \\ \mathrm{e}^{\mathrm{i}k^{(2)-}_{s\nu}(x-x_4)} \end{pmatrix} \mathrm{e}^{-\mathrm{i}\omega_s t} \tag{3.29}$$

with

$$\alpha_{s\nu} = \alpha_s + \frac{\nu V_2}{r_0}, \quad k^{(2)\pm}_{s\nu} = \pm\sqrt{\left(\frac{\omega_s}{c_0}\right)^2 - \alpha^2_{s\nu}}$$

The downstream and upstream acoustic fields in the $m_2^{\text{th}}$ channel are given by

$$\begin{pmatrix} \phi^{(2)}_{d,2}(x,z,t) \\ \phi^{(2)}_{u,2}(x,z,t) \end{pmatrix} = \sum_{s=-\infty}^{+\infty} \sum_{\mu=0}^{+\infty} \begin{pmatrix} D^{(2)}_{s\mu} \\ U^{(2)}_{s\mu} \end{pmatrix} \mathrm{e}^{im_2\alpha_s H_2} \cos\Big(\alpha_\mu \left[z - m_2 H_2\right]\Big) \begin{pmatrix} \mathrm{e}^{\mathrm{i}k^{(2)+}_{\mu}(x-x_3)} \\ \mathrm{e}^{\mathrm{i}k^{(2)-}_{\mu}(x-x_4)} \end{pmatrix} \mathrm{e}^{-\mathrm{i}\omega_s t} \tag{3.30}$$

with

$$\alpha_\mu = \mu\frac{\pi}{a_2}, \quad k^{(2)\pm}_{\mu} = \pm\sqrt{\left(\frac{\omega_s}{c_0}\right)^2 - \alpha^2_{\mu}}$$

#### 3.3.1.3 Scattering of $\phi^{(2)}_r$ by the rotor channels (Third step)

The last step of this methodology deals with the diffraction of the waves reflected back towards the rotor channels (see Figure 3.14). In the same way, the acoustic field reflected by the stator channels is expanded in a series of oblique plane waves having various propagation angles. The expression of a single excitation at the outlet interface of the rotor channels $x = x_2$, is given by

$$\phi^{(2)}_{r,2,s\nu}(x_2,z,t) = R^{(2)}_{s\nu}\mathrm{e}^{\mathrm{i}\alpha_{s\nu}z}\mathrm{e}^{-\mathrm{i}k^{(2)-}_{s\nu}d}\mathrm{e}^{-\mathrm{i}\omega_s t} \tag{3.31}$$

The model presented in the previous section is again used in the opposite direction of $x$ to determine the modal coefficients of the different fields.

After superposing all possible solutions, one obtains

$$\begin{pmatrix} \phi^{(1)}_{r,3}(x,z,t) \\ \phi^{(1)}_{t,3}(x,z,t) \end{pmatrix} = \sum_{s=-\infty}^{+\infty} \sum_{\nu=-\infty}^{+\infty} \sum_{l=-\infty}^{+\infty} \begin{pmatrix} R^{(1)}_{s\nu l} \\ T^{(1)}_{s\nu l} \end{pmatrix} \mathrm{e}^{\mathrm{i}\alpha_{s\nu l} z} \begin{pmatrix} \mathrm{e}^{\mathrm{i}k^{(1)+}_{s\nu l}(x-x_1)} \\ \mathrm{e}^{\mathrm{i}k^{(1)-}_{s\nu l}(x-x_2)} \end{pmatrix} \mathrm{e}^{-\mathrm{i}\omega_{sl} t} \tag{3.32}$$

with

$$\alpha_{s\nu l} = \alpha_{s\nu} + \frac{lV_1}{r_0}, \quad k^{(1)\pm}_{s\nu l} = \pm\sqrt{\left(\frac{\omega_{sl}}{c_0}\right)^2 - \alpha^2_{s\nu l}} \quad , \omega_{sl} = \omega_s + lV_1\Omega$$

It should be emphasized here that the rotor channels are excited by several frequencies

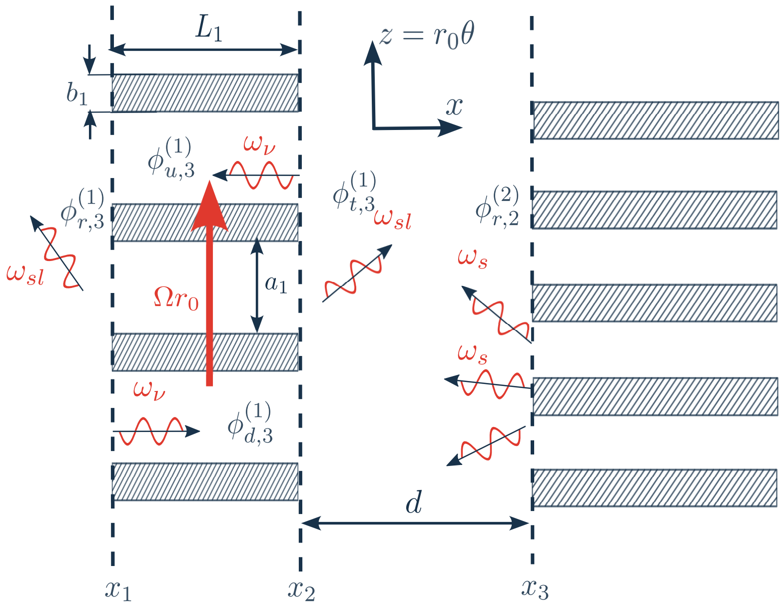

**Figure 3.14:** Scattering of the reflected field $\phi^{(r)}_{r,2}$ by the rotor channels.

at this step. The different fields propagating inside the rotor channels, read

$$\begin{pmatrix}\phi^{(1)}_{d,3}(x,z,t)\\ \phi^{(1)}_{u,3}(x,z,t)\end{pmatrix} = \sum_{s=-\infty}^{+\infty}\sum_{\nu=-\infty}^{+\infty}\sum_{q=0}^{+\infty}\begin{pmatrix}D^{(1)}_{s\nu q}\\ U^{(1)}_{s\nu q}\end{pmatrix}\begin{pmatrix}\mathrm{e}^{\mathrm{i}k^{(1)+}_{q\nu}(x-x_1)}\\ \mathrm{e}^{\mathrm{i}k^{(1)-}_{q\nu}(x-x_2)}\end{pmatrix} \times \mathrm{e}^{\mathrm{i}m_1H_1\alpha_{s\nu}}\cos\Big(\alpha_q\left[z-m_1H_1-\Omega r_0 t\right]\Big)\mathrm{e}^{-\mathrm{i}\omega_\nu t} \qquad (3.33)$$

where

$$k^{(1)\pm}_{q\nu} = \pm\sqrt{\left(\frac{\omega_\nu}{c_0}\right)^2 - \alpha_q} \qquad ,\omega_\nu = \omega_s - \alpha_{s\nu} r_0\Omega = \omega - (n+\nu V_2 r_0)\Omega \qquad (3.34)$$

In the following, the second and the third steps must be repeated alternately until convergence, by taking the output of one subsystem as the input of the other one.

All the solutions must be superposed to get the total acoustic field in each subdomain:

$$\phi^{(1,2)}_{\xi}(x,z,t) = \sum_{\gamma=1}^{i_{\max}}\phi^{(1,2)}_{\xi,\gamma}(x,z,t), \quad \xi = \{r,t,d,u\}\,, \quad \gamma = \begin{cases}1,3,5,\ldots.i_{\max}-1, & \text{if } \phi^{(1,2)} = \phi^{(1)}\\ 2,4,6,\ldots.i_{\max}, & \text{if } \phi^{(1,2)} = \phi^{(2)}\end{cases}$$

where $i_{\max}$ is the maximum number of iterations.

### 3.3.2 Results

In this section the mode-matching technique is applied to a configuration consisting of $V_1 = 9$ rotor channels and $V_2 = 15$ stator channels, separated by a distance $d/L_1 = 0.5$. The test case parameters are listed in Table 3.2. The channels rotate in the opposite direction of $z$ with a negative Mach number $M_z = -0.231$. The analytical model is

| $k_0a_1$ | $a_1/H_1$ | $a_2/H_2$ | $r_0$ $(m)$ | $L_1/a_1$ | $L_2/a_2$ | $d/L_1$ | $M_z$ | $n$ |
|---|---|---|---|---|---|---|---|---|
| 5.22 | 0.7 | 0.6 | 0.15 | 2.7284 | 5.3052 | 0.5 | $-0.231$ | 3 |

**Table 3.2:** Test-case parameters

applied to the diffraction of an incident wave composed of $n = 3$ azimuthal lobes. In order to examine the effects due to the rotation of the rotor channels, a comparison between the instantaneous acoustic pressure fields obtained with ($M_z = -0.231$) and without ($M_z = 0$) channel rotation is shown in Figure 3.15. Figure 3.15a indicates that

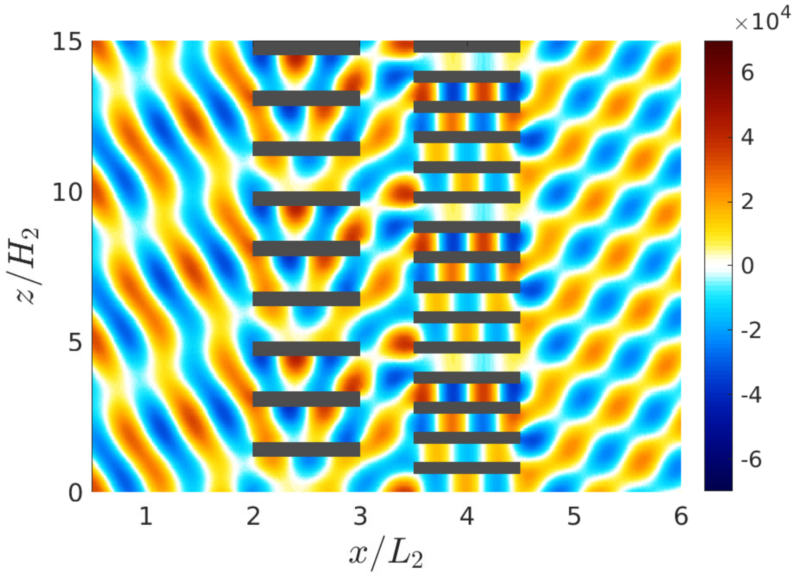

(a)

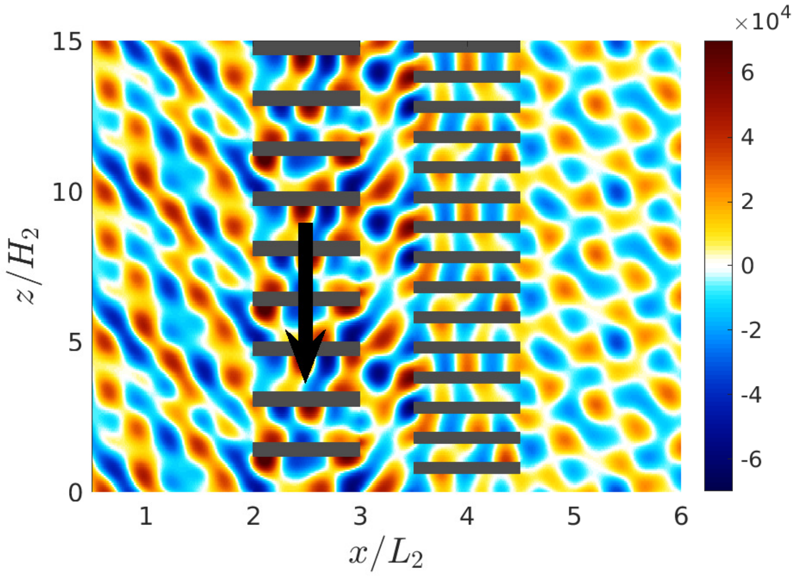

(b)

**Figure 3.15:** Instantaneous acoustic pressure field obtained by the mode-matching technique. (a) $M_z = 0$, (b) $M_z = -0.231$. $k_0a_1 = 5.22$, $a_1/H_1 = 0.7$, $a_2/H_2 = 0.6$, $r_0 = 0.15$m, $L_1/a_1 = 2.7284$, $L_2/a_2 = 5.3052$, $d/L_1 = 0.5$, $n = 3$

without rotation, the incident wave is scattered into several modes propagating at the same angular frequency $\omega$. As can be seen the sound field transmitted through the rotor channels is dominated by the mode $n_s = -6$ and slightly modulated by the mode $n_s = 3$. These are scattered by the stator channels without generating other azimuthal modes. As can be seen only plane waves can propagate inside the stator channels. The cut-off frequency of the first higher order mode is higher than the excitation frequency. However, the acoustic response of the system is strongly modified in the presence of rotation (see Figure 3.15b). The interferences between the different acoustic fields are more complex compared to the case without channel rotation. This may be attributed to the propagation of several higher order modes at different frequencies induced by the rotor channels. However, the acoustic field transmitted downstream the stator channels is no longer dominated by the mode $n_s = -6$. Additionally, the sound field inside the stator channels is not homogeneous, which confirms the presence of more than one cut-on mode inside each channel. In fact, the higher order modes can be excited by the different frequencies generated by the rotor scattering $\omega_s$, which are typically higher than the frequency of the incident wave $\omega$. Therefore, if the proper condition is fulfilled, the mode becomes cut-on.

It is important to note that the scattering of the frequency of the incident wave by the rotor channels can lead to unexpected resonances in some practical applications. For that, care should be taken when choosing the dimensions of the cooling channels integrated in the rotor and the stator cores in order to avoid these frequencies.

## 3.4 Diffraction of an oblique plane wave by two periodic rows of rotating channels

The last problem addressed in this chapter deals with the transmission of acoustic waves through a system composed of two rotating sub-systems. In practice, this kind of systems can be found in some parts of the ventilation systems integrated in non self-ventilated motors. It should be recalled here that in a self-ventilated motor, the cooling fan (radial impeller) and the rotor core are both mounted on the motor shaft. Consequently, these rotating parts of the motor may rotate in the same direction and at the same rotational speed as the motor. However, for high speed-motors with more than 6000 revolutions per minute (rpm), the noise generated by the cooling fan increases rapidly. To avoid this problem, designers need to use another cooling technique, known as the autonomous ventilation. In these architectures, the cooling fan is no longer mounted on the motor shaft, but powered by another small electrical motor. The speed and direction of rotation of the cooling fan can thus be controlled independently of the motor shaft. This allows the fan speed to be reduced at high rotational speeds of the motor, and also avoids using impellers with poorly efficient radial blades. However, since the motor must rotate in both directions of rotation, the cooling fan and the rotor channels can rotate in the same direction or in opposite directions and at different rotational speeds, as depicted in Figure 3.16a. As what has been already discussed, the transmission of an acoustic wave through the radial impeller, requires the use of three different sub-models [58, 90, 59]. Note here that the effect of the geometry of the radial impeller on the propagation of acoustic waves is not considered in this analysis. The system investigated in this work consists of two rows of rotating channels separated by a certain distance in a two-dimensional representation, as depicted in Figure 3.16b. The first and the second sub-systems correspond respectively to the cooling fan and the rotor cooling channels, and their tangential Mach numbers are given by $M_{z1} = \Omega_1 r_0/c_0$ and $M_{z2} = \Omega_2 r_0/c_0$.

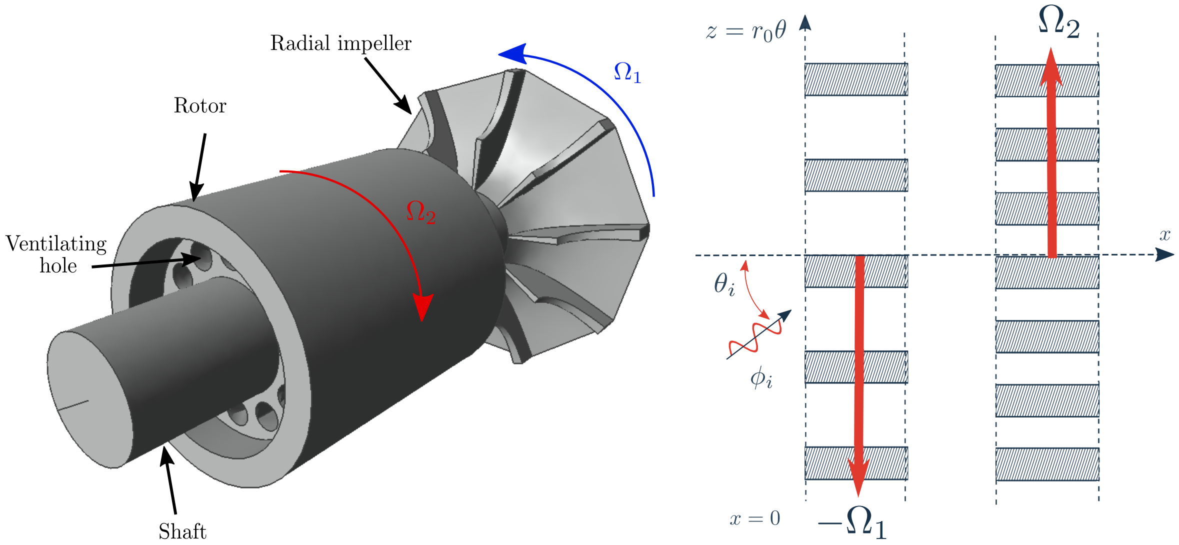

(a) (b)

**Figure 3.16:** Typical configuration of the rotor ducts and the cooling fan integrated in open motor (autonomous ventilation).

The same methodology as presented previously is used in this section. In the following only the mathematical expressions of the different fields produced at each step of the methodology are given.

## 3.4.1 Acoustic potentials

### 3.4.1.1 Sound fields generated in the first step

As before, in the first step, an incident oblique plane wave is scattered by the first sub-system. The acoustic potentials of the different acoustic fields generated by the diffraction are given by

$$\begin{pmatrix} \phi_{r,1}^{(1)}(x,z,t) \\ \phi_{t,1}^{(1)}(x,z,t) \end{pmatrix} = \sum_{s=-\infty}^{+\infty} \begin{pmatrix} R_s^{(1)} \\ T_s^{(1)} \end{pmatrix} \mathrm{e}^{\mathrm{i}\alpha_s z} \begin{pmatrix} \mathrm{e}^{\mathrm{i}k_s^{(1)-}(x-x_1)} \\ \mathrm{e}^{\mathrm{i}k_s^{(1)+}(x-x_2)} \end{pmatrix} \mathrm{e}^{-\mathrm{i}\omega_s t} \tag{3.35}$$

with

$$k_s^{(1)\pm} = \pm\sqrt{\left(\frac{\omega_s}{c_0}\right)^2 - \alpha_s^2} \quad ,\omega_s = \omega + s\Omega_1 V_1$$

$$\begin{pmatrix} \phi_{d,1}^{(1)}(x,z,t) \\ \phi_{u,1}^{(1)}(x,z,t) \end{pmatrix} = \sum_{q=0}^{+\infty} \begin{pmatrix} D_q^{(1)} \\ U_q^{(1)} \end{pmatrix} \mathrm{e}^{\mathrm{i}m_1 H_1 \alpha_i} \cos\Big(\alpha_q\left[z - m_1 H_1 - \Omega_1 r_0 t\right]\Big) \begin{pmatrix} \mathrm{e}^{\mathrm{i}k_q^{(1)+}(x-x_1)} \\ \mathrm{e}^{\mathrm{i}k_q^{(1)-}(x-x_2)} \end{pmatrix} \mathrm{e}^{-\mathrm{i}\omega_r t}$$
$$k_q^{(1)\pm} = \pm\sqrt{\left(\frac{\omega_r}{c_0}\right)^2 - \alpha_q^2} \quad ,\omega_r = \omega - n\Omega_1 \tag{3.36}$$

#### 3.4.1.2 Sound fields generated in the second step

As explained in the previous section, the modes $T_{s,1}^{(1)}$ transmitted downstream the first sub-system propagate with different frequencies $\omega_s$. Each of these is scattered into new frequencies induced by the other sub-system. These depend on the rotational speeds of the two sub-systems $\omega_{s\nu} = \omega_s + \nu V_2 \Omega_2$. The acoustic fields generated at this step read

$$\begin{pmatrix} \phi_{r,2}^{(2)}(x,z,t) \\ \phi_{t,2}^{(2)}(x,z,t) \end{pmatrix} = \sum_{s=-\infty}^{+\infty} \sum_{\nu=-\infty}^{+\infty} \begin{pmatrix} R_{s\nu}^{(2)} \\ T_{s\nu}^{(2)} \end{pmatrix} \mathrm{e}^{\mathrm{i}\alpha_{s\nu} z} \begin{pmatrix} \mathrm{e}^{\mathrm{i}k_{s\nu}^{(2)+}(x-x_3)} \\ \mathrm{e}^{\mathrm{i}k_{s\nu}^{(2)-}(x-x_4)} \end{pmatrix} \mathrm{e}^{-\mathrm{i}\omega_{s\nu} t} \tag{3.37}$$

with

$$k_{s\nu}^{(2)\pm} = \pm\sqrt{\left(\frac{\omega_{s\nu}}{c_0}\right)^2 - \alpha_{s\nu}^2}$$

The downstream and upstream acoustic fields in the $m_2^{\mathrm{th}}$ channel are given by

$$\begin{aligned} \begin{pmatrix} \phi_{d,2}^{(2)}(x,z,t) \\ \phi_{u,2}^{(2)}(x,z,t) \end{pmatrix} = \sum_{s=-\infty}^{+\infty} \sum_{\mu=0}^{+\infty} \begin{pmatrix} D_{s\mu}^{(2)} \\ U_{s\mu}^{(2)} \end{pmatrix} \mathrm{e}^{\mathrm{i}m_2 \alpha_s H_2} \begin{pmatrix} \mathrm{e}^{\mathrm{i}k_{\mu s}^{(2)+}(x-x_3)} \\ \mathrm{e}^{\mathrm{i}k_{\mu s}^{(2)-}(x-x_4)} \end{pmatrix} \\ \times \cos\Big(\alpha_\mu\left[z - m_2 H_2 - \Omega_2 r_0 t\right]\Big) \mathrm{e}^{-\mathrm{i}(\omega_s - \alpha_s r_0 \Omega_2)t} \end{aligned} \tag{3.38}$$

where

$$k_{\mu,s}^{(2)\pm} = \pm\sqrt{\left(\frac{\omega_s - \alpha_s r_0 \Omega_2}{c_0}\right)^2 - \alpha_\mu^2}$$

#### 3.4.1.3 Sound fields generated in the third step

The field reflected by the second sub-system propagates in the negative $x$ direction towards the other one. After superposing all possible solutions, the different fields can be written as

$$\begin{pmatrix} \phi_{r,3}^{(1)}(x,z,t) \\ \phi_{t,3}^{(1)}(x,z,t) \end{pmatrix} = \sum_{s=-\infty}^{+\infty} \sum_{\nu=-\infty}^{+\infty} \sum_{l=-\infty}^{+\infty} \begin{pmatrix} R_{s\nu l}^{(1)} \\ T_{s\nu l}^{(1)} \end{pmatrix} \mathrm{e}^{\mathrm{i}\alpha_{s\nu l} z} \begin{pmatrix} \mathrm{e}^{\mathrm{i}k_{s\nu l}^{(1)+}(x-x_1)} \\ \mathrm{e}^{\mathrm{i}k_{s\nu l}^{(1)-}(x-x_2)} \end{pmatrix} \mathrm{e}^{-\mathrm{i}\omega_{s\nu l} t} \tag{3.39}$$

with

$$k_{s\nu l}^{(1)\pm} = \pm\sqrt{\left(\frac{\omega_{s\nu l}}{c_0}\right)^2 - \alpha_{s\nu l}^2} \quad ,\omega_{s\nu l} = \omega_{s\nu} + lV_1\Omega_1$$

It should be emphasized here that the rotor channels are excited by several frequencies at this step. The different fields propagating inside the rotor channels, read

$$\begin{pmatrix}\phi_{d,3}^{(1)}(x,z,t)\\ \phi_{u,3}^{(1)}(x,z,t)\end{pmatrix} = \sum_{s=-\infty}^{+\infty}\sum_{\nu=-\infty}^{+\infty}\sum_{q=0}^{+\infty}\begin{pmatrix}D_{s\nu q}^{(1)}\\ U_{s\nu q}^{(1)}\end{pmatrix}\begin{pmatrix}\mathrm{e}^{\mathrm{i}k_{q\nu}^{(1)+}(x-x_1)}\\ \mathrm{e}^{\mathrm{i}k_{q\nu}^{(1)-}(x-x_2)}\end{pmatrix}$$
$$\times\, \mathrm{e}^{\mathrm{i}m_1H_1\alpha_{s\nu}}\cos\Big(\alpha_q\left[z - m_1H_1 - \Omega_2 r_0 t\right]\Big)\mathrm{e}^{-\mathrm{i}(\omega_{s\nu}-\alpha_{s\nu}r_0\Omega_1)t} \quad (3.40)$$

where

$$k_{q\nu}^{(1)\pm} = \pm\sqrt{\left(\frac{\omega_{s\nu}-\alpha_{s\nu}r_0\Omega_1}{c_0}\right)^2 - \alpha_q^2}, \quad (3.41)$$

As before, the second and the third steps must be repeated alternately until convergence.

### 3.4.2 Results

In order to quantify the effects due to the rotation of the second sub-system on the sound propagation mechanism, a comparison between two configurations has been carried out. Each of these configurations is composed of $V_1 = 9$ fan blades and $V_2 = 15$ rotor channels, separated by a small distance given by $d/L_1 = 0.5$. The test case parameters used for the two configurations are listed in Table 3.2. In the first setup, the fan blades (first sub-system) and the rotor channels (second sub-system) are rotating in the same direction of rotation, with different rotational speeds, given by $M_{z1} = -0.231$ and $M_{z2} = -0.277$. In the second one, the direction of rotation of the rotor channels is reversed, with the same rotational speed $M_{z2} = +0.277$. In this case, the two sub-systems rotate in opposite directions. The analytical model is applied in this section to the diffraction of an incident mode of order $n = 3$. The instantaneous acoustic pressure fields obtained for the two configurations are illustrated in Figure 3.17. Figure 3.17a indicates clearly that when the two sub-systems rotate in the same direction, the sound field upstream the fan blades (first sub-system) is dominated by the incident wave, and slightly modulated by the reflected field. Furthermore, the acoustic field transmitted downstream the rotor channels (second sub-system) is dominated by the mode $n_s = -6$ and slightly modulated by the mode $n_s = 3$. These are generated by the diffraction of the indent mode $n = 3$ by the fan blades, as expected by the equation $n_s = n + sV_1 = 3 + s\times 9 = [-6, 3]$. They respectively propagate at the relative frequencies $\omega_{s=-1}/\omega = 1.25$ and $\omega_{s=0}/\omega = 1$ towards to the rotor channels. The diffraction of these modes by the latter, generates only cut-on modes with same modal orders. All the other modes are cut-off, and their cut-off frequencies are sufficiently large compared to the excitation frequencies imposed by the modes $n_s = 3$

and $n_s = -6$. In fact, the mode $n_s = -6$ and the rotor channels are rotating in the same direction. The second lower order mode generated by the scattering of the mode $n_s = -6$ by the rotor channels is $n_{s\nu} = 9$. Its cut-off frequency is given by $\omega_{c,9}/\omega = 1.08$. Note here that the frequency of the latter is decreased by the motion of the channels, as confirmed by the equation $\omega_{s\nu}/\omega = (\omega_s + \nu V_2 \Omega_2)/\omega = 0.75$. However, when the rotor channels rotate in the opposite direction (see Figure 3.17b), the acoustic field upstream the first sub-system remains dominated by the incident wave, but modulated by the presence of various modes generated by the diffraction. Moreover, downstream the second sub-system, the sound field is composed mainly of the modes $-6$ and 9. This is explained by the fact that the

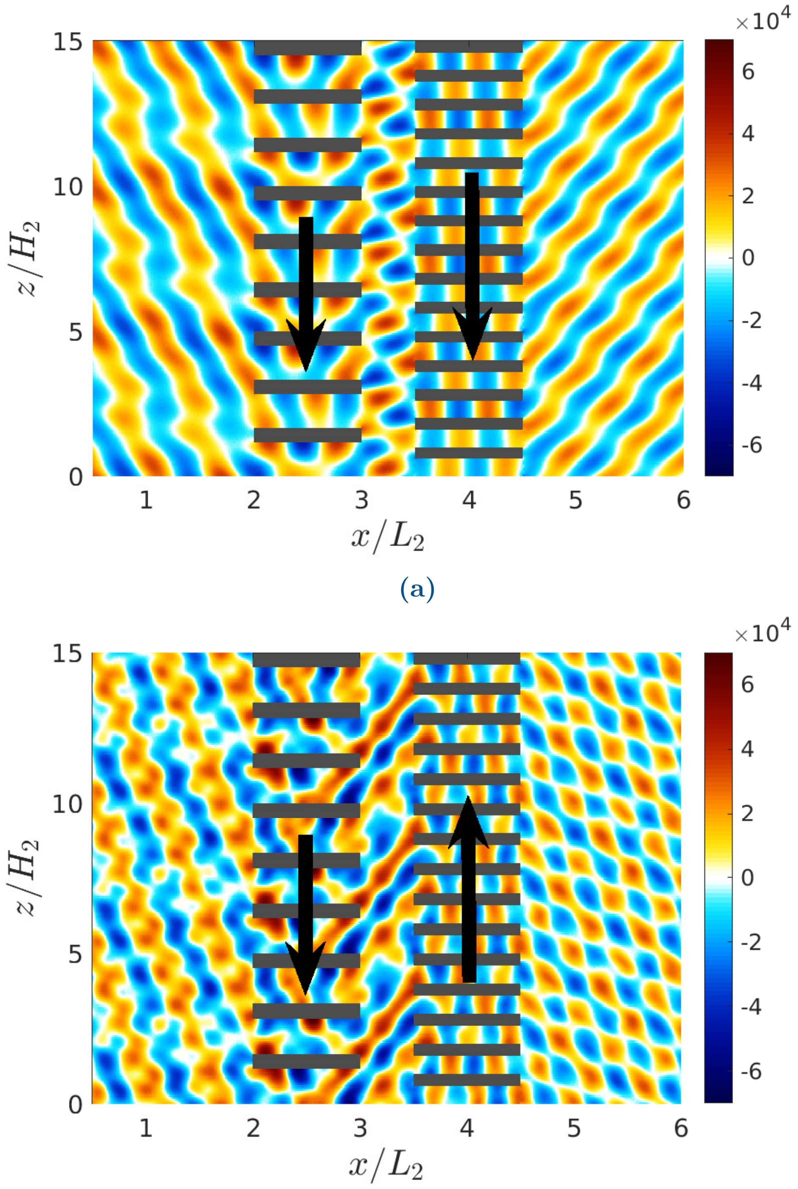

(a)

(b)

**Figure 3.17:** Instantaneous acoustic pressure fields obtained by the mode-matching technique. (a) $M_{z2} = -0.277$. (b) $M_{z2} = +0.277$. $M_{z1} = -0.231$, $n = 3$, $V_1 = 9$, $V_2 = 15$, $k_0 a = 5.22$, $r_0 = 0.15$.

frequency of the mode $n_{s\nu} = 9$ is increased by the rotation of the rotor channels. Note here that this particular mode $n_{s\nu} = 9$ is rotating in the opposite direction to the rotor channels. Therefore, its frequency becomes $\omega_{s\nu}/\omega = 1.75$, which is typically higher than its cut-off frequency.

## 3.5 Conclusion

An analytical model based on the mode-matching technique has been presented in this chapter in order to deal with problems of sound transmission through a system consisting of two periodic rows of rotating channels. The aim of this model is to investigate how the sound can be transmitted through the rotating parts of the ventilation system integrated in open motors. The first part of this chapter was devoted to the diffraction of an oblique plane wave by a single periodic row of rotating channels by taking into account the influence of their thicknesses. This model was first applied to a system composed of a rotating part and a stationary part, and then it was extended to a system consisting of two rotating parts, having different rotational speeds. An iterative procedure was used to take into account the multiple diffractions of the acoustic waves between the two subsystems. The effect of the rotational speed of the two sub-systems and the direction of rotation has been investigated in this work. The results obtained have shown that the acoustic response of the coupled system is strongly affected by the rotation of the channels.

Furthermore, it must be kept in mind that in a system coupling two periodic arrays of bifurcated waveguides, with different speeds, the sound scattering problem is no longer monochromatic. The interest of the mode-matching technique is that it can be used with a set of pre-identified frequencies, at the price of an iterative procedure, even if it is basically solving the Helmholtz equation.

# Conclusions and perspectives

## Conclusions

This work was dealing with the analytical modelling of sound generation and propagation in ventilation systems integrated in traction motors used in railway applications.

The first part of this study was devoted to the sound transmission through a system consisting of guide vanes and cooling channels, in order to investigate how acoustic waves can propagate inside the ventilation system integrated in totally-enclosed motors. This system was considered as two periodic rows of thick-walled channels separated by a certain distance. The sound propagation in this configuration is achieved by the use of two transmission models, based on a two-dimensional mode-matching technique. These models take into account the influence of wall-thickness on sound transmission. An iterative method has been used to account for the multiple diffractions of acoustic waves between the two subsystems. The results obtained by this model have been systematically compared to the finite element method for validation purposes. A very good agreement was found between the results obtained by the two methods at most frequencies of interest. Furthermore, this study has shown that the presence of guide vanes in the ventilation system affects significantly the acoustic response of the cooling channels. The interaction between back-and-forth acoustic waves propagating in the space between the guide vanes and cooling channels can lead to acoustic resonances. The sound generation mechanism resulting from the impingement of the impeller wakes on the guide vanes has been investigated in this work by the use of the concept of equivalent dipoles. The results obtained by this analytical model have shown that the cooling channels have a significant influence on the amplitude of the acoustic field radiated upstream of the guide vanes. This acoustic field can either be amplified or completely attenuated when the distance between the guide vanes and the cooling channels is modified.

In the second part of this work, the mode-matching method was applied to significantly more complicated architectures to study the propagation of sound inside the stationary part of the ventilation system integrated in an open motor. The geometry was first simplified and then divided into 15 interconnected subdomains, mainly composed of 14 annular ducts and a periodic row of cooling channels. Then, the sound field was expressed as a sum of orthogonal modes in the various subdomains of this configuration. These subdomains were connected by imposing the continuity of the acoustic pressure and the axial velocity at each interface separating two regions with different transverse dimensions. In order to validate the analytical model, a comparison with the finite element method was conducted. In the first step, both methods were applied to a simplified configuration of an open motor for mathematical validation. A very good agreement was found between the results obtained by the two methods. Then, the finite element method was applied to the realistic configuration of an open motor, including all the curvatures present in the stationary part of the motor. The results obtained by two methods agree well at particularly low and medium frequencies of interest. However, the difference between the two results seems to be significant at relatively high frequencies. From a certain frequency, the effects due to the axial variation of the duct cross-section become important and they cannot be neglected in the analysis. This model was used for parametric studies to predict the resonant frequencies of the ventilation system. These frequencies were identified by analysing the variation of the acoustic power transmitted outside the ventilation system. However, it was observed that acoustic resonances can occur at various locations in the ventilation system.

The problem of sound transmission through a system consisting of two periodic rows of rotating channels has been addressed in the last chapter of this work. The main objective was to investigate how sound can be transmitted through the rotating parts of the ventilation system integrated in open motors. To achieve this, the mode-matching method was first applied to the diffraction of an oblique plane wave by a single periodic row of rotating channels. Initially, this model was applied to a system consisting of both a rotating part and a stationary part. Subsequently, this model was extended to consider a system composed of two rotating rows of channels, having different rotational speeds. In order, to account for the multiple reflections of acoustic waves between the two subsystems, an iterative procedure was employed in this work. The results obtained have shown that the acoustic response of the coupled system is strongly affected by the rotation of the channels. The incident acoustic wave is scattered into several azimuthal modes propagating at different frequencies. These frequencies are induced by the rotation of the channels. They mainly depend on the rotational speed of channels and the modal order of the generated modes. In addition, the resonant frequencies of the rotor channels are shifted by their rotational motion, which means that rotational effects must necessarily be taken into account during the motor design stage to correctly predict the resonant frequencies.

Finally, the aeraulic performance of self-ventilated motors has been addressed in Appendix C, in order to predict the flow rate inside the ventilation system. The results obtained for totally-enclosed motors have been validated by comparison with measurements then with numerical simulations based on the Lattice Boltzmann Method (LBM).

# Perspectives

Several perspectives can be suggested in order to improve the different analytical models developed in the present work. The comparison with the finite element method has shown that these models are valid up to a certain frequency. These limitations are mainly attributed to the geometrical approximations considered in this work.

The analytical model proposed in this work to simulate the sound propagation in the stationary part of an open motor can be improved by introducing the effects due to the axial variation of the duct cross-section. These can be considered in the analysis using the multimodal approach [70, 42, 40, 81, 4, 44]. Note here that this semi-analytical approach takes into account the coupling effects between acoustic modes, offering a more comprehensive analysis.

Another aspect to be improved in this work concerns the geometry of the end-windings in the case of an open motor. These have been assumed to be perfectly rigid in this study, but the influence of this assumption becomes more pronounced as frequency increases, especially when the space between two conductors is large enough. The analytical model can be improved by considering the end-windings as a porous region. However, the analytical solution in this particular region of the ventilation system can be obtained by applying a non-rigid boundary condition on the walls of the duct.

In this study, the noise generation mechanism was investigated using of the equivalent dipoles [92, 18]. Specifically, this technique has been applied to the noise generation by the impingement of impeller wakes of the guide vanes, without calibrating the amplitude of the equivalent dipoles. However, this requires further attention in future research to obtain more accurate and reliable results.

Furthermore, it is important to note that the different analytical models presented in this work remain valid up to a certain value of the Mach number. As the Mach number increases in the ventilation system, its effects on sound propagation become increasingly significant and cannot be neglected. Consequently, this becomes an essential issue that requires further investigation in future studies.

# Appendix A

# Scattering matrices

The matching equations derived in Section 2.3.4 are solved by a direct matrix inversion. The system of linear equations has been divided into two subsystems, in which a direct matrix inversion can be used. The terms of both matrices are given is this section.

## A.1 Matrix terms - First block

The matrix form of the matching equations defined for the first block is given by

$$\underline{\boldsymbol{\mathcal{C}}} = \begin{pmatrix}
\underline{\boldsymbol{\mathcal{C}}}_{1}^{1} & \underline{\boldsymbol{\mathcal{C}}}_{1}^{2} & \underline{\boldsymbol{\mathcal{C}}}_{1}^{3} & \underline{\boldsymbol{\mathcal{C}}}_{1}^{4} & \mathbf{0} & \mathbf{0} & \mathbf{0} & \mathbf{0} & \mathbf{0} & \mathbf{0} & \mathbf{0} & \mathbf{0} & \mathbf{0} & \mathbf{0} \\
\underline{\boldsymbol{\mathcal{C}}}_{2}^{1} & \mathbf{0} & \underline{\boldsymbol{\mathcal{C}}}_{2}^{3} & \underline{\boldsymbol{\mathcal{C}}}_{2}^{4} & \mathbf{0} & \mathbf{0} & \mathbf{0} & \mathbf{0} & \mathbf{0} & \mathbf{0} & \mathbf{0} & \mathbf{0} & \mathbf{0} & \mathbf{0} \\
\mathbf{0} & \underline{\boldsymbol{\mathcal{C}}}_{3}^{2} & \underline{\boldsymbol{\mathcal{C}}}_{3}^{3} & \underline{\boldsymbol{\mathcal{C}}}_{3}^{4} & \mathbf{0} & \mathbf{0} & \mathbf{0} & \mathbf{0} & \mathbf{0} & \mathbf{0} & \mathbf{0} & \mathbf{0} & \mathbf{0} & \mathbf{0} \\
\mathbf{0} & \mathbf{0} & \underline{\boldsymbol{\mathcal{C}}}_{4}^{3} & \underline{\boldsymbol{\mathcal{C}}}_{4}^{4} & \underline{\boldsymbol{\mathcal{C}}}_{4}^{5} & \underline{\boldsymbol{\mathcal{C}}}_{4}^{6} & \underline{\boldsymbol{\mathcal{C}}}_{4}^{7} & \underline{\boldsymbol{\mathcal{C}}}_{4}^{8} & \mathbf{0} & \mathbf{0} & \mathbf{0} & \mathbf{0} & \mathbf{0} & \mathbf{0} \\
\mathbf{0} & \mathbf{0} & \underline{\boldsymbol{\mathcal{C}}}_{5}^{3} & \underline{\boldsymbol{\mathcal{C}}}_{5}^{4} & \mathbf{0} & \mathbf{0} & \underline{\boldsymbol{\mathcal{C}}}_{5}^{7} & \underline{\boldsymbol{\mathcal{C}}}_{5}^{8} & \mathbf{0} & \mathbf{0} & \mathbf{0} & \mathbf{0} & \mathbf{0} & \mathbf{0} \\
\mathbf{0} & \mathbf{0} & \mathbf{0} & \mathbf{0} & \underline{\boldsymbol{\mathcal{C}}}_{6}^{5} & \underline{\boldsymbol{\mathcal{C}}}_{6}^{6} & \underline{\boldsymbol{\mathcal{C}}}_{6}^{7} & \underline{\boldsymbol{\mathcal{C}}}_{6}^{8} & \mathbf{0} & \mathbf{0} & \mathbf{0} & \mathbf{0} & \mathbf{0} & \mathbf{0} \\
\mathbf{0} & \mathbf{0} & \mathbf{0} & \mathbf{0} & \mathbf{0} & \mathbf{0} & \underline{\boldsymbol{\mathcal{C}}}_{7}^{7} & \underline{\boldsymbol{\mathcal{C}}}_{7}^{8} & \underline{\boldsymbol{\mathcal{C}}}_{7}^{9} & \underline{\boldsymbol{\mathcal{C}}}_{7}^{10} & \underline{\boldsymbol{\mathcal{C}}}_{7}^{11} & \underline{\boldsymbol{\mathcal{C}}}_{7}^{12} & \mathbf{0} & \mathbf{0} \\
\mathbf{0} & \mathbf{0} & \mathbf{0} & \mathbf{0} & \mathbf{0} & \mathbf{0} & \underline{\boldsymbol{\mathcal{C}}}_{8}^{7} & \underline{\boldsymbol{\mathcal{C}}}_{8}^{8} & \underline{\boldsymbol{\mathcal{C}}}_{8}^{9} & \underline{\boldsymbol{\mathcal{C}}}_{8}^{10} & \mathbf{0} & \mathbf{0} & \mathbf{0} & \mathbf{0} \\
\mathbf{0} & \mathbf{0} & \mathbf{0} & \mathbf{0} & \mathbf{0} & \mathbf{0} & \underline{\boldsymbol{\mathcal{C}}}_{9}^{7} & \underline{\boldsymbol{\mathcal{C}}}_{9}^{8} & \mathbf{0} & \mathbf{0} & \underline{\boldsymbol{\mathcal{C}}}_{9}^{11} & \underline{\boldsymbol{\mathcal{C}}}_{9}^{12} & \mathbf{0} & \mathbf{0} \\
\mathbf{0} & \mathbf{0} & \mathbf{0} & \mathbf{0} & \mathbf{0} & \mathbf{0} & \mathbf{0} & \mathbf{0} & \underline{\boldsymbol{\mathcal{C}}}_{10}^{9} & \underline{\boldsymbol{\mathcal{C}}}_{10}^{10} & \underline{\boldsymbol{\mathcal{C}}}_{10}^{11} & \underline{\boldsymbol{\mathcal{C}}}_{10}^{12} & \underline{\boldsymbol{\mathcal{C}}}_{10}^{13} & \mathbf{0} \\
\mathbf{0} & \mathbf{0} & \mathbf{0} & \mathbf{0} & \mathbf{0} & \mathbf{0} & \mathbf{0} & \mathbf{0} & \underline{\boldsymbol{\mathcal{C}}}_{11}^{9} & \underline{\boldsymbol{\mathcal{C}}}_{11}^{10} & \mathbf{0} & \mathbf{0} & \underline{\boldsymbol{\mathcal{C}}}_{11}^{13} & \mathbf{0} \\
\mathbf{0} & \mathbf{0} & \mathbf{0} & \mathbf{0} & \mathbf{0} & \mathbf{0} & \mathbf{0} & \mathbf{0} & \mathbf{0} & \mathbf{0} & \underline{\boldsymbol{\mathcal{C}}}_{12}^{11} & \underline{\boldsymbol{\mathcal{C}}}_{12}^{12} & \underline{\boldsymbol{\mathcal{C}}}_{12}^{13} & \mathbf{0} \\
\mathbf{0} & \mathbf{0} & \mathbf{0} & \mathbf{0} & \underline{\boldsymbol{\mathcal{C}}}_{13}^{5} & \underline{\boldsymbol{\mathcal{C}}}_{13}^{6} & \mathbf{0} & \mathbf{0} & \mathbf{0} & \mathbf{0} & \mathbf{0} & \mathbf{0} & \mathbf{0} & \underline{\boldsymbol{\mathcal{C}}}_{13}^{14} \\
\mathbf{0} & \mathbf{0} & \mathbf{0} & \mathbf{0} & \underline{\boldsymbol{\mathcal{C}}}_{14}^{5} & \underline{\boldsymbol{\mathcal{C}}}_{14}^{6} & \mathbf{0} & \mathbf{0} & \mathbf{0} & \mathbf{0} & \mathbf{0} & \mathbf{0} & \mathbf{0} & \underline{\boldsymbol{\mathcal{C}}}_{14}^{14}
\end{pmatrix} \tag{A.1}$$

$$\boldsymbol{X_1} = \left\{ \boldsymbol{U}^{\boldsymbol{R_d}}, \boldsymbol{U}^{\boldsymbol{G}}, \boldsymbol{D}^{\boldsymbol{R_1}}, \boldsymbol{U}^{\boldsymbol{R_1}}, \boldsymbol{U}^{\boldsymbol{S_1}}, \boldsymbol{R}^{\boldsymbol{S_1}}, \boldsymbol{T}^{\boldsymbol{A_1}}, \boldsymbol{R}^{\boldsymbol{A_1}}, \boldsymbol{D}^{\boldsymbol{T}}, \boldsymbol{U}^{\boldsymbol{T}}, \boldsymbol{D}^{\boldsymbol{B}}, \boldsymbol{U}^{\boldsymbol{B}}, \boldsymbol{T}^{\boldsymbol{E}}, \boldsymbol{D}^{\boldsymbol{S_d}} \right\} \tag{A.2}$$

$$\boldsymbol{\mathcal{V}} = \{\boldsymbol{\mathcal{V}}_{\mathbf{1}}, \boldsymbol{\mathcal{V}}_{\mathbf{2}}, \mathbf{0}, \mathbf{0}, \mathbf{0}, \mathbf{0}, \mathbf{0}, \mathbf{0}, \mathbf{0}, \mathbf{0}, \mathbf{0}, \mathbf{0}, \boldsymbol{\mathcal{V}}_{\mathbf{13}}, \boldsymbol{\mathcal{V}}_{\mathbf{14}}\} \tag{A.3}$$

where

$$\begin{aligned}
\underline{\boldsymbol{\mathcal{C}}^{\mathbf{1}}_{\mathbf{1}}}(\varrho_{\xi'}, \varrho_{\gamma}) &= k^{+}_{n_s\gamma}\mathcal{F}^{n'_s\xi'}_{n_s\gamma}\delta_{s's} \\
\underline{\boldsymbol{\mathcal{C}}^{\mathbf{1}}_{\mathbf{1}}}(\varrho_{\xi'}, \varrho_{\gamma}) &= k^{+}_{n_s\gamma}\mathcal{F}^{n'_s\xi'}_{n_s\gamma}\delta_{s's}, \\
\underline{\boldsymbol{\mathcal{C}}^{\mathbf{2}}_{\mathbf{1}}}(\varrho_{\xi'}, \varrho_{g}) &= k^{+}_{n_sg}\mathcal{W}^{n'_s\xi'}_{n_sg}\delta_{s's}, \\
\underline{\boldsymbol{\mathcal{C}}^{\mathbf{3}}_{\mathbf{1}}}(\varrho_{\xi'}, \varrho_{\xi'}) &= -\mathbf{diag}\left(k^{-}_{n'_s\xi'}r^2_R\right), \\
\underline{\boldsymbol{\mathcal{C}}^{\mathbf{4}}_{\mathbf{1}}}(\varrho_{\xi'}, \varrho_{\xi'}) &= -\mathbf{diag}\left(k^{+}_{n'_s\xi'}\mathrm{e}^{\mathrm{i}k^{+}_{n'_s\xi'}L_{R_1}}r^2_R\right) \\
\underline{\boldsymbol{\mathcal{C}}^{\mathbf{1}}_{\mathbf{2}}}(\varrho_{\gamma'}, \varrho_{\gamma'}) &= r^2_{R_d}I_{n'_s\gamma'}, \\
\underline{\boldsymbol{\mathcal{C}}^{\mathbf{3}}_{\mathbf{2}}}(\varrho_{\gamma'}, \varrho_{\xi}) &= -\mathcal{F}^{n'_s\gamma'[T]}_{n_s\xi}, \\
\underline{\boldsymbol{\mathcal{C}}^{\mathbf{4}}_{\mathbf{2}}}(\varrho_{\gamma'}, \varrho_{\xi}) &= -\mathrm{e}^{\mathrm{i}k^{+}_{n_s\xi}L_{R_1}}\mathcal{F}^{n'_s\gamma'[T]}_{n_s\xi}\delta_{s's} \\
\underline{\boldsymbol{\mathcal{C}}^{\mathbf{2}}_{\mathbf{3}}}(\varrho_{g'}, \varrho_{g'}) &= r^2_{g_2}I_{n'_sg'}, \\
\underline{\boldsymbol{\mathcal{C}}^{\mathbf{3}}_{\mathbf{3}}}(\varrho_{g'}, \varrho_{\xi}) &= -\mathcal{W}^{n'_sg'[T]}_{n_s\xi}, \\
\underline{\boldsymbol{\mathcal{C}}^{\mathbf{4}}_{\mathbf{3}}}(\varrho_{g'}, \varrho_{\xi}) &= -\mathrm{e}^{\mathrm{i}k^{+}_{n_s\xi}L_{R_1}}\mathcal{W}^{n'_sg'[T]}_{n_s\xi}\delta_{s's}, \\
\underline{\boldsymbol{\mathcal{C}}^{\mathbf{3}}_{\mathbf{4}}}(\varrho_{\beta'}, \varrho_{\xi}) &= k^{-}_{n_s\xi}\mathrm{e}^{-\mathrm{i}k^{-}_{n_s\xi}L_{R_1}}\mathcal{K}^{n'_s\beta'}_{n_s\xi}\delta_{s's}, \\
\underline{\boldsymbol{\mathcal{C}}^{\mathbf{4}}_{\mathbf{4}}}(\varrho_{\beta'}, \varrho_{\xi}) &= k^{+}_{n_s\xi}\mathcal{K}^{n'_s\beta'}_{n_s\xi}\delta_{s's}, \\
\underline{\boldsymbol{\mathcal{C}}^{\mathbf{5}}_{\mathbf{4}}}(\varrho_{\beta'}, \varrho_{\eta}) &= k^{+}_{n_s\eta}\mathcal{X}^{n'_s\beta'}_{n_s\eta}\delta_{s's}, \\
\underline{\boldsymbol{\mathcal{C}}^{\mathbf{6}}_{\mathbf{4}}}(\varrho_{\beta'}, \varrho_{\eta}) &= k^{-}_{n_s\eta}\mathrm{e}^{-\mathrm{i}k^{-}_{n_s\eta}L_{S_1}}\mathcal{X}^{n'_s\beta'}_{n_s\eta}\delta_{s's}, \\
\underline{\boldsymbol{\mathcal{C}}^{\mathbf{7}}_{\mathbf{4}}}(\varrho_{\beta'}, \varrho_{\beta'}) &= -\mathbf{diag}\left(k^{-}_{n'_s\beta'}r^2_2\right), \\
\underline{\boldsymbol{\mathcal{C}}^{\mathbf{8}}_{\mathbf{4}}}(\varrho_{\beta'}, \varrho_{\beta'}) &= -\mathbf{diag}\left(k^{+}_{n'_s\beta'}\mathrm{e}^{\mathrm{i}k^{+}_{n'_s\beta'}d_1}r^2_2\right), \\
\underline{\boldsymbol{\mathcal{C}}^{\mathbf{3}}_{\mathbf{5}}}(\varrho_{\xi'}, \varrho_{\xi'}) &= \mathbf{diag}\left(\mathrm{e}^{-\mathrm{i}k^{-}_{n'_s\xi'}L_{R_1}}r^2_R\right), \\
\underline{\boldsymbol{\mathcal{C}}^{\mathbf{4}}_{\mathbf{5}}}(\varrho_{\xi'}, \varrho_{\xi'}) &= r^2_RI^{s'\xi'}_{s'\xi'}, \\
\underline{\boldsymbol{\mathcal{C}}^{\mathbf{7}}_{\mathbf{5}}}(\varrho_{\xi'}, \varrho_{\beta}) &= -\mathcal{K}^{n'_s\xi'[T]}_{n_s\beta}\delta_{s's}, \\
\underline{\boldsymbol{\mathcal{C}}^{\mathbf{8}}_{\mathbf{5}}}(\varrho_{\xi'}, \varrho_{\beta}) &= -\mathrm{e}^{\mathrm{i}k^{+}_{n_s\beta}d_1}\mathcal{K}^{n'_s\xi'[T]}_{n_s\beta}\delta_{s's} \\
\underline{\boldsymbol{\mathcal{C}}^{\mathbf{5}}_{\mathbf{6}}}(\varrho_{\eta'}, \varrho_{\eta'}) &= r^2_2I_{eta'\eta'}, \\
\underline{\boldsymbol{\mathcal{C}}^{\mathbf{6}}_{\mathbf{6}}}(\varrho_{\eta'}, \varrho_{\eta'}) &= \mathbf{diag}\left(\mathrm{e}^{-\mathrm{i}k^{-}_{n'_s\eta'}L_{S_1}}r^2_2\right), \\
\underline{\boldsymbol{\mathcal{C}}^{\mathbf{7}}_{\mathbf{6}}}(\varrho_{\eta'}, \varrho_{\beta}) &= -\mathcal{X}^{n'_s\eta'[T]}_{n_s\beta}\delta_{s's}, \\
\underline{\boldsymbol{\mathcal{C}}^{\mathbf{8}}_{\mathbf{6}}}(\varrho_{\eta'}, \varrho_{\beta}) &= -\mathrm{e}^{\mathrm{i}k^{+}_{n_s\beta}d_1}\mathcal{X}^{n'_s\eta'[T]}_{n_s\beta}\delta_{s's}
\end{aligned}$$

$$
\begin{aligned}
\underline{\boldsymbol{\mathcal{C}}_{\mathbf{7}}^{\mathbf{7}}}(\varrho_{\beta'}, \varrho_{\beta'}) &= \mathbf{diag}\left(k^{-}_{n'_s\beta'}\mathrm{e}^{-\mathrm{i}k^{-}_{n'_s\beta'}d_1} r_2^2\right), \\
\underline{\boldsymbol{\mathcal{C}}_{\mathbf{7}}^{\mathbf{8}}}(\varrho_{\beta'}, \varrho_{\beta'}) &= \mathbf{diag}\left(k^{+}_{n'_s\beta'} r_2^2\right), \\
\underline{\boldsymbol{\mathcal{C}}_{\mathbf{7}}^{\mathbf{9}}}(\varrho_{\beta'}, \varrho_{\mu}) &= -k^{-}_{n_s\mu}\mathcal{Q}^{n'_s\beta'}_{n_s\mu}\delta_{s's}, \\
\underline{\boldsymbol{\mathcal{C}}_{\mathbf{7}}^{\mathbf{10}}}(\varrho_{\beta'}, \varrho_{\mu}) &= -k^{+}_{n_s\mu}\mathrm{e}^{\mathrm{i}k^{+}_{n_s\mu}L_D}\mathcal{Q}^{n'_s\beta'}_{n_s\mu}\delta_{s's}, \\
\underline{\boldsymbol{\mathcal{C}}_{\mathbf{7}}^{\mathbf{11}}}(\varrho_{\beta'}, \varrho_{\nu}) &= -k^{-}_{n_s\nu}\mathcal{Y}^{n'_s\beta'}_{n_s\nu}\delta_{s's}, \\
\underline{\boldsymbol{\mathcal{C}}_{\mathbf{7}}^{\mathbf{12}}}(\varrho_{\beta'}, \varrho_{\nu}) &= -k^{+}_{n_s\nu}\mathrm{e}^{\mathrm{i}k^{+}_{n_s\nu}L_D}\mathcal{Y}^{n'_s\beta'}_{n_s\nu}\delta_{s's}, \\
\underline{\boldsymbol{\mathcal{C}}_{\mathbf{8}}^{\mathbf{7}}}(\varrho_{\mu'}, \varrho_{\beta}) &= \mathrm{e}^{-\mathrm{i}k^{-}_{n_s\beta}d_1}\mathcal{Q}^{n'_s\mu'[T]}_{n_s\beta}\delta_{s's}, \\
\underline{\boldsymbol{\mathcal{C}}_{\mathbf{8}}^{\mathbf{8}}}(\varrho_{\mu'}, \varrho_{\beta}) &= \mathcal{Q}^{n'_s\mu'[T]}_{n_s\beta}\delta_{s's}, \\
\underline{\boldsymbol{\mathcal{C}}_{\mathbf{8}}^{\mathbf{9}}}(\varrho_{\mu'}, \varrho_{\mu'}) &= -r_{w_3}^2 I^{s'\mu'}_{s'\mu'}, \\
\underline{\boldsymbol{\mathcal{C}}_{\mathbf{8}}^{\mathbf{10}}}(\varrho_{\mu'}, \varrho_{\mu'}) &= -\mathbf{diag}\left(\mathrm{e}^{\mathrm{i}k^{+}_{n'_s\mu'}L_D} r_{w_3}^2\right), \\
\underline{\boldsymbol{\mathcal{C}}_{\mathbf{9}}^{\mathbf{7}}}(\varrho_{\nu'}, \varrho_{\beta}) &= \mathrm{e}^{-\mathrm{i}k^{-}_{n_s\beta}d_1}\mathcal{Y}^{n'_s\nu'[T]}_{n_s\beta}\delta_{s's}, \\
\underline{\boldsymbol{\mathcal{C}}_{\mathbf{9}}^{\mathbf{8}}}(\varrho_{\nu'}, \varrho_{\beta}) &= \mathcal{Y}^{n'_s\nu'[T]}_{n_s\beta}\delta_{s's}, \\
\underline{\boldsymbol{\mathcal{C}}_{\mathbf{9}}^{\mathbf{11}}}(\varrho_{\nu'}, \varrho_{\nu'}) &= -\mathbf{diag}\left(r_{d_1}^2\right)\delta_{s's}, \\
\underline{\boldsymbol{\mathcal{C}}_{\mathbf{9}}^{\mathbf{12}}}(\varrho_{\nu'}, \varrho_{\nu'}) &= -\mathbf{diag}\left(\mathrm{e}^{\mathrm{i}k^{+}_{n'_s\nu'}L_D} r_{d_1}^2\right) \\
\underline{\boldsymbol{\mathcal{C}}_{\mathbf{10}}^{\mathbf{9}}}(\varrho_{m'}, \varrho_{\mu}) &= k^{-}_{n_s\mu}\mathrm{e}^{-\mathrm{i}k^{-}_{n_s\mu}L_D}\mathcal{A}^{n'_sm'}_{n_s\mu}\delta_{s's}, \\
\underline{\boldsymbol{\mathcal{C}}_{\mathbf{10}}^{\mathbf{10}}}(\varrho_{m'}, \varrho_{\mu}) &= k^{+}_{n_s\mu}\mathcal{A}^{n'_sm'}_{n_s\mu}\delta_{s's}, \\
\underline{\boldsymbol{\mathcal{C}}_{\mathbf{10}}^{\mathbf{11}}}(\varrho_{m'}, \varrho_{\nu}) &= k^{-}_{n_s\nu}\mathrm{e}^{-\mathrm{i}k^{-}_{n_s\nu}L_D}\mathcal{G}^{n'_sm'}_{n_s\nu}\delta_{s's}, \\
\underline{\boldsymbol{\mathcal{C}}_{\mathbf{10}}^{\mathbf{12}}}(\varrho_{m'}, \varrho_{\nu}) &= k^{+}_{n_s\nu}\mathcal{G}^{n'_sm'}_{n_s\nu}\delta_{s's}, \\
\underline{\boldsymbol{\mathcal{C}}_{\mathbf{10}}^{\mathbf{13}}}(\varrho_{m'}, \varrho_{m'}) &= -\mathbf{diag}\left(k^{-}_{n'_sm'} r_{e_2}^2\right), \\
\underline{\boldsymbol{\mathcal{C}}_{\mathbf{11}}^{\mathbf{9}}}(\varrho_{\mu'}, \varrho_{\mu'}) &= \mathbf{diag}\left(\mathrm{e}^{-\mathrm{i}k^{-}_{n'_s\mu'}L_D} r_{w_3}^2\right), \\
\underline{\boldsymbol{\mathcal{C}}_{\mathbf{11}}^{\mathbf{10}}}(\varrho_{\mu'}, \varrho_{\mu'}) &= r_{w_3}^2 I^{s'\mu'}_{s'\mu'}, \\
\underline{\boldsymbol{\mathcal{C}}_{\mathbf{11}}^{\mathbf{13}}}(\varrho_{\mu'}, \varrho_{m}) &= -\mathcal{A}^{n'_s\mu'[T]}_{n_sm}\delta_{s's}, \\
\underline{\boldsymbol{\mathcal{C}}_{\mathbf{12}}^{\mathbf{11}}}(\varrho_{\nu'}, \varrho_{\nu'}) &= \mathbf{diag}\left(\mathrm{e}^{-\mathrm{i}k^{-}_{n'_s\nu'}L_D} r_{d_1}^2\right), \\
\underline{\boldsymbol{\mathcal{C}}_{\mathbf{12}}^{\mathbf{12}}}(\varrho_{\nu'}, \varrho_{\nu'}) &= r_{d_1}^2 I^{s'\nu'}_{s'\nu'}, \\
\underline{\boldsymbol{\mathcal{C}}_{\mathbf{12}}^{\mathbf{13}}}(\varrho_{\nu'}, \varrho_{m}) &= -\mathcal{G}^{n'_s\nu'[T]}_{n_sm}\delta_{s's}
\end{aligned}
$$

$$\underline{\boldsymbol{\mathcal{C}}^{\mathbf{5}}_{\mathbf{13}}}(\varrho_{\eta'}, \varrho_{\eta'}) = \mathbf{diag}\left(\frac{2\pi}{V} r_2^2 k^{+}_{n'_s\eta'} \mathrm{e}^{\mathrm{i}k^{+}_{n_s\eta} L_{S_1}}\right),$$

$$\underline{\boldsymbol{\mathcal{C}}^{\mathbf{6}}_{\mathbf{13}}}(\varrho_{\eta'}, \varrho_{\eta'}) = \mathbf{diag}\left(\frac{2\pi}{V} r_2^2 k^{-}_{n'_s\eta'}\right),$$

$$\underline{\boldsymbol{\mathcal{C}}^{\mathbf{14}}_{\mathbf{13}}}(\varrho_{\eta'}, \varsigma) = -k^{+}_{n'_q p'} \varphi_{n'_s q} \Upsilon^{n'_s\eta'[T]}_{n_q p},$$

$$\underline{\boldsymbol{\mathcal{C}}^{\mathbf{5}}_{\mathbf{14}}}(\varsigma', \varrho_{\eta}) = \mathrm{e}^{\mathrm{i}k^{+}_{n_s\eta} L_{S_1}} \Lambda_{q'n_s} \Upsilon^{n'_q p'}_{n_s\eta},$$

$$\underline{\boldsymbol{\mathcal{C}}^{\mathbf{6}}_{\mathbf{14}}}(\varsigma', \varrho_{\eta}) = \Lambda_{q'n_s} \Upsilon^{n'_q p'}_{n_s\eta},$$

$$\underline{\boldsymbol{\mathcal{C}}^{\mathbf{14}}_{\mathbf{14}}}(\varsigma', \varsigma') = -\mathbf{diag}\left(\frac{\theta_a}{2} r^2_{S_{d2}} \left(1 + \delta_{q'0}\right) \delta_{p'p}\right)$$

$$\boldsymbol{\mathcal{V}}_{\mathbf{1}}(\varrho_{\xi'}, 1) = -A^{(R_d)}_{nj} k^{-}_{nj} \mathrm{e}^{-\mathrm{i}k^{-}_{nj} L_{p_1}} \mathcal{F}^{n'_s\xi'}_{nj} \delta_{s'0} - \sum_{s=-\infty}^{+\infty} \sum_{g=0}^{+\infty} k^{-}_{n_s g} D^{(G)}_{n_s g} \mathrm{e}^{-\mathrm{i}k^{-}_{n_s g} L_G} \mathcal{W}^{n'_s\xi'}_{n_s g} \delta_{s's}$$

$$\boldsymbol{\mathcal{V}}_{\mathbf{2}}(\varrho_{\gamma'}, 1) = -A^{(R_d)}_{nj} \mathrm{e}^{-\mathrm{i}k^{-}_{nj} L_{p_1}} \delta_{j\gamma'} \delta_{s'0} r^2_{R_d}$$

$$\boldsymbol{\mathcal{V}}_{\mathbf{13}}(\varrho_{\eta'}, 1) = \sum_{q=0}^{+\infty} \sum_{p=0}^{+\infty} U^{(S_d)}_{n_q p} \mathrm{e}^{-\mathrm{i}k^{-}_{n_q q} L_{S_d}} \varphi_{n'_s q} \Upsilon^{n'_s\eta'[T]}_{n_q p}$$

$$\boldsymbol{\mathcal{V}}_{\mathbf{14}}(\varsigma, 1) = U^{(S_d)}_{n'_q p'} \mathrm{e}^{-\mathrm{i}k^{-}_{n'_q p'} L_d} \frac{\theta_a}{2} r^2_{S_{d2}} \left(1 + \delta_{q'0}\right)$$

## A.2 Matrix terms - Second block

The matrix form of the matching equations is given by

$$\underline{\boldsymbol{\mathcal{H}}} \boldsymbol{X}_{\mathbf{2}} = \boldsymbol{\mathcal{S}} \tag{A.4}$$

where

$$\underline{\boldsymbol{\mathcal{H}}} = \begin{pmatrix}
\underline{\boldsymbol{\mathcal{H}}^{\mathbf{1}}_{\mathbf{1}}} & \underline{\boldsymbol{\mathcal{H}}^{\mathbf{2}}_{\mathbf{1}}} & \underline{\boldsymbol{\mathcal{H}}^{\mathbf{3}}_{\mathbf{1}}} & \underline{\boldsymbol{\mathcal{H}}^{\mathbf{4}}_{\mathbf{1}}} & \mathbf{0} & \mathbf{0} & \mathbf{0} & \mathbf{0} & \mathbf{0} & \mathbf{0} & \mathbf{0} & \mathbf{0} \\
\underline{\boldsymbol{\mathcal{H}}^{\mathbf{1}}_{\mathbf{2}}} & \mathbf{0} & \underline{\boldsymbol{\mathcal{H}}^{\mathbf{3}}_{\mathbf{2}}} & \underline{\boldsymbol{\mathcal{H}}^{\mathbf{4}}_{\mathbf{2}}} & \mathbf{0} & \mathbf{0} & \mathbf{0} & \mathbf{0} & \mathbf{0} & \mathbf{0} & \mathbf{0} & \mathbf{0} \\
\mathbf{0} & \underline{\boldsymbol{\mathcal{H}}^{\mathbf{2}}_{\mathbf{3}}} & \underline{\boldsymbol{\mathcal{H}}^{\mathbf{3}}_{\mathbf{3}}} & \underline{\boldsymbol{\mathcal{H}}^{\mathbf{4}}_{\mathbf{3}}} & \mathbf{0} & \mathbf{0} & \mathbf{0} & \mathbf{0} & \mathbf{0} & \mathbf{0} & \mathbf{0} & \mathbf{0} \\
\mathbf{0} & \mathbf{0} & \underline{\boldsymbol{\mathcal{H}}^{\mathbf{3}}_{\mathbf{4}}} & \underline{\boldsymbol{\mathcal{H}}^{\mathbf{4}}_{\mathbf{4}}} & \underline{\boldsymbol{\mathcal{H}}^{\mathbf{5}}_{\mathbf{4}}} & \underline{\boldsymbol{\mathcal{H}}^{\mathbf{6}}_{\mathbf{4}}} & \underline{\boldsymbol{\mathcal{H}}^{\mathbf{7}}_{\mathbf{4}}} & \underline{\boldsymbol{\mathcal{H}}^{\mathbf{8}}_{\mathbf{4}}} & \mathbf{0} & \mathbf{0} & \mathbf{0} & \mathbf{0} \\
\mathbf{0} & \mathbf{0} & \underline{\boldsymbol{\mathcal{H}}^{\mathbf{3}}_{\mathbf{5}}} & \underline{\boldsymbol{\mathcal{H}}^{\mathbf{4}}_{\mathbf{5}}} & \mathbf{0} & \mathbf{0} & \underline{\boldsymbol{\mathcal{H}}^{\mathbf{7}}_{\mathbf{5}}} & \underline{\boldsymbol{\mathcal{H}}^{\mathbf{8}}_{\mathbf{5}}} & \mathbf{0} & \mathbf{0} & \mathbf{0} & \mathbf{0} \\
\mathbf{0} & \mathbf{0} & \mathbf{0} & \mathbf{0} & \underline{\boldsymbol{\mathcal{H}}^{\mathbf{5}}_{\mathbf{6}}} & \underline{\boldsymbol{\mathcal{H}}^{\mathbf{6}}_{\mathbf{6}}} & \underline{\boldsymbol{\mathcal{H}}^{\mathbf{7}}_{\mathbf{6}}} & \underline{\boldsymbol{\mathcal{H}}^{\mathbf{8}}_{\mathbf{6}}} & \mathbf{0} & \mathbf{0} & \mathbf{0} & \mathbf{0} \\
\mathbf{0} & \mathbf{0} & \mathbf{0} & \mathbf{0} & \mathbf{0} & \mathbf{0} & \underline{\boldsymbol{\mathcal{H}}^{\mathbf{7}}_{\mathbf{7}}} & \underline{\boldsymbol{\mathcal{H}}^{\mathbf{8}}_{\mathbf{7}}} & \underline{\boldsymbol{\mathcal{H}}^{\mathbf{9}}_{\mathbf{7}}} & \underline{\boldsymbol{\mathcal{H}}^{\mathbf{10}}_{\mathbf{7}}} & \underline{\boldsymbol{\mathcal{H}}^{\mathbf{11}}_{\mathbf{7}}} & \mathbf{0} \\
\mathbf{0} & \mathbf{0} & \mathbf{0} & \mathbf{0} & \mathbf{0} & \mathbf{0} & \underline{\boldsymbol{\mathcal{H}}^{\mathbf{7}}_{\mathbf{8}}} & \underline{\boldsymbol{\mathcal{H}}^{\mathbf{8}}_{\mathbf{8}}} & \underline{\boldsymbol{\mathcal{H}}^{\mathbf{9}}_{\mathbf{8}}} & \underline{\boldsymbol{\mathcal{H}}^{\mathbf{10}}_{\mathbf{8}}} & \mathbf{0} & \mathbf{0} \\
\mathbf{0} & \mathbf{0} & \mathbf{0} & \mathbf{0} & \mathbf{0} & \mathbf{0} & \underline{\boldsymbol{\mathcal{H}}^{\mathbf{7}}_{\mathbf{9}}} & \underline{\boldsymbol{\mathcal{H}}^{\mathbf{8}}_{\mathbf{9}}} & \mathbf{0} & \mathbf{0} & \underline{\boldsymbol{\mathcal{H}}^{\mathbf{11}}_{\mathbf{9}}} & \mathbf{0} \\
\mathbf{0} & \mathbf{0} & \mathbf{0} & \mathbf{0} & \mathbf{0} & \mathbf{0} & \mathbf{0} & \mathbf{0} & \underline{\boldsymbol{\mathcal{H}}^{\mathbf{9}}_{\mathbf{10}}} & \underline{\boldsymbol{\mathcal{H}}^{\mathbf{10}}_{\mathbf{10}}} & \mathbf{0} & \mathbf{0} \\
\mathbf{0} & \mathbf{0} & \mathbf{0} & \mathbf{0} & \underline{\boldsymbol{\mathcal{H}}^{\mathbf{5}}_{\mathbf{11}}} & \underline{\boldsymbol{\mathcal{H}}^{\mathbf{6}}_{\mathbf{11}}} & \mathbf{0} & \mathbf{0} & \mathbf{0} & \mathbf{0} & \mathbf{0} & \underline{\boldsymbol{\mathcal{H}}^{\mathbf{12}}_{\mathbf{11}}} \\
\mathbf{0} & \mathbf{0} & \mathbf{0} & \mathbf{0} & \underline{\boldsymbol{\mathcal{H}}^{\mathbf{5}}_{\mathbf{12}}} & \underline{\boldsymbol{\mathcal{H}}^{\mathbf{6}}_{\mathbf{12}}} & \mathbf{0} & \mathbf{0} & \mathbf{0} & \mathbf{0} & \mathbf{0} & \underline{\boldsymbol{\mathcal{H}}^{\mathbf{12}}_{\mathbf{12}}}
\end{pmatrix} \tag{A.5}$$

$$\boldsymbol{X_2} = \left\{\boldsymbol{U}^{\boldsymbol{R_{d2}}}, \boldsymbol{D}^{\boldsymbol{G}}, \boldsymbol{D}^{\boldsymbol{R_2}}, \boldsymbol{U}^{\boldsymbol{R_2}}, \boldsymbol{U}^{\boldsymbol{S_2}}, \boldsymbol{T}^{\boldsymbol{S_2}}, \boldsymbol{T}^{\boldsymbol{A_2}}, \boldsymbol{R}^{\boldsymbol{A_2}}, \boldsymbol{T}^{\boldsymbol{W}}, \boldsymbol{R}^{\boldsymbol{W}}, \boldsymbol{T}^{\boldsymbol{F}}, \boldsymbol{U}^{\boldsymbol{S_d}}\right\} \tag{A.6}$$

$$\boldsymbol{S} = \{\boldsymbol{\mathcal{S}_1}, \boldsymbol{\mathcal{S}_2}, \mathbf{0}, \mathbf{0}, \mathbf{0}, \mathbf{0}, \mathbf{0}, \mathbf{0}, \mathbf{0}, \mathbf{0}, \boldsymbol{\mathcal{S}_{11}}, \boldsymbol{\mathcal{S}_{12}}\} \tag{A.7}$$

where

$$\begin{aligned}
\underline{\boldsymbol{\mathcal{H}}^{\mathbf{1}}_{\mathbf{1}}}(\varrho_{\xi'}, \varrho_{\gamma}) &= k^{-}_{n_s\gamma}\mathcal{F}^{n'_s\xi'}_{n_s\gamma}\delta_{s's}, \\
\underline{\boldsymbol{\mathcal{H}}^{\mathbf{2}}_{\mathbf{1}}}(\varrho_{\xi'}, \varrho_{g}) &= k^{-}_{n_sg}\mathcal{W}^{n'_s\xi'}_{n_sg}\delta_{s's}, \\
\underline{\boldsymbol{\mathcal{H}}^{\mathbf{3}}_{\mathbf{1}}}(\varrho_{\xi'}, \varrho_{\xi'}) &= -\mathbf{diag}\left(k^{+}_{n'_s\xi'}r^2_R\right), \\
\underline{\boldsymbol{\mathcal{H}}^{\mathbf{4}}_{\mathbf{1}}}(\varrho_{\xi'}, \varrho_{\xi'}) &= -\mathbf{diag}\left(k^{-}_{n'_s\xi'}\mathrm{e}^{-\mathrm{i}k^{-}_{n'_s\xi'}L_{R_2}}r^2_R\right), \\
\underline{\boldsymbol{\mathcal{H}}^{\mathbf{1}}_{\mathbf{2}}}(\varrho_{\gamma'}, \varrho_{\gamma'}) &= r^2_{R_d}I^{n'_s\gamma'}_{n'_s\gamma'}, \\
\underline{\boldsymbol{\mathcal{H}}^{\mathbf{3}}_{\mathbf{2}}}(\varrho_{\gamma'}, \varrho_{\xi}) &= -\mathcal{F}^{n'_s\gamma'[T]}_{n_s\xi}\delta_{s's}, \\
\underline{\boldsymbol{\mathcal{H}}^{\mathbf{4}}_{\mathbf{2}}}(\varrho_{\gamma'}, \varrho_{\xi}) &= -\mathrm{e}^{-\mathrm{i}k^{-}_{n_s\xi}L_{R_2}}\mathcal{F}^{n'_s\gamma'[T]}_{n_s\xi}\delta_{s's}, \\
\underline{\boldsymbol{\mathcal{H}}^{\mathbf{2}}_{\mathbf{3}}}(\varrho_{g'}, \varrho_{g'}) &= r^2_{g_2}I^{n'_sg'}_{n'_sg'}, \\
\underline{\boldsymbol{\mathcal{H}}^{\mathbf{3}}_{\mathbf{3}}}(\varrho_{g'}, \varrho_{\xi}) &= -\mathcal{W}^{n'_sg'[T]}_{n_s\xi}\delta_{s's}, \\
\underline{\boldsymbol{\mathcal{H}}^{\mathbf{4}}_{\mathbf{3}}}(\varrho_{g'}, \varrho_{\xi}) &= -\mathrm{e}^{-\mathrm{i}k^{-}_{n_s\xi}L_{R_2}}\mathcal{W}^{n'_sg'[T]}_{n_s\xi}\delta_{s's}, \\
\underline{\boldsymbol{\mathcal{S}_1}}(\varrho_{\xi'}, 1) &= -A^{(R_{d2})}_{nj}k^{+}_{nj}\mathrm{e}^{\mathrm{i}k^{+}_{nj}L_{p_2}}\mathcal{F}^{n'_s\xi'}_{nj}\delta_{s'0} - \sum_{s=-\infty}^{+\infty}\sum_{g=0}^{+\infty}k^{+}_{n_sg}U^{(G)}_{n_sg}\mathrm{e}^{\mathrm{i}k^{+}_{n_sg}L_G}\mathcal{W}^{n'_s\xi'}_{n_sg}\delta_{s's}, \\
\underline{\boldsymbol{\mathcal{S}_2}}(\varrho_{\gamma'}, 1) &= -A^{(R_{d2})}_{nj}\mathrm{e}^{\mathrm{i}k^{+}_{nj}L_{p_2}}\delta_{j\gamma'}\delta_{s'0}r^2_{R_d}, \\
\underline{\boldsymbol{\mathcal{H}}^{\mathbf{3}}_{\mathbf{4}}}(\varrho_{\beta'}, \varrho_{\xi}) &= k^{+}_{n_s\xi}\mathrm{e}^{\mathrm{i}k^{+}_{n_s\xi}L_{R_2}}\mathcal{K}^{n'_s\beta'}_{n_s\xi}\delta_{s's}, \\
\underline{\boldsymbol{\mathcal{H}}^{\mathbf{4}}_{\mathbf{4}}}(\varrho_{\beta'}, \varrho_{\xi}) &= k^{-}_{n_s\xi}\mathcal{K}^{n'_s\beta'}_{n_s\xi}\delta_{s's}, \\
\underline{\boldsymbol{\mathcal{H}}^{\mathbf{5}}_{\mathbf{4}}}(\varrho_{\beta'}, \varrho_{\xi}) &= k^{-}_{n_s\eta}\mathcal{X}^{n'_s\beta'}_{n_s\eta}\delta_{s's}, \\
\underline{\boldsymbol{\mathcal{H}}^{\mathbf{6}}_{\mathbf{4}}}(\varrho_{\beta'}, \varrho_{\xi}) &= k^{+}_{n_s\eta}\mathrm{e}^{\mathrm{i}k^{+}_{n_s\eta}L_{S_2}}\mathcal{X}^{n'_s\beta'}_{n_s\eta}\delta_{s's}, \\
\underline{\boldsymbol{\mathcal{H}}^{\mathbf{7}}_{\mathbf{4}}}(\varrho_{\beta'}, \varrho_{\beta}) &= -\mathbf{diag}\left(k^{-}_{n'_s\beta'}r^2_2\right), \\
\underline{\boldsymbol{\mathcal{H}}^{\mathbf{8}}_{\mathbf{4}}}(\varrho_{\beta'}, \varrho_{\beta}) &= -\mathbf{diag}\left(k^{+}_{n'_s\beta'}\mathrm{e}^{-\mathrm{i}k^{-}_{n'_s\beta'}d_2}r^2_2\right), \\
\underline{\boldsymbol{\mathcal{H}}^{\mathbf{3}}_{\mathbf{5}}}(\varrho_{\xi'}, \varrho_{\xi'}) &= \mathbf{diag}\left(\mathrm{e}^{\mathrm{i}k^{+}_{n'_s\xi'}L_{R_2}}r^2_R\right), \\
\underline{\boldsymbol{\mathcal{H}}^{\mathbf{4}}_{\mathbf{5}}}(\varrho_{\xi'}, \varrho_{\xi'}) &= r^2_RI^{n'_s\xi'}_{n'_s\xi'}, \\
\underline{\boldsymbol{\mathcal{H}}^{\mathbf{7}}_{\mathbf{5}}}(\varrho_{\xi'}, \varrho_{\beta}) &= -\mathcal{K}^{n'_s\xi'[T]}_{n_s\beta}\delta_{s's}, \\
\underline{\boldsymbol{\mathcal{H}}^{\mathbf{8}}_{\mathbf{5}}}(\varrho_{\xi'}, \varrho_{\beta}) &= -\mathrm{e}^{-\mathrm{i}k^{-}_{n_s\beta}d_2}\mathcal{K}^{n'_s\xi'[T]}_{n_s\beta}\delta_{s's},
\end{aligned}$$

$$
\begin{aligned}
\underline{\boldsymbol{\mathcal{H}}_{\mathbf{6}}^{\mathbf{5}}}(\varrho_{\eta'},\varrho_{\eta'}) &= r_2^2 I_{n_s'\eta'}^{n_s'\eta'},\\
\underline{\boldsymbol{\mathcal{H}}_{\mathbf{6}}^{\mathbf{6}}}(\varrho_{\eta'},\varrho_{\eta'}) &= \mathbf{diag}\left(\mathrm{e}^{\mathrm{i}k_{n_s'\eta'}^{+}L_{S_2}} r_2^2\right),\\
\underline{\boldsymbol{\mathcal{H}}_{\mathbf{6}}^{\mathbf{7}}}(\varrho_{\eta'},\varrho_{\beta}) &= -\mathcal{X}_{n_s\beta}^{n_s'\eta'[T]}\delta_{s's},\\
\underline{\boldsymbol{\mathcal{H}}_{\mathbf{6}}^{\mathbf{8}}}(\varrho_{\eta'},\varrho_{\beta}) &= -\mathrm{e}^{-\mathrm{i}k_{n_s\beta}^{-}d_2}\mathcal{X}_{n_s\beta}^{n_s'\eta'[T]}\delta_{s's},\\
\underline{\boldsymbol{\mathcal{H}}_{\mathbf{7}}^{\mathbf{7}}}(\varrho_{\beta'},\varrho_{\beta'}) &= \mathbf{diag}\left(k_{n_s'\beta'}^{-}\mathrm{e}^{\mathrm{i}k_{n_s'\beta'}^{+}d_2} r_2^2\right),\\
\underline{\boldsymbol{\mathcal{H}}_{\mathbf{7}}^{\mathbf{8}}}(\varrho_{\beta'},\varrho_{\beta'}) &= \mathbf{diag}\left(k_{n_s'\beta'}^{+} r_2^2\right),\\
\underline{\boldsymbol{\mathcal{H}}_{\mathbf{7}}^{\mathbf{9}}}(\varrho_{\beta'},\varrho_{w}) &= -k_{n_sw}^{+}\mathcal{B}_{n_sw}^{n_s'\beta'}\delta_{s's},\\
\underline{\boldsymbol{\mathcal{H}}_{\mathbf{7}}^{\mathbf{10}}}(\varrho_{\beta'},\varrho_{w}) &= -k_{n_sw}^{-}\mathrm{e}^{-\mathrm{i}k_{n_sw}^{-}L_W}\mathcal{B}_{n_sw}^{n_s'\beta'}\delta_{s's},\\
\underline{\boldsymbol{\mathcal{H}}_{\mathbf{7}}^{\mathbf{11}}}(\varrho_{\beta'},\varrho_{\alpha}) &= -k_{n_s\alpha}^{+}\mathcal{O}_{n_s\alpha}^{n_s'\beta'}\delta_{s's},\\
\underline{\boldsymbol{\mathcal{H}}_{\mathbf{8}}^{\mathbf{7}}}(\varrho_{w'},\varrho_{\beta}) &= \mathrm{e}^{\mathrm{i}k_{n_s\beta}^{+}d_2}\mathcal{B}_{n_s\beta}^{n_s'w'[T]}\delta_{s's},\\
\underline{\boldsymbol{\mathcal{H}}_{\mathbf{8}}^{\mathbf{8}}}(\varrho_{w'},\varrho_{\beta}) &= \mathcal{B}_{n_s\beta}^{n_s'w'[T]}\delta_{s's},\\
\underline{\boldsymbol{\mathcal{H}}_{\mathbf{8}}^{\mathbf{9}}}(\varrho_{w'},\varrho_{w'}) &= -r_2^2 I_{n_s'w'}^{n_s'w'},\\
\underline{\boldsymbol{\mathcal{H}}_{\mathbf{8}}^{\mathbf{10}}}(\varrho_{w'},\varrho_{w'}) &= -\mathbf{diag}\left(\mathrm{e}^{-\mathrm{i}k_{n_s'w'}^{-}L_W} r_2^2\right),\\
\underline{\boldsymbol{\mathcal{H}}_{\mathbf{9}}^{\mathbf{7}}}(\varrho_{\alpha'},\varrho_{\beta}) &= \mathrm{e}^{\mathrm{i}k_{n_s\beta}^{+}d_2}\mathcal{O}_{n_s\beta}^{n_s'\alpha'[T]}\delta_{s's},\\
\underline{\boldsymbol{\mathcal{H}}_{\mathbf{9}}^{\mathbf{8}}}(\varrho_{\alpha'},\varrho_{\beta}) &= \mathcal{O}_{n_s\beta}^{n_s'\alpha'[T]}\delta_{s's},\\
\underline{\boldsymbol{\mathcal{H}}_{\mathbf{9}}^{\mathbf{11}}}(\varrho_{\alpha'},\varrho_{\alpha'}) &= -r_{f_2}^2 I_{n_s'\alpha'}^{n_s'\alpha'},\\
\underline{\boldsymbol{\mathcal{H}}_{\mathbf{11}}^{\mathbf{5}}}(\varrho_{\eta'},\varrho_{\eta'}) &= \mathbf{diag}\left(\frac{2\pi}{B} r_2^2 k_{n_s'\eta'}^{-}\mathrm{e}^{-\mathrm{i}k_{n_s\eta}^{-}L_{S_2}}\right),\\
\underline{\boldsymbol{\mathcal{H}}_{\mathbf{11}}^{\mathbf{6}}}(\varrho_{\eta'},\varrho_{\eta'}) &= \mathbf{diag}\left(\frac{2\pi}{B} r_2^2 k_{n_s'\eta'}^{+}\right),\\
\underline{\boldsymbol{\mathcal{H}}_{\mathbf{11}}^{\mathbf{12}}}(\varrho_{\eta'},\varsigma) &= -k_{n_q'p'}^{-}\varphi_{n_s'q}\Upsilon_{n_qp}^{n_s'\eta'[T]},\\
\underline{\boldsymbol{\mathcal{H}}_{\mathbf{12}}^{\mathbf{5}}}(\varsigma,\varrho_{\eta'}) &= \mathrm{e}^{-\mathrm{i}k_{n_s\eta}^{-}L_{S_2}}\Lambda_{q'n_s}\Upsilon_{n_s\eta}^{n_q'p'},\\
\underline{\boldsymbol{\mathcal{H}}_{\mathbf{12}}^{\mathbf{6}}}(\varsigma,\varrho_{\eta'}) &= \Lambda_{q'n_s}\Upsilon_{n_s\eta}^{n_q'p'},\\
\underline{\boldsymbol{\mathcal{H}}_{\mathbf{12}}^{\mathbf{12}}}(\varsigma,\varsigma) &= -\mathbf{diag}\left(\frac{\theta_a}{2} r_{S_{d2}}^2\left(1+\delta_{q'0}\right)\right),\\
\boldsymbol{\mathcal{S}}_{\mathbf{11}}(\varrho_{\eta'},1) &= \sum_{q=0}^{+\infty}\sum_{p=0}^{+\infty} D_{n_qp}^{(S_d)}\mathrm{e}^{\mathrm{i}k_{n_qq}^{+}L_{S_d}}\varphi_{n_s'q}\Upsilon_{n_qp}^{n_s'\eta'[T]},\\
\boldsymbol{\mathcal{S}}_{\mathbf{12}}(\varsigma,1) &= D_{n_q'p'}^{(S_d)}\mathrm{e}^{\mathrm{i}k_{n_q'p'}^{+}L_d}\frac{\theta_a}{2} r_{S_{d2}}^2\left(1+\delta_{q'0}\right)
\end{aligned}
$$

# Appendix B

# Finite Element Method

## B.1 Variational formulation of the Helmholtz equation (3D)

The simulation domain is divided into five different regions (see Figure B.1):

- The physical domain: represents the simulation domain in which the solution of the problem is found.
- Three perfectly matched layers to attenuate the acoustic waves coming from the physical domain and avoid their reflection.
- An active perfectly matched layer, in which the incident wave ($\phi_i = \phi_i^{(F)}$) is imposed.

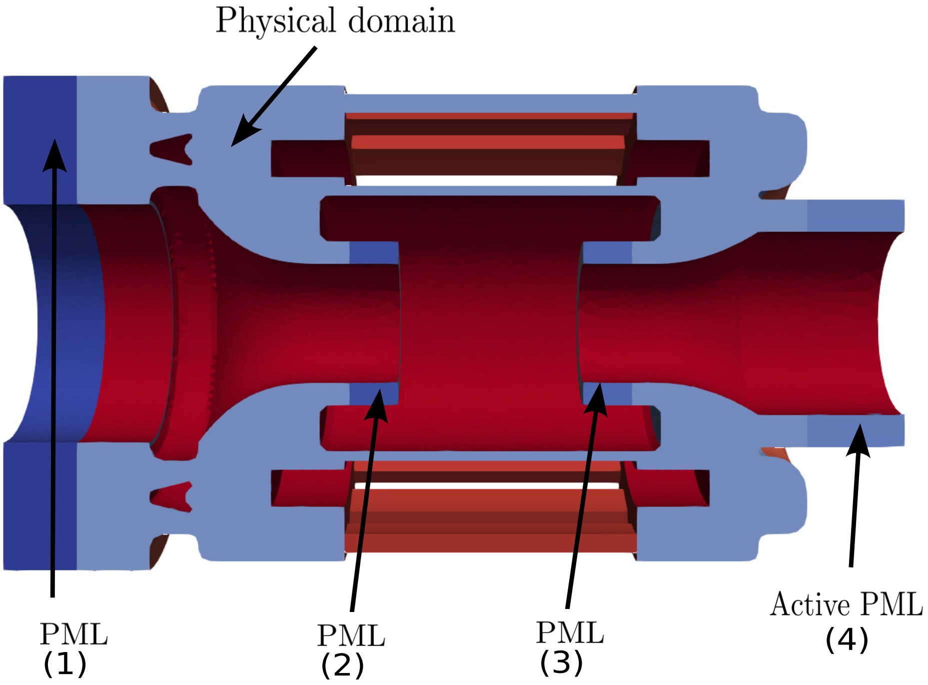

**Figure B.1:** Different regions defined in the finite element simulation.

The use of the open source solver `FreeFem++` [51] requires the implementation of the variational formulation of the Helmholtz equation.

$$\underbrace{\iiint\limits_{\Omega_{\text{phy}}} \left( \frac{\partial \phi}{\partial x}\frac{\partial q}{\partial x} + \frac{\partial \phi}{\partial y}\frac{\partial q}{\partial y} + \frac{\partial \phi}{\partial z}\frac{\partial q}{\partial z} - \phi q k_0^2 \right) \mathrm{d}x\mathrm{d}y\mathrm{d}z}_{\text{Acoustic field in the physical domain}}$$

$$+ \underbrace{\iiint\limits_{\Omega^{i}_{\text{pml}}} \left( \frac{\partial \phi_i}{\partial x}\frac{\partial q}{\partial x} + \frac{\partial \phi_i}{\partial y}\frac{\partial q}{\partial y} + \frac{\partial \phi_i}{\partial z}\frac{\partial q}{\partial z} - \phi_i q k_0^2 \right) \mathrm{d}x\mathrm{d}y\mathrm{d}z}_{\text{Incident field in the Active PML domain}}$$

$$+ \underbrace{\iiint\limits_{\Omega^{(4)}_{\text{pml}}} \left( \frac{1}{\gamma_x^{(4)}}\frac{\partial\left(\phi-\phi_i\right)}{\partial x}\frac{\partial q}{\partial x} + \gamma_x^{(4)}\frac{\partial\left(\phi-\phi_i\right)}{\partial y}\frac{\partial q}{\partial y} + \gamma_x^{(4)}\frac{\partial\left(\phi-\phi_i\right)}{\partial z}\frac{\partial q}{\partial z} - \left(\phi-\phi_i\right) q k_0^2 \gamma_x^{(4)} \right) \mathrm{d}x\mathrm{d}y\mathrm{d}z}_{\text{The reflected field in the active PML domain}}$$

$$+ \underbrace{\iiint\limits_{\Omega^{(1)}_{\text{pml}}} \left( \frac{1}{\gamma_x^{(1)}}\frac{\partial \phi}{\partial x}\frac{\partial q}{\partial x} + \gamma_x^{(1)}\frac{\partial \phi}{\partial y}\frac{\partial q}{\partial y} + \gamma_x^{(1)}\frac{\partial \phi}{\partial z}\frac{\partial q}{\partial z} - \phi q k_0^2 \gamma_x^{(1)} \right) \mathrm{d}x\mathrm{d}y\mathrm{d}z}_{\text{Acoustic field in the PML region (1)}}$$

$$+ \underbrace{\iiint\limits_{\Omega^{(2)}_{\text{pml}}} \left( \frac{1}{\gamma_x^{(2)}}\frac{\partial \phi}{\partial x}\frac{\partial q}{\partial x} + \gamma_x^{(2)}\frac{\partial \phi}{\partial y}\frac{\partial q}{\partial y} + \gamma_x^{(2)}\frac{\partial \phi}{\partial z}\frac{\partial q}{\partial z} - \phi q k_0^2 \gamma_x^{(2)} \right) \mathrm{d}x\mathrm{d}y\mathrm{d}z}_{\text{Acoustic field in the PML region (2)}}$$

$$+ \underbrace{\iiint\limits_{\Omega^{(3)}_{\text{pml}}} \left( \frac{1}{\gamma_x^{(3)}}\frac{\partial \phi}{\partial x}\frac{\partial q}{\partial x} + \gamma_x^{(2)}\frac{\partial \phi}{\partial y}\frac{\partial q}{\partial y} + \gamma_x^{(2)}\frac{\partial \phi}{\partial z}\frac{\partial q}{\partial z} - \phi q k_0^2 \gamma_x^{(3)} \right) \mathrm{d}x\mathrm{d}y\mathrm{d}z}_{\text{Acoustic field in the PML region (3)}} = 0 \qquad \text{(B.1)}$$

where $\phi_i$ is the acoustic potential incident wave generated by the fan blades ($\phi_i^{(F)}$), $\phi$ the acoustic potential, and $q$ is the test function.

# Appendix C

# Aeraulic performance of self-ventilated motors

## C.1 Introduction

The last part of this work is devoted to the aeraulic performance of self-ventilated motors. The aim of this chapter is to provide a calculation tool that can predict the flow rate in various ventilation systems outlined in the preceding chapters. In practice, the flow rate can be obtained by analyzing the characteristic curve of the cooling fan and considering the pressure losses in the ventilation circuits of each motor. The point where these two curves intersect is known as the operating point of the fan (see Figure C.1). It is important to note that the fan performance prediction has already been extensively covered by various authors in the literature using a one-dimensional approach [37, 65]. As such, this chapter primarily delves into the discussion of pressure losses in the ventilation systems. The first part examines the flow resistance of totally-enclosed motors, while the second part addresses the losses in open motors. The impact of rotor core rotation and the porosity

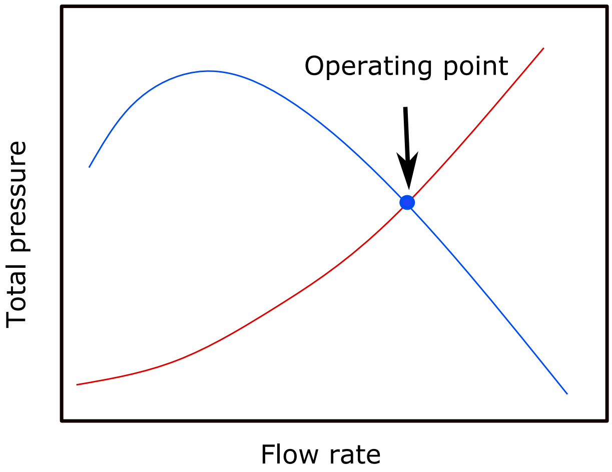

**Figure C.1:** Illustration of the operating point. The fan characteristic curve is represented in blue. The resistance curve of the ventilation system is depicted in red.

of the end-windings are discussed in the final part of this chapter.

## C.2 Totally-enclosed motors

The pressure losses in the ventilation circuit of a totally-enclosed motor are mainly attributed to the fan cover, the guide vanes, and the cooling channels. Since these components are arranged in series, the total pressure loss of the ventilation system $\Delta p_{\mathrm{sys}}$ can be evaluated by superimposing the pressure losses of each cooling system component $(i)$.

$$\Delta p_{\mathrm{sys}} = \sum_{i} \Delta p_i \tag{C.1}$$

with

$$\Delta p_i = \frac{1}{2}\xi_i \rho U_i^2 \tag{C.2}$$

where $\xi_i$ and $U_i$ represent respectively the loss coefficient and the flow velocity in the element $(i)$.

By analogy with electrical circuits, Equation C.1 can be expressed as a function of the total resistance $R_{\mathrm{sys}}$ and the flow rate of the cooling system $Q_v$

$$\Delta p_{\mathrm{sys}} = R_{\mathrm{sys}} Q_{\mathrm{sys}}^2 \tag{C.3}$$

with

$$R_{\mathrm{sys}} = \sum_{i=1}^{n_{\max}} \frac{\rho \xi_i}{2A_i^2} \tag{C.4}$$

$$Q_{\mathrm{sys}} = U_i A_i \tag{C.5}$$

where $A_i$ and $n_{\max}$ represent respectively the cross-sectional area of each component, and the maximum number of components in the ventilation system.

### C.2.1 Motor resistance

As discussed in Chapter 1, in the case of a truncated motor, the flow is distributed over its different blocks. This distribution may depend on the flow resistance of each block. If the motor blocks are identical or similar (see Figures C.2), the flow rate will be uniformly distributed to each motor block. It is given by

$$Q_{\mathrm{block}} = \frac{Q_{\mathrm{sys}}}{n_{\mathrm{blocks}}} \tag{C.6}$$

where $n_{\mathrm{blocks}}$ is the number of motor blocks.

In this specific case, the pressure drop of the ventilation system $\Delta p_{\text{sys}}$ becomes:

$$\Delta p_{\text{sys}} = \left( R_{\text{grid}} + \frac{R_{\text{block}}}{n_{\text{blocks}}^2} \right) Q_{\text{sys}}^2 \tag{C.7}$$

where $R_{\text{grid}}$ and $R_{\text{block}}$ represent the flow resistance of the fan cover and the resistance of a single motor block respectively.

(a) 1 block (b) 2 blocks

**Figure C.2:** Types of motor blocks. (a) Ventilation system composed of a single block. (b) Truncated ventilation system composed of two blocks.

It should be recalled here that each motor block consists of guide vanes and cooling channels. Since these two components are arranged in series, the resistance of a single block $R_{\text{block}}$ can be expressed as

$$R_{\text{block}} = R_{\text{vanes}} + R_{\text{ducts}} \tag{C.8}$$

where $R_{\text{vanes}}$ is the resistance of the guide vanes and $R_{\text{ducts}}$ is the resistance of the cooling channels. Note here that the latter can be deduced from the resistance of a single cooling channel $R_{\text{duct}}$

$$R_{\text{ducts}} = \frac{R_{\text{duct}}}{n_{\text{ducts}}^2} \tag{C.9}$$

The resistance of a single channel can divided into three different resistances:

$$R_{\text{duct}} = R_{\text{in}} + R_{\text{fric}} + R_{\text{out}} \tag{C.10}$$

where $R_{\text{in}}$, $R_{\text{fric}}$ and $R_{\text{out}}$ represent the flow resistances due to channel inlet, friction and channel outlet respectively.

After substituting the expressions of the different resistances in Equation C.7, we get

$$\Delta p_{\text{sys}} = \frac{1}{2}\rho \left( \xi_{\text{grid}}/A_{\text{grid}}^2 + \frac{\xi_{\text{vanes}}/A_{\text{vanes}}^2 + \left(\xi_{\text{in}} + \xi_{\text{friq}} + \xi_{\text{out}}\right)/\left(n_{\text{ducts}}^2 A_{\text{duct}}^2\right)}{n_{\text{blocks}}^2} \right) Q_{\text{sys}}^2 \tag{C.11}$$

where $A_{\text{grid}}$, $A_{\text{vanes}}$ and $A_{\text{ducts}}$ represent respectively the cross-sectional areas of the fan cover, inter-vanes channels and the cooling channels.

### C.2.2 Loss coefficients

The only unknowns in this problem are the resistance coefficients $\xi_{\text{grid}}$, $\xi_{\text{vanes}}$, $\xi_{\text{in}}$, $\xi_{\text{friq}}$ and $\xi_{\text{out}}$. They can be evaluated empirically from the different formulas existing in the literature [12, 33, 57, 1].

- The fan cover, placed at the motor inlet, can be considered as a perforated plate, as illustrated in Figure C.3. The loss coefficient of the latter $\xi_{\text{grid}}$ can be calculated as follows [57]:

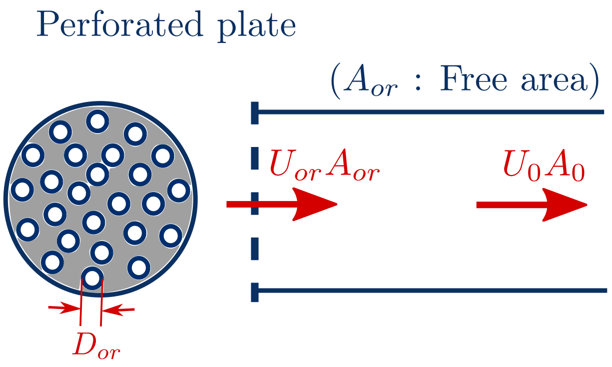

**Figure C.3:** Inlet grid (Idelchik [57])

$$\xi_{\text{grid}} = \begin{cases} \xi_\varphi + \epsilon_0^{-Re}(1.707 - f)^2 \dfrac{1}{f^2} & \text{, if} \quad Re < 10^5 \\ (1.707 - f)^2 \dfrac{1}{f^2} & \text{, if} \quad Re \geq 10^5 \end{cases} \tag{C.12}$$

where $f = A_{or}/A_0$ is the area ratio. The different values of $\epsilon_0^{Re}$ and $\xi_\varphi$ are listed in Table C.4.

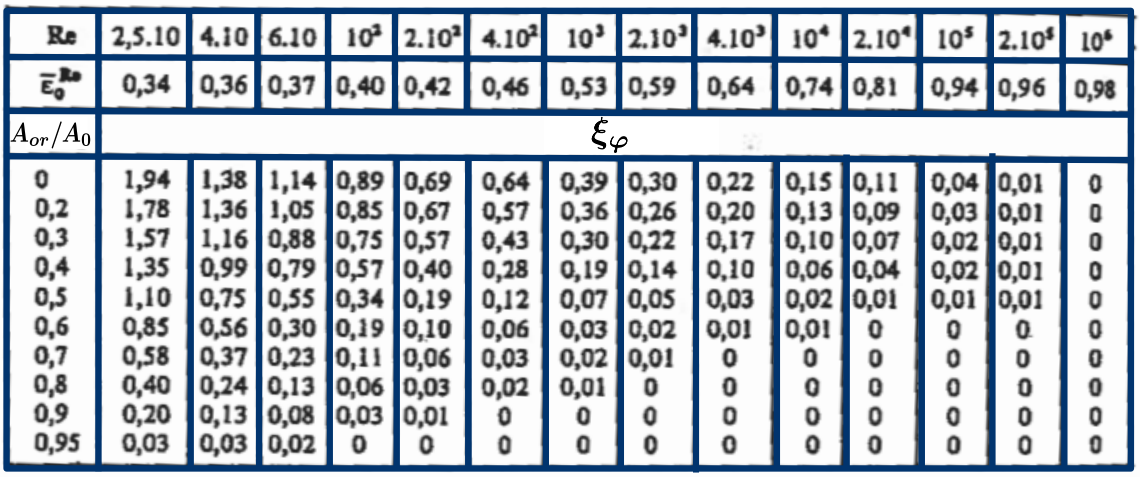

| Re | 2,5.10 | 4.10 | 6.10 | $10^2$ | $2.10^2$ | $4.10^2$ | $10^3$ | $2.10^3$ | $4.10^3$ | $10^4$ | $2.10^4$ | $10^5$ | $2.10^5$ | $10^6$ |
|---|---|---|---|---|---|---|---|---|---|---|---|---|---|---|
| $\bar{\varepsilon}_0^{Re}$ | 0,34 | 0,36 | 0,37 | 0,40 | 0,42 | 0,46 | 0,53 | 0,59 | 0,64 | 0,74 | 0,81 | 0,94 | 0,96 | 0,98 |
| $A_{or}/A_0$ | $\xi_\varphi$ | | | | | | | | | | | | | |
| 0 | 1,94 | 1,38 | 1,14 | 0,89 | 0,69 | 0,64 | 0,39 | 0,30 | 0,22 | 0,15 | 0,11 | 0,04 | 0,01 | 0 |
| 0,2 | 1,78 | 1,36 | 1,05 | 0,85 | 0,67 | 0,57 | 0,36 | 0,26 | 0,20 | 0,13 | 0,09 | 0,03 | 0,01 | 0 |
| 0,3 | 1,57 | 1,16 | 0,88 | 0,75 | 0,57 | 0,43 | 0,30 | 0,22 | 0,17 | 0,10 | 0,07 | 0,02 | 0,01 | 0 |
| 0,4 | 1,35 | 0,99 | 0,79 | 0,57 | 0,40 | 0,28 | 0,19 | 0,14 | 0,10 | 0,06 | 0,04 | 0,02 | 0,01 | 0 |
| 0,5 | 1,10 | 0,75 | 0,55 | 0,34 | 0,19 | 0,12 | 0,07 | 0,05 | 0,03 | 0,02 | 0,01 | 0,01 | 0,01 | 0 |
| 0,6 | 0,85 | 0,56 | 0,30 | 0,19 | 0,10 | 0,06 | 0,03 | 0,02 | 0,01 | 0,01 | 0 | 0 | 0 | 0 |
| 0,7 | 0,58 | 0,37 | 0,23 | 0,11 | 0,06 | 0,03 | 0,02 | 0,01 | 0 | 0 | 0 | 0 | 0 | 0 |
| 0,8 | 0,40 | 0,24 | 0,13 | 0,06 | 0,03 | 0,02 | 0,01 | 0 | 0 | 0 | 0 | 0 | 0 | 0 |
| 0,9 | 0,20 | 0,13 | 0,08 | 0,03 | 0,01 | 0 | 0 | 0 | 0 | 0 | 0 | 0 | 0 | 0 |
| 0,95 | 0,03 | 0,03 | 0,02 | 0 | 0 | 0 | 0 | 0 | 0 | 0 | 0 | 0 | 0 | 0 |

**Figure C.4:** $\epsilon_0^{Re}$ and $\xi_\varphi$ as functions of $f$ (Idelchik [57])

- The loss coefficient of the guide vanes depends mainly on the angle of attack $\alpha_0$ (see Figure C.5a) and the vane profile (see Figure C.5b).

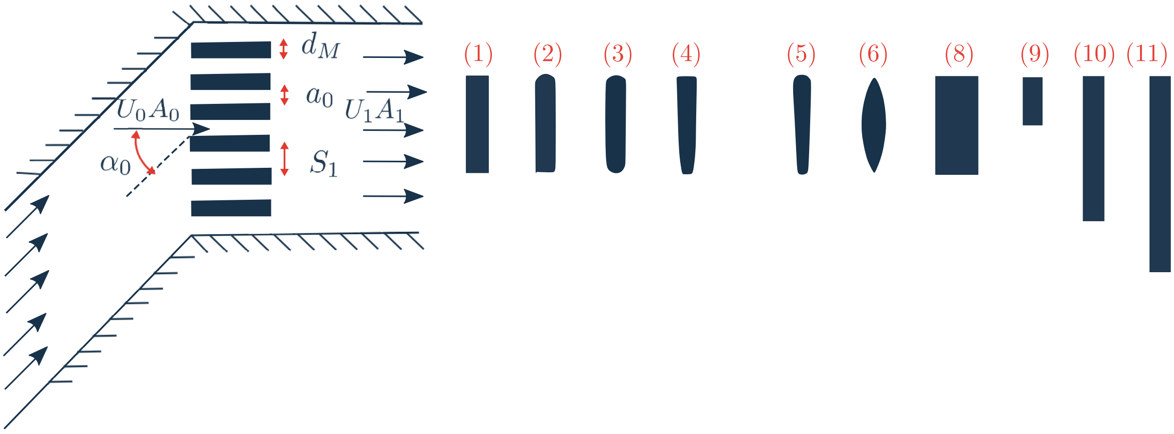

(a) (b)

**Figure C.5:** (a) Angle of attack of the guide vanes. (b) Guide vane shape. (Idelchik [57])

In the case where the angle of attack is not equal to zero ($\alpha_0 \neq 0$), the loss coefficient $\xi_{\text{vanes}}$ can be calculated as follows:

$$\xi_{\text{vanes}} = \sigma_1 \sigma_2 \tag{C.13}$$

where $\sigma_1$ and $\sigma_2$ are respectively extracted from Figures C.6a and C.6b. In contrast

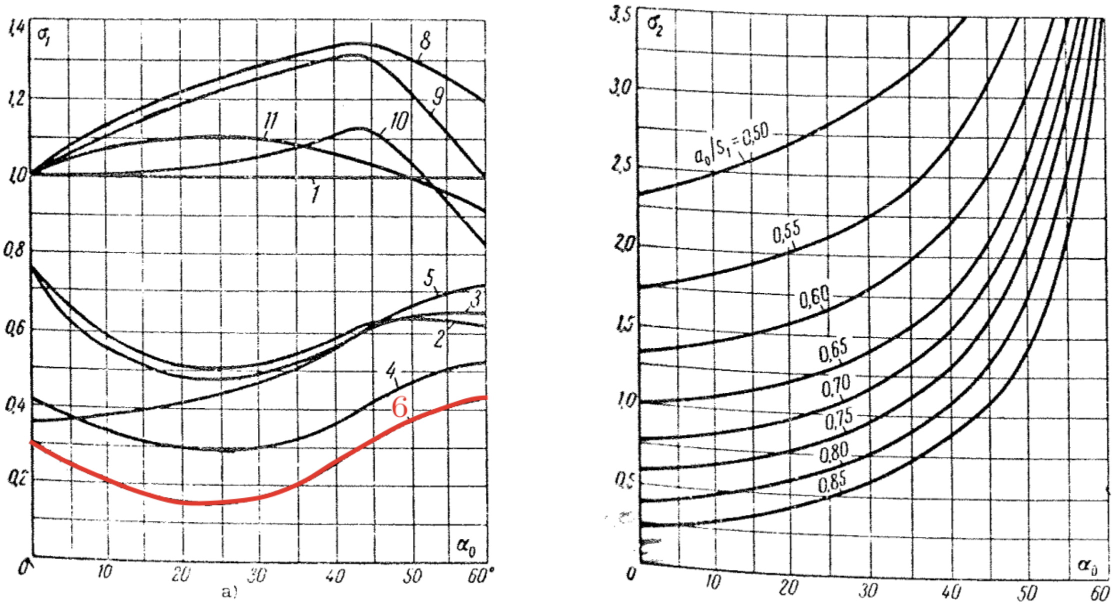

(a) $\sigma_1$ (b) $\sigma_2$

**Figure C.6:** Variations of $\sigma_1$ and $\sigma_2$ as functions of $\alpha_0$ (Idelchik [57])

when the angle of attack is equal to zero ($\alpha_0 = 0$), the loss coefficient $\xi_{\text{vanes}}$ can be evaluated as follows

$$\xi_{\text{vanes}} = \beta_2 \left(\frac{S_1}{a_0} - 1\right)^{3/4} \tag{C.14}$$

The different values of $\beta_2$ are given in table C.1 for 6 different vane profiles.

| **Profile** | 1 | 2 | 3 | 4 | 5 | 6 |
|---|---|---|---|---|---|---|
| $\boldsymbol{\beta_1}$ | 2.34 | 1.77 | 1.77 | 1.00 | 0.87 | 0.71 |
| $\boldsymbol{\beta_2}$ | 1.00 | 0.76 | 0.76 | 0.43 | 0.37 | 0.30 |

**Table C.1:** Values of $\beta_1$ and $\beta_2$ (Idelchik [57])

- the resistance coefficient of a sudden contraction (see Figure C.7a) can be evaluated as [28]

$$\xi_{\text{in}} = 0.5085 - 0.1979 \left(\frac{A_{\text{duct}}}{A_{\text{upst}}}\right) - 0.3148 \left(\frac{A_{\text{duct}}}{A_{\text{upst}}}\right)^2 \tag{C.15}$$

where $A_{\text{upst}}$ is the cross-section of the annular sector located upstream the cooling channels. It is given by

$$A_{\text{upst}} = \frac{\Delta\theta_{\text{block}}/2}{n_{ducts}} \left(r_2^2 - r_1^2\right) \tag{C.16}$$

- The friction coefficient $\xi_{\text{fric}}$ depends on the relative roughness $\epsilon$, duct cross-section and on the Reynolds number $R_e$. It can be calculated by [33]

$$\xi_{\text{fric}} = \frac{L}{D_h} 0.25 \left[\log\left(\frac{\epsilon}{3.7D_h} + \frac{5.74}{R_e^{0.9}}\right)\right]^{-2} \tag{C.17}$$

where $L$ and $D_h$ are respectively the channel length and the hydraulic diameter.

- The use of diffusers (see Figure C.7b) allows one to minimise significantly the pressure losses in channels with abrupt expansion. The loss coefficient of a diffuser can be evaluated by using the following formula [57].

$$\xi_{\text{out}} = (1 + \sigma')\left(\xi_d + \frac{S_0^2}{S_2^2}\right) \tag{C.18}$$

where

$$\sigma' = -0.05\frac{L}{D_h} + 0.5 \tag{C.19}$$

$$\xi_d = 3.2 \tan\left(\alpha/2\right)^{5/4} \left(1 - S_0^2/S_2^2\right) + \frac{\lambda}{8 \sin\left(\alpha/2\right)} \left(1 - S_0^2/S_2^2\right) \tag{C.20}$$

where $\alpha$ denotes the diffuser angle. Note here that this angle should not be excessive to maintain the maximum efficiency of the diffuser.

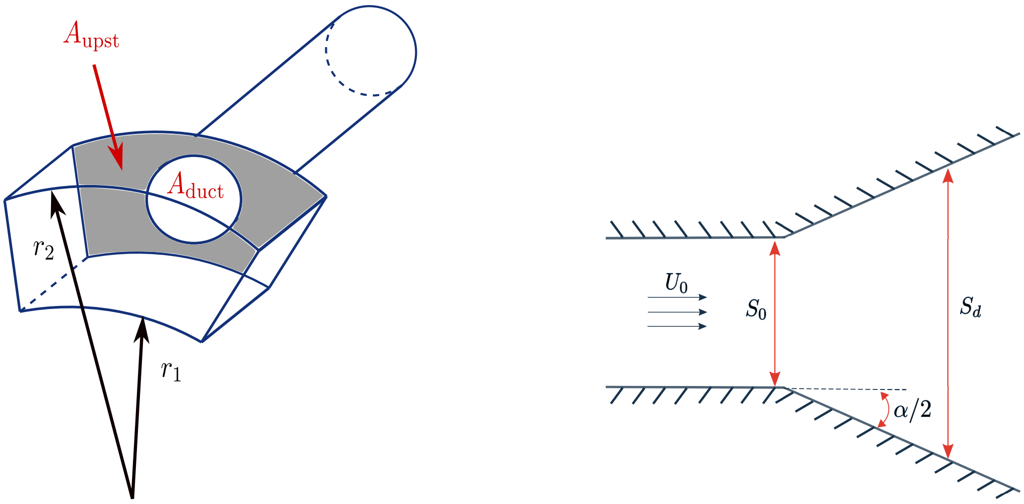

(a) (b)

**Figure C.7:** (a) Channel inlet, (b) Channel outlet (Idelchik [57]).

## C.2.3 Validation

### C.2.3.1 Comparison with measurements

In order to assess the validity and relevance of the analytical model, a comparison with measurements was carried out. The analytical model is applied in this section to the ventilation system of a truncated motor, consisting of 17 channels with circular cross-sections and 5 guide vanes. The results obtained from the analytical model were then compared to the measurements, excluding the cooling fan and fan cover. It should be important to note, in the absence of the cooling fan, the airflow passes axially through the guide vanes and cooling channels, resulting in an angle of attack of zero for this specific test-case. The total pressures obtained from both the analytical model and measurements are plotted as functions of flow rate in Figure C.8. As can be seen, a very good agreement is found between the two results.

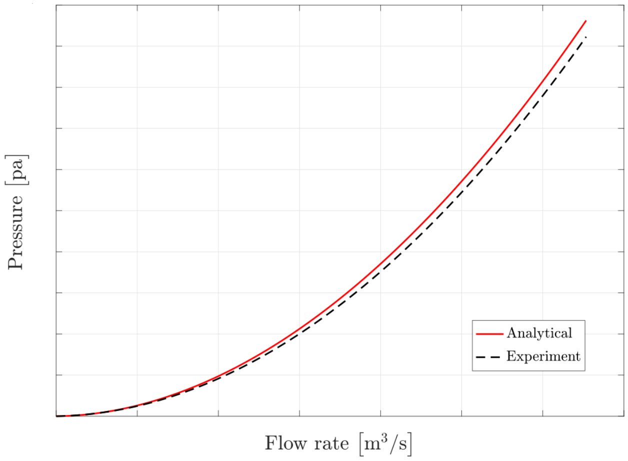

**Figure C.8:** Comparison between the total pressures obtained from the analytical model and measurements.

### C.2.3.2 Comparison with the LBM (Lattice Boltzmann Method)

In order to evaluate the pressure losses in each component of the ventilation system, a comparative study with numerical simulation results has bee conducted. The numerical simulation was perfumed using the LBM (Lattice Boltzmann Method) applied to the entire ventilation system configuration. The total pressure was evaluated on axial planes positioned at various locations within the ventilation system. Figure C.9 shows the variation of total pressure calculated by the LBM in the ventilation system. Comparisons between the results obtained from the two calculation methods are depicted in Figures C.10 and C.11. These figures clearly indicate a good agreement between the total pressures predicted by both methods.

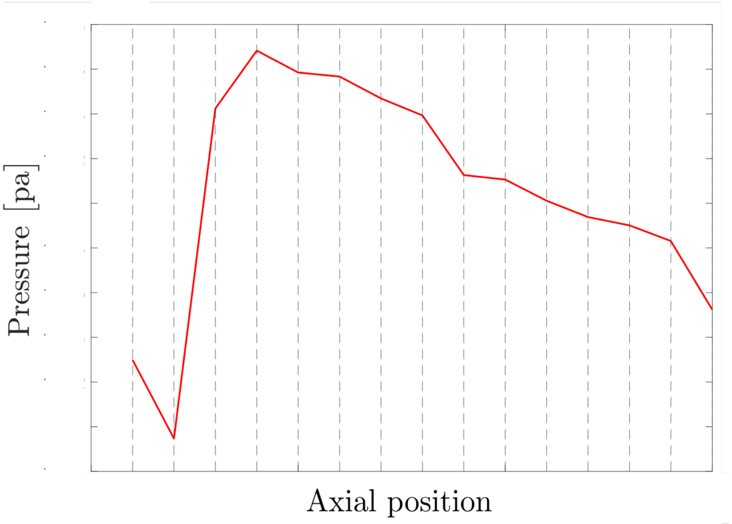

**Figure C.9:** Variation of the total pressure obtained from the Lattice Boltzmann Method in the ventilation system

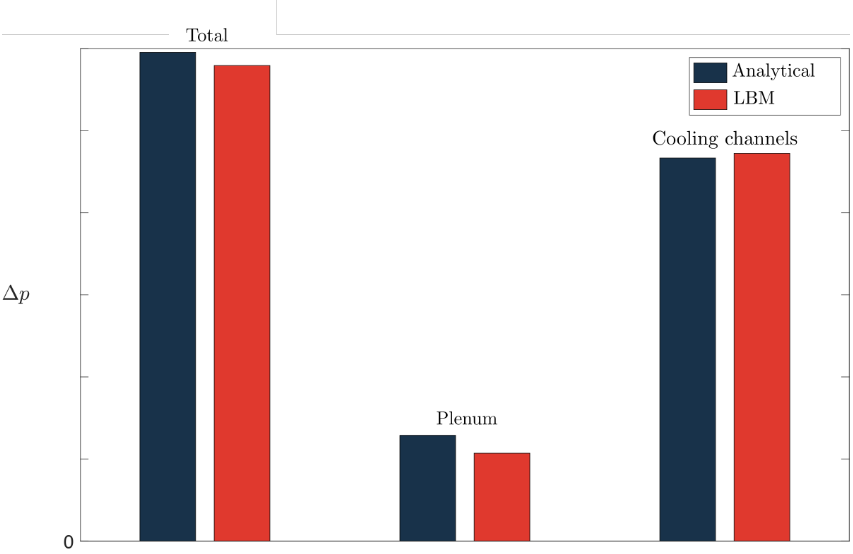

**Figure C.10:** Pressure losses of the ventilation system obtained from the analytical model and the Lattice Boltzmann Method.

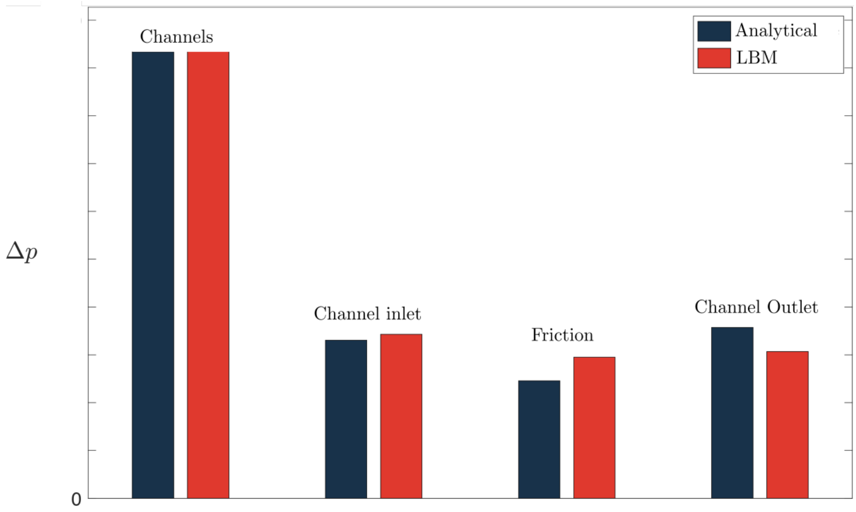

**Figure C.11:** Pressure losses of the cooling channels obtained from the analytical model and the Lattice Boltzmann Method.

## C.3 Open motors

This section focuses on the pressure drop in the ventilation systems integrated in open motors. It is important to note that this ventilation circuit is significantly more complex than that of an enclosed motor. The complexity comes from the fact that the air flow passes through three distinct circuits, corresponding to the rotor, stator, and air gap, as illustrated in Figure C.12. Additionally, the pressure losses are significantly affected by the rotation of the rotor cooling channels and the air gap. These additional complexities require careful consideration in the current investigation. However, calculating the flow resistance of an open motor requires prior knowledge of the flow rate distribution in each sub-circuit of the ventilation system. In the case of multiple circuits arranged in parallel, the flow is distributed differently based on the resistance of each circuit. Therefore, establishing a relationship between the different circuits becomes crucial to determine the flow distribution inside the ventilation system. The airflow provided by the cooling fan is divided into three different parts:

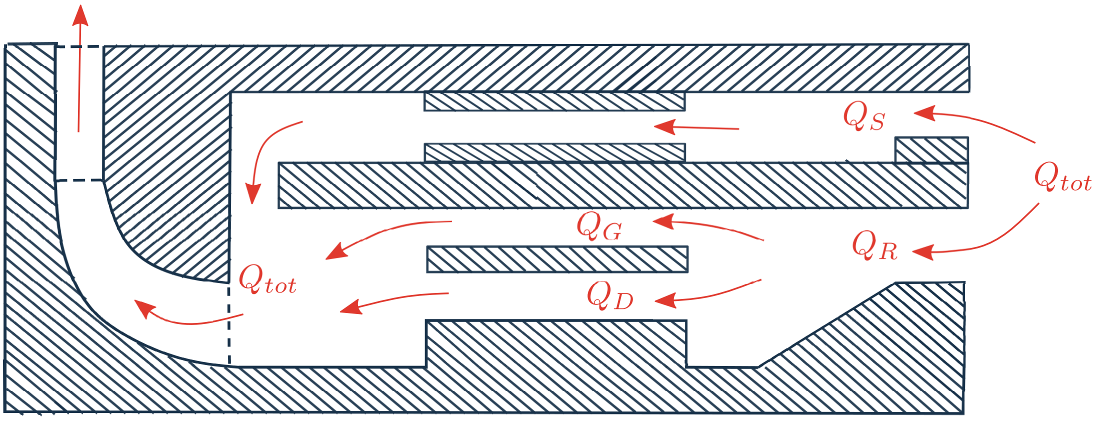

**Figure C.12:** Typical configuration of the ventilation circuit integrated in an open motor.

- $Q_S$: is the flow rate passing through the ventilating holes integrated in the stator core.
- $Q_D$: is the flow rate passing through the rotor channels
- $Q_G$: is the flow rate passing through the air gap.

At the motor inlet, the total flow rate $Q_{tot}$ is divided into:

$$Q_{\text{tot}} = Q_S + Q_R \tag{C.21}$$

As these two cooling circuits are in parallel, they may have the same pressure drop. The relationship between these two circuits is expressed as follows

$$R^S Q_S^2 = R^R Q_R^2 \tag{C.22}$$

A part of the rotor flow passes through the rotor channels and another part passes through the air gap

$$Q_R = Q_D + Q_G \tag{C.23}$$

The pressure losses in these circuits are identical

$$R^R_{gap/ducts} Q_R^2 = R^S Q_D^2 \tag{C.24}$$

$$R^G Q_G^2 = R^D Q_D^2 \tag{C.25}$$

After combining Equations C.24 and C.25, one obtains

$$R^S Q_S^2 = R^R_{\text{def}} Q_R^2 + R^D R_D^2 \tag{C.26}$$

The equations above can be written as

$$\begin{pmatrix} -1 & -1 & 0 & 0 \\ R^S Q_S & -R^R_{\text{def}} Q_R & 0 & -R^D Q_D \\ 0 & 1 & -1 & -1 \\ 0 & 0 & R^G Q_G & -R^D Q_D \end{pmatrix} \begin{pmatrix} Q_S \\ Q_R \\ Q_G \\ Q_D \end{pmatrix} = \begin{pmatrix} Q_{tot} \\ 0 \\ 0 \\ 0 \end{pmatrix} \tag{C.27}$$

This system of non-linear equations can be solved, for instance, by the Newton-Raphson method [85]

The next step is to define the different resistances of the ventilation system.

- The resistance of the stator circuit $R^S$ is calculated by summing up all the individual resistances of this circuit. It is expressed as:

$$R^S = \underbrace{R^S_{\text{def}}}_{\text{Deflector}} + \underbrace{\left( \frac{R^S_{\text{in}} + R^S_{\text{fric}} + R^S_{\text{out}}}{n_S^2} \right)}_{\text{Stator channels}} + \underbrace{R^S_{\text{winding}}}_{\text{End-winding}} \tag{C.28}$$

  where $R^S_{\text{def}}$ and $R^S_{\text{winding}}$ are respectively the resistances of the flow deflector and the end-windings. The resistance of the channel inlet, friction and channel outlet are respectively denoted by $R^S_{\text{in}}$, $R^S_{\text{fric}}$ and $R^S_{\text{out}}$. $n_S$ is the number of stator channels.

- The resistance of the rotor circuit $R^D$ is given by

$$R^R = \left( \underbrace{R^R_{\text{in}}}_{\text{Channel inlet}} + \underbrace{R^R_{\text{fric}}}_{\text{Friction}} + \underbrace{R^R_{\text{out}}}_{\text{Channel outlet}} \right) / n_R^2 \tag{C.29}$$

  where $n_R$ is the number of rotor channels.

- The resistance of the air gap circuit $R^G$ is given by

$$R^G = \left( \underbrace{R^G_{\text{in}}}_{\text{Inlet}} + \underbrace{R^G_{\text{fric}}}_{\text{Friction}} + \underbrace{R^G_{\text{out}}}_{\text{Outlet}} \right) \tag{C.30}$$

## C.3.1 Loss coefficients

As mentioned in Section C.2, the only unknown variables in the problem are the loss coefficients. In the rest of this chapter, a particular emphasis will be placed on the impact of channel rotation on the pressure losses in the ventilation system. It is important to note that the loss coefficients presented earlier for the stator circuit are once again applied in this analysis.

### C.3.1.1 Rotor cooling channels

The effects of rotation on the pressure losses have been already investigated by Chong [28]. The author has demonstrated that the rotation induces an additional flow resistance to the ventilation system. The pressure loss at the channel inlet can be expressed as the sum of stationary and rotating losses

$$\Delta p_{in} = \underbrace{\Delta p_0}_{\text{Stationary loss}} + \underbrace{\Delta p_r}_{\text{Additional loss}} \tag{C.31}$$

where

$$\Delta p_r = \xi_r \frac{\rho U^2}{2} \tag{C.32}$$

The resistance coefficient $\xi_r$ is given by [28]

$$\xi_r = c_1 \left(\frac{V_t}{U}\right)^2 + c_2 \left(\frac{V_t}{U}\right) \tag{C.33}$$

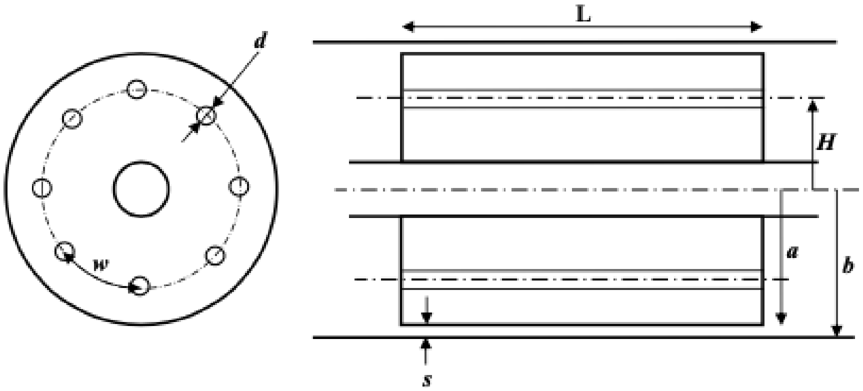

**Figure C.13:** Typical configuration of the rotor channels (Reproduced from Chong [28]).

The coefficients $c_1$ and $c_2$ depend only on the ratio $H/a$ (see Figure C.13). They are listed C.2 in Table for four different values [28].

| $H/a$ | $c_1$ | $c_2$ |
|---|---|---|
| 0.50 | 0.360 | 0.031 |
| 0.60 | 0.303 | 0.150 |
| 0.71 | 0.230 | 0.067 |
| 0.75 | 0.170 | 0.160 |

**Table C.2:** Coefficients $c_1$ et $c_2$ for different values of $H/a$ (Chong [28]).

The friction coefficient $f_r$ is also increased by the rotation of the cooling channels. It can be expressed as [28]

$$f_r = f_0 c_3 J^{c_4} Re^{c_5} \tag{C.34}$$

with

$$J = \frac{\Omega d^2}{\nu} \tag{C.35}$$

where $\nu$ is the kinematic viscosity of air. The coefficients $c_3$, $c_4$ and $c_5$ depend on the Reynolds number and the ratio $L/d$. They are given in Table C.3.

| $L/d$ | $Re$ | $c_3$ | $c_4$ | $c_5$ |
|---|---|---|---|---|
| 10.6 | $900 < Re < 9880$ | 0.503 | 0.16 | -0.03 |
| 10.6 | $Re \geq 9880$ | 0.842 | 0.023 | 0.002 |
| 31.8 | $900 < Re < 7000$ | 0.312 | 0.21 | 0.01 |
| 31.8 | $Re \geq 7000$ | 0.783 | 0.05 | -0.01 |

**Table C.3:** Coefficients $c_1$ and $c_2$ for different values of $H/a$ and $R_e$ (Chong [28]).

### C.3.1.2 Air gap

In a similar manner, additional losses must be considered for the air gap. The pressure loss at the entrance of the air gap is expressed as [28, 29, 27]

$$\Delta p_{in} = \Delta p_0 + \xi_r \frac{\rho U^2}{2} \tag{C.36}$$

with

$$\xi_r = 0.043 \left(\frac{V_t}{U}\right)^2 \tag{C.37}$$

The additional friction in the air gap is given by [28]

$$f_r = f_0 c_3 J^{c_4} Re^{c_5} \tag{C.38}$$

where the coefficients $c_3$, $c_4$ and $c_5$ depend on the Reynolds number and the ratio $L/d$. They are listed in Table C.4 [28].

| $L/d$ | $Re$ | $c_3$ | $c_4$ | $c_5$ |
|---|---|---|---|---|
| 10.6 | $900 < Re < 9880$ | 0.503 | 0.16 | -0.03 |
| 10.6 | $Re \geq 9880$ | 0.842 | 0.023 | 0.002 |
| 31.8 | $900 < Re < 7000$ | 0.312 | 0.21 | 0.01 |
| 31.8 | $Re \geq 7000$ | 0.783 | 0.05 | -0.01 |

**Table C.4:** Coefficients $c_1$ et $c_2$ for different values of $H/a$ and $R_e$ (Chong [28]).

#### C.3.1.3 End-windings

Various studies have been reported in the literature to predict the pressure drop of the stator end-windings using numerical simulations [83, 95, 63]. The straightforward way for estimating the pressure losses is to consider the geometry of the end-windings as a porous medium. A.Kholghi *et al* [63] proposed an empirical model based on RANS (Reynolds-averaged Navier–Stokes) simulations to calculate the friction coefficient of the end-windings. This model is used in this work to compute the pressure losses in the end-windings.

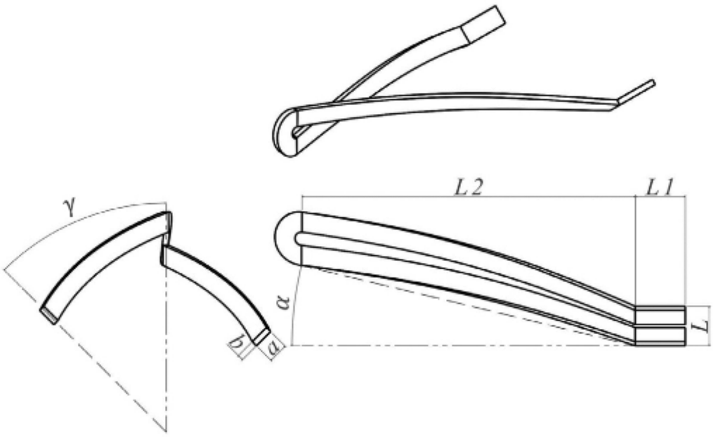

**Figure C.14:** Typical configuration of the end-windings (Reproduced from Kholghi *et al* [63])

A.Kholghi *et al* [63] have shown that the friction coefficient of the stator end-windings $\xi_{winding}$ can be expressed as follows

$$\xi_{winding} = \left(\frac{1}{R_{e_K} Da^{0.5}}\right) + CD_h \tag{C.39}$$

where $Da$ is the Darcy number and $R_{e_K}$ the Reynolds number. These are given by

$$R_{e_K} = \frac{\rho U \sqrt{K}}{\mu}, \qquad Da = \frac{K}{D_h^2}$$

where $K$ is the permeability of the windings. It is given by

$$K = \frac{\phi^{12.8} D_h^2}{0.248 D_h/a + 0.0038} \tag{C.40}$$

The coefficient $C$ can be extracted from a RANS simulation [63]. It is given by

$$C = \frac{0.107 D_h / a + 0.0124}{\phi^{6.3} D_h} \tag{C.41}$$

The porosity coefficient $\phi$ can be calculated for any geometry of the end-windings (see Figure C.14) by using the following formula [63]:

$$\phi = 0.908 + 0.055 \cos(\gamma) + 0.63 \tan(\alpha) + 0.0044N \tag{C.42}$$

where $N$ represents the number of conductors. The angles $\gamma$ and $\alpha$ are depicted in Figure C.14.

The variation of the friction coefficient $\xi_{\text{winding}}$ as a function of the winding porosity is illustrated in Figure C.15. As can be seen, the loss coefficient decreases with porosity. This indicates that the distance between the conductors of the end-windings plays an important role in determining the pressure losses.

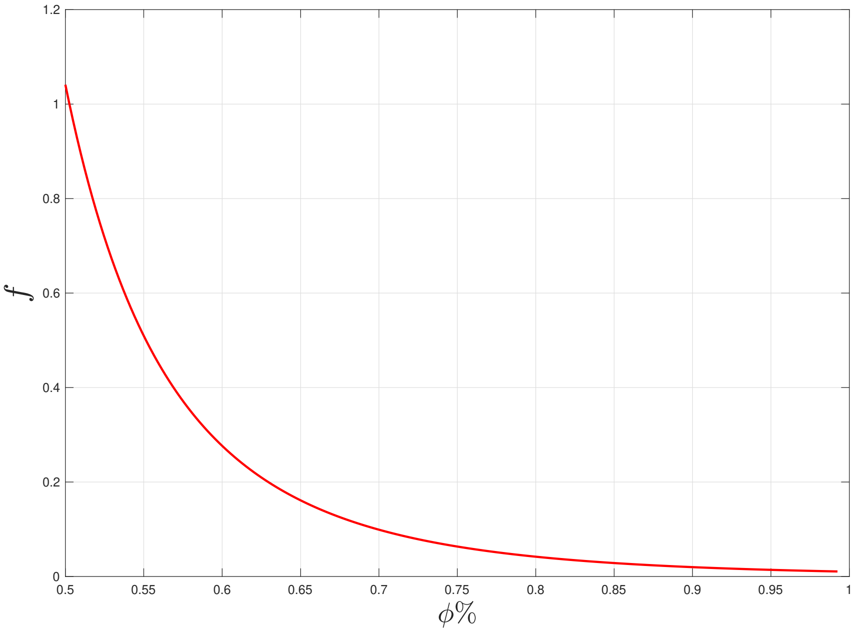

**Figure C.15:** Loss coefficient as a function of the porosity of the end-windings

The different empirical models mentioned earlier are used in the mathematical expressions of the resistances of the different circuits, to calculate the pressure drop of the ventilation system integrated in an open motor. By incorporating these models, a complete analysis of the pressure losses in the cooling system can be performed, leading to a more complete understanding of its aeraulic performance.

# Bibliography

[1] *Flow of fluids through valves, fittings and pipei. Metric edition - SI units.* CRANE CO, 1988. (Cited on page 166)

[2] Milton Abramowitz and Irene A. Stegun. *Handbook of Mathematical Functions with Formulas, Graphs, and Mathematical Tables.* Dover, New York, ninth dover printing, tenth gpo printing edition, 1964. (Cited on page 67)

[3] R.J. Alfredson. The propagation of sound in a circular duct of continuously varying cross-sectional area. *Journal of Sound and Vibration*, 23(4):433 – 442, 1972. (Cited on pages 4 and 14)

[4] N. Amir, V. Pagneux, and J. Kergomard. A study of wave propagation in varying cross-section waveguides by modal decomposition. part ii. results. *The Journal of the Acoustical Society of America*, 101(5):2504–2517, 1997. (Cited on pages 5 and 154)

[5] Y. Ando. On the sound radiation from semi-infinite circular pipe of certain wall thickness. *Acustica*, 22:219–225, 1969. (Cited on page 28)

[6] C. M. Angulo. Discontinuities in a rectangular waveguide partially filled with dielectric. *IRE Transactions on Microwave Theory and Techniques*, 5(1):68–74, January 1957. (Cited on page 10)

[7] A.Roure. *Propagation guidée, études des discontinuités.* Theses, Université d'Aix Marseille, 1976. (Cited on page 4)

[8] Y. Aurégan, A. Debray, and R. Starobinski. low frequency sound propagation in a coaxial cylindrical duct: application to sudden area expansions and to dissipative silencers. *Journal of Sound and Vibration*, 243(3):461–473, 2001. (Cited on page 4)

[9] Yves Aurégan, Rudolf Starobinski, and Vincent Pagneux. Influence of grazing flow and dissipation effects on the acoustic boundary conditions at a lined wall. *Acoustical Society of America Journal*, 109:59–64, 01 2001. (Cited on page 130)

[10] Rolf Bader. *Springer Handbook of Systematic Musicology.* 2018. (Cited on page 28)

[11] Eliane Bécache, Anne-Sophie Bonnet-Ben Dhia, and Guillaume Legendre. Perfectly matched layers for the convected Helmholtz equation. *SIAM Journal on Numerical Analysis*, 42(1):409–433, 2004. (Cited on page 21)

[12] Robert P. Benedict. *Handbook of Specific Losses in Flow Systems.* Springer Science & Business Media, 2012. (Cited on page 166)

[13] Jean-Pierre Berenger. A perfectly matched layer for the absorption of electromagnetic waves. *Journal of Computational Physics*, 114(2):185–200, 1994. (Cited on page 21)

[14] Hadrien Beriot and Michel Tournour. Perfectly matched layers for time harmonic acoustics. 01 2016. (Cited on pages 21 and 23)

[15] Susann Boij. Flow effects on the acoustic end correction of a sudden in-duct area expansion. *The Journal of the Acoustical Society of America*, 126(3):995–1004, 2009. (Cited on page 28)

[16] Susann Boij and B. Nilsson. Reflection of sound at area expansions in a flow duct. *Journal of Sound and Vibration*, 260(3):477–498, 2003. QC 20100429. (Cited on page 4)

[17] Simon Bouley. *Modélisations analytiques du bruit tonal d'interaction rotor / stator par la technique de raccordement modal.* PhD thesis, 01 2017. (Cited on pages 10 and 82)

[18] Simon Bouley, Arthur Finez, and Michel Roger. Rotor-stator wake-interaction tonal noise modeling with an edge-dipole approach. In *22nd AIAA/CEAS Aeroacoustics Conference*, Lyon, France, 2016. (Cited on pages 10, 52, 53, and 154)

[19] Simon Bouley, Benjamin François, Michel Roger, Hélène Posson, and Stéphane Moreau. On a two-dimensional mode-matching technique for sound generation and transmission in axial-flow outlet guide vanes. *Journal of Sound and Vibration*, 403:190–213, 2017. (Cited on pages 4, 52, and 53)

[20] E. J. Brambley and N. Peake. Sound transmission in strongly curved slowly varying cylindrical ducts with flow. *Journal of Fluid Mechanics*, 596:387–412, 2008. (Cited on pages 5 and 62)

[21] Guillaume Brès, Franck Pérot, and David Freed. Properties of the lattice boltzmann method for acoustics. In *15th AIAA/CEAS Aeroacoustics Conference (30th AIAA Aeroacoustics Conference).* (Cited on page 4)

[22] Hadrien Bériot, Albert Prinn, and Gwénaël Gabard. Efficient implementation of high-order finite elements for helmholtz problems. *International Journal for Numerical Methods in Engineering*, 106(3):213–240, 2016. (Cited on page 21)

[23] Karal F C. The analagous acoustical impedance for discontinuities and constrictions of circular cross-section. *J Acoustic Soc*, pages 25:327–34, 1953. (Cited on page 4)

[24] I.-J. Chang and A. Cummings. Higher order mode and multimode acoustic transmission through the walls of flat-oval ducts. *Journal of Sound and Vibration*, 108(1):157–164, 1986. (Cited on page 62)

[25] C. J. Chapman. Sound radiation from a cylindrical duct. part 1. ray structure of the duct modes and of the external field. *Journal of Fluid Mechanics*, 281:293–311, 1994. (Cited on pages 110 and 111)

[26] Zhiming Chen and Xinming Wu. An adaptive uniaxial perfectly matched layer method for time-harmonic scattering problems. *Numerical Mathematics: Theory, Methods and Applications*, 1, 05 2008. (Cited on page 21)

[27] Y. C. Chong, D. A. Staton, M. A. Mueller, and J. Chick. Pressure loss measurement in rotor-stator gap of radial flux electrical machines. In *2014 International Conference on Electrical Machines (ICEM)*, pages 2172–2178, 2014. (Cited on page 175)

[28] Yew Chuan Chong. *Thermal analysis and air flow modelling of electrical machines.* PhD thesis, 06 2015. (Cited on pages xix, xx, 168, 174, 175, and 176)

[29] Yew Chuan Chong, Dave A. Staton, Markus A. Mueller, and John Chick. An experimental study of rotational pressure loss in rotor-stator gap. *Propulsion and Power Research*, 6(2):147–156, 2017. Volume 6 Issue 2 (Special Issue) 2017. (Cited on page 175)

[30] A. Cummings and I.-J. Chang. Noise breakout from flat-oval ducts. *Journal of Sound and Vibration*, 106(1):17–33, 1986. (Cited on page 62)

[31] A. Cummings and I.-J. Chang. Sound propagation in a flat-oval waveguide. *Journal of Sound and Vibration*, 106(1):35–43, 1986. (Cited on page 62)

[32] Erkan Dokumacı. *Duct Acoustics: Fundamentals and Applications to Mufflers and Silencers.* Cambridge University Press, 2021. (Cited on page 4)

[33] D.S.Miller. *Internal flows systems. Second edition.* BHRA (Information services), 1990. (Cited on pages 166 and 168)

[34] Yuting Duan. *Trapped modes and acoustic resonances.* PhD thesis, , 2004. (Cited on page 58)

[35] P.E. Duncan and B. Dawson. Reduction of interaction tones from axial flow fans by suitable design of rotor configuration. *Journal of Sound and Vibration*, 33(2):143–154, 1974. (Cited on page 53)

[36] Ignaicio Duran and Stephane Moreau. Numerical simulation of acoustic and entropy waves propagating through turbine blades. In *19th AIAA/CEAS Aeroacoustics Conference*. (Cited on page 125)

[37] Bruno Eck. *Fans: Design and Operation of Centrifugal, Axial-flow, and Cross-flow Fans*. Pergamon Press, 1973. (Cited on page 163)

[38] D. V. EVANS. Trapped acoustic modes. *IMA Journal of Applied Mathematics*, 49(1):45–60, 01 1992. (Cited on page 58)

[39] Donald Ewald, Armin Pavlovic, and John G. Bollinger. Noise reduction by applying modulation principles. *The Journal of the Acoustical Society of America*, 49(5A):1381–1385, 1971. (Cited on page 53)

[40] Simon Félix and V. Pagneux. Multimodal analysis of acoustic propagation in three-dimensional bends. *Wave Motion*, 36(2):157–168, August 2002. (Cited on pages 5, 62, 102, and 154)

[41] Y.A. Fiagbedzi. Reduction of blade passage tone by angle modulation. *Journal of Sound and Vibration*, 82(1):119–129, 1982. (Cited on page 53)

[42] S. Félix and V. Pagneux. Sound propagation in rigid bends: A multimodal approach. *The Journal of the Acoustical Society of America*, 110(3):1329–1337, 2001. (Cited on pages 5, 62, 102, and 154)

[43] S. Félix and V. Pagneux. Sound attenuation in lined bends. *The Journal of the Acoustical Society of America*, 116(4):1921–1931, 2004. (Cited on page 102)

[44] Simon Félix. *Propagation acoustique dans les guides d'ondes courbes et problème avec source dans un écoulement cisaillé*. PhD thesis, 2002. (Cited on pages 5 and 154)

[45] Leo Girier, Michel Roger, Hadrien Beriot, Anthony Lafitte, and Hélène Posson. A Two-Dimensional Model of Sound Transmission Through Curved and Staggered OGV: Effect of Inter-Vane Channel Mode Transitions. In *25th AIAA/CEAS Aeroacoustics Conference*, Delft, France, 2019. American Institute of Aeronautics and Astronautics. (Cited on pages 4 and 62)

[46] Goldstein. *Aeroacoustics*. New York: McGraw-Hill International Book Co, 1976. (Cited on page 138)

[47] Alain Guedel. *Acoustique des ventilateurs, Génération du bruit et moyens de réduction*. Pyc livres, 1999. (Cited on page 3)

[48] Alain Guedel. *Fan Acoustics Noise Generation and Control Methods*. Amca, 2007. (Cited on page 3)

[49] Alain Guedel. *Les ventilateurs, bruit et techniques de réduction*. Dunod, 2015. (Cited on page 3)

[50] Donald Hanson. Acoustic reflection and transmission of rotors and stators including mode and frequency scattering. 1997. (Cited on pages 125 and 138)

[51] F. Hecht. New development in freefem++. *Journal of Numerical Mathematics*, 20(3-4):251–266, 2012. (Cited on pages 22 and 162)

[52] Cyril W. Hirt, Anthony A. Amsden, and J. L. Cook. An arbitrary lagrangian-eulerian computing method for all flow speeds. *Journal of Computational Physics*, 135:203–216, 1997. (Cited on page 125)

[53] Dorel Homentcovschi and Ronald N. Miles. A re-expansion method for determining the acoustical impedance and the scattering matrix for the waveguide discontinuity problem. *The Journal of the Acoustical Society of America*, 128(2):628–638, 2010. (Cited on page 14)

[54] Dorel Homentcovschi and Ronald N. Miles. The analysis of plane discontinuities in offset cylindrical waveguides. *The Journal of the Acoustical Society of America*, 137(6):3127–3138, 2015. (Cited on page 63)

[55] Ruifeng Huang and Daming Zhang. Application of mode matching method to analysis of axisymmetric coaxial discontinuity structures used in permeability and/or permittivity measurement. *Progress in Electromagnetics Research-pier - PROG ELECTROMAGN RES*, 67:205–230, 01 2007. (Cited on page 10)

[56] Herbert Hudde and Uwe Letens. Scattering matrix of a discontinuity with a nonrigid wall in a lossless circular duct. *The Journal of the Acoustical Society of America*, 78(5):1826–1837, 1985. (Cited on page 4)

[57] Isaak E. Idelchik. *Handbook of Hydraulic Resistance*. Begell House, New York, 4 edition, 2007. (Cited on pages xviii, xix, xx, 166, 167, 168, and 169)

[58] Johanna Ingenito. *Vers une modélisation d'aide à la conception acoustique d'étages de compresseurs subsoniques de turbomachines*. PhD thesis, 2010. Thèse de doctorat dirigée par Roger, Michel Acoustique Ecully, Ecole centrale de Lyon 2010. (Cited on pages 10, 130, and 147)

[59] Johanna Ingenito and Michel Roger. Analytical modelling of sound transmission through the passage of centrifugal compressors. In *13th AIAA/CEAS Aeroacoustics Conference (28th AIAA Aeroacoustics Conference)*, Rome, Italy, 2007. (Cited on pages 4, 5, 10, 82, 130, and 147)

[60] Johanna Ingenito and Michel Roger. Measurement and prediction of the tonal noise of a centrifugal compressor at inlet. In *15th AIAA/CEAS Aeroacoustics Conference (30th AIAA Aeroacoustics Conference)*, Miami, Florida, 2009. (Cited on pages 5 and 62)

[61] S. Kaji and T. Okazaki. Generation of sound by rotor-stator interaction. *Journal of Sound and Vibration*, 13(3):281–307, 1970. (Cited on page 3)

[62] Jean Kergomard. Calculation of discontinuities in waveguides using mode-matching method: An alternative to the scattering matrix approach. *J. Acoustique*, 4:111–138, 01 1991. (Cited on page 10)

[63] Seyed Ali Kholghi, Sina Karbalaee M, and Mehdi Ashjaee. Analysis of air flow and heat transfer in a winding using porous medium approach. *International Communications in Heat and Mass Transfer*, 112, 02 2020. (Cited on pages xix, 176, and 177)

[64] Joon-Hyung Kim, Ho-Cheol Ki, and Sung-Jun Byun. Improving the design of the traction motor of trains to reduce the aerodynamic noise. *Proceedings of the Institution of Mechanical Engineers, Part F: Journal of Rail and Rapid Transit*, 234(1):3–16, 2020. (Cited on page 4)

[65] R. J. Kind. Prediction of Flow Behavior and Performance of Squirrel-Cage Centrifugal Fans Operating at Medium and High Flow Rates. *Journal of Fluids Engineering*, 119(3):639–646, 09 1997. (Cited on page 163)

[66] M. L.Munjal. *Acoustics of ducts and mufflers*, page 51. Department of Mechanical Engireening. Indian Institute of Science. Bangalore. India, 1987. (Cited on pages 4, 28, and 62)

[67] Serge Léwy. Theoretical study of the acoustic benefit of an open rotor with uneven blade spacings. *The Journal of the Acoustical Society of America*, 92(4):2181–2185, 1992. (Cited on page 53)

[68] Cheuk Ming Mak and Wing Man Au. A turbulence-based prediction technique for flow-generated noise produced by in-duct elements in a ventilation system. *Applied Acoustics*, 70(1):11–20, 2009. (Cited on page 3)

[69] Cheuk Ming Mak, Xu Wang, and Zhengtao Ai. Prediction of flow noise from in-duct spoilers using computational fluid dynamics. *Applied Acoustics*, 76:386–390, 2014. (Cited on page 3)

[70] Agnès Maurel, Jean-François Mercier, and Vincent Pagneux. Improved multimodal admittance method in varying cross section waveguides. *Proceedings of the Royal*

*Society A: Mathematical, Physical and Engineering Sciences*, 470(2164):20130448, 2014. (Cited on pages 5, 62, 102, and 154)

[71] Jean-François Mercier and Agnès Maurel. Acoustic propagation in non-uniform waveguides: revisiting webster equation using evanescent boundary modes. *Proceedings of the Royal Society A: Mathematical, Physical and Engineering Sciences*, 469(2156):20130186, 2013. (Cited on page 102)

[72] R. Mittra. *Analytical techniques in the theory of guided waves.* The Macmillan Company, 1971. (Cited on pages 4 and 10)

[73] Masaaki Mori. Wake-body interaction noise simulated by the coupling method using cfd and bem. In Zambri Harun, editor, *Vortex Dynamics Theories and Applications*, chapter 6. IntechOpen, Rijeka, 2020. (Cited on page 3)

[74] M. L. Munjal. Advances in the acoustics of flow ducts and mufflers. *Sadhana*, 15:57–72, 1990. (Cited on page 4)

[75] Manohar Munjal. Recent advances in muffler acoustics. *International Journal of Acoustics and Vibrations*, 18:71–85, 06 2013. (Cited on page 4)

[76] M.L. Munjal, M.V. Narasimhan, and A.V. Sreenath. A rational approach to the synthesis of one-dimensional acoustic filters. *Journal of Sound and Vibration*, 29(3):263–280, 1973. (Cited on page 4)

[77] W. Neise and G.H. Koopmann. Reduction of centrifugal fan noise by use of resonators. *Journal of Sound and Vibration*, 73(2):297–308, 1980. (Cited on page 3)

[78] W. Neise and Ulf Michel. *Aerodynamic noise of turbomachines.* 07 1994. (Cited on page 3)

[79] A.P. Orfanidis, George Kyriacou, Theodoros Samaras, and J.N. Sahalos. Mode matching analysis of multiple offset coaxial irises in circular waveguide. *Electronics Letters*, 40:127 – 128, 02 2004. (Cited on page 63)

[80] N.C. Ovenden. A uniformly valid multiple scales solution for cut-on cut-off transition of sound in flow ducts. *Journal of Sound and Vibration*, 286(1):403–416, 2005. (Cited on page 62)

[81] V. Pagneux, N. Amir, and J. Kergomard. A study of wave propagation in varying cross-section waveguides by modal decomposition. part i. theory and validation. *The Journal of the Acoustical Society of America*, 100(4):2034–2048, 1996. (Cited on pages 4, 5, 62, 102, and 154)

[82] Miguel Pestana. *Impact of a heterogeneous stator on the rotor-stator interaction-noise: an analytical, experimental and numerical investigation.* PhD thesis, 01 2020. (Cited on page 4)

[83] J. Mugglestone D.Lampard S.J. Pickering. Effects of end winding porosity upon the flow field and ventilation losses in the end region of tefc induction machines. *IEE Proc.-Electr. Power Appl., Vol. 145, No. 5*, September 1998. (Cited on page 176)

[84] D.E.Spencer P.Moon. *Field Theory Handbook. Including Coordinate Systems, Differential Equations and Their Solutions. Second Edition.* Springer-Verlag Berlin Heidelberg NewYork London Paris Tokyo, 1988. (Cited on page 65)

[85] J.Douglas Faires Richard Burden. *Numerical Analysis.* Cengage Learning, Inc, ninth edition edition, 2010. (Cited on pages 67, 78, and 173)

[86] Sjoerd Rienstra. Sound transmission in slowly varying circular and annular ducts with flow. *Journal of Fluid Mechanics - J FLUID MECH*, 380:279–296, 02 1999. (Cited on page 62)

[87] S.W. Rienstra. Acoustic radiation from a semi-infinite annular duct in a uniform subsonic mean flow. *Journal of Sound and Vibration*, 94(2):267–288, 1984. (Cited on pages 65 and 66)

[88] S.W. Rienstra and A. Hirschberg. *An introduction to acoustics.* IWDE report. Technische Universiteit Eindhoven, 2001. (Cited on pages 14, 18, and 66)

[89] M. Roger. Controle de bruit aerodynamique des machines tournantes axiales par modulation de pales. *Acustica*, 80:247–259, 1994. (Cited on pages 53 and 54)

[90] Michel Roger. Analytical modelling of wake-interaction noise in centrifugal compressors with vaned diffuser. In *10th AIAA/CEAS Aeroacoustics Conference*, Manchester, Great britain, 2004. (Cited on pages 4, 5, 10, and 147)

[91] Michel Roger, Stephane Moreau, and Aurelien Marsan. Generation and transmission of spiral acoustic waves in multi-stage subsonic radial compressors. In *20th AIAA/CEAS Aeroacoustics Conference*, Atlanta, GA, 2014. (Cited on pages 4 and 10)

[92] Michel Roger and Stéphane Moreau. Towards cascade trailing-edge noise modeling using a mode-matching technique. In *21st AIAA/CEAS Aeroacoustics Conference*, Dallas, Texas, 2015. (Cited on pages 10, 52, and 154)

[93] Rahul Sen. *Acoustic scattering by discontinuities in waveguides.* PhD thesis, , 1988. (Cited on page 4)

[94] Zhongxiang Shen and R.H. MacPhie. Scattering by a thick off-centered circular iris in circular waveguide. *IEEE Transactions on Microwave Theory and Techniques*, 43(11):2639–2642, 1995. (Cited on page 63)

[95] Wei Tong. Numerical analysis of flow field in generator end-winding region. *International Journal of Rotating Machinery*, Volume 2008, Article ID 692748, 10 pages, 2008. (Cited on page 176)

[96] C. Angelberger V. R. Moureau, O. V. Vasilyev and T. J. Poinsot. *Commutation errors in Large Eddy Simulations on moving grids: Application to piston engine flows*, pages 157–168. 2004. (Cited on page 125)

[97] Miles J W. The analysis of plane discontinuities in cylindrical tube. part 1. *J Acoustic Soc*, pages 17(3):259–17, 1945. (Cited on page 4)

[98] Miles J W. The analysis of plane discontinuities in cylindrical tube. part 2. *J Acoustic Soc*, pages 17(3):259–17, 1945. (Cited on page 4)

[99] Xiaoyu Wang, Di Zhou, and Xiaofeng Sun. Investigation on effect of rotor blades on the sound propagation. 07 2015. (Cited on page 125)

[100] Björn Widenberg. *A General Mode Matching Technique applied to Bandpass Radomes*, volume TEAT-7098 of *Technical Report LUTEDX/(TEAT-7098)/1-33/(2001).* [Publisher information missing], 2001. (Cited on page 10)

[101] Ignacio Zurbano Fernandez. *Reduction of the broadband noise of centrifugal fans used for HVAC in buildings.* Theses, Université de Lyon, July 2021. (Cited on page 3)

[102] Ignacio Zurbano Fernández, Alain Guedel, and Mirela Robitu. Experimental investigation of the noise reduction of a plug fan by leading-edge serrations. 09 2019. (Cited on page 3)

*dernière page de la thèse*

# AUTORISATION DE SOUTENANCE

Vu les dispositions de l'arrêté du 25 mai 2016,

Vu la demande du directeur de thèse

Monsieur M. ROGER

et les rapports de

M. Y. AUREGAN
Directeur de Recherche CNRS - LAUM - Université du Maine - Avenue Olivier Messiaen
72085 Le Mans

et de

M. S. MOREAU
Professeur - Département Génie Mécanique - Université de Sherbrooke - J1K 2R1 - Québec
Canada

**Monsieur OULMI Mohcene**

est autorisé à soutenir une thèse pour l'obtention du grade de **DOCTEUR**

**Ecole doctorale** Mécanique, Energétique, Génie civil, Acoustique

Fait à Ecully, le 16 septembre 2022

Pour le directeur de l'Ecole centrale de Lyon
Le directeur des Formations

Grégory VIAL